UNIVERSITY OF SOUTHAMPTON

Investigation of Steady State Characteristics of Hollow Cathode Internal Plasmas using Optical Emission Spectroscopy

Sabrina Pottinger, MSci

Thesis Submitted for Doctor of Philosophy

Astronautics Research Group
School of Engineering Sciences
October 2005

UNIVERSITY OF SOUTHAMPTON

ABSTRACT

FACULTY OF ENGINEERING AND APPLIED SCIENCES

AERONAUTICS AND ASTRONAUTICS

Doctor of Philosophy

INVESTIGATION OF STEADY STATE CHARACTERISTICS OF HOLLOW CATHODE INTERNAL PLASMAS USING OPTICAL EMISSION SPECTROSCOPY

By Sabrina Pottinger

Electron bombardment ion thrusters are at the forefront of advances in alternative forms of spacecraft propulsion. They offer advantages over chemical rockets in terms of mass savings and propellant utilisation and are suited to missions requiring high specific impulse and high delta V. The technology has been successfully tested on the Deep Space 1 mission and has been proposed for use on more demanding missions to the outer planets.

Electron bombardment ion thrusters may require lifetimes in excess of 50,000 hrs for future missions. In order to extend lifetime and enhance performance the operation of critical components must be thoroughly investigated. One such component is the hollow cathode (HC) acting as the primary electron source for the thruster.

The use of alternative propellants such as argon and krypton must be investigated as they offer cost savings over xenon propellant. Any adverse effects that arise due to the use of these propellants must be identified. The underlying physics of HC operation must be incorporated into the development of accurate theoretical models. To this end experimental data sets may be used for code validation, hence avoiding further costly experimental characterisation and testing.

The hollow cathode internal plasma has been investigated using optical emission spectroscopy. Localised measurements were recorded at three positions along the hollow cathode axis. The insert temperature and plasma parameters have been calculated for various discharge currents, mass flow rates and electrode separations. The ratio of continuum radiation was used to calculate the insert surface temperature and the ratio of discrete spectral line radiation was used to calculate the electron temperature and ionisation fraction. The determined electron temperature values enabled the electron density to be calculated. The dependence of plasma parameters and insert temperature on hollow cathode operating parameters has been assessed.

Acknowledgements

I would like to thank Prof. S. B. Gabriel for instigating this project. He has provided invaluable support throughout and has always made himself available to offer technical advice and assistance.

Thanks are due to Dr. I. M. A. Rudwan who carried out much of the initial work for this investigation in terms of the design and procurement of diagnostic equipment.

Many thanks to N. Wallace and M. Kelly of QinetiQ for the manufacture of the modified hollow cathode, without which this investigation would not be possible.

I would also like to thank the members of the electric propulsion group for technical assistance and moral support. Starting with those who have or are about to graduate, P. Gessini, Dr. F. Crawford, Dr. M. D. Paine and the newer members of the group D. J. Webb and R. Intini Marques.

Many thanks to my office mates C. Schwingshackl who was always happy to help me with various IT related problems, Dr. B. Kumar, D. N. O. Goulty, Dr. G. Gittins and Dr. N. Williams who have now moved on to better things.

I owe a great debt of gratitude to my family. I thank my parents for emphasising the importance of education throughout my childhood and adolescence, the lessons and values they have imparted to me I will never forget. A special thank you to my sisters Sophia and Lisa, I couldn't get by without the both of you and little Zara who always manages to make me smile.

Contents

List of Figures

Chapter 1

Introduction

1.1 The Benefits of Electric Propulsion

The use of ionised gas as a potential method to propel space vehicles was proposed in the early 1900's by pioneers Robert Goddard and Hermann Oberth. Feasibility studies for the development of a new technology and missions appropriate for its use were carried out in the 1950's and established the benefits of electric propulsion for on orbit manoeuvres and interplanetary missions [5]. A rapid development phase followed in the 1950's, encouraged by government funding and culminated in flight tests in the 1960's [6].

A comparison of the performance of electric thrusters to chemical rockets demonstrates the advantages of this technology. Electric thrusters achieve values of specific impulse typically in the range of 1,000–10,000s. This is typically an order of magnitude greater than that achieved by the best chemical rockets; the specific impulse of bi propellant rockets lies in the range of 300–450s [7]. The reason for this improved performance can be seen from the Tsiolkowsky rocket equation (Equ. 1.1) [8],

$$\Delta V = v_E \ln \frac{m_i}{m_f} \tag{1.1}$$

where ΔV is the velocity increment resulting from a thrusting event that causes the spacecraft mass to change from initial mass m_i to the final mass m_f with exhaust velocity v_E. The exhaust velocity achieved by chemical rockets is dependent on the energy released

when chemical bonds are broken, hence chemical rockets are said to be energy limited. In contrast electric thrusters are said to be power limited as the exhaust velocity achieved is dependent on the size of the power plant, which is in turn limited by mass restrictions due to cost. High exhaust velocities of $v_E \sim 10^4 - 10^5 ms^{-1}$ are achieved by electric thrusters compared to $v_E \sim 4 \times 10^3 ms^{-1}$ for bi propellant chemical rockets. As a consequence electric thrusters are suited for missions requiring high ΔV and high specific impulse such as interplanetary missions. The specific impulse I_{SP} is defined as the ratio of thrust F to the propellant mass flow rate $\dot{m}$ multiplied by the acceleration due to gravity at the Earth's surface g, see Equ. 1.2. The specific impulse may also be related to the exhaust velocity, mass flow rate and weight flow rate $\dot{w}$ via Equ. 1.2 [8].

$$I_{SP} = \frac{\dot{m} v_E}{\dot{w}} = \frac{F}{\dot{m} g} = \frac{v_E}{g} \tag{1.2}$$

Electric thrusters provide mass savings in terms of propellant and engine mass (not including power conditioner). They also offer high reliability over long operating lifetimes and high efficiencies associated with the consumption of propellant and power. Typical thrust efficiencies, defined as the ratio of the mean thrust power of the exhaust beam to the input electrical power (Equ. 1.3) achieved by hydrazine resistojets are 88%, lower efficiencies of 43% and 55% are achieved by Hall thrusters and electron bombardment ion thrusters operating on xenon propellant respectively [9]. Although the efficiencies may range from $20 - 70\%$ for ion thrusters and $52 - 77\%$ for Hall thrusters depending on size and power consumption.

$$\eta = \frac{\frac{1}{2}\dot{m} v_E^2}{V_T I_T} = \frac{F v_E}{2 P_T} = \frac{F g I_{SP}}{2 P_T} \tag{1.3}$$

Where F is the effective thrust, $\dot{m}$ is the average mass flow rate, V_T the thruster voltage, I_T the thruster current and P_T is the thruster input power. The benefits offered by electric thrusters relative to conventional rockets have resulted in continued research in the field. Refinement of engine components continues as well as design optimisation in order to further enhance performance and increase engine lifetime.

1.2 Missions for Electric Propulsion Systems

Electric propulsion is now an established field with technology approaching maturity. There is now on offer a variety of electric thrusters with varying levels of design complexity and ranges of performance. Electric thrusters may be classified into three groups [10]:

- **Electrothermal propulsion**. A gaseous propellant is heated electrically and passed through a nozzle; examples of electrothermal engines include resistojets and arcjets.
- **Electromagnetic propulsion** devices operate by applying either an applied or self induced magnetic field. This magnetic field creates a magnetic pressure that results in the acceleration of ionised propellant e.g. pulsed plasma thrusters (PPTs), Hall effect thrusters (HETs) and magnetoplasmadynamic (MPD) thrusters.
- **Electrostatic propulsion**. Ionised propellant is extracted and accelerated by an applied electric field; examples include the colloid thruster, field effect electrostatic propulsion (FEEP), radio frequency ion thruster (RIT) and electron bombardment ion thrusters.

Interest in electrothermal devices has waned as missions require longer lifetimes and high precision thrusting, electrostatic and electromagnetic thrusters are favoured for current missions. Electric thrusters may function in either a primary or secondary propulsion role. Primary propulsion enables the spacecraft to reach its destination and secondary propulsion tasks involve small adjustments once the spacecraft is in the desired orbit. Early operational fights utilized electric thrusters for north–south station keeping (NSSK), correcting for the gravitational pull of the sun and the moon and east–west station keeping (EWSK), correcting for the instabilities caused by the Earth's elliptical shape at the equator [9]. Current and proposed future missions are more ambitious and place increasing demands on propulsion systems.

Electric propulsion systems are now used in primary propulsion roles. The failure of the launcher's upper stage on ARTEMIS (Advanced relay and technology mission satellite)

launched in July 2001 provided the opportunity for an ion propulsion package of two electron bombardment ion thrusters and two RIT assemblies to be used for orbit raising [11]. Initially, two thrusters were operated at a time, producing a thrust of $15mN$ each, which increased the orbit radius at a rate of $\sim 15km$ per day. Failures at a later stage resulted in only one thruster being used. The ion propulsion package was shut down in February 2003 when ARTEMIS achieved its required orbital slot. The capability of electric thrusters to function as the primary propulsion system on interplanetary missions has been discussed in Refs. [12, 13, 14] and was put to the test by the DS1 (Deep Space 1) mission launched in October of 1998 as part of the NSTAR programme (NASA Solar Electric Propulsion Technology Applications Readiness) [15]. During this mission high risk technologies were tested. Electron bombardment ion thrusters with a thrust range of $19-92mN$ were used to perform a 15 minute fly by of asteroid Braille where spectrometer data was collected. Due to the initial success the mission was extended. The spacecraft encountered comet Borrelly after 14000hrs of thruster operation [16]. European Space Agency's (ESA) SMART 1 (Small Mission for Advanced Research in Technology) mission launched in September 2003 utilises a HET model PPS–1350 [17, 18, 19]. This is the first attempt at combining electric propulsion with gravity assists with the objective of getting to the moon. By June 2004 the thrusters had operated for 2535hrs, lunar capture successfully occurred with the spacecraft completing its first orbit on the 19th of November 2004. The mission has accomplished its primary objective of demonstrating the viability of solar electric propulsion and has been granted a one year extension to August 2006. The BepiColumbo mission to Mercury will be propelled by a cluster of ion thrusters capable of achieving a maximum thrust of 200mN each. It will take four years and two months for the ion thrusters to propel the spacecraft to Mercury, the expected launch date is September 2012 [20].

High precision missions are also planned for the future. The Laser Interferometer Space Antenna (LISA) mission will detect and study gravitational waves from massive black holes [21, 22]. For this mission to be successful satellite positions will have to be controlled to nanometer precision. FEEP thrusters have been proposed to provide controlled thrusting in the range of $1-100\mu N$ with a noise level below $0.1\mu N$, higher thrust electric engines such as ion bombardment thrusters or HETs may be used for orbit transfer. The expected

launch date for this mission is 2011. The InfraRed Space Interferometry Mission (IRSI–DARWIN) has the aim of detecting Earth like planets in other solar systems [23]. Five or six coordinated spacecraft will be propelled by FEEP thrusters.

The experimental and operational missions performed to date have demonstrated the capability of electric thrusters to perform a variety of propulsion tasks. Future missions have been planned that require low thrust high accuracy positioning as well as high specific impulse interplanetary missions.

1.3 Motivation of the Study and Novel Aspects

It is advantageous to thoroughly investigate the physical principles underlying the operation of ion propulsion system (IPS) components such as the HC in order to establish sound design principles and the best operating conditions. This results in improved performance for existing models and the accurate design of new models. Although the HC is a critical component of ion bombardment thrusters very little experimental work has been carried out on the plasma discharge within it. This is due to the small scale of the plasma, which makes it difficult to gain physical access to the region under investigation. The high temperature environment of the internal plasma requires diagnostic equipment with a high temperature tolerance to be used and this equipment must not cause plasma perturbations [2]. These factors have prohibited experimental investigations on the internal plasma of commercial models of HCs. These issues have been overcome with the implementation of an original experimental design. A modified T6 HC and novel optical probes described in Chapter 3 have been used to record optical emission spectra at three different axial positions allowing spatial resolution of the internal plasma. This marks the first occasion that a non invasive diagnostic technique has been used to investigate the variation of plasma properties and thermal characteristics as a function of axial position within the insert region of HCs .

The main objectives of the investigation are as follows;

- Determine plasma parameters (electron temperature, density and ion fraction) as

a function of axial distance using optical emission spectroscopy and investigate the possible influence of the propellant gas used.

- Measure the temperature of the insert surface as a function of axial distance and establish the influence of operating parameters such as anode current and propellant flow rate on temperature.
- Gain insight into thermal balance processes and electron emission mechanisms in order to provide an experimental basis for comparison with HC numerical models.
- Aid in the understanding of life limiting factors such as barium depletion and facilitate lifetime calculations that may result in possible design improvements.

It is of paramount importance for the future viability of HCs used for missions requiring extended life and high performance ($I_{sp} > 3000s$) that reliable data for temperature profiles and plasma parameters are obtained. The determination of plasma parameters as a function of axial distance may provide experimental verification of the active region theory discussed in Section 2.4.2. The variation of electron density with axial distance may have implications for future HC design in terms of the chosen insert length. The temperature profile of the insert surface dictates operating stability due to the fact that the electrons are emitted by field enhanced thermionic emission. Therefore the temperature influences electron emission and hence the characteristics of the resulting plasma discharge. The lifetime of the HC is a life limiting factor for ion bombardment thrusters as whole. The main mechanism limiting HC life is the depletion of barium in the insert. The rate of barium depletion is dependent on the operating temperature of the HC. Hence the maximum operating temperature effects HC lifetime and as a consequence the lifetime of proposed mission using IPS. It is imperative that reliable information is obtained for temperature values in order to identify operating conditions that should be avoided in order for HCs to operate at an optimum temperature, hence maximising the lifetime of the component.

1.4 Thesis Outline

Following this introductory chapter, Chapter 2 will provide a background into the principles concerned with the operation of ion bombardment thrusters and HCs. Previous experimental and theoretical work performed on HCs will be reviewed. This will put the current investigation into context and demonstrate the novelty of the work undertaken.

Chapter 3 provides a detailed description of the experimental apparatus used as well as the experimental procedures employed.

Chapter 4 outlines the various plasma models that may be used to analyse laboratory as well as space plasmas. Quantitative spectroscopy techniques that use these models are discussed in the context of how they may be applied in order to determine plasma parameters.

Results are presented in Chapters 5 and 6. This includes a characterisation of the HC performance over a range of operating parameters. The variations in optical emission spectra recorded at difference axial positions are described, followed by a qualitative and quantitative analysis of the spectra. The electron temperature values calculated using a variety of methods are presented. The electron number density is determined, allowing the plasma to be classified at different points along the insert length. The results of the thermal characterisation of the the insert are presented.

A discussion of the experimental results obtained takes place in Chapter 7. The observed trends in the experimental data are analysed and theoretical calculations performed.

The thesis is concluded with a summary of the main research findings and a statement of the future work required.

Chapter 2

Background and Literature Review

2.1 Electron Bombardment Ion Thrusters: Principles of Operation

Electron bombardment ion thrusters, also known as Kaufman–type ion thrusters operate by using electrostatic forces to accelerate ionised gas which produces a propulsive force. The components of the thruster are mounted to a ferromagnetic backplate as shown in Fig. 2.1. The propellant gas (usually xenon) is passed through a cylindrical discharge chamber via a bypass distributor and a hollow cathode. The hollow cathode (HC) produces electrons that interact with the propellant gas, this gas is then ionised in the discharge chamber between the HC and concentric cylindrical anode. The optimum ionisation efficiency is achieved with the application of an azimuthal divergent magnetic field that confines electrons, hence preventing their escape to the anode. The magnetic field is generated by several equispaced solenoids or permanent magnets placed around the outside of the discharge chamber. These solenoids/magnets are connected at one end to an inner polepiece that surrounds a non magnetic baffle disc that separates the coupling plasma (in the region of the HC) from the main discharge plasma. At the opposite end they are connected to an outer polepiece. The ionised plasma moves towards a set of grids at the end of the discharge chamber. These grids extract and accelerate positive ions by the application of electric fields. The velocity achieved by the ions is in the range of $30 - 50kms^{-1}$. The resulting external ion beam

is neutralised by electrons emitted from an external HC known as the neutraliser. The neutraliser HC utilises an enclosed keeper to maintain the discharge and operates on mass flow rates of typically $\dot{m} \leq 0.04mgs^{-1}$. In order to prevent electrons from the external plasma from being attracted to the positive thruster a perforated earth screen surrounds the thruster, electrical isolators are also used on propellant feed lines.

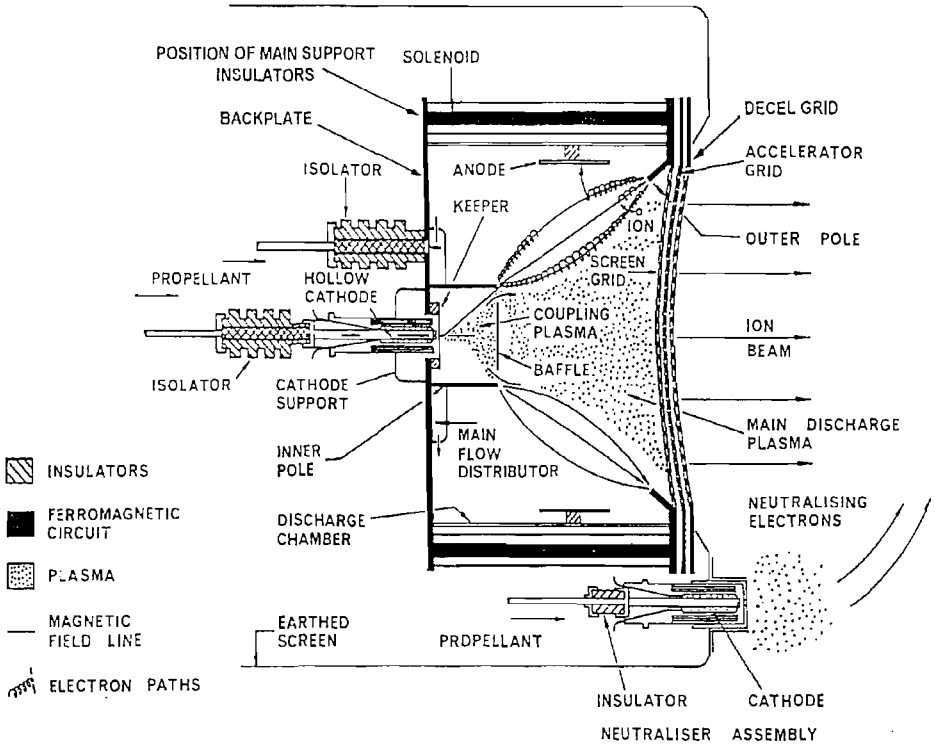

Figure 2.1: Electron bombardment ion thruster schematic [1]

2.2 Electron Bombardment Ion Thruster Development

The Kaufman design developed at the NASA Lewis Research Center in the 1960's described in detail in Ref. [24] has been modified countless times. These modifications were made with the aim of improving the cost, lifetime, performance and reliability of the thruster [25]. Critical modifications have focussed on the following subsystems:

- **The propellant**: Mercury was rejected in favour of inert gas propellants. This was

due to the possible contamination of spacecraft surfaces and the high cost associated with handling mercury for ground testing because of its toxicity. Xenon is now the propellant of choice as it is convenient to store and safe to handle. The propellant feed systems containing vaporisers required for mercury propellant are not needed for inert gases. The high atomic mass of xenon results in a lower thermal speed for a given atomic temperature than for lighter gases such as argon and krypton, causing the rate of loss of neutral species through the grids to be reduced, thus increasing propellant utilisation efficiency. Xenon provides the best balance for meeting performance goals (thruster efficiency increases with increasing atomic weight) and materials compatibility. The main disadvantage of using xenon propellant is it's high cost relative to alternative propellants such as argon and krypton.

- **The grid system**: Changes have been made to the fabrication of grids. Chemical etching is now used in the USA and spark erosion in the UK to create grid apertures instead of drilling. This improves the accuracy of their positioning and reduces cost. A move towards the use of carbon composite materials rather than molybdenum is being made as they provide an extremely low coefficient of thermal expansion over the temperature range of ion thruster operation. They are thin but have high stiffness. These factors prevent thermal warping and unwanted grid deflections. Carbon also has a very low sputtering yield compared to molybdenum, which results in reduced grid erosion and therefore an increase in the lifetime of the grid. Changes in the mounting and alignment of the grids attempt to reduce grid erosion while minimizing beam divergence hence improving lifetime without reducing efficiency.

- **The cathode**: The electron source for ion thrusters has evolved from a filament wire to cylindrical tube containing of an impregnated tungsten insert, as discussed in detail in the following section. The HCs in current use provide a more stable discharge and vastly longer life than previous models and consume considerably less power.

Research continues into improving the durability and performance of ion propulsion systems (IPS) as well as fundamental physics studies. Much knowledge has also been gained

from experimental flights such as SERT I, SERT II and Deep Space 1 [26, 27, 15]. The knowledge and flight experience gained have now been applied to designing IPS for specific applications requiring differing ranges of performance in terms of thrusting capabilities and specific impulse requirements. As a result of this many types of electron bombardment ion thruster exist at present. In the UK alone four different ion bombardment thrusters have been developed over four decades. The UK thrusters differ from others due to three specific features, which result in a narrow beam divergence and a flexibility that is demonstrated by a wide throttling range (200:1 for the T5 thruster) [1]. These features are as follows:

- Inward dishing of grids (opposite to that of similar thrusters). A temperature gradient exists from the inner to outer grid which may lead to thermal expansion. This configuration provides dimensional stability as the thruster warms up, minimizes inter grid arcing and focuses the ion beam.
- External solenoids are used instead of permanent magnets allowing real time control over the plasma conditions but requires an additional power supply.
- Separately controllable flows for the discharge chamber, HC and neutraliser allows independent control of the various components resulting in longer lifetime and improved propellant utilisation.

The four models of UK electron bombardment ion thruster in operation at present are the T5, UK–10, T6 and UK–25 IPS [28]. These models are the product of research and development programmes that began in the 1960's. The first design was a $10cm$ diameter thruster that used mercury propellant and incorporated a filament electron source, and was called the T1. Successful testing of the T1 led to the development of the T2. This model used a HC electron source and provided a thrust of $10mN$ with beam diameter of $10cm$. Although designated and built the T3 truster was never operated. Various T4 models followed, each showing improved performance and lifetimes in excess of $1000hrs$. The flight standard model, the T5 IPS was selected for the ESA H-Sat communications satellite for a NSSK role but this mission was abandoned. A change to xenon propellant was later implemented, and the UK–10 IPS (a triple grid version of the T5) was flown

on the Artemis mission. The UK–10 has now been selected for the Gravity and Ocean Circulation Exploration (GOCE) mission due for launch in 2006 [11, 29]. With increasing interest in interplanetary missions it became apparent that a larger thruster was required for these applications. The UK–25 was developed for this purpose, this model achieved specific impulse approaching $5000s$ and thrusts of $320mN$, greater thrusts may be achieved but this was limited by the pumping ability of the test facility used. To date no mission has been funded that would require the UK–25. As a result an intermediate thruster with beam diameter of $22cm$ and thrust $200mN$ was developed and designated the T6 [30]. There now exists three IPSs that cover three thrust ranges; $1 - 30mN$, $50 - 200mN$ and $200 - 300mN$ for station keeping, orbit raising and interplanetary missions respectively. This range of performance could not be achieved without extensive research into thruster components and support systems.

2.3 The Hollow Cathode

The hollow cathode (HC) is used in electric thrusters as either the primary electron source as is the case for ion bombardment thrusters or as an external neutraliser as shown in Fig. 2.2. HCs may also be used to increase the current collection capacity of tethered satellites as the tether is used to generate electrical power from motion through a geomagnetic field [31, 32]. They may also function as plasma contactors that control the electric potential of spacecraft orbiting in plasma environments [33, 34].

Figure 2.2: T6 truster neutraliser manufactured by QinetiQ

The HC is one of the main components of ion thrusters, affecting the stability of the plasma

discharge produced and hence the thruster performance. The lifetime of the HC is critical in dictating the life of the thruster as a whole, for this reason efforts have been made to study the behaviour of the component and improve its performance as mentioned in the previous section. The electron source in the early ion thrusters was a tungsten or tantalum filament wire, which emitted electrons thermionically [24]. Oxide cathodes consisting of a spiral ribbon of nickel tungsten mesh coated with alkaline earth carbonates that formed the oxide emitter were also used [6]. These electron sources were soon superseded by HCs for the following reasons,

- They are rugged and mechanically simple,
- Possess long lives well in excess of 20,000hrs,
- Restart reliably and repeatedly even after long shutdown periods,
- Can be easily tested on the ground and may even be exposed to the atmosphere.

The HCs in use today consist of a porous tungsten insert impregnated with a mixture of earth metal oxides that lower the workfunction of the material allowing electron emission. The HC insert is surrounded by a tantalum tube closed off at one end with what is referred to as an orificed tip. The orifice diameter is typically an order of magnitude smaller than the insert diameter(see Fig. 2.3). This tube is then surrounded by bifilar heater coils and enclosed in a layer of insulation. The HC outer casing is stainless steel. The HC operates by passing propellant through the dispenser tube. The HC is then heated to a temperature of $T \sim 1000^{o}C$ to facilitate the thermionic emission of electrons. Electrical breakdown then occurs at the keeper electrode, which is at a positive potential. The plasma generated in the region between the keeper and the HC tip then expands into the orifice and via a mechanism which is not understood, an internal plasma is generated. The process of electrical breakdown occurs over a time period of less than one millisecond. The increased electron emission from this plasma results in an electric field being established across the plasma sheath adjacent to the insert surface encouraging further emission. This electron emission mechanism is known as field enhanced thermionic emission. The electrons released from the insert (primary electrons) interact with the propellant gas causing excitation and

ionisation. The resulting plasma is a self sustaining discharge that is expelled through the HC orifice and its electrons are accelerated by the application of external electric fields in order to ionise the main discharge or maintain the neutral charge of a spacecraft.

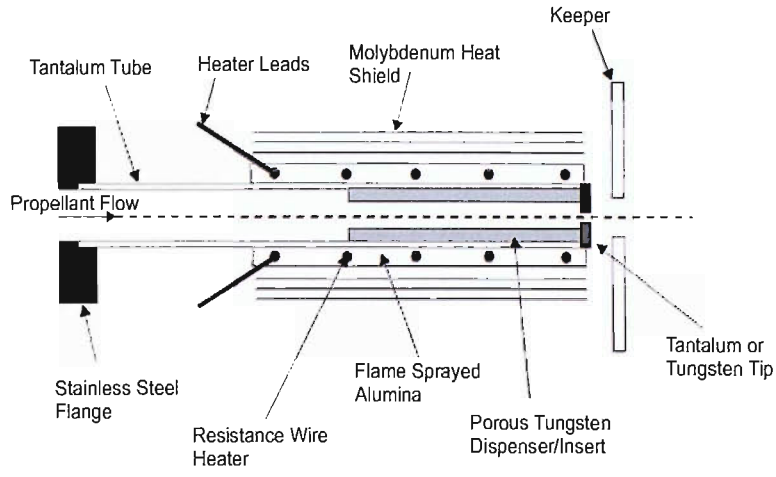

Figure 2.3: Typical hollow cathode schematic

The factors that may cause HC failures are,

- Overheating,
- Insert contamination,
- Cathode sputtering by high energy species.

The first two factors cause barium depletion and impede the release of sufficient quantities of barium thus preventing adequate electron production. These issues may be overcome by good design and the implementation of appropriate operating procedures; propellants of sufficient purity must also be used [35]. The erosion of HC material by sputtering is a more complex problem to overcome as the mechanism that leads to the creation of high energy ions in the region of the HC is not fully understood [36]. The lifetimes of HCs are more than adequate for use on current missions of interest; however, if interplanetary missions propose to use IPS this issue will have to be addressed.

2.4 Mechanisms of Hollow Cathode Operation

2.4.1 Insert Chemistry

The HC impregnate composition is a $4:1:1:$ mixture of $BaO:CaO:Al_2O_3$, where the ratio represents the stoichiometric coefficient of the earth metal oxides. Heating the HC to approximately 1000^oC causes the impregnate to react with the tungsten matrix producing gaseous free Ba. The thermal decomposition of impregnate materials may be represented by Equ. 2.1 which shows the dominant reaction for the production of free Ba [37].

$$6BaO(g) + W(s) \rightleftharpoons Ba_3WO_6(s) + 3Ba(g) \tag{2.1}$$

The Ba spreads over the porous tungsten surface forming a monolayer. This Ba monolayer is strongly bonded to the tungsten surface by an underlying monolayer of oxygen resulting in a reduction of the workfunction of the material from $4.5eV$ to $2.1eV$ [38]. This decreased workfunction facilitates the thermionic emission of electrons.

The chemistry of the HC impregnate is critically important for the component's operation in terms of electron emission and lifetime. The diffusion of impregnate material along the pores of the tungsten insert not only replenishes the Ba monolayer but may also cause blockages of the pores that prohibit further Ba production. The impregnate material may also react with impurities to produce contaminants such as $BaWO_4$ and Ba_2CaWO_6 that poison the insert surface. These impurities may cause the workfunction of the material to increase by displacing the Ba on O monolayer. Operating the HC at high temperatures causes Ba evaporation and loss through the orifice. These factors may result in decreased electron emission. For these reasons the stability of electron emission as a function of time, operating temperature and Ba depletion continue to be studied in an attempt to understand Ba loss mechanisms, hence increasing HC lifetime and improving performance.

2.4.2 Emission Mechanisms

The thermionic emission of electrons results in an increase in electron density near the insert surface. For the case of the HC a plasma sheath forms, which has a thickness of

the order of a few Debye lengths (see Equ. 2.14). As the electron number density is high ($\sim 10^{18} - 10^{20} m^{-3}$) and the electron temperature moderate ($\sim 1eV$) the sheath thickness is small therefore the resulting the potential across the sheath gives rise to a large electric field. This electric field, which further assists electron emission as the applied field causes a further decrease in the materials workfunction. This is known as field enhanced thermionic emission or Schottky emission and is thought to be the main emission mechanism for HCs. The electron current density produced via this mechanism is described by Equ. 2.2 [39].

$$j_e = A_o T^2 \exp\left(-\frac{e\phi_{eff}}{kT}\right) \tag{2.2}$$

Where j_e is the current density, $A_o = 1.2 \times 10^6 Am^{-2}K^{-2}$ is the Richardson constant, k is Boltzmann constant, T is the temperature of the insert, e is the electron charge and ϕ_{eff} is the effective work function. The effective work function is related to the surface workfunction, ϕ_s by Equ. 2.3, where E is the electric field strength and ϵ_o is the permittivity of free space.

$$\phi_{eff} = \phi_s - \left(\frac{e|E|}{4\pi\epsilon_o}\right)^{\frac{1}{2}} \tag{2.3}$$

Alternative processes often referred to as secondary emission mechanisms may further enhance electron emission. Electrons may be released from the insert surface by impact from ions or metastable species. Ionisation of the bulk plasma also contributes to the total emission. Electromagnetic radiation incident on the insert surface may cause electrons to be released (this is known as the photoelectric effect), but the contribution of photoelectrons to the overall emission current is thought to be negligible. Secondary electron emission is thought to contribute less than 5% to the electron current for mercury HCs and less than 1% for HCs operating on xenon [2, 39].

Electron emission is not uniform throughout the length of the HC. Plasma and temperature gradients exists in the axial direction, which influences the electron density released from a given point. The zone responsible for the majority of the observed electron current density is referred to as the active region. This region was thought to be centred at the point of maximum temperature but this explanation was not applicable to all conditions. At high mass flow rates where the active region is near the HC tip ($\approx 3mm$) the theory is adequate, however at low mass flow rates the maximum temperature may occur several

centimetres from the tip showing that the maximum temperature and maximum electron current density do not always occur at precisely the same position [40]. This discrepancy may occur because electric fields were not considered, therefore this theory is not valid for HCs with a main electron emission mechanism of field enhanced thermionic emission. The position and the extent of the active region is also influenced by neutral gas pressure. An empirical theory was suggested by Delcroix and Trindade in the 1970s stating that the active region occurred at the position where the neutral gas pressure was constant at $\sim 2\ Torr$ ($\sim 267Pa$) for constant discharge current, but this observation was not true for all HC diameters and geometries [40, 41]. The theory was developed to consider atomic processes. The active region was thought to be established where the neutral gas density was most suitable for metastable atom production. Assuming that ionisation occurs by electron impact and fast electrons released from the insert have an energy of $12eV$ (for a tantalum HC tube operating on argon), a neutral density of $2 \times 10^{16} cm^{-3}$ was determined for the active region using a balance equation of metastable production. This approach over – simplified the problem by not considering the inhomogeneity of the HC sheath and is therefore is only applicable to short HCs. A complete theory describing the nature of the active region has yet to be developed.

2.4.3 Thermal Balance

The processes which contribute to internal HC heating in order of importance are as follows: 1) Ion bombardment, 2) Joule heating in the bulk material, 3) Atomic bombardment, 4) Bombardment by electrons and 5) Radiation from the plasma. Thermal energy is dissipated via the following processes: 1) Electron extraction, 2) Surface evaporation, 3) Thermal conduction and 4) Radiation to the plasma.

The main mechanisms responsible for heat input and output for HCs result as a consequence of processes that occur at the interface between the plasma and the insert. At this interface the plasma is adjacent to a solid surface, therefore charge neutrality does not apply; this region is known as the plasma sheath or space charge zone [42]. The intermediate region between the sheath and the bulk plasma is referred to as the presheath or ionisation

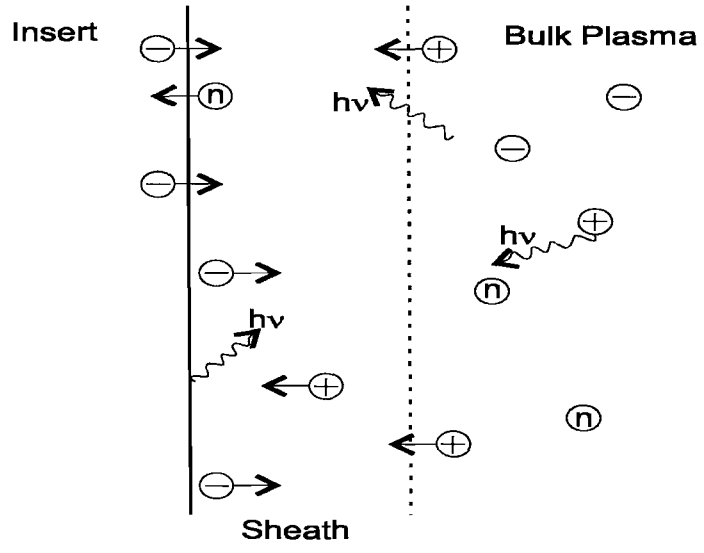

Figure 2.4: Interface between the plasma and insert surface

zone, see Fig. 2.4. The electrons are accelerated towards the plasma by the potential drop in the sheath; on reaching the presheath region they have acquired the energy to excite or ionise atoms. The ionised species accelerate towards the insert surface according to the Bohm criterion [43, 44]. This criterion is requisite for the formation of a stable stationary sheath. The Bohm criterion dictates that ions cross the plasma sheath boundary at a velocity, v_i that is equal to or greater than the ion sound velocity, c_s.

$$v_i \geq c_s \geq \sqrt{\frac{kT_e}{m_i}} \tag{2.4}$$

$$v_B = \sqrt{\frac{kT_e}{m_i}} \tag{2.5}$$

Where m_i is the ion mass, T_e is the electron temperature and k is Boltzmann constant. The ions therefore cross the sheath edge at a minimum velocity equal to the Bohm velocity v_B (see Equ. 2.5) and bombard the insert surface causing heating. The heat flux to the insert q_i resulting as a consequence of ion bombardment is shown by Equ. 2.6 [45].

$$q_i = j_i\{\varphi + \frac{1}{e}(\chi - \phi_{eff})\} \tag{2.6}$$

Where φ is the potential drop across the sheath, χ is the first ionisation potential and j_i is the ion current density as shown by Equ. 2.7 for an ion number density n_i.

$$j_i = en_i v_B \tag{2.7}$$

The contribution to the thermal energy input by Joule heating is described in terms of the HC electrical resistivity ρ and the current density in the HC body j_{cat} (see Equ. 2.8).

$$q_j = \rho j_{cat}^2 \tag{2.8}$$

The Joule effect is caused by electric current passing through a material and contributes to heating the bulk of the insert as well as its surface.

The remainder of the processes stated above input a small fraction of thermal energy to the insert compared with ion bombardment. The heat flux on the insert surface induces vaporisation and the emission of atoms. Only a small proportion of these atoms relative to ions return to the surface as they must possess a sufficient velocity component in the direction of the insert. The same argument holds for electron bombardment as they must possess sufficient energy to overcome the potential drop across the sheath.

The internal plasma emits electromagnetic radiation that interacts with the insert causing heating; this may be balanced by the insert dissipating energy by the emission of radiation. The radiation from a plasma at temperature T_{pl} provides a heat flux to the insert q_{pl} while the opposite process radiates heat q_s from the insert surface at temperature T as shown by the Stefan–Boltzmann formula for an optically thin plasma, see Equ. 2.9 and Equ. 2.10.

$$q_{pl} = \epsilon(\lambda, T_{pl})\sigma T_{pl}^4 \tag{2.9}$$

$$q_s = \epsilon(\lambda, T)\sigma T^4 \tag{2.10}$$

Where $\epsilon(\lambda, T_{pl})$ and $\epsilon(\lambda, T_{pl})$ are the emissivities of plasma and the insert surface respectively, both parameters are a function of wavelength λ and temperature.

Insert heating via ion bombardment is counter balanced by electron emission. The extraction of electrons from the porous tungsten insert is an endothermic process that results in the cooling of the insert surface and is the main heat loss mechanism. The heat loss due to electron extraction q_c is shown by Equ. 2.11

$$q_c = \frac{1}{e}\underbrace{A_o T^2 \exp\left(-\frac{e\phi_{eff}}{kT}\right)}_{je}\phi_{eff} \tag{2.11}$$

The emission of surface atoms from the insert also cools the HC. Heat may also be transported away from the insert surface by thermal conduction.

The mechanisms stated above may be grouped together to form a thermal balance equation for the HC insert. For the steady state case there is no variation in temperature over temperature over time for constant operating parameters.

$$0 = -\kappa \nabla^2 T + q_{NET} \tag{2.12}$$

Where κ is the thermal conductivity and q_{NET} is the net thermal flux.

$$0 = -\kappa \nabla^2 T + j_i\{\varphi + \frac{1}{e}(\chi - \phi_{eff})\} + \rho J_{cat}^2 + \sigma(\epsilon(\lambda, T_{pl})T_{pl}^4 - \epsilon(\lambda, T)T^4) - \frac{1}{e} j_e \phi_{eff} \tag{2.13}$$

Equ. 2.13 considers the main contributions to HC heating/cooling [46]. The second to fourth terms represent energy inputs to the HC via ion bombardment, Joule heating and radiation heating respectively. The first and final terms represent cooling via conduction and electron extraction. As previously mentioned it is of key importance that the thermal processes occurring within the HC are understood in order to increase lifetime and enhance performance.

2.4.4 Hollow Cathode Modes of Operation

The steady state operation of HCs cannot be described in terms of a single type of discharge. The performance of the HC is critically dependent on external factors including the HC configuration i.e. the position and dimensions of the electrodes used. HCs are typically tested as components in isolation with a pair of electrodes (diode configuration) mounted concentrically in order to facilitate the formation of a stable plasma. The performance of the HC in these test configurations shows differences to that observed for HCs in a thruster configuration. Two distinct modes of operation are typically observed when HCs are tested in either open diode or diode configuration: 1) The plume mode and 2) The spot mode. This is not the case for HCs operating in a thruster configuration where only the spot mode appears to be observed.

The plume mode is characterised by a high voltage noisy discharge; a bright luminous plume extends downstream of the HC tip. The plume mode occurs at low mass flow rates, low discharge currents and large anode to HC separations. The spot mode is associated with a low voltage, low noise discharge. An intense luminous spot is observed near the orifice. The spot mode occurs for high mass flow rates, high discharge currents and small anode to HC separations. The transition between the two modes occurs rapidly if operating

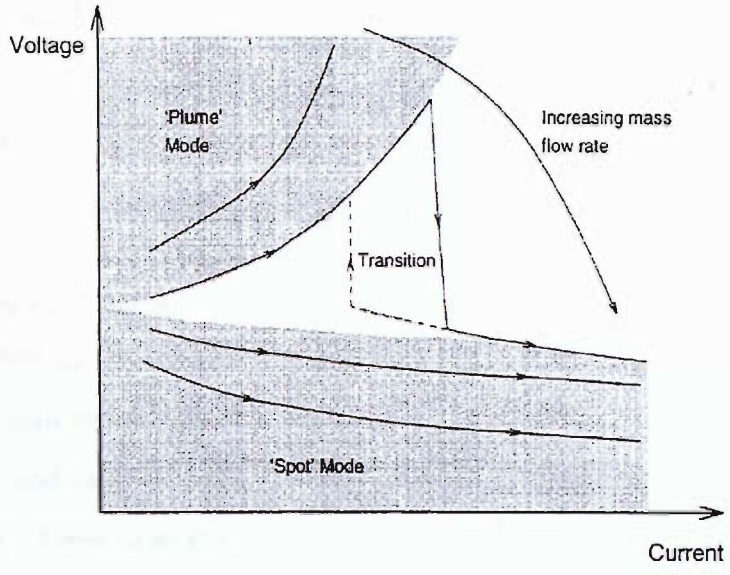

Figure 2.5: Current voltage characteristics for the spot to plume mode transition

parameters such as mass flow rate and discharge current are varied and is accompanied by hysteresis as shown by Fig. 2.5.

A variety of theories have been put forward in an attempt to explain mode change characteristics. The physical phenomena that may be responsible for plume to spot mode transitions are listed below.

- Movement of the HC sheath boundary
- Expansion of current emission from the orifice
- Keeper current collection mechanism
- Anode current collection mechanism

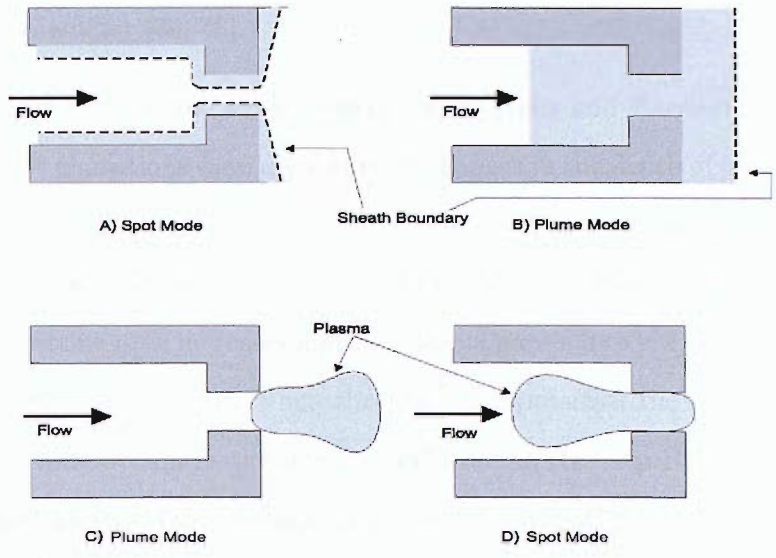

Figure 2.6: Theories of Mode change characteristics

Csiky performed experiments on a HC in the diode configuration operating on mercury propellant in 1969 [47]. Langmuir probes placed in the plume region (measurements were taken no closer than 3mm to the tip) were used to determine the plasma potential, electron number density and electron temperature, an optical pyrometer was used to estimate the tip temperature. These experimental values were used to determine the sheath thickness over the HC inner surface. It was found that the sheath thickness was 3% of the orifice diameter ($\sim 7 \times 10^{-6} m$) for the spot mode whilst for the plume mode the sheath thickness was approximately equal to the orifice diameter ($\sim 3 \times 10^{-5} m$). The position of the sheath edge appeared to correlate with the observed modes, the sheath boundary was said to be inside the HC for the spot mode (see Fig. 2.6A) but extended beyond the HC for the plume mode (see Fig. 2.6B). The high degree of ionisation observed for the spot mode suggested that the electrons were confined to the orifice region by the internal sheath hence explaining the visual appearance of the intense spot. Whilst operating in the plume mode the extended sheath does not confine electrons, this results in the appearance of a bright plume. Although this theory appears to explain the visual differences between the modes the conclusions drawn are inconsistent with later research. Subsequent investigations have shown that the electron density in the spot and the plume mode are approximately equal and the sheath thickness for both operating modes is at least an order of magnitude smaller

than the orifice diameter [39, 48].

Philip reported in 1971 on the work carried out by Wells and Harrison on mercury HCs where plume/spot transitions were attributed to changes in the depth of plasma penetration [49]. The plume mode was thought to arise due to electron emission occurring at the furthest downstream position of the orifice. As the current drawn from the HC increases the size of the emitting area increases and the plasma moves into the orifice. The transition from plume to spot mode occurs when the plasma approaches the upstream edge of the orifice, emission then occurs at the internal walls of the HC (see Fig. 2.6C and D). This explanation does not take into account the effect of mass flow rate on mode change or the influence of the HC configuration.

A theoretical investigation carried out by Mandell proposed that mode changes occur due to current collection mechanisms associated with the keeper electrode [50]. This theory is based on the principle of current balance. It was suggested that at high mass flow rates and discharge currents, ion production was sufficient that the keeper was able to "passively" collect current via diffusion processes. For the case of a passive current that is greater than the discharge current the keeper will be negative with respect to the plasma potential, therefore electron acceleration towards the keeper is less likely to occur and the HC operates in the spot mode. If the passive current is less than the discharge current the keeper must actively collect charge, a positive sheath forms in the region of the keeper that accelerates electrons resulting in a luminous glow and the plume mode. This theory does not explain the persistence of mode changes when the HC is operated in the open diode configuration.

It has been suggested that the keeper electrode is typically able to collect current passively as it is located in close proximity to the HC it is in a region of high current density. An alternative anode current collection mechanism has been described by Rudwan which, is based on the fact that the current collection capabilities of an electrode are dependent on its surface area [2]. An electrode that is positively charged with respect to the surrounding plasma will collect electrons in its vicinity that form a sheath. This electron sheath will act as a shield, therefore the field of the electrode will have no effect on the plasma beyond the

outer edge of the sheath. As a consequence the current collected by the anode is dependent on the rate of arrival of electrons to the outer edge of the sheath; if sufficient discharge current cannot be collected the anode potential increases to a point where ionisation may occur in the sheath by accelerating electrons interacting with the gas. This results in the breakdown of the sheath and the development of a luminous region characterised by a positive inner space of high ionisation surrounded by a layer of negative charge referred to as a double layer. The outer edge of the double layer becomes the new collection area for electrons. This region of positive charge enveloped by electrons is known as the "virtual anode". When operating the HC with low discharge currents and mass flow rates, current collection is limited, the sheath breaks down and a virtual anode is formed with a larger area that is capable of collecting a greater current; this represents the plume mode. The spot mode occurs for passive current collection. This theory is in agreement with plasma potential and electron number density profiles obtained from Langmuir probe experiments [39]. The presence of anode noise is said to be due to the impingement of the double layer into the keeper/HC space causing perturbations and interfering with electron emission. To date this provides the most complete explanation of mode change characteristics and the associated physical phenomena. However, this theory only provides a qualitative analysis. Mode change may be influenced by factors other than external electrode geometry. The orifice geometry i.e. aspect ratio has been shown to effect changes from spot to plume mode and these factors must be incorporated into the theory of mode change characteristics.

2.5 Experimental Investigations

Early research on HCs was concerned with design optimisation and the manufacture of cathodes with long life and reproducible performance. The work of Charlton et. al. in the 1970's characterised HCs using mercury propellant in the diode configuration [51]. Cathodes were run with a few starts for up to 2400 hrs with a current of $3A$ and voltages of $12-15V$. Ion bombardment was found to cause tip erosion. This erosion was dependent on discharge energy and tip temperature and was found to worsen as orifice diameter decreased. The main cause of HC failure was erosion of the weld between the HC wall and

tip. It was found that the cause of this erosion was chemical attack due to residual gases in test equipment, therefore this process would not affect the HC in space. Orifice blocking due to deposited material also resulted in end of life. Barium dispensers/inserts were found to improve starting and HC current voltage characteristics. Two types of insert were investigated: a roll of tantalum foil coated in barium strontium carbonate and a porous tungsten tube impregnated with barium calcium aluminate. Tantalum foil became brittle after use, not facilitating long life. Tungsten inserts were found to have greater reservoirs of barium, which evolved controllably resulting in an easier start up. This design is still in use today as it is rugged and defines the geometry inside of the cathode, but it initially requires a higher plasma potential to facilitate a stable discharge. Current voltage characteristics were recorded at constant mass flow rates for $I = 1 - 4A$ and transitions between plume and spot mode were observed. This transition occurred at higher currents as mass flow rate decreased in agreement with the theory stated in Sec. 2.4.4. The mass flow rate was found to relate inversely to tip temperature at constant current. Tip temperature is also a function of current increasing as current is increased. Temperatures approaching $2000^{o}C$ were recorded for $I = 4A$. These findings formed the basis for future HC designs.

2.5.1 Mercury Hollow Cathodes

An experimental investigation was carried out on HCs operating on mercury propellant by Csiky in the late 1960's [47, 52]. The type of HC investigated was the same model as that used for the SERT II mission. A cylindrical Langmuir probe was used in the external discharge region to measure plasma potential, electron density and electron temperature. The HC used was in diode configuration with the anode distance varied between $0.2cm$ (for open diode configuration) to $7.2cm$, in this case a keeper electrode was used. It was found that the HC's mode of operation was influenced by the anode distance. Plume mode occurred for large anode distances and low mass flow rates while for spot mode the anode distance was small and high mass flow rates were used. Langmuir probe traces were taken along the discharge axis of symmetry as well as off axis. The measurements showed that the electron density in the spot mode was higher than that in the plume mode and the

degree of ionisation was also higher. The plasma potential was uniform at $\approx 11V$ for both modes. Typical values of the electron temperature and density were as follows: for the spot mode $T_e = 0.5eV$, $n_e \approx 10^{18}m^{-3}$; for the plume mode $T_e = 1.0-2.3eV$, $n_e \approx 10^{17}m^{-3}$. At that time a satisfactory model for the steady state operation of the HC was not available. It was suggested that the sheath thickness is of the order of the Debye length λ_D,

$$\lambda_D = \sqrt{\frac{kT_e\epsilon_o}{n_e e^2}} \tag{2.14}$$

Spot to plume mode transitions were related to this thickness as discussed in Sec. 2.4.4 but later investigations showed that the electron number density in both modes of operation are approximately equal.

Fearn et. al. put forward conclusions regarding the physical processes occurring within the HC based on experimental data [53]. Electron emission in the HC was said to occur at current densities of $j_e = 2 - 5 \times 10^5 Am^{-2}$. The mechanisms suggested include field enhanced thermionic emission and the release of electrons due to the impact of metastable atoms on the insert surface. A Langmuir probe was placed near the keeper orifice and another was inserted into the HC to determine the internal plasma parameters. It was found that the external electron temperature increased with decreasing mass flow rate and increasing current from $1-2.5 \times 10^4 K$ $(0.9-2.2eV)$, this corresponded to an electron number density of the order of $10^{18}m^{-3}$. The internal probe obtained values for the plasma potential of $V_p \approx 4.5-7.4V$, which were typically $12V$ below those found using the external probe. In this region an electron temperature of $4-6 \times 10^3 K$ $(0.3-0.5eV)$ was obtained with a number density of $10^{19}m^{-3}$.

The work of Siegfried and Wilbur constitutes some of the first investigations of the insert region of HCs [48]. The aim of their investigation was to determine the plasma parameters upstream (the insert) and downstream (the plume) of the orifice plate. To this end Langmuir probes were placed downstream and upstream of the orifice on the centre line, as shown in figure 2.7. These probes could be moved axially over a distance of $25mm$ but the authors were unable to collect data in the orifice region due to the destruction of the probes. Anode currents ranging from $0.5A-9.0A$ with mass flow rates of $100-150mAequiv$ $(0.05-0.07mgs^{-1})$ were investigated. In the insert region the electrons were found to have

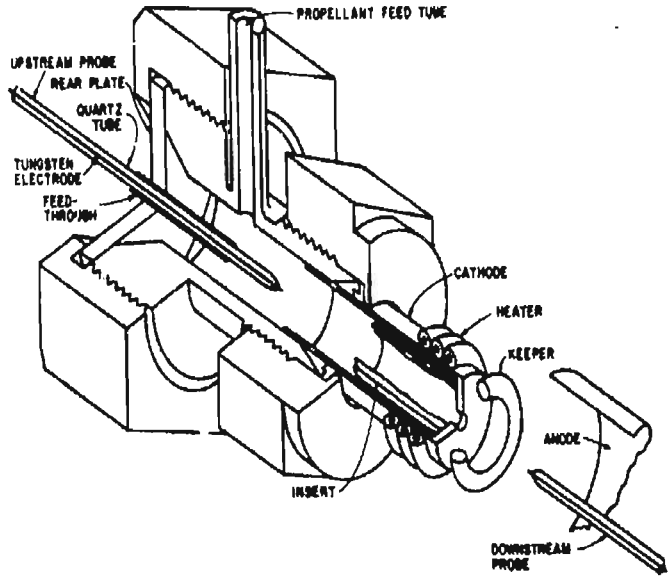

Figure 2.7: Experimental set up, Siegfried et. al.

a Maxwellian distribution with the electron temperature $T_e \approx 0.5 - 0.8eV$ in the plume and spot modes. In the plume region in the plume mode T_e is considerably higher than that of the internal plasma peaking $7mm$ from the orifice with $T_e = 5.0eV$ (see figure 2.8). For the spot mode T_e remains constant at $\sim 0.8eV$ (see Fig. 2.9). The plasma potential is also a function of distance from the orifice peaking externally at $7mm$ at the same point as the electron temperature with $V_p = 30V$ in the plume mode but plateaus at $12V$ in the spot mode. The electron temperature and plasma potential are dependent on the mode of operation of the HC. Far downstream both are considerably lower in the spot mode than in the plume mode, while the reverse is true of the electron density. Spectroscopic data were collected for the external discharge. The observed number and intensity of discrete spectral lines increased as the discharge current increased in the plume mode, for both neutral and singly ionised species. In the spot mode many lines disappeared with some reappearing at higher discharge currents. No quantitative analysis was carried out using the spectroscopic data. A micro – optical pyrometer was used to determine the temperature at seven points along the insert. These temperature measurements were subject to error because the oblique viewing angle used caused the measurements to be influenced by reflected radiation. Temperatures of $T \approx 900 - 1140^oC$ were recorded in the insert region

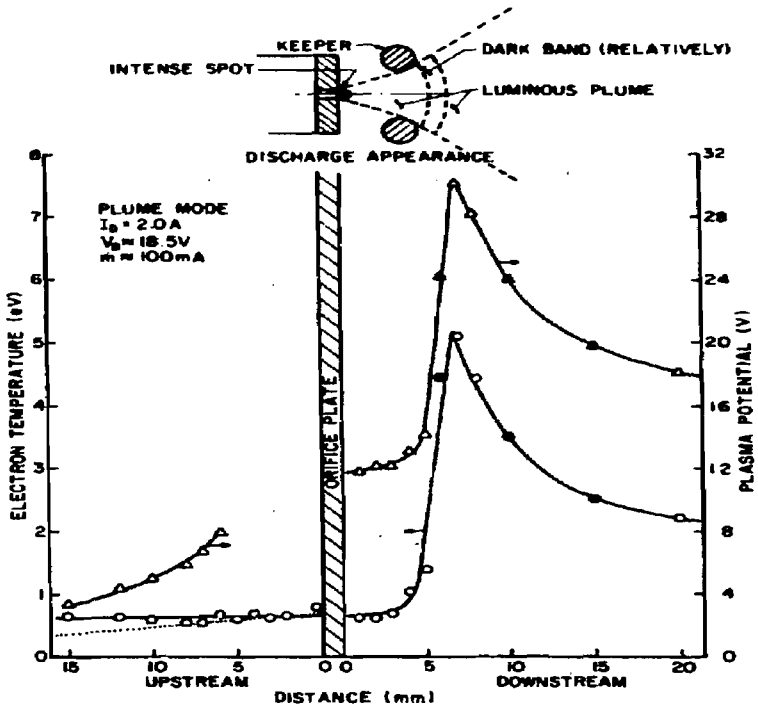

Figure 2.8: V_p and T_e (plume mode), Siegfried et. al.

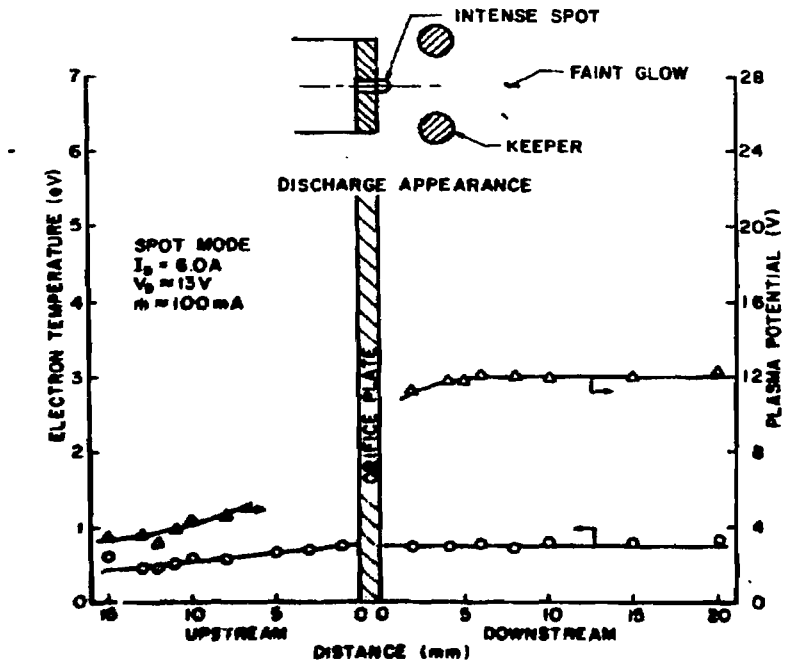

Figure 2.9: V_p and T_e (spot mode), Siegfried et. al.

for the plume mode with, $T \approx 1050 - 1320°C$ for the spot mode. The ionisation fraction

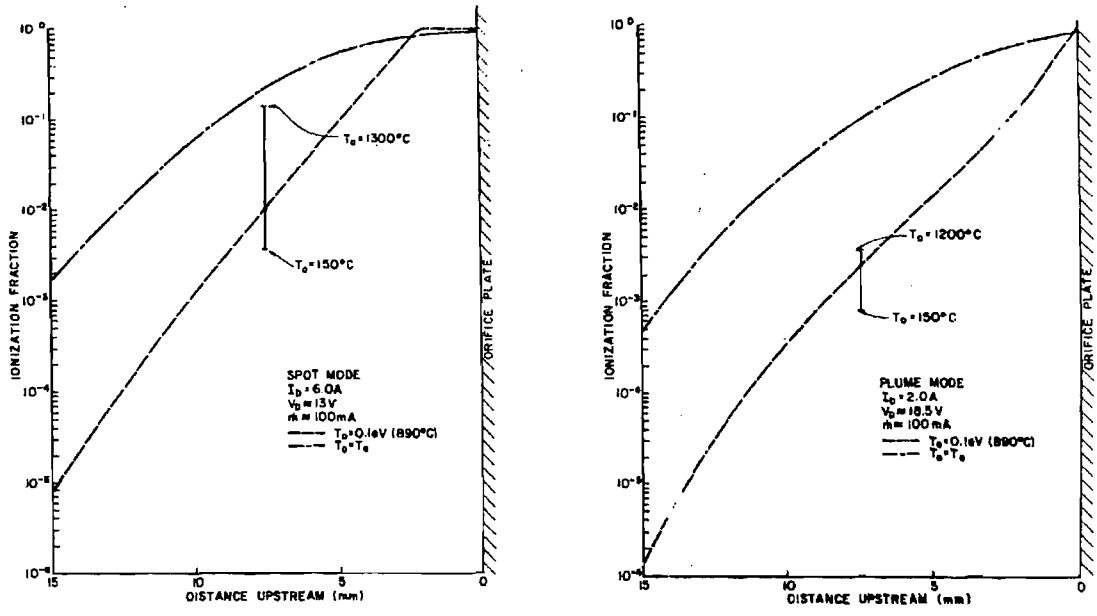

Figure 2.10: Ionisation fractions in spot and plume mode, Siegfried et. al.

was shown to increase by orders of magnitude as the orifice was approached from the insert region, in keeping with the increases in electron density, as shown in figure 2.10.

The current density was determined using the available plasma property profiles with estimated electric fields in conjunction with the Schottky equation (Equ. 2.2) The results obtained clearly demonstrate the active region theory. The current density rapidly increases as the orifice is approached in both spot and plume mode achieving a maximum of $20Acm^{-2}$ for the spot mode at the edge of the orifice and decreasing to $4Acm^{-2}$ $5mm$ into the insert; a maximum of $7Acm^{-2}$ was determined for the plume mode. These results provided the basis of the computation work carried out by Siegfried and Wilbur discussed below.

A phenomenological model was developed which provided a qualitative description of the basic physical processes occurring within the HC. The model was concerned with emission processes from an idealised "ion production region" and the charge carriers within the internal plasma. This active region was said to be on the order of two electron mean free paths (approximately $2mm$) in length, which is equivalent to the insert diameter. The

main electron emission mechanism was field enhanced thermionic emission [54]. It was found that $\approx$ 70% of the total HC current was due to electron emission from the active region. The remaining 30% was due to volume ionisation caused by multi-step processes in the region adjacent to the active region. This model was later developed to provide an order of magnitude value of the insert temperature and the length of the active zone [39]. An electron temperature of $T_e = 0.71 \pm 0.1eV$ (determined experimentally using Langmuir probes as described above) was one of the inputs for the model. The theoretical results were compared with those obtained experimentally using a cathode fabricated from a quartz tube with the internal surfaced covered in tantalum foil [55]. The results show good agreement with experiments for the dependence of insert temperature on discharge current, increasing as current is increased and peaking at $\sim 1100^oC$ at $5A$ for $\dot{m} = 100mAequiv$. There is a discrepancy between theoretical and experimental results for the dependence of insert temperature on internal pressure. This may be due to the assumption that plasma properties are uniform in the emitting region. The difference between theoretical and experimental results increases as the pressure decreases, suggesting that for low internal pressures temperature gradients become significant.

2.5.2 Inert Gas Hollow Cathodes

Mercury was originally the preferred propellant used for HCs with electric propulsion applications. Alternative propellants were typically investigated for use with terrestrial applications. It was found that the performance of HCs was not adversely affected by the use of inert gas propellants. Inert gas propellants have a higher ionisation potential than mercury and operating voltages increase with increasing ionisation potential. This increase in voltage and hence operating power may cause increased sputtering, but the advantages associated with the use of inert gases were found to outweigh this disadvantage. Studies again focussed on enhancing performance and extending lifetime with the use of alternative propellants. The HC used in the T5 ion thrusters was derived from the principles used for the development of the HC used in SERT II thrusters. The life tests of the T5 HC exceed $20,000hrs$. These HCs were tested over a range of discharge currents from $0.1 - 30A$ with

a variety of propellants, although the normal operating range was restricted to $0.1 - 5A$ in order to facilitate long life. It was believed that the qualitative HC behaviour should not be influenced by a change of propellant. Data were obtained using a standard T5 HC with orifice diameter of $0.3mm$ for xenon, krypton, neon, argon and helium, which agreed with this assumption. Decreased electrical noise was observed with the use of inert gas propellants but a slight decrease in the thruster efficiency occurred [56].

Kaufman described advances in component technology for inert gas thrusters [25]. It was stated that the maximum electron emission could be increased $60 - 70\%$ with the use of an enclosed keeper. The limiting factor for electron emission was the rapid increase in anode voltage when the anode current was increased for inert gases, but no similar limit was reported with the use of mercury propellant. A range of keeper hole diameters of $2 - 6mm$ was investigated in increments of $1mm$ and the cathode keeper separation was varied from $1 - 9mm$. The optimum configuration was defined as the spacing that gave the highest ratio of electron emission to gas flow at an anode potential of $30V$. The best keeper locations and hole diameters were found to be similar to those of an open keeper configuration, as they do not intrude on the central current carrying region that occupies a large angle conical volume.

Experimental investigations of a HC utilising argon propellant carried out by Stillwell mark the first instance where holes were drilled along the insert in an attempt to provide access for diagnostics [57]. The HC used was specially fabricated for research purposes and hence was not a commercial model. The HC consisted of an oxide – free rolled tantalum foil insert that was mechanically assembled (no welding was used). Graphite and tungsten tips were used. Tungsten tips recorded a consistently lower temperature than the graphite tips of $\sim 100K$. Optical pyrometers provided the temperature of the insert surface as shown in Fig. 2.11. Maximum temperatures approaching $2500K$ where observed nearest to the tip. Figure 2.11 shows that there is a drop in temperature at $\approx 6mm$ from the tip. The temperature profile suggests the majority of emission occurs within the region near the orifice up to $6mm$. This provides another example of the active region theory, which is in agreement with the work of Siegfried outlined above. It was also shown that increasing

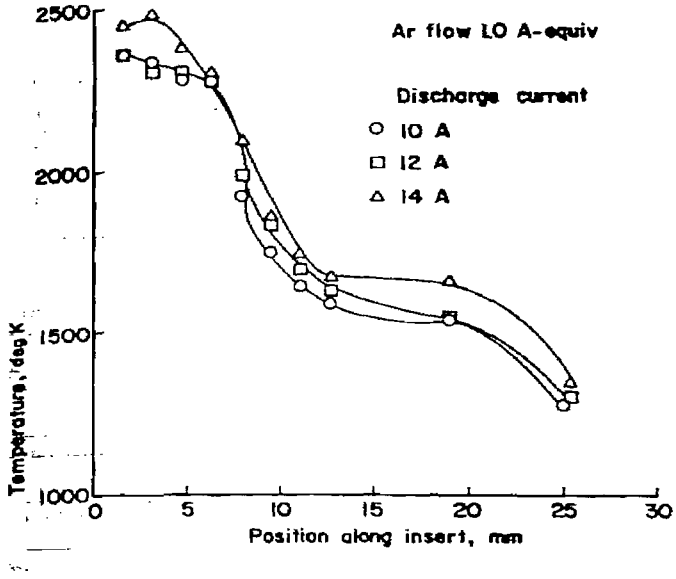

Figure 2.11: Insert temperature profile, Stillwell et. al.

the mass flow rate decreases the power required to maintain a given emission current.

HCs were operated in a high power quasisteady magnetoplasmadynamic (MPD) accelerator at discharge currents of $I = 0.25kA$ to $I = 30kA$ with argon propellant [58]. At these power levels HCs an order of magnitude larger than those used in ion bombardment thrusters are required (in this case an inner diameter of $1.9cm$). The increased size of the HC allowed access for diagnostic equipment. Langmuir probes were used in the HC cavity. The current densities and mass flux densities are commensurate to those achieved by the low power devices typically used. On increasing the current the location of the maximum current density moves downstream towards the orifice. Decreasing the mass flow rate from $0.4 - 0.1gs^{-1}$ causes an increase in the peak current density this peak also moves downstream from $1.9 - 0.3cm$ from the orifice. Outside of this range of mass flow rates it becomes difficult to identify trends.It was suggested that the static pressure component of the flowing gas in the HC determines the cavity current pattern and hence the cavity conduction is determined by the electrostatic potential pattern. Fig. 2.12 shows the dependence of current density on axial position with varying discharge current, increasing the discharge current results in a shift downstream of the position of maximum emission.

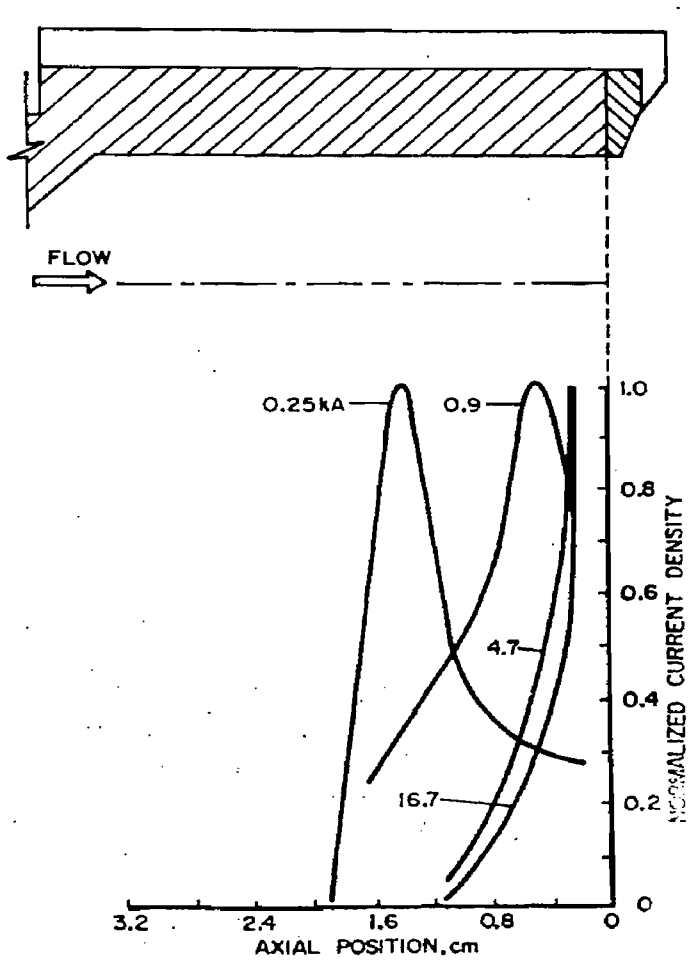

Figure 2.12: Current density distribution, $\dot{m} = 0.2gs^{-1}$ Krishnan et. al.

Recently much work has been carried out on the characterisation of HCs in order to determine the conditions leading to improved operation [59, 60]. Investigations continue on the development of both low and high current HCs. Research carried out at the Plasmadynamics and Electric Propulsion Laboratory in Michigan on HCs for low power applications established that HC performance is not insensitive to orifice geometry [61]. It was found that the smallest orifice aspect ratio (orifice length divided by diameter) consumed the least amount of power for a given current. When operating in an enclosed keeper configuration the power consumption decreased by $5 - 10\%$ compared to the open keeper configuration, but no mechanism exists that explains this phenomena. Thermocouples attached to the body of the HC provided an axial temperature distribution; for a mass flow rate of $2sccm$ of xenon the temperature was found to peak at the tip with $T = 950^{o}C$ for the enclosed

keeper case and $T = 625^oC$ for the open keeper, in both cases the temperature decreased to $\approx 600^oC$ $10mm$ from the tip. The tip temperature was proportional to the aspect ratio.

Investigations into high current HCs were carried out independently at DERA and NASA Glen Research Center [62, 63, 64]. For missions requiring xenon ion thrusters of specific impulse $3400 - 3500s$ and thrusts of $150mN$, discharge currents of $\approx 20A$ are needed. At DERA this range of performance was investigated. Cylindrical Langmuir probes placed $10mm$ from the keeper orifice collected traces that resulted in an electron temperature of $2.4eV$ with number density of $1.2 \times 10^{11} cm^{-3}$ being determined, the plasma potential was $17.5V$. The orifice diameter was varied from $0.75mm$ to $1.0mm$ to $1.3mm$ but this had little effect on the stability of the discharge. The noise generated by the discharge on the keeper and anode was monitored using a digital oscilloscope. A stable discharge was observed at high mass flow rates and anode currents. The keeper noise typically displayed a lower amplitude than the anode noise. It was concluded that the cathode keeper separation should be made as small as possible in order to eliminate the less stable oscillatory regions observed at low mass flow rates and currents. Ideally the mass flow rate should be controllable so that transitions to noisy regimes may be avoided if throttling is undertaken by varying the anode current.

Research performed at the NASA facilities utilised HCs with a $1.27cm$ inner diameter to sustain currents of up to $100A$ with mass flow rates of $4sccm$. A low energy particle analyzer was mounted on the HC axis separated by $23cm$. The ion energy distribution peaked for ions with an energy of $15eV$ for all discharge currents, increasing the current increased the peak amplitude. Ions with energy greater than the discharge voltage were observed, implying that ions gain energy by mechanisms other than acceleration through the potential field of the keeper and anode electrodes. The proportion of ions with energy greater than the sputtering threshold of molybdenum was 15%, as a consequence the risk of sputter erosion increases for HCs operating in a high current regime.

HCs have demonstrated an ability to operate effectively over a range of operating conditions for a range of applications from attitude control to primary propulsion for interplanetary missions. Research has even been carried out on the application of HCs as micro ion

thrusters [65, 60]. However, without a suitable physical model extensive testing and characterisation of the HC will need to be performed, which is labour intensive and in many cases not economically viable. The sustained interest in HCs for various applications reinforces the need to understand the physical processes occurring within HCs with the aim of developing a universal theory that describes all observed phenomena. The theoretical work discussed in the following section in most cases attempts to address specific aspects of HC performance, but a generic theory for the description of macroscopic properties and plasma properties has yet to be found.

2.6 Theoretical Investigations

Theoretical work as it is known at present using computer technology to simulate observed phenomena did not exist when ion bombardment thrusters and supporting components were first developed. Theoretical investigations began by applying fundamental gas dynamic and plasma physics to HC geometry and operating conditions in order to obtain physical explanations for the experimental results obtained. One such work was carried out by Delcroix et. al. producing a review paper on the theory of HC arcs in the early 1970's. This work described the general working regimes of HCs and the various applications of the device [40]. The principles stated in this paper were expanded on by Ferreira and Delcroix [41]. The basic gas flow inside of the HC was studied. The calculation of the Reynolds number for typical operating conditions showed that the flow is laminar. The internal (P_C) and external pressures (P_E) were calculated for an argon discharge. It was concluded that in general $P_C \gg P_E$, therefore the velocity of the flow is sonic at the exit of the HC. It was demonstrated that the gas pressure at the rear end of the HC increases when the discharge is turned on and as discharge current increases, in good agreement with experimental work. This increase in pressure may be attributed to a gas dynamic effect, the increase in temperature that occurs with the presence of a plasma discharge results in an increase in pressure. However, the HC plasma is complex and it has been suggested that the back flow of positive ions may contribute to an increase in pressure. A physical model was developed using a cascade theory to describe the thermalisation of primary

electrons and the excitation or ionisation of argon atoms. The cascade theory states that primary electrons do not possess sufficient energy to cause ionisation by single collision; rather, atoms undergo several electron collisions each resulting in further excitation of the atom until the electrons are thermalised and the atom ionised. The transport theory applicable to the ions in the internal positive column (IPC) is an intermediate theory between classical ambipolar diffusion (where the diffusion process is due to a build up of spatial charge, which creates an electric field that causes electrons and ions to leave the plasma at the same rate) and free fall theory for $\frac{\lambda_{mfp}}{R} \leq 1$ where λ_{mfp} is the mean free path for momentum exchange between ions and neutrals and R is the scale length of the plasma. This provides the radial profile of the IPC ion concentration for different values of the parameter A, which represents the ratio of the neutral – ion collision frequency and the ion – ion collision frequency. The ion density peaks at the centre of the profile decreasing towards the walls of the HC. The plasma density at the sheath boundary was determined to be of the order of $10^{14} cm^{-3}$ for $T_e = 1eV$.

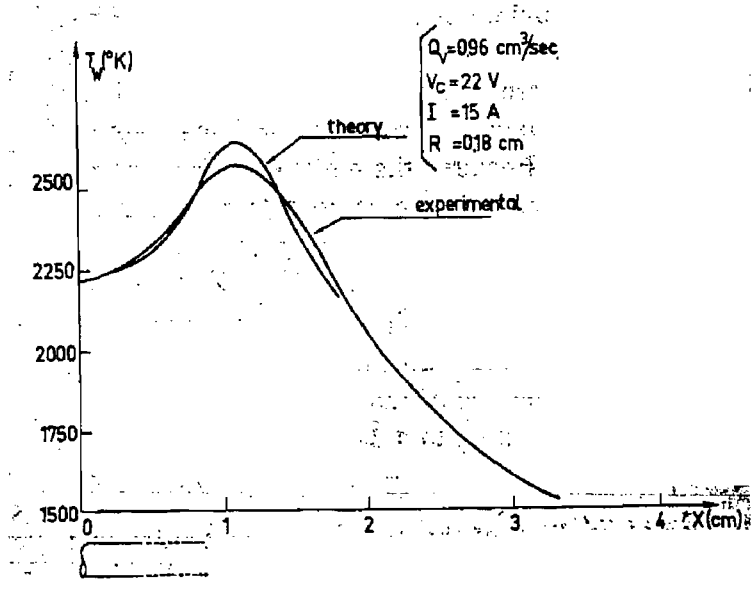

Figure 2.13: Insert temperature profile; where $X = 0$ corresponds to the orifice position, Ferreira et. al

The wall temperature was determined as a function of axial position for a tantalum HC using a thermal balance method. A surface workfunction of $4.12eV$ was used for a HC with

an internal radius of $1.8mm$, mass flow rate of $\dot{m} = 1.7mgs^{-1}$ and discharge current of $15A$; the results are shown in figure 2.13. The theoretical profile is compared to experimental results and shows good agreement. A maximum temperature of $2575K$ was found $11mm$ from the HCs exit. The temperature values appear to be an overestimate when compared to the tip temperature values in the range of $1500K$ obtained in recent studies [56, 59, 60, 64]. However the HC used in this investigation has different dimensions to those used in electric propulsion applications and utilises a tantalum insert instead of impregnated tungsten. Also the only electron emission mechanism considered was thermionic emission.

2.6.1 Continuum Modelling

Continuum models solve sets of equations describing the behaviour of gas dynamic properties in order to determine plasma properties and macroscopic quantities such as density, temperature and pressure at any location in the flow. The validity of the continuum method is dependent on the degree of rarefaction of the gas. This is represented by the Knudsen number K_n, defined as the ratio of the mean free path, λ_{mfp} to the characteristic scale length R.

$$K_n = \frac{\lambda_{mfp}}{R} \tag{2.15}$$

For the continuum method to be applicable $K_n < 0.1$ implying that the fluid is dense; this is typically the case for the internal plasma of the HC. The assumption is made that the velocity distribution is Maxwellian.

Kennedy developed a one dimensional model which predicted HC temperature profile and surface current density [66]. A collisionless sheath approach was used to determine particle flux to the HC and the bulk plasma was assumed to lie in the LTE (local thermodynamic equilibrium) regime (see Chapter 4.3). The results were compared with the experimental work carried out by Krishnan on a MPD (magnetoplasmadynamic) HC with an internal radius of $0.95cm$, discharge current of $250A$ and mass flow rate $0.2gs^{-1}$ operating on argon propellant [58]. The trends for the current density profile show the same characteristics. The current density increases approaching its peak upstream of the HC tip and then falls off rapidly after the peak, this is in agreement with the active region theory described in

Sec. 2.4.2. The peaks for the experimental and theoretical curves do not occur at the same axial position or have the same height, the experiment produces a maximum current density of $50Acm^{-2}$ occurring $1.6cm$ from the tip compared with $40Acm^{-2}$ at $1.2cm$ for the model. The temperature profile obtained in the same study for a HC with internal radius $1mm$ displays peak temperatures in the range of $2768 - 3269K$ for discharge currents of $2 - 10A$. Increasing the discharge current results in an increase in the peak temperature and a downstream shift in its axial position. The temperature values are an overestimate compared to the results obtained in this investigation (see Sec. 6.6). This may be due to the fact that the properties of the impregnate material are not considered in this model.

An analytical model developed at Centrospazio solved a series of equations in order to describe the interactions of the insert with the plasma discharge [46]. The model is one dimensional; radial gradients were neglected for simplicity. A description of HC behaviour when operating in the steady state spot mode was provided. The HC flow was treated as laminar and subsonic and the plasma was treated as a mixture of three perfect gases of electrons, ions and neutrals. Ionisation was assumed to occur via a single step collision of primary electrons with neutrals; excitation processes were neglected. The model was applied to a tantalum HC with inner radius of $1.8mm$, $0.2mm$ wall thickness and $100mm$ length. Argon propellant was used. Temperature and pressure profiles were produced. The general trends of the insert surface or wall temperature profiles show good agreement with literature. The peak temperature occurs upstream of the orifice and shifts further upstream with decreasing mass flow rate. Increasing the mass flow rate results in a decrease in temperature at a fixed axial position. These trends arise as a consequence of the pressure distribution within the HC, varying the mass flow rate influences this distribution. The number of ionising collisions that take place is affected by the pressure distribution, therefore the rate of ion bombardment at the insert surface varies causing shifts in the peak temperature position. Peak temperatures of $\sim 2500K$ were obtained for mass flow rates of 1 and $1.4mgs^{-1}$. This overestimate may arise from the fact that the model does not treat the insert as an impregnated material, also the thermal balance equation used did not incorporate surface evaporation as a method of cooling the insert. It was found that the insert's workfunction can greatly influence the peak temperature. Increasing the

workfunction from $3eV$ to $4.12eV$ corresponds to a $800K$ increase in peak temperature from $1700K$ to $2500K$ at $\dot{m} = 1.3mgs^{-1}$. This work requires further validation.

It has been suggested that the HC may be used for of space propulsion applications in the low power, low specific impulse regimes e.g. station keeping [65]. A phenomenological model was developed by Turchi with the aim of predicting HC operating parameters and establishing the feasibility of a HC type thruster [67]. The model allows heavy particle temperatures to be substantially higher than the HC surface temperature. Radial gas temperature profiles for argon propellant show a parabolic distribution. The temperature increases with discharge current. A maximum temperature of $\sim 3800K$ is achieved along the centre line for a current of $10A$. The gas temperature was said never to exceed half of the electron temperature. It was stated that temperatures of $3000K$ may be obtained without the insert surface temperature exceeding $1500K$. It is stated that the heavy particle flux leaving the HC is not highly ionised, although this is in disagreement with other studies. It was concluded that a realistic achievable specific impulse of $1017s$ relates to a thruster efficiency of less than 4%.

A model concerned with describing the orifice region of a plasma contactor was developed by Katz in an attempt to reconcile observed differences in performance when the HC was operated in different experimental facilities [34]. The ion production rate was related to the ion current density, number density and volume of the orifice (as shown by Equ. 2.16) and was used to determine the maximum current that could be supported by the HC.

$$I_{prod} = \pi r^2 L.4\sigma_{ion}.j_e n \tag{2.16}$$

Where I_{prod} is the ion production rate, r is the orifice radius and L is its length, σ_{ion} is the ionisation cross section, j_e is the electron current density and n the neutral density. Three energy loss mechanisms were considered; ionisation, radiation and convection. The equations were solved in an iterative process to calculate the ion output, plasma density, electron temperature and power dissipation. The electron temperature was found to decrease with increasing mass flow rate. When the electron and ion temperatures were assumed equal a maximum electron temperature of $2.5eV$ was achieved for a mass flow rate of $1sccm$ of xenon and decreased to $1.8eV$ at $10sccm$. For an ion temperature of $0.1eV$

a maximum electron temperature of $1.8eV$ was achieved for a mass flow rate of $1sccm$ of xenon and decreased to $1.5eV$ at $10sccm$. For the case of negligible ion production the electron temperature was independent of plasma density and was only weakly dependent on ion and neutral temperatures.

The model described in the previous paragraph was applied in order to evaluate the sensitivity of HC performance to orifice diameter, orifice length, propellant flow rate and keeper current in an attempt to improve design [68]. It was found that decreasing the orifice length resulted in improved performance as resistive losses were reduced and less ions were lost to the orifice walls. However, the model breaks down if the orifice length is less than the orifice diameter. Decreasing the orifice diameter caused the electron current density to increase substantially, ion production increased but at the cost of increased resistance. As a consequence of increased power dissipation due to this resistance the cost per ion produced increased. The performance of the HC was insensitive to propellant flow rate unless the flow was sufficiently low to cause high levels of ionisation in the orifice. Increasing the keeper current resulted in increased resistance but a reduction in the cost of ion production. On the basis of the model predictions the HC with the smallest diameter and length was deemed to be most efficient. A HC with dimensions recommended by the model results underwent laboratory testing and produced 30% more emission current operating at $20V$ with 30% less power and 15% less propellant flow compared to a baseline HC with a larger orifice. Although links were made between orifice dimensions and performance the model does not posses sufficient accuracy to predict relative differences in performance between several operating conditions on various HCs.

A model developed by Katz based on the ambipolar diffusion of ions suggested an alternative process of barium transport [69]. Gaseous barium was said to be ionised within less than a micro second and accelerated by the electric field within the plasma in the opposite direction to the neutral gas flow with velocities an order of magnitude greater than that of the flow. This theory attempts to explain observed barium deposits upstream of the active region. An electron temperature of $1.075eV$ was determined for the HC internal plasma. This increased to $1.5eV$ in the centre of the orifice and $2eV$ in the chamfer region. The

variations of the plasma density in the orifice in the axial direction display a similar profile as the erosion pattern of HCs undergoing life testing. As the HC sheath environment was not incorporated into the model and doubly ionised species were not considered, sputtering rates could not be determined. The maximum ion current to the wall found in the orifice was $2 \times 10^6 Am^{-2}$ and maximum plasma densities of $6 \times 10^{22} m^{-3}$ were found in the centre of the orifice. One third of electrons produced were thought to be produced by ionisation in the orifice. Power loss due to radiation was neglected as the plasma was said to be optically thick.

The use of HCs on ion thrusters sent on interplanetary missions requires that the component must operate for extended periods of time. As a result a resurgence in the research field of HC life limiting factors has occurred. Katz et. al. developed a one dimensional analytical model which relates the life time of the insert to its temperature [70]. Barium depletion and hence the maximum current that may be drawn from the HC is dependent on temperature. It was concluded that if the insert surface is able to provide the required emission current a reduction of the insert operating temperature by $\approx 40^oC$ results in a factor of two increase in the insert life. A maximum insert life of $1.4 \times 10^5 hrs$ was achieved for an insert temperature of $1423K$. Modifying the HC to operate at lower temperatures would significantly increase the lifetime of the component.

A thermochemical model coupled with a diffusion model developed by Kovaleski at NASA's Goddard Research Center evaluated the life limiting mechanism of HCs related to the evolution and transport of Ba away from the insert surface [37]. The partial pressures inside the pores of the tungsten insert and within the HC tube dictate the rate of free molecular flow of Ba gas out of the insert, whilst diffusion through the inert gas propellant determines the rate of loss of Ba through the orifice and upstream end of the HC. The model was tested for a HC with an impregnate composition of $4:1:1$ of $BaO:CaO:Al_2O_3$ and insert inner diameter of $3.8mm$ with length $25.4mm$. It was found that the BaO content in the downstream region was more quickly depleted than in the upstream region. For a HC operating at full power the model predicts that after $10,000hrs$ up to 90% of the BaO originally present in the downstream region is depleted compared with only 16% for a HC

operating at minimum power (values of the output power were not provided). The Ba density was found to be an order of magnitude higher for the high power case than for the minimum power case. The higher temperature downstream end of the HC in the vicinity of the orifice was found to be most active in the production of Ba and BaO and displayed the higher fraction of Ba lost. This can be related to the active electron emission region as it is expected that the region with the highest concentration of Ba will coincide with the region of highest current density.

A three dimensional model was developed by Murray that describes neutral gas flow through the HC [71]. The effect of HC geometry on the gas flow was investigated but the code was never fully developed to incorporate a description of a three species plasma. The temperature distributions show that the gas temperature remains constant and equal to the wall temperature within the HC. On reaching the orifice the temperature drops corresponding to the expansion of the flow in the tip. The temperature then increases further downstream. The viscosity of the flow causes a pressure decrease to occur along the length of the HC accompanied by a decrease in density. At the orifice the nature of the flow changes dramatically, there are falls in pressure, density and temperature and a rapid increase in axial velocity, the flow becomes transonic and then supersonic approximately 2/3 along the orifice. The velocity continues to increase, reaching its maximum of $\sim 700ms^{-1}$ 1.5 diameters downstream of the orifice exit. The position of the downstream boundary was found to have little influence on the flow characteristics. The position of the radial boundary conditions did have a significant effect, in particular on the width of the plume from the orifice. This is in agreement with experiments that show that the dimensions of test facilities have an effect on HC performance.

2.6.2 Direct Simulation

The direct simulation method models ions and/or neutrals as direct simulation Monte Carlo (DSMC) species. Electrostatic interactions are included using the particle–in–cell (PIC) plasma physics method. This allows charged plasma species to be modelled as individual macro particles in a cell (each macro particle represents some large value of real particles).

The motion of the particles in the plasma is dictated by Newton's laws and self consistently calculated electric field strengths resulting from applied voltages and interparticle coulomb forces. This technique is more computationally involved than the continuum approach but offers the advantage of being valid for all values of K_n and velocity distribution functions.

Applying this technique to high density plasma like that found within the HC has typically been avoided because a relatively high number of interactions must be computed compared to a low density plasma such as the discharge chamber plasma. This requires large computing power and the time taken to obtain results is typically 12hrs using a standard PC [1]. As a consequence the DSMC PIC method was originally applied to the discharge chamber or the HC plume.

The main chamber discharge of a Kaufman type ion thruster was modelled using the DSMC method. The behaviour of charged and neutral particles in the presence of magnetic and electric fields was investigated, ionisation processes were also included. This model provided information on the number density and distribution of particles [72]. The number density of electrons was found to drop significantly at the grid region, whilst the number density of ions was high in this region.

Plume expansion was modelled by Crofton and Boyd using a PIC–DSMC code. The code was validated by comparing the results with those obtained from experimental investigations. The diagnostic equipment used to characterise a T6 HC using xenon included a retarding potential analyzer, quadrupole mass spectrometer and Langmuir probe [73]. There was good agreement between the experimental and simulated results for ion energy distribution functions with peaks occurring for ion energies of $40eV$ per ion charge on the centre line ($\phi = 0^o$ with $\phi \equiv$ the angle between the retarding potential analyzer and the HC), the ion distribution was insensitive to changes in mass flow rate. There were discrepancies for the ion emission angular distribution, with emission being over predicted by an order of magnitude.

The flow within the HC was modelled using a PIC–DSMC code for the first time at the University of Southampton [74]. The model developed by Crawford initially simulated neu-

[1] F. Crawford private communication

tral gas flow. The results obtained agree well with the work Murray discussed previously. The flow through the HC is said to be choked at the orifice. Subsonic behaviour occurs prior to the tip. At the tip a sonic line is present, after which the Mach number increases. The model was developed to describe the variations in sheath structure, the surface electric field and current density emitted from the HC insert in order to understand discharge scaling with applications to the fabrication of micro HCs. It was established that HCs with internal radii of less than $10^{-4}m$ (0.1mm) could not produce the currents required for electric propulsion applications [75].

Crawford's model was applied to a HC in an enclosed keeper configuration with a $2mm$ internal diameter and $20mm$ length. The neutral gas flow temperature distribution showed that the region of highest temperature occurs at the HC wall and decreases radially within the HC. Strong temperature gradients in the axial direction were not observed as this phenomena is related to the presence of a plasma. A peak temperature of $1100K$ was found adjacent to the wall for a mass flow rate of $2mgs^{-1}$ of xenon. Initial plasma breakdown was investigated and was found to start in the keeper region and then move upstream to the insert region. This process was said to take $14\mu s$. Ions were observed after $3\mu s$ in the region $13 - 17mm$ downstream of the keeper where electrons possessed energy greater than the first ionisation potential of xenon. Comparisons have been made with experimental work where the thrust produced by a HC was investigated [76]. The experimental and theoretical work show good agreement for the cold gas case [77]. Improvements to the model may be made regarding the interaction of the gas with the walls and surface interaction physics, e.g. secondary electron emission and other complex surface reactions. The temperature distribution after breakdown has occurred should also be determined [78].

2.7 Life Studies and Impregnate Material Depletion

The impregnated cathode was developed in the 1950's and offered advantages over earlier cathode types in terms of simplified fabrication, increased processing speed and improved thermal properties. Investigations into the factors that contribute to end of life were carried out on planar cathodes without the presence of a plasma[79]. Accelerated life tests were

performed by operating a cathode with impregnate composition of $5BaO : 2Al_2O_3$ at a higher than normal temperature of 1190^oC. A current density of $5Acm^{-2}$ was produced for most of the cathode life but rapidly dropped to $1Acm^{-2}$ after $\sim 10^4hrs$. The majority of the Ba evolved from the cathode (60%) came from the front end, it was thought that the presence of the heater and the molybdenum body at the rear impeded evaporation. A third of the evaporated material was BaO. The Ba evaporation rate was found to be a linear function of time with a gradient of -0.52 up to $2000hrs$ of operation after which the evaporation rate fell off substantially. This corresponds to a Ba evaporation rate of $100\mu gcm^{-2}hr^{-1}$ after $1hr$ of operation and $1\mu gcm^{-2}hr^{-1}$ after 10^4hrs. It was concluded that cathode life terminated due to exhaustion of the Ba reservoir.

The cathode impregnate material was later developed to incorporate CaO as this resulted in a higher emission rate, lower evaporation rate and increased life. Life tests were performed on porous tungsten pellets with a $3mm$ diameter and $1mm$ thickness. The impregnate composition was $5BaO : 2Al_2O_3 : 3CaO$ [80]. The life tests showed that a decrease in operating temperature of 115^oC from 1190^oC to 1075^oC results in a order of magnitude increase in life of $7000hrs$ to $70,000hrs$. A life time of 10^5hrs was projected for an operating temperature of 1060^oC with emission current $5Acm^{-2}$. The theory was confirmed which suggested that the Ba evolved from the pellet forming a Ba on O monolayer that adhered itself to the surface facilitating increased electron emission by decreasing the workfunction of the material.

Further studies on the electron source for microwave tubes related the depletion of impregnate materials to operating time [81]. The build up of a Ba or Ca monolayer on a tungsten wire exposed to the discharge was measured over time. This is known as the Becker method. The depletion of Ba was found to be linear with a gradient of 0.5 for operating times between 10^2 to 10^5hrs, the long term depletion (for lifetimes in excess of 10^5hrs) was proportional to the square root of the operating time ($t^{\frac{1}{2}}$) whilst the evaporation rate was proportional to $t^{\frac{-1}{2}}$. The depletion of Ca was proportional to $t^{\frac{1}{3}}$.

Increasingly sophisticated techniques were used to investigate the behaviour of impregnate materials [82]. X-ray spectroscopy was used to map Ba on pellets impregnated with a

$4:1:1$ composition of $BaO:CaO:Al_2O_3$. It was found that as operating time increased the Ba originated from deeper and deeper within the tungsten pores. Quadrupole mass spectroscopy was used to monitor the Ba evaporation rate and found it to be proportional to $t^{\frac{1}{2}}$ which is in agreement with previous studies.

An investigation into the dynamics of Ba formation and loss was carried out on a scandate coated dispenser with a $4:1:1$ earth metal oxide composition [83]. Quadrupole mass spectroscopy was used to measure the relative pressures of Ba and BaO as a function of time. It was found that the BaO evaporation rate was proportional to $t^{\frac{-1}{4}}$. The generation of Ba far exceeded the production of BaO; the ratio of Ba to BaO decreased as temperature increased in the range of $1250-1450K$. The temperature was monitored using a disappearing filament pyrometer. End of life was said to occur when there was an equal ratio of Ba to BaO.

Accelerated life tests were carried out on a barium strontium cathode by operating at increased temperature, increased continuous load or by the introduction of poisons (oxygen was admitted via a leak valve) [84]. Operating the cathode at a temperature 100^oC higher than the standard temperature of 780^oC resulted in a reduction in life from $20,000hrs$ to $1800hrs$. The influence of increased load (i.e higher discharge current) dominated over temperature in dictating life time when the load was sufficiently high. This may be due to a combination of effects such as current enhanced Ba evaporation, field assisted desorption and an increase in the loss of ionised Ba to the cathode bulk. The sensitivity of the cathode to poisoning was found to be dependent on the type and amount of doping and the time of operation. Following a poisoning event there was a decline in the DC current drawn followed by a recovery period where the current level returned to the level achieved prior to the poisoning. Although the cathode appeared to recover there was a memory of the poisoning event which resulted in a permanent effect on life and reduced survival time in the event of future doping.

The cathodes investigated in the works discussed above were not models used for electric propulsion applications. However, the results obtained provide an insight into the factors that contribute to decreased life time and may form a basis for future investigations into

life limiting factors for electric propulsion HCs. It has been established that operating at increased temperature significantly decreases cathode life. The relationship between Ba, Ca and BaO depletion as a function of operating time was determined for various types of cathodes and all are in agreement.

2.8 Spectroscopic Investigations

The first use of emitted spectral radiation as a means to analyse plasmas occurred in the mid 1920's. Later, techniques were developed in order to study plasmas with the aim of developing advanced plasma sources for a variety of applications such as cathode ray tubes (CRT) for television, materials processing and plasma etching [85]. Spectroscopic studies of laboratory plasmas have now been made over four orders of magnitude in temperature and approximately nine orders of magnitude in density, such is the versatility of the technique [86]. For brevity only investigations utilising optical emission spectroscopy will be reviewed, even though alternative techniques including laser induced fluorescence (LIF) and interferometry are widely used for electric propulsion applications [87, 88, 89, 90, 91].

Spectroscopic investigations have been performed on cathodes used for terrestrial applications such as arc welding, plasma cutting and surface treatments. The cathodes studied separately in work by Pellerin, Pokrzywka and Dzierżega consist of a water cooled thoriated tungsten tip and a copper disc acting as the anode; this is known as a fluid convective cathode [92, 93, 94]. These cathodes were operated using argon gas at atmospheric pressure and high power, typically in the kW range. The plasma $0.25mm$ to $5mm$ downstream of the tip in the axial direction was investigated using optical emission spectroscopy. Spectral line profiles were used to determine the plasma temperature distribution and electron number density. A maximum plasma temperature of $\sim 20,000K$ was observed nearest to the tip; temperature decreased as the distance from the cathode tip increased. Electron number densities of $10^{23}m^{-3}$ were calculated; this suggests that the plasma lies in the local thermodynamic equilibrium (LTE) range. However departures from the LTE regime were observed in the near cathode region up to $3mm$ from the tip. This deviation was attributed to pressure gradients. The cathodes under investigation in these experiments

display stark differences to the cathodes used for electric propulsion applications. However, diagnostic techniques were applied to obtain information that is of interest regardless of the application or operating parameters. This demonstrates the wide range of conditions in which optical emission spectroscopy may be used.

Spectroscopic studies of the internal plasma of an electric propulsion type HC were carried out by Malik and Monterde in order to understand the physical principles underlying plasma formation and electron emission mechanisms [95, 96]. Radiation in the vacuum ultra violet to visible range ($\lambda = 100 - 590nm$) was recorded from the back end of the HC using a monochromator and a photomultiplier as shown in Fig 2.14. In this way results were obtained that represent the average plasma parameters along the HC's length. The HC used in the investigation was the UK-25 ion thruster HC operating in diode

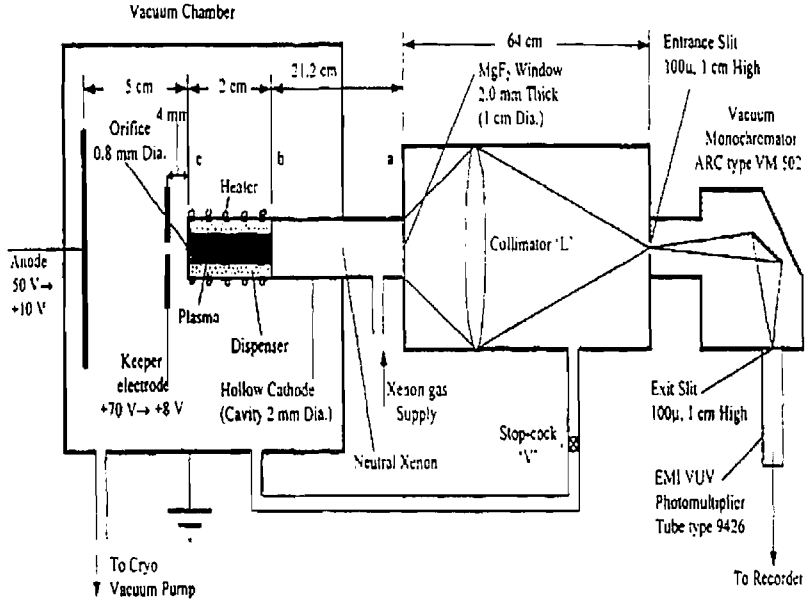

Figure 2.14: Malik et. al Experimental Set Up

configuration with xenon propellant. Two modes of operation were reported: spot mode and plume mode. In the plume mode impurity line intensities increased. A computer simulation using a "coronal radiative model" was under development to determine the electron temperature. The experimental results presented in table 2.1 were determined using spectral line intensity ratios and assuming the plasma is in the LTE regime. The electron density was found to be $n_e = 10^{14} cm^{-3}$.

Mode	V_A (V)	I_A (A)	V_K (V)	I_K (A)	$\dot{m}$ $(ccmin^{-1})$	T_e (eV)
Spot (old)[1]	10	10	10	1	25	0.94
Plume	25	10	9	1	26	0.86
Plume	25	10	9	1	26	0.91
Spot	10	7	8	1	59	0.83
Plume (severe)	32	5	9	1	52	0.84
Spot	10	10	9	1	46.5	0.84
Spot	10	10	9	1	46.5	0.84

Table 2.1: Experimental values: The electron temperature averaged along the length of the plasma column, Monterde et. al.[96]

Further spectroscopic investigations were carried out using the experimental set up described above [3]. The electron temperature was calculated using the intensity ratio of continuum Bremsstrahlung radiation. This method was chosen as it depends less critically on the plasma being in the LTE regime, but it requires the electron energy distribution to be Maxwellian. The Bremsstrahlung radiation was recognised as the linear section of a log plot of the intensity against wavelength. This method resulted in a value of the electron temperature of $T_e = 1.1eV$. Application of the Saha equation (see Equ. 4.30) using the discrete line intensities and the calculated electron temperature yielded an electron density of $n_e = 10^{14}cm^{-3}$. The plasma parameters were determined under the conditions of mass flow rate of 13cc per min ($1.27mgs^{-1}$). The plasma was said to be optically thin to continuum radiation and optically thick to discrete lines. An attempt was made to obtain a more accurate value of n_e by introducing a small amount of hydrogen (100ppm) into the bulk xenon plasma and observing the Stark broadening of H_β lines. However, the weak hydrogen emission lines could not be observed. It was established that the HC internal plasma is neither in LTE or coronal state but is best described by the intermediate "Semi–coronal" or collisional radiative model.

The T6 HC operating in diode configuration with an enclosed keeper was investigated

[1] "Old" refers to a HC that had been operated for 100 hrs before the commencement of the experiment. The remaining results are for a new HC.

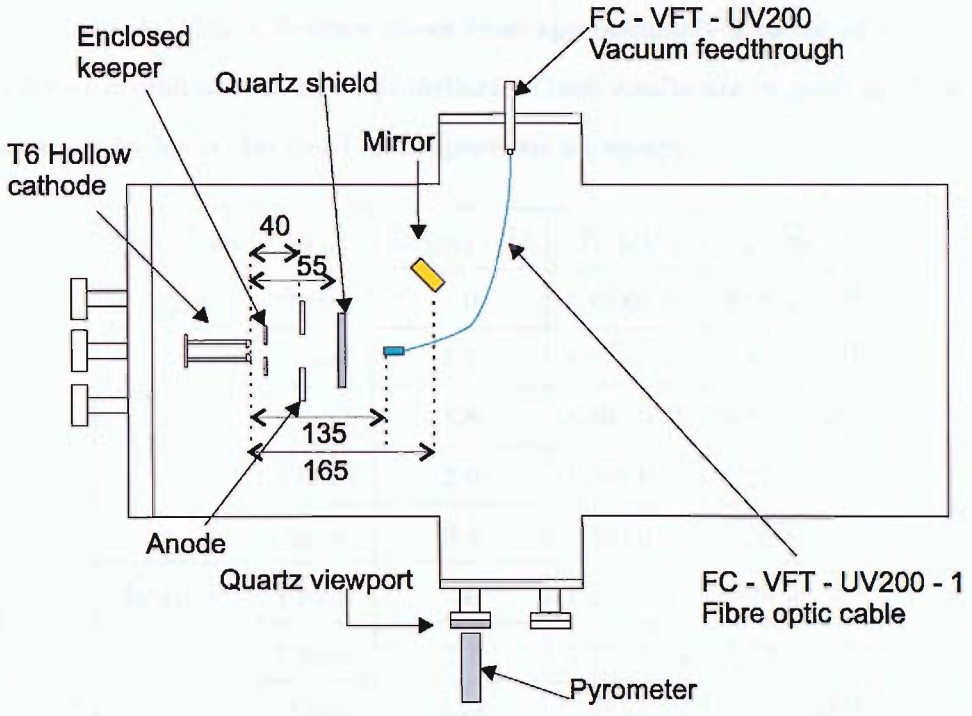

Figure 2.15: Schematic of the HC and optical system arrangement (dimensions in mm) [2]

using optical emission spectroscopy amongst other methods by Rudwan at the University of Southampton [2]. An optical probe was placed external to the internal plasma, located downstream of the HC tip in the plume, as shown in Fig. 2.15. Spectra were recorded over wavelength ranges of $\lambda = 250 - 750nm$ and $\lambda = 400 - 470nm$ for xenon propellant and a wavelength range of $\lambda = 400 - 470nm$ alone for argon and krypton. The plasma was found to emit strongly in the visual region of the spectrum and spectral line intensities were monitored as a function of discharge power. For singly ionised species (ArII 434.8064nm, KrII 435.5477nm, XeII 460.300nm) line intensity related to discharge power as an order 2 polynomial. Neutral spectral lines were less sensitive to discharge power. Line intensity was found to decrease with increasing mass flow rate. The collisional radiative plasma model was applied with the ladder approximation to determine plasma parameters; the results are shown in Table 2.2.

In the plume mode electron temperature and number density increase with increasing mass flow rate. No clear trends were established between atomic mass/propellant type and the plasma parameters. In the spot mode the electron number density is less than that achieved

in the plume mode. The difference varies from approximately a factor of two for xenon to an order of magnitude for argon propellant. These results are in good agreement with those obtained by Malik discussed in the previous paragraph.

Propellant	Mode	$\dot{m}$ (mgs^{-1})	T_e (eV)	n_e (cm^{-3})
Argon	Plume	1.0	1.12±0.05	3.10×10^{14}
	Plume	1.5	1.17±0.04	8.85×10^{15}
	Plume	1.8	1.30±0.05	8.51×10^{16}
	Plume	2.0	1.38±0.05	1.27×10^{17}
	Spot	3.4	1.32±0.05	7.30×10^{15}
Krypton	Plume	1.0	1.19±0.14	4.20×10^{15}
	Plume	2.1	1.31±0.14	3.06×10^{16}
	Spot	3.78	1.28±0.14	1.35×10^{16}
Xenon	Plume	1.0	1.05±0.17	1.38×10^{16}
	Plume	1.56	0.95±0.19	1.09×10^{16}
	Spot	3.29	0.98±0.20	6.99×10^{15}

Table 2.2: Experimental values of electron temperature and number density for $I_A = 5.0A$, Rudwan[2]

2.9 Summary of Research

The experimental work reviewed in this chapter provides a general description of HC characteristics and performance. To date investigations have identified the conditions that result in mode change from monitoring V-I characteristics as a function of mass flow rate and anode geometry and qualitative theories exist that explain the phenomenon. Langmuir probes have been used to investigate the interior of the HC and provide values for the electron temperature, number density and plasma potential. This technique may cause severe plasma perturbations to occur and may interfere with the plasma processes occurring in the region under investigation, thus bringing the reliability of the data collected under question. The temperature distributions obtained for tantalum inserts using opti-

cal pyrometry cannot be applied to current impregnated tungsten inserts because of the differences in the thermal characteristics of the materials. Accurate temperature profiles are of great importance if HC life limiting factors are to be fully understood. Studies into the production of high energy ions have yet to explain the presence of ions with energies greater than the discharge potential, which may cause HC failure from tip erosion. Spectroscopic investigations have used externally placed diagnostic equipment, therefore the data collected is integrated along the line of sight of the optics used i.e. along the length of the HC. As a consequence the plasma may not be resolved in the axial direction and information regarding gradients in plasma parameters and temperature distributions cannot be collected. The lack of data pertaining to the internal plasma hinders the development of reliable HC simulations, which require experimental results for code validation.

The previous experiments performed on HCs have highlighted the areas of HC operation which require further investigation. The mechanisms responsible for observed phenomena such as increased electron emission due to the use of enclosed keepers and the production of high energy ions have yet to be identified. A complete theory of mode change characteristics needs to be developed. This theory must incorporate the influence of orifice geometry on mode transitions. Also, the applicability of research findings obtained for HCs operated in diode configuration to HCs operated in full thruster configuration must be assessed, as only one mode (the spot mode) is observed in thrusters. This implies that the characteristics of HC operation must be decoupled from external factors including anode geometry and test facility background pressure in order to develop a universal theory for HC operation.

The plasma processes occurring within the orifice require extensive investigation. The small scale of the plasma (typically diameters less than 1mm) and the presence of high energy ions has prohibited experimental investigations. The contribution made to the electron current due to orifice processes is not known and the ion fractions within the orifice need to be determined. Within the insert region experimental investigation has been prohibited for the same reasons. Temperature gradients for the insert surface and electrons within the HC need to be determined and their dependence on operating parameters assessed. Radial distributions of the internal plasma have yet to be investigated.

The chemistry of the tungsten impregnate material may provide an insight into the end of life mechanisms for the component. The mobility of barium atoms and ions requires investigation in order to explain observed deposits at the rear of HCs.

A precise mechanism for plasma breakdown has yet to be established. In order to understand the HC start up mechanism, the region where breakdown initially occurs and the transfer of this plasma to the insert region of the HC needs to be investigated.

The research objectives of this investigation outlined in Chapter 1 will aim to address the dependence of plasma parameters and insert temperature on axial position. The influence of external factors such as electrode geometry and the inert gas propellant used will be investigated. These results will provide a basis for comparison with results obtained for the HC discharge plasma, which includes the plasma within the orifice and inter electrode space as well as the insert region. This comparison will provide an insight into the processes which occur within the orifice and between the electrodes and will indicate the difference between the HC internal plasma and the orifice plasma.

The following chapter will describe the equipment developed and the techniques used in order to record spectra at various positions along the axis of a modified T6 HC with the aim of calculating temperature distributions and plasma parameters.

Chapter 3

Experimental Apparatus

3.1 The Vacuum Facility

The experimental rig consists of a stainless steel vacuum chamber of diameter $0.5m$ and length $0.5m$. Within the chamber is a water cooled copper shroud that dissipates the heat generated by the HC during operation, preventing the chamber from over heating. Access for diagnostic equipment, propellant feed lines and electrical power is provided by a variety of vacuum chamber feedthroughs that are connected to either the main door of the vacuum chamber or an ISO160 port (see figure 3.1).

The power supply system was originally designed to function as the power supply of a fully operational UK25–Ion Thruster [97]. This has resulted in a complex system that requires independent supplies for grids, electromagnets, three electrodes and two HC heaters. This system is still operational at present but in the current investigation only the four power supplies listed below were used.

- The HC heater power supply,
- The keeper electrode low voltage power supply,
- The keeper high voltage power supply,
- The anode power supply.

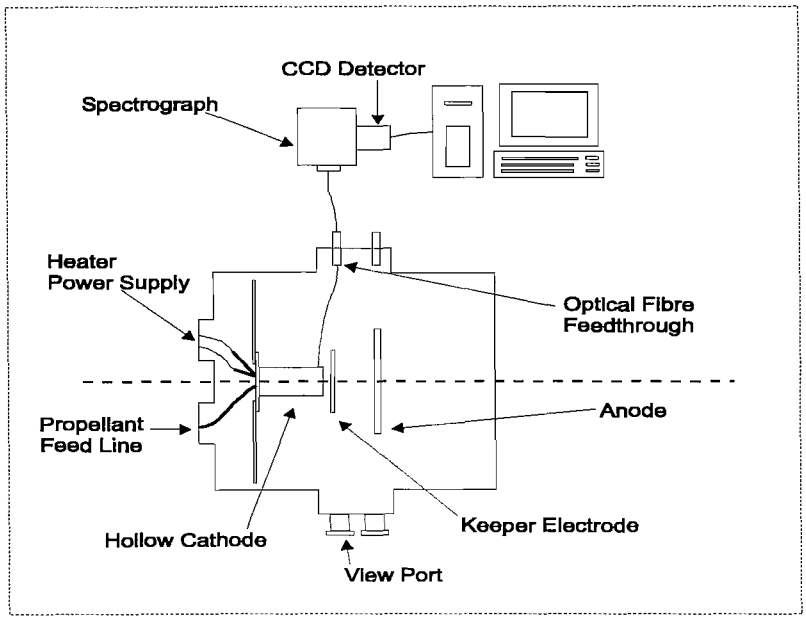

Figure 3.1: Experimental Facilities

The propellant feed system utilises a Negretti needle valve to control the propellant flow to the HC. Upstream of the valve are two oxygen traps (a low capacity indicating trap and a high capacity non indicating trap) that filter the inert gas propellant to ensure that there are no impurities (oxygen contamination) in the gas. This oxygen trap is connected to a high accuracy two stage pressure regulator that controls the outlet pressure of the propellant gas from its cylinder. The propellant flow is calibrated by passing the gas into an evacuated sampling cylinder of volume V and measuring the rate of change of pressure using a piezo–electric pressure transducer (Druck PDCR910). The temperature of the gas is monitored with a k–type (general purpose, $0-480^{o}C$) thermocouple. The mass flow rate $\dot{m}$ for a gas at temperature T with gas constant R is calculated by a computer programme using Equ. 3.1. In this way $\dot{m}$ is known for a given valve setting.

$$\frac{dp}{dt} = \dot{m}\frac{RT}{V} \tag{3.1}$$

The vacuum system is capable of achieving high vacuum ($P \sim 10^{-7} mbar$), which is necessary for the operation of the HC in order to prevent contamination of the insert with residual oxygen. The vacuum chamber pressure achieved under load is typically $\sim 10^{-4} mbar$. It is also desirable to run the HC in a low pressure environment to minimise the influ-

ence of the background pressure on HC operation and its characteristics. The pumping system used to obtain the required background pressure utilises a rotary vane pump connected in series with a water cooled turbomolecular pump with a pump speed of $500ls^{-1}$. The vacuum chamber pressure is monitored with a pirani gauge in the pressure range of $1000 - 5.4 \times 10^{-4}mbar$ and a cold cathode gauge in the range of $5 \times 10^{-3} - 1 \times 10^{-9}mbar$. Switching between the two gauges occurs automatically and the chamber pressure is digitally displayed. The vacuum chamber system is described in detail in Ref. [97]

3.2 Instrumented Hollow Cathode

The HC used in this investigation was designed and manufactured in collaboration with QinetiQ (formerly Dera). Technical consultation led to the conclusion that modifying the T6 HC would provide for investigation a reliable well tested model with a long heritage. This model of HC is space rated and has demonstrated its reliability in extensive testing and characterisation [59, 62]. The data collected during these tests provide a basis for comparison with the performance of the modified HC. The modified HC has dimensions:

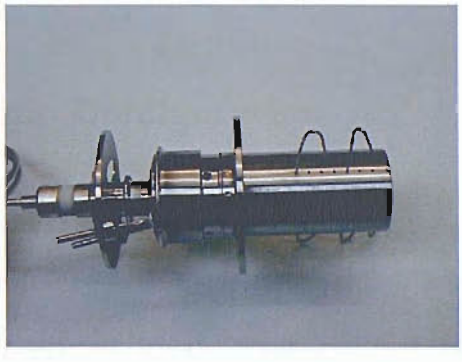

Figure 3.2: Modified HC with probe access

$36.9mm$ length from tip to flange, $18.9mm$ outer diameter and $1.98mm$ dispenser inner diameter. There are 14 radial holes with diameter of $0.6mm$ which may be used for probe access as shown in Fig. 3.2. When the probe access holes are not in use they are blocked off with tantalum pins to ensure there are no propellant leaks. The differences between the standard T6 and the modified model are as follows;

- The modified T6 has only one heater. The redundant heater coil has been removed to allow space for probe access holes.
- The modified T6 has fourteen axial holes with diameter of $0.6mm$. There are seven probe access holes on opposite sides of the HC offset by $1.4mm$ to provide maximum coverage of the plasma.
- The modified HC has a blanked off radial hole in the tip. A thermocouple may be placed in this hole in order to obtain accurate tip temperature measurements.

Aside from these modifications the instrumented T6 consists of the same elements as a standard model. It has a layered design incorporating a stainless steel outer casing, radiation shield and insulation as described in Chapter 2. The HC insert is a porous tungsten tube impregnated with a mixture of earth metal oxides that lower the work function of the material facilitating the thermionic emission of electrons. This HC design allows the spatial resolution of the internal plasma in the axial direction with a variety of diagnostic equipment. To the best of the author's knowledge this type of measurement has not been previously attempted.

3.3 Hollow Cathode Configuration

Throughout this investigation the HC was mounted in alignment with two concentric electrodes known as the keeper electrode and the anode; this is known as the diode configuration. The keeper was not enclosed in the HC casing, this is referred to as an open keeper. It has been shown that the HC – keeper separation influences HC performance and the HC – anode separation influences the transition from plume to spot mode [98]. In order to minimise both anode and keeper noise as well as the production of electromagnet interference, a HC – keeper separation of $3mm$ was chosen. This separation enables discharge initiation to occur at relatively low keeper voltages compared to other distances [99]. Experiments were carried out using either a keeper anode separation of $60mm$, referred to as geometry 1 or a separation of $30mm$ described as geometry 2 (see figure 3.3).

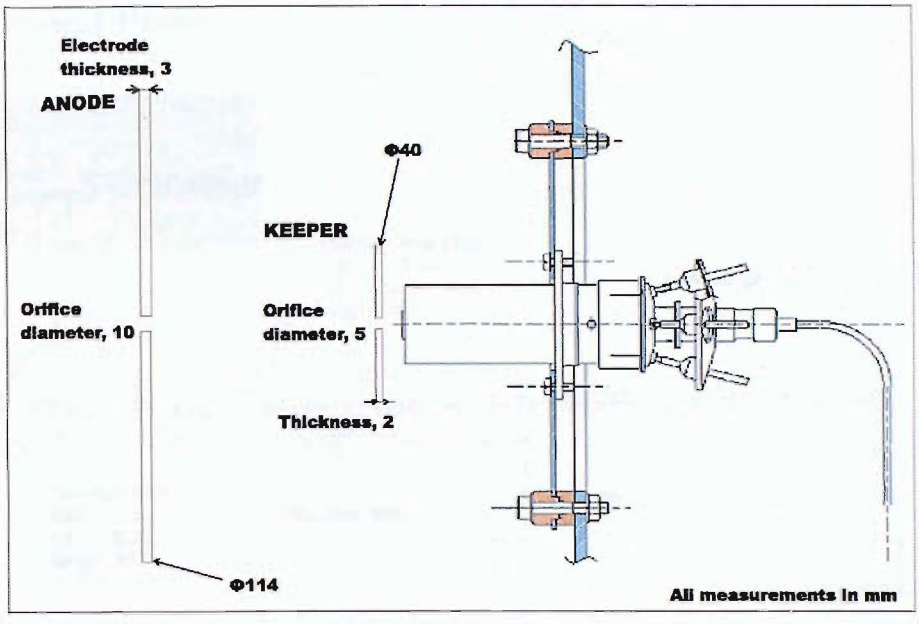

Figure 3.3: Cathode Configuration.

3.4 Diagnostic Equipment

The diagnostic equipment used in this investigation was specially developed in order to function in the environment of the internal plasma. Langmuir probes are widely used for plasma diagnostics due to fact that they allow localised plasma parameter measurements; the probes may also be displaced radially or axially to provide profiles of parameters and they are simple and inexpensive to construct [100, 101, 102, 103, 104]. However, immersing the probe in the plasma results in the formation of a sheath about the electrode which attracts either electrons or ions depending on its bias voltage. As a consequence the electrode of the probe influences the region under investigation and may cause serious plasma perturbations to occur. If the mean free paths of the constituent particles of the plasma are greater than the dimensions of the probe the results obtained are the same as those found in the absence of a probe [105]. This is not the case for the HC internal plasma; for this reason the use of Langmuir probes was prohibited for use in the current investigation. The most appropriate technique for investigating the internal plasma was found to be optical emission spectroscopy as this method is noninvasive [2].

3.4.1 Optical Probe

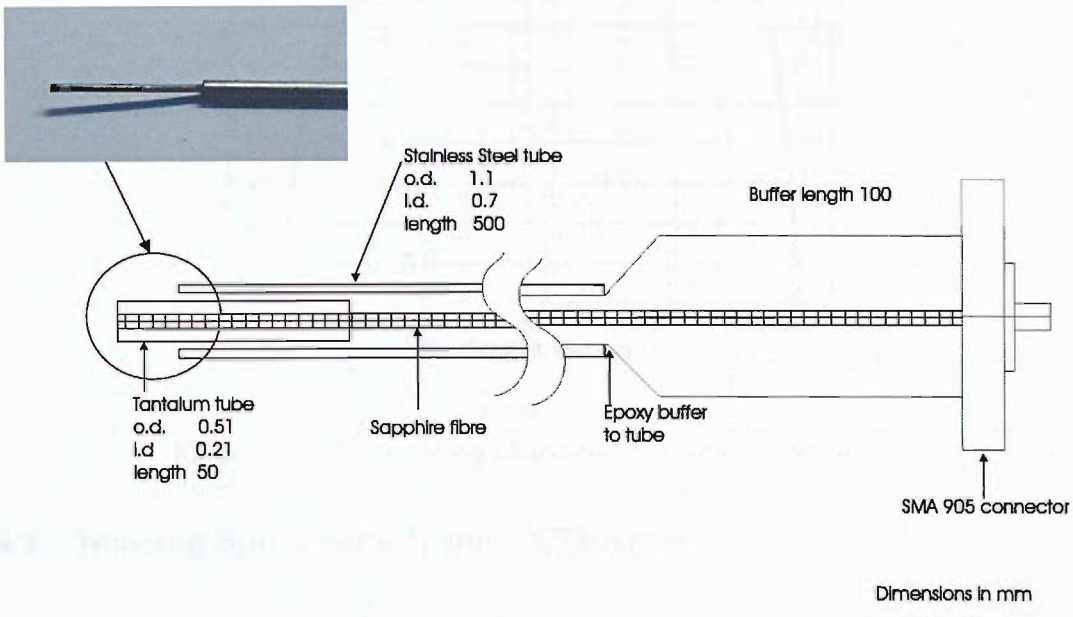

Figure 3.4: Optical Probe

The optical probes used in this investigation were designed by Dr. I. Rudwan of the University of Southampton. These probes were designed to function in a high temperature environment in the presence of high energy ions that may bombard the probe and possibly cause damage. For this reason typical fibre optic materials such as silicon were not used. Sapphire fibres (UV grade) of chemical composition Al_2O_3 were used. They have a temperature rating of $\approx 2000°C$ and excellent transmission characteristics for the region of interest ($\lambda \approx 200 - 900nm$), as shown in Fig. 3.5. The fibre has a diameter of $0.15mm$ and is surrounded by a tantalum tube of outer diameter $0.5mm$ and inner diameter $0.2mm$. A stainless steel tube of diameter $1.1mm$ provides the protective outer casing as shown in figure 3.4. These probes have a field of view of 30° half angle which allows an approximate area of $4mm^2$ of the insert surface to be seen by each probe, this corresponds to each probe collecting data from a conical volume of $2.7mm^3$.

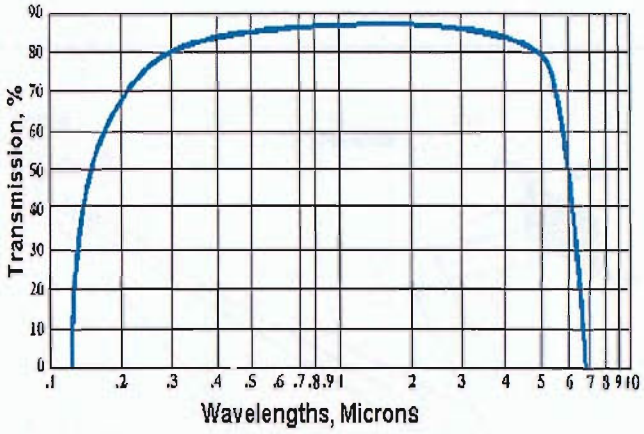

Figure 3.5: Transmission characteristics of sapphire fibre.

3.4.2 Imaging Spectrograph and CCD Array

The $MS127i^{TM}$ distributed by Oriel Instruments was the imaging spectrograph used during this investigation (see Fig. 3.6)[106]. The spectrograph was designed using the Czerny–Turner optical layout with the addition of an astigmatism correcting mirror (see Fig. 3.7). This instrument has the capability to perform multi–track spectroscopy i.e. different spectra may be recorded simultaneously. The use of interchangeable gratings and slits allows the spectral range and resolution to be varied according to the requirements of the experiment. In this investigation the diffraction grating used to spatially separate light

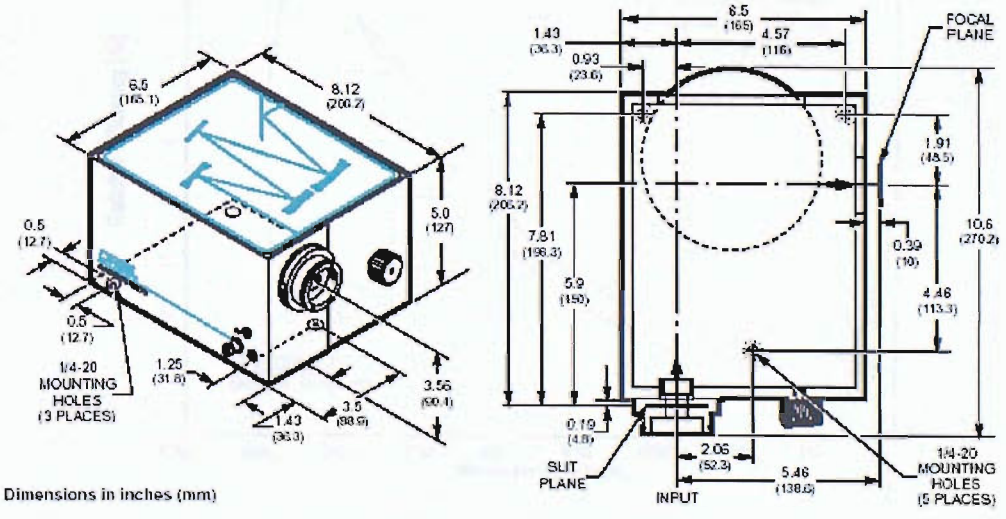

Figure 3.6: Diagram of the $MS127i^{TM}$ spectrograph.

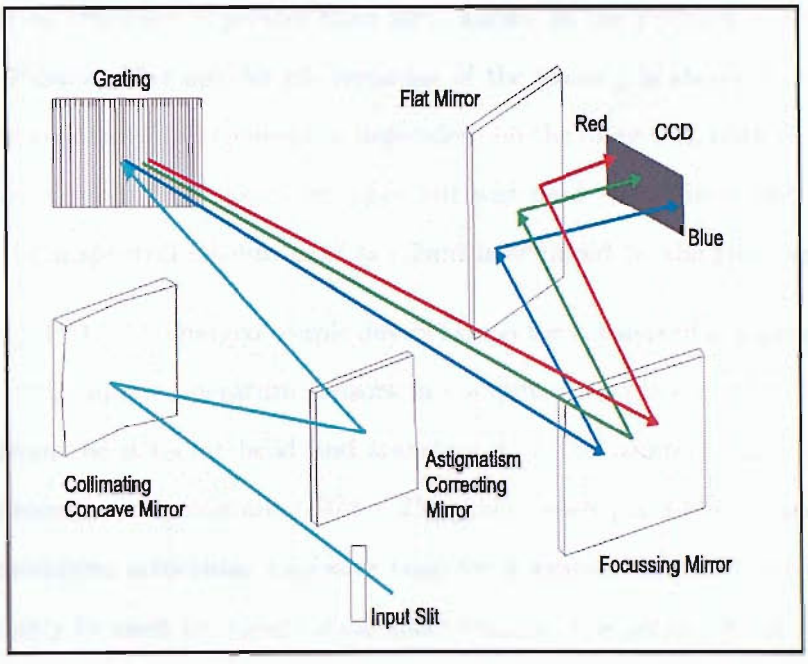

Figure 3.7: Spectrograph optical layout.

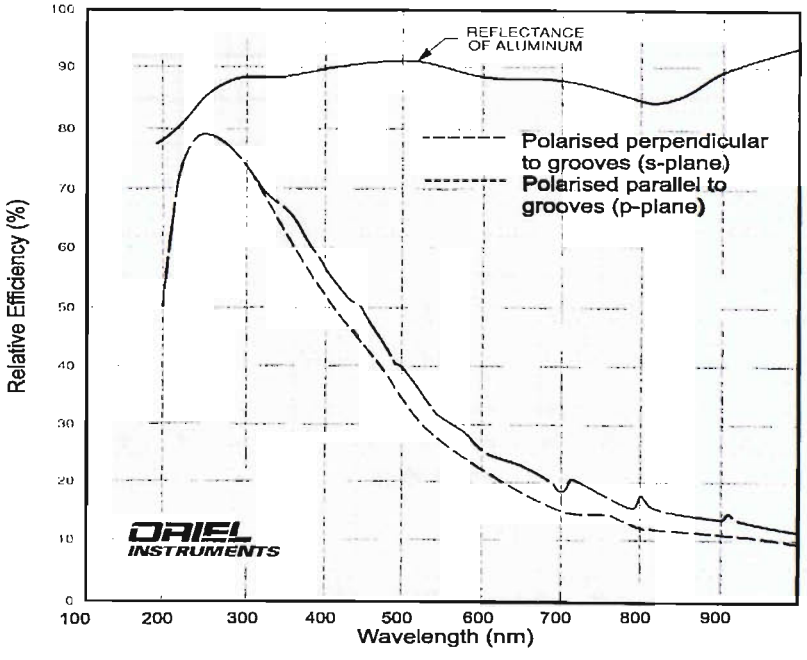

Figure 3.8: Grating efficiency curve

of different wavelengths was a ruled grating with a line density of $300l/mm$. The region where the grating efficiency is greater than 20%, known as the primary wavelength region is $\lambda = 200 - 750nm$. The wavelength response of the grating is shown in Fig. 3.8. The spectral resolution of any spectrograph is dependent on the input slit, optical magnification and reciprocal dispersion. A $25\mu m$ entrance slit was used throughout the investigation. With this set up a spectral resolution of $\approx 1.7nm$ is achieved by the spectrograph.

The IntaSpec^{TM}IV CCD (charged couple device) Detector consists of a detector head which contains the CCD and temperature sensors, a computer interface card which digitalizes analog data from the detector head and transfers it to the computer and a single stage cooler. The detector array contains 1024×256 pixels; each pixel has an area of $27\mu m \times 27\mu m$. The minimum achievable exposure time for a signal is $25ms$, therefore this CCD detector may only be used for steady state spectroscopy. The sensitivity of the detector is dependent on wavelength as shown by Fig. 3.9, therefore all spectra must be corrected for the variation in quantum efficiency prior to any calculations. The error of the quantum efficiency values plotted in Fig. 3.9 is $\pm 5\%$.

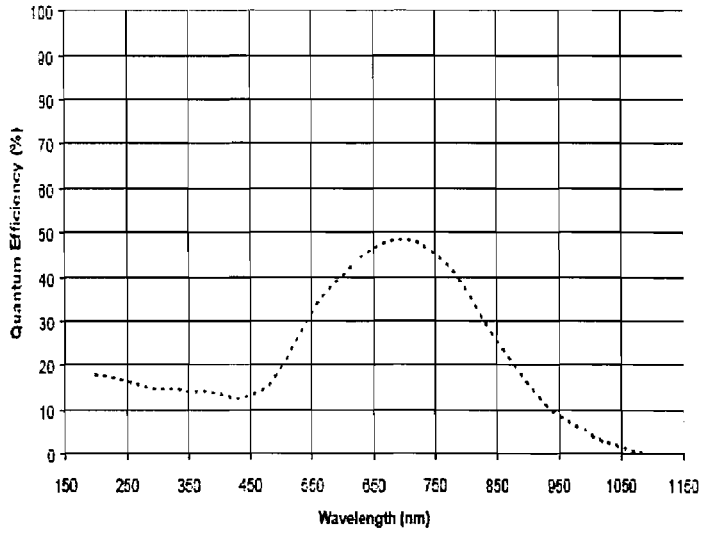

Figure 3.9: IntaSpec^{TM}IV CCD quantum efficiency curve.

3.5 Experimental Procedures

The instrumented HC was operated using three inert gas propellants, argon (Ar), krypton (Kr) and xenon (Xe). Experiments have been carried out over a range of anode currents, I_A and mass flow rates $\dot{m}$ with the aim of investigating the thermal and plasma processes that occur within the HC and how they vary as a function of axial position. Prior to

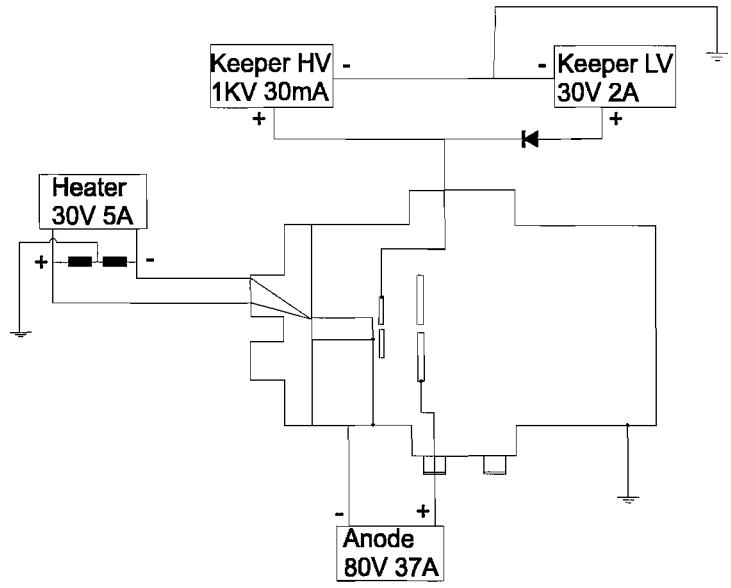

Figure 3.10: Schematic of the electrical power supplies and connections

performing experiments the HC and its electrodes were set up in the vacuum chamber. The HC flange was secured to the backplate which was in turn connected to a support structure attached to the vacuum chamber door. The electrodes were also screwed into the backplate but electrically isolated from the HC and vacuum chamber. Each component was connected to its respective power supply, as shown in Fig. 3.10 and the connection between the propellant feed line was made. The probe support structure was attached to the backplate in alignment with the HC probe access holes. A single optical probe was connected to an optical fibre feedthrough. At its opposite end it was threaded through the probe support and inserted into the desired probe access hole. The remainder of the probe access holes were plugged with tantalum pins to ensure that there were no propellant leaks. The vacuum chamber was then sealed and pump down initiated. The time taken to achieve sufficient vacuum for experiments to commence i.e. $P < 5 \times 10^{-7} mbar$ was

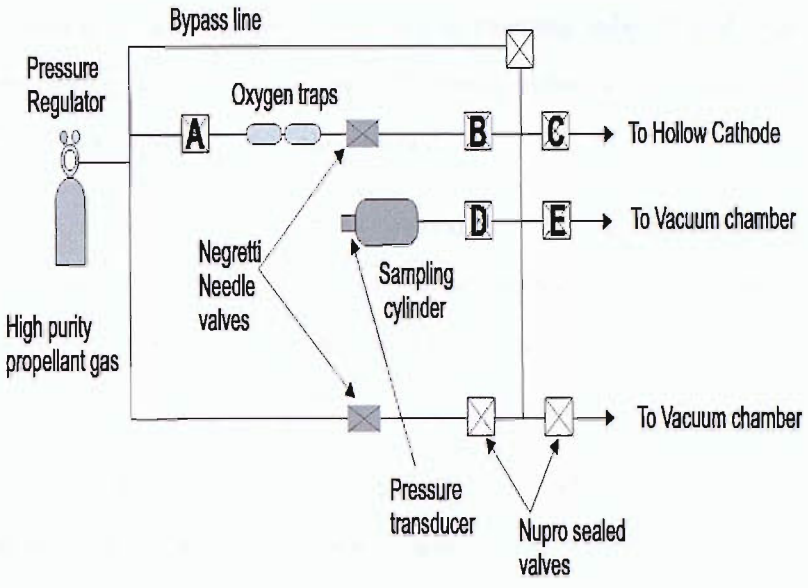

Figure 3.11: Schematic of the propellant feed system

typically 24 hours.

3.5.1 Mass Flow Rate Calibration

The HC flow calibration may only be performed when the vacuum chamber background pressure is less than $5 \times 10^{-7} mbar$. If this was the case the "datalink" software was run. The gas constant R of the propellant, determined using Equ. 3.2 was entered into the programme. The values of the gas constants are 208.1, 99.2 and $63.3 Jmol^{-1}K^{-1}g^{-1}$ for Ar, Kr, and Xe respectively.

$$R_G = \frac{R_U}{A_M} \tag{3.2}$$

Where the universal gas constant $R_U = 8.31 Jmol^{-1}K^{-1}$ and A_M is the atomic mass. With reference to Fig. 3.11 the following procedure was performed to calibrate the Negretti needle valve.

- Initially all Nupro valves (A, B, C, D) were closed. In order to evacuate the propellant feed line valves B, C and D valves were opened. When the evacuation was complete the valves were closed. This ensures that a pure gas is feed to the HC with no residuals from former propellants and is necessary if the previous experiment was carried out using a different propellant gas.

- The gas sampling cylinder was evacuated by opening valve D and gradually opening and then closing valve E until the PC readout displayed a pressure of less than $10mbar$. Valves D and E were then closed.

- The propellant gas bottled was then opened and the regulator outlet pressure set to the desired value. The regulator outlet valve and valve A were opened to charge the feed line with propellant. The Negretti needle valve was set to the required value and valves B and C were opened.

- To begin data acquisition a command was sent via the computer keyboard, immediately followed by the closing of valve C and opening of D.

- The gas flow, set by the needle valve, was directed into the sampling cylinder. The rate of rise of pressure within this cylinder was then used to calculate the mass flow rate.

- When data acquisition was completed the mass flow rate was automatically displayed on the PC monitor. Further measurements were taken by evacuating the sampling cylinder, setting the needle valve to the desired value and resending the command to begin data acquisition.

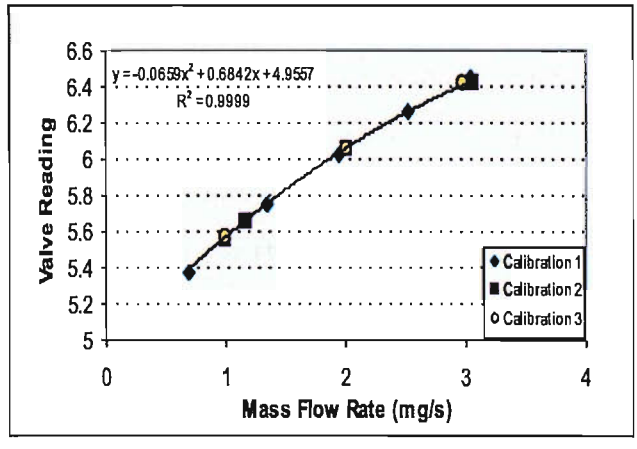

Figure 3.12: Mass flow rate calibrations for krypton propellant

	Temperature (K)		
Valve Reading	Calibration 1	Calibration 2	Calibration 3
Reading 1	296.7	293.8	294.2
Reading 2	296.7	294.0	294.2
Reading 3	296.7	294.0	294.3
Reading 4	296.7	293.9	-

Table 3.1: Temperature readings corresponding to the calibrations shown in Fig. 3.12

After collecting a data set the needle valve readings were plotted against the corresponding mass flow rates and an order 2 polynomial curve was fitted through the data. The equation of this curve was then used to determine the needle valve value for any given $\dot{m}$. Fig. 3.12 shows an example of the resulting plots. The calibrations were carried out for Kr propellant over a three week period at non regular intervals. This demonstrates the repeatability of the calibration process. The resulting needle valve calculations are reliable as the polynomial curve provides a good fit for the data. The correlation coefficient R^2, which represents the deviation of the curve fit from the actual data is ~ 1 for all calibrations. The main source of error for this calibration is due to temperature shifts. A temperature shift of $15K$ from $295K$ corresponds to a 5% error in $\dot{m}$; assuming a negligable error in the pressure measurent (see Equ. 3.1). Table 3.1 shows the temperatures recorded for each calibration point on Fig. 3.12. There is a maximum temperature difference of $0.2K$ for calibration 2. There is a maximum temperature difference of $2.9K$ between all three calibrations, which has little effect on the distribution of the calibration points. Therefore it is fair to assume that temperature ranges of less than $3K$ do not result in any hysteresis effects and hence contribute a negligible error to the mass flow rate calibration. HC flow calibrations were carried out prior to performing experiments and post calibrations were performed when experiments were completed to ensure that no variations in $\dot{m}$ had occurred due to temperature shifts.

3.5.2 Spectrograph Wavelength Calibration

The interface card of the IntaSpec^{TM} reads the CCD detector in terms of the discrete elements of the detector. It is preferable to relate the measurement being made to the physical quantity under investigation. For this reason it was necessary to calibrate the x and y axis to the required units. The y axis calibration was performed automatically when the calibrate menu displayed on the PC monitor was selected followed by "System Y Cal" and then the unit "counts". An array calibration was performed for the x axis where the calibration was stored in four constants α_1, α_2, α_3 and α_4 that form a cubic polynomial to convert the element number P to the new x axis value X.

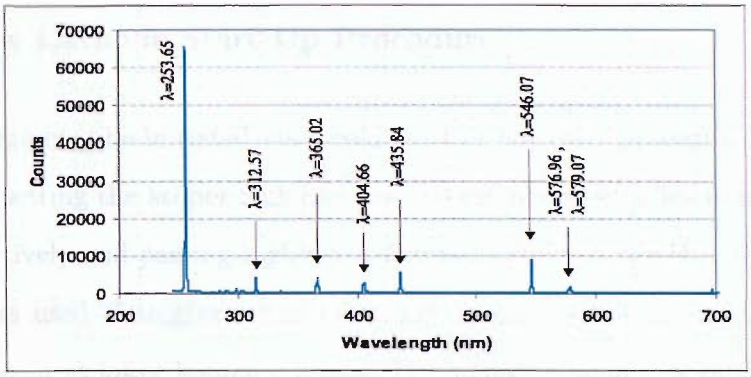

Figure 3.13: Tpyical Hg(Ar) lamp spectra

$$X = \alpha_1 + \alpha_2 P + \alpha_3 P^2 + \alpha_4 P^3 \tag{3.3}$$

Manual entry calibrations were performed throughout this investigation as this is the most accurate method for calibrating the x axis. In order to perform a manual calibration the pixel position and its corresponding calibration value must be known. For this purpose a mercury argon (Hg(Ar)) calibration lamp was used. This type of calibration lamp was chosen as the spectral lines produced as a result of the excitation of Ar atoms with Hg vapours are intense and reproducible. The calibration lamp has a 1.5 inch series female flange that was coupled directly to the spectrograph. To begin the calibration process the spectrum produced, similar to that shown in Fig. 3.13, was recorded.

The calibrate menu was chosen followed by "System X Cal". A prompt was then displayed requesting the calibration type; wavelength in units of nm was selected. This was followed

by a prompt to enter the calibration values. In order to do this the cursor was moved to the appropriate pixel position corresponding to a calibration spectral line (identified by comparison with the relative line intensity and position stated in calibration data); after pressing "enter" a new prompt asks for the calibration value at that point. After entering the calibration value "enter" was pressed again, this process was repeated until the desired number of calibration points have been entered; "E" was then selected to complete the calibration. The IntaSpec^{TM} software fits a smooth curve through the calibration points using Equ. 3.3 in order to convert and display the pixel number in the chosen units. Wavelength calibrations were performed at the beginning of all spectroscopic experiments.

3.5.3 Hollow Cathode Start Up Procedure

The HC discharge may be initiated via a cold start or hot start procedure. The cold start option requires setting the keeper high and low voltage power supplies to maximum, $1KV$ and $32V$ respectively and passing high mass flow rates through the HC. However, the hot start option was used throughout this investigation as this allows repeatable discharge breakdown to occur at lower keeper voltages. The following actions were taken in order to facilitate HC discharge breakdown.

- The HC start up procedure required that the power supply output voltages and current limits were set. The anode power supply limiting current was set to $1.0A$, with the corresponding voltage of $\approx 82V$.

- The keeper low voltage was set by turning both the current and voltage to zero; the output terminals were connected to cause a short circuit. The current was then adjusted to $0.5A$ and the voltage turned to the maximum of $32V$.

- A HC propellant flow of $\sim 0.5Aequiv$ determined using Equ. 3.4 for an ion with mass m_i in mg was initiated; e is the electronic charge. In units of mgs^{-1} the mass flow rates used for the inert gas propellants are as follows; Ar: $0.2mgs^{-1}$, Kr: $0.4mgs^{-1}$ and Xe: $0.7mgs^{-1}$.

$$\dot{m}(Aequiv) = \frac{e}{m_i}\dot{m}(mgs^{-1}) \tag{3.4}$$

- The current and voltage of the heater power supply were set to zero and the mains power supply turned on. The HC was heated slowly over a period of 10 minutes to prevent thermal shocks. The power to the heater was increased over this 10 minute period by adjusting the current in increments of $\approx 0.2A$ per minute until a power of $40W$ was achieved. The HC was then heated at this power level for a further 5–10 minutes.

- The keeper and anode power supplies were turned on and $\dot{m}$ increased to $\sim 1Aequiv.$ The keeper high voltage was increased until plasma breakdown occurred. At the point of plasma initiation the HC heater and keeper high voltage power supplies were immediately turned off.

- The anode power supply was enabled, thus allowing the discharge to transfer to the anode. The anode current was then set to the desired value and experiments commenced.

The above procedure was not followed for the initial HC run. The first attempt to achieve plasma breakdown required the HC to be heated to high power ($\approx 60W$) for a period of $\approx$ 30mins. Subsequent breakdowns occurred more easily.

3.5.4 Steady State Spectroscopic Experiments

The procedures stated above for the installation of equipment, HC flow and spectrograph calibration and the HC hot start were followed. The standard experimental practice of varying one parameter whilst keeping the remainder constant was employed throughout the investigation. Optical emission spectra were recorded by probes placed in the probe access holes shown in figure 3.2. Data were collected by one probe at a time. When the characterisation was complete the probe was repositioned. Throughout the experiments the CCD array was cooled to $-10°C$ to reduce thermal noise. The keeper current was set to $I_K = 0.5A$ for all experiments. After discharge initiation the anode current was increased to $I_A = 2.0A$ and the mass flow rate was set to $\dot{m} = 1.1mgs^{-1}$ for Ar and $\dot{m} = 1.0mgs^{-1}$ for Kr and Xe. The discharge was allowed to run for 10 minutes under

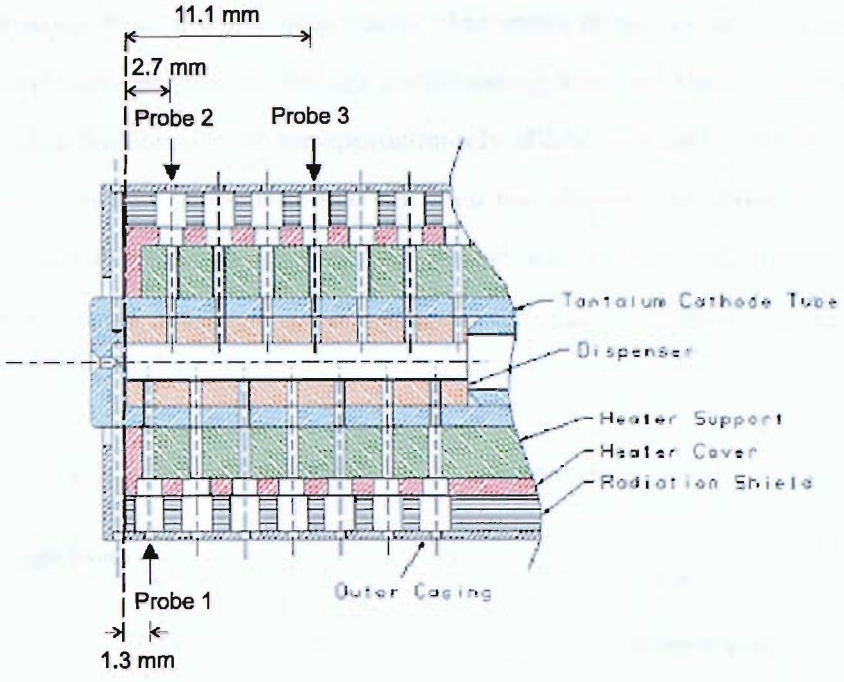

Figure 3.14: Optical probe positions

these conditions prior to recording spectra. The propellant flow to the HC was set to the lowest value and the anode current stepped up manually in $1A$ increments at regular time intervals of $\sim 3mins$ from $I_A = 2.0A - 10A$ as was the case for initial experiments or $I_A = 2.0A - 15A$ for later experiments. When spectra were recorded at the maximum anode current the current was then decreased to the minimum value of $I_A = 2.0A$ and the mass flow rate was increased, the process was then repeated. The range of mass flow rates utilised was typically $\dot{m} = 1.0 - 3.0mgs^{-1}$. For Kr and Xe propellants spectra were recorded for $\dot{m} > 0.5mgs^{-1}$. During initial experiments the exposure time of the recorded signal was $60s$. After approximately 50hrs of operation this was increased to $90s$ as it was noticed that the probe transmission had decreased after exposure to the plasma (see Section 3.5.5).

3.5.5 Probe Transmission Experiment

An experiment was devised to monitor the spectral response of the optical probe when used in conjunction with the imaging spectrograph. The set up shown in Fig. 3.15 was used to monitor the deterioration of transmission characteristics after exposure to the plasma

discharge. Radiation from a white light source that emits in the visual to near infra red range of the spectrum was passed through a collimating lens and then focussed onto the tip of a probe that had been used for approximately $60hrs$ (not including heating time) and for comparison a new probe that had not seen the plasma; the results are shown in Fig. 3.16. The exposure time for the recorded spectra was $30s$, one integration was used. The transmission curves show the same trends as the quantum efficiency curve for the

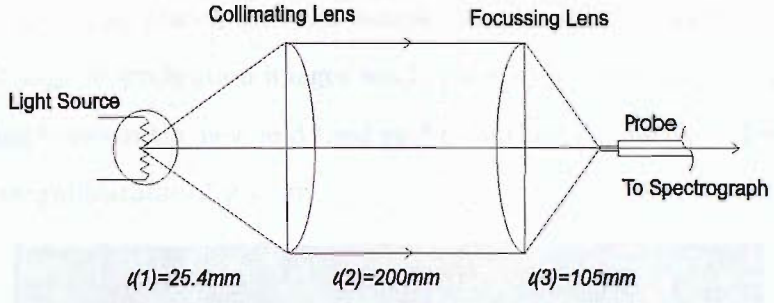

Figure 3.15: Probe transmission experimental set up

CCD detector, with both peaking in the region of $\lambda = 700nm$ (see Fig. 3.9). The spectral response of both probes are similar up to $\approx 450nm$ after which the counts recorded for new probe are an order of magnitude greater than those recorded for the used probe. The decreased transmission may be caused by energetic atoms and/or ions sputtering the surface of the fibre resulting in damage that impedes light transmission. Also, particles may be deposited on the fibre that prevent light from passing through it.

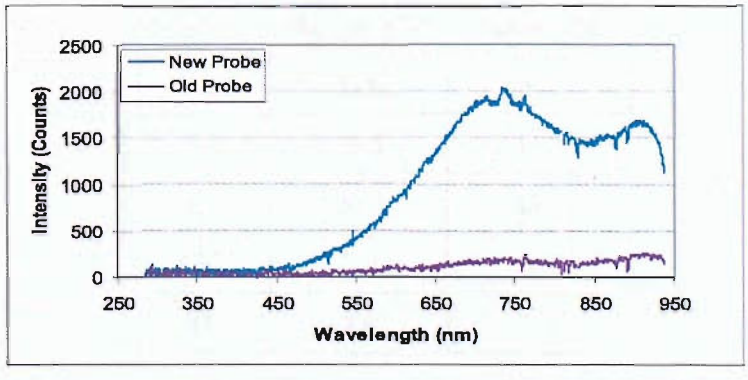

Figure 3.16: Deterioration of probe transmission after exposure to plasma

3.5.6 Scanning Electron Microscopy Analysis

As described in the previous section, exposure of optical probes to the plasma resulted in reduced probe transmission. Scanning electron microscopy (SEM) analysis was carried out in order to establish the cause of the deterioration. Acetate replicas were taken of the tips of an unused probe and a used probe. This required a layer of acetone to be poured onto an acetate block. The probe tip was placed into the acetone until it began to set. The probe was then removed, leaving its imprint in the acetone. The replicas were then sprayed with a layer of gold and placed into the sample chamber of the electron microscope. It was hoped that high magnification images would show differences in the level of structural stress or damage between the new and used probes but unfortunately differences were not discernible at magnifications of 2×10^5.

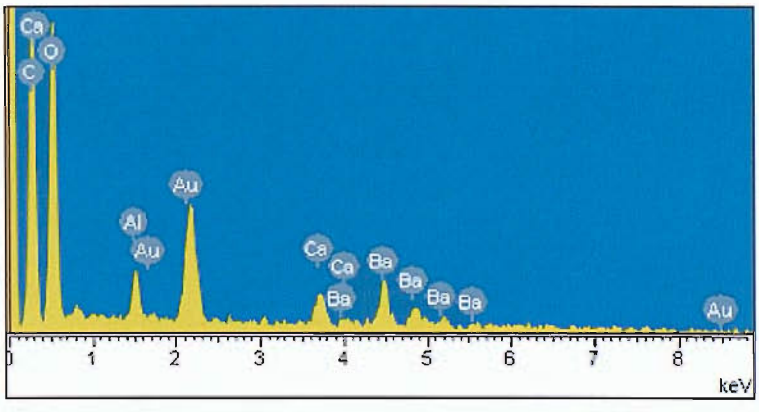

Figure 3.17: Chemical abundances

Element	Weight (%)	Atomic (%)
Ba	45.0	8.4
O	26.5	42.3
C	20.3	43.2
Ca	5.2	3.3
Al	3.6	2.8

Table 3.2: Chemical composition of particles found on probe tip.

Back scattered electron images taken of the acetate block allowed chemical analyses to be carried out in order to determine if particles had been deposited on the probe tip. The data shown in figure 3.17 were collected from the used probe after $60hrs$ of exposure to the plasma. This shows that barium and calcium had been deposited on the tip. No traces of these elements were found for the new probe. From table 3.2 it can be seen that barium is the most abundant element by weight. This implies that barium and calcium freed by the heating process migrate along the insert and later form deposits on the surface of the dispenser.

Chapter 4

Plasma Models

The quantitative analysis of optical emission spectra requires plasma models to be used that relate the observed quantities i.e. intensity and wavelength to plasma parameters such as electron density and temperature. In order to simulate the behaviour of plasmas both collisional and radiative processes should be considered. For any given species (N) with charge z in the atomic states p, q or ground state g these processes are outlined below [107].

$$N(z,p) + e \rightleftharpoons N(z,q) + e \tag{4.1}$$

$$N(z,p) + e \rightleftharpoons N(z+1,g) + e + e \tag{4.2}$$

$$N(z,p) \rightarrow N(z,q) + h\nu \tag{4.3}$$

$$N(z+1,g) + e \rightarrow N(z,p) + h\nu \tag{4.4}$$

Equs. 4.1 and 4.2 describe collisional processes. Equ. 4.1 refers to transitions between two bound levels that are induced by electron collisions, where collisional excitation is balanced by its reverse decay mechanism. Collisional ionisation from any bound state is described by Equ. 4.2 and is balanced by three body recombination. The remaining equations describe the radiative processes. Equ. 4.3 shows the spontaneous decay of an electron in an upper level and the emission of radiation (a photon) due to the conservation of energy. Its inverse process, radiative recombination is described by Equ. 4.4.

Laboratory plasmas may be described using the following three models,

- Local thermodynamic equilibrium (LTE)
- Corona (CO) model
- Collisional radiative (CR) model

In the following discussion two assumptions have been made.

- The plasma is optically thin.
- The free electrons have a Maxwellian velocity distribution.

For the optically thin case the radiation produced in the bulk of the plasma does not interact with the plasma as it travels out towards diagnostic equipment. If this were not the case radiation would be trapped. This would affect the population densities of the energy levels and the observed radiation intensities would not be the sum of the incremental intensities from the volume elements along the line of sight of the detector. A Maxwellian distribution is described by Equ. 4.5 [108].

$$f^M(V) = \left(\frac{m}{2\pi kT}\right)^{\frac{3}{2}} \exp\left(\frac{-mV^2}{2kT}\right) \tag{4.5}$$

Where V and m are the particle velocity and mass respectively, T is the temperature of the plasma species under consideration and k is the Boltzmann constant. The mean velocity of heavy particles is less than the electron velocity in the HC plasma due to the fact that the mass of the heavy particles is four orders of magnitude higher than the electron mass. If this was not the case heavy particle collisions would become important and it would become necessary to establish a distribution function for the heavy particles.

4.1 Conditions for a Maxwellian Distribution

The Maxwellian distribution may only be applied to plasmas that conform to a set of conditions, which arise as a consequence of kinetic theory. Kinetic theory describes the interaction of the constituent particles of ionised or neutral gases. The derivations of electron distribution functions are described in detail in Ref. [109] and give rise to the

conditions for a Maxwellian distribution stated in Equ. 4.6–Equ. 4.9. An additional requirement is that departures of the electron distribution from an isotropic distribution are small which is the case for the HC plasma. As it is fair to expect that the velocity distribution is independent of direction due to the high collision frequency of the plasma species and a small mean free path.

$$\sum_h \frac{m_e}{m_h}\frac{\bar{\nu}_{eh}}{\bar{\nu}_{ee}} << 1 \tag{4.6}$$

$$\frac{1}{\bar{\nu}_{ee}\tau} << 1 \tag{4.7}$$

$$\frac{\bar{C}_e}{\bar{\nu}_{ee}L} << 1 \tag{4.8}$$

$$u \leq \bar{C}_e \tag{4.9}$$

The first condition (Equ. 4.6) is satisfied as the electron mass $m_e = 9.110 \times 10^{-31} kg$ is orders of magnitude smaller than the heavy particle mass m_h (atom or ion) whilst the mean electron–heavy particle collision frequency $\bar{\nu}_{eh}$ is of the same order as the electron–electron collision frequency $\bar{\nu}_{ee}$, as can be seen from Equs. 4.10 and 4.13. The mean collision frequency for electron–electron interactions $\bar{\nu}_{ee}$ is defined as follows [42],

$$\bar{\nu}_{ee} = n_e \frac{8\sqrt{\pi}}{3}\left(\frac{m_e}{kT_e}\right)^{\frac{3}{2}}\left(\frac{e^2}{4\pi\epsilon_0 m_e}\right)^2 \ln\Lambda \tag{4.10}$$

The parameter Λ is defined as the ratio of the Debye length λ_D to the average impact parameter $\bar{b}_o$; e_r and e_s are the thermal energies per unit mass of species r and s respectively.

$$\lambda_D = \left(\frac{\epsilon_0 kT_e}{e^2 n_e}\right)^{\frac{1}{2}}, \bar{b}_o = \frac{|e_s e_r|}{12\pi\epsilon_0 kT_e} \tag{4.11}$$

$$\Lambda \equiv \frac{\lambda_D}{\bar{b}_o} = 12\pi n_e \lambda_D^3 \left|\frac{e^2}{e_s e_r}\right| \tag{4.12}$$

$$\bar{\nu}_{ei} = n_i \frac{8\sqrt{\pi}}{3}\left(\frac{m_e}{kT_i}\right)^{\frac{3}{2}}\left(\frac{e^2}{4\pi\epsilon_0 m_e}\right)^2 \ln\Lambda \tag{4.13}$$

Equs. 4.7 and 4.8 relate the characteristic time for macroscopic change to occur τ and the scale length of the plasma L. For the case of the internal plasma of a HC $\tau \sim 10^{-6} s$ and $L \approx 2cm$ as stated in Ref. [2]. $\bar{C}_e$ is the thermal velocity of the electrons.

$$\bar{C}_e = \sqrt{\frac{3kT_e}{m_e}} \tag{4.14}$$

Using Equ. 4.10 and Equ. 4.12 to determine the collision frequency with $T_e = 1eV$ and $n_e = 1 \times 10^{20} m^{-3}$ (typical observed values) results in $\bar{\nu}_{ee} \sim 1 \times 10^9 s^{-1}$ and the electron thermal speed $\bar{C}_e = 7 \times 10^5 m s^{-1}$

$$\frac{1}{\bar{\nu}_{ee}\tau} \sim 1 \times 10^{-4} << 1, \tag{4.15}$$

$$\frac{\bar{C}_e}{\bar{\nu}_{ee}L} \sim 1 \times 10^{-2} << 1 \tag{4.16}$$

As can be seen from Equ. 4.15 and Equ. 4.16 the conditions stated in Equ. 4.7 and Equ. 4.8 are satisfied by the HC internal plasma. The electron electron collision frequency is sensitive to the electron temperature; decreasing T_e causes an increase in ν_{ee} therefore the criteria hold for cooler plasmas.

The final condition (see Equ. 4.9) requires the mean speed of the plasma flow u to be less than the electron thermal speed $\bar{C}_e$. The HC is typically treated as a choked nozzle, the flow is said to be subsonic in the cathode channel and sonic on exit.

$$u_{sonic} = \sqrt{\gamma R_c T} \tag{4.17}$$

The sonic speed u_{sonic} represents the maximum achievable speed of the propellant flow within the cathode and is related to the ratio of specific heat γ, the gas constant R_c and the temperature T via Equ. 4.17 [110].

$$u \sim 10^2 << \bar{C}_e \tag{4.18}$$

Element	γ	R_c $(Jmol^{-1}K^{-1}g^{-1})$	u_{sonic} (ms^{-1})
Argon	1.67	208.1	833
Krypton	1.67	99.2	575
Xenon	1.67	63.3	460

Table 4.1: Speed of sound for inert gas propellant, $T = 2000K$

The speed of sound for the inert gas propellants are presented in table 4.1 for a gas temperature of $2000K$ (an over estimate). It is clear from the speeds obtained that the final condition (see Equ. 4.9) is met by the HC plasma. However, the equation above relates to a simple mono atomic gas flow. The HC plasma consists of neutral and charged

particles under the influence of electrostatic forces and possibly a magnetic field in the region of the orifice. As a result there may be an error associated with describing the mass characteristics of the plasma flow. It has been demonstrated that the internal plasma conforms to the conditions required for a Maxwellian velocity distribution to be used to describe the properties of free electrons within the plasma.

4.2 Optical Depth

In this section the second assumption made for the treatment of the HC plasma regarding radiation trapping will be discussed. The definition of optical depth is obtained from the theory of radiative transfer. If a beam of radiation of intensity $I(\nu)$ with frequency ν passes through a layer of thickness dx with mass density ρ and absorption coefficient $\chi(\nu)$, the loss of radiation intensity on passing through this layer is $dI(\nu)$.

$$dI(\nu) = I(\nu)\chi(\nu)\rho dx \tag{4.19}$$

where the optical depth of a plasma with thickness l is

$$\tau(\nu) = \int_0^l \chi(\nu)dx \tag{4.20}$$

These relations give rise to the equation of radiative transfer which describes the change in intensity due to an absorbing and emitting plasma layer(see Equ. 4.21).

$$\frac{dI(\nu)}{d\tau(\nu)} = -I(\nu) + \frac{J(\nu)}{\chi(\nu)} \tag{4.21}$$

Where the emission coefficient $J(\nu)$ represents the increase in intensity due to the power generated per unit mass per unit solid angle and the ratio $\frac{J(\nu)}{\chi(\nu)}$ is known as the source function.

The optical depth is a function of frequency. As a consequence a plasma may be optically thick for one spectral line and optically thin for another. The intensity of spectral lines is spread over a finite frequency range, therefore the optical depth may also vary over the width of a discrete spectral line. The mechanisms that contribute to broadening spectral lines may be classified as follows [111].

- Natural broadening as a consequence of spontaneous emission.
- Pressure broadening caused by particle interactions
  - Holtzmark (resonance/self) broadening, interactions with like neutral particles.
  - Lorentz or van der Waals, interactions with unlike neutral particles.
  - Stark broadening, interactions with charged particles.
- Doppler broadening resulting from thermal motions.
- Combination of the above broadening mechanisms.

In partially ionised gases Stark and/or Doppler broadening are typically the dominant line broadening mechanisms [42]. It has been observed that Doppler broadening dominates at high temperatures and low electron number densities whilst Stark broadening prevails for the reverse conditions [112].

The maximum optical depth is found in the centre of the discrete spectral line. The mean optical depth τ_0 taken at the central frequency ν_0 (c/λ) may be defined in terms of the characteristic depth of the plasma l, taken as the HC inner radius assuming that the radiation originates from the centre of the discharge and the absorption coefficient $\chi(\nu_0)$ which takes into account absorption and induced emission processes.

$$\tau_0 = \chi(\nu_0)l \tag{4.22}$$

For a plasma in local thermodynamic equilibrium the absorption coefficient is as follows [113],

$$\chi(\nu_0) = \frac{e^2}{4\epsilon_0 m_e c}\frac{N_a f_{pq}}{Z}\exp -\frac{E_p}{kT_e}\left(1-\exp -\frac{\chi_{pq}}{kT_e}\right)\phi(\nu_0) \tag{4.23}$$

Where N is the number density of the emitting species, f_{pq} is the oscillator strength, E_p is the energy of lower state p, χ_{pq} is the energy difference between states p and q, m_e is the electron mass, T_e is the electron temperature, ϵ_0 is the permittivity of free space and $\phi(\nu_0)$ is the line shape factor at the central frequency. Equ. 4.23 reduces to the following expression; as the partition function $Z \approx 1$ for inert gas atoms and $\exp \frac{-\chi_{pq}}{kT_e} << 1$.

$$\chi(\nu_0) \approx \frac{e^2}{4\epsilon_0 m_e c}N_a f_{pq}\exp -\frac{E_p}{kT_e}\phi(\nu_0) \tag{4.24}$$

For particles with a Maxwellian velocity distribution the line shape factor $\phi(\nu_0)$ for a spectral line exhibiting Doppler broadening is shown in Equ. 4.25 [42].

$$\phi(\nu_0) = \frac{2}{\Delta\nu_D}\left(\frac{\ln 2}{\pi}\right)^{\frac{1}{2}} \tag{4.25}$$

Where the Doppler half width $\Delta\nu_D$ is described by Equ. 4.26 for an absorbing particle of mass m_a and temperature T.

$$\Delta\nu_D = \frac{\nu_0}{c}\left(\frac{8kT\ln 2}{m_a}\right)^{\frac{1}{2}} \tag{4.26}$$

Species	λ (nm)	ν_0 (s^{-1})	f_{pq}	E_p (eV)	$\Delta\nu_D(s^{-1})$	$\phi(\nu_0)(s)$	$\tau_0(10^{-3})$
ArI	763.511	3.929×10^{14}	0.214	11.54835	4.792×10^{9}	1.960×10^{-10}	0.107
ArI	794.818	3.774×10^{14}	0.529	11.72316	4.603×10^{9}	2.041×10^{-10}	0.232
ArI	811.531	3.697×10^{14}	0.458	11.54835	4.508×10^{9}	2.084×10^{-10}	0.244
ArI	826.452	3.630×10^{14}	0.157	11.82807	4.427×10^{9}	2.122×10^{-10}	0.0645
ArI	840.821	3.568×10^{14}	0.394	11.82807	4.351×10^{9}	2.159×10^{-10}	0.165
ArI	852.144	3.521×10^{14}	0.151	11.82807	4.294×10^{9}	2.188×10^{-10}	0.0639
KrI	760.154	3.947×10^{14}	0.27	9.91523	3.323×10^{9}	2.827×10^{-10}	1.000
KrI	785.482	3.819×10^{14}	0.64	10.56242	3.216×10^{9}	2.921×10^{-10}	1.283
KrI	805.950	3.722×10^{14}	0.56	10.56242	3.135×10^{9}	2.997×10^{-10}	1.152
KrI	850.887	3.526×10^{14}	0.26	10.64364	2.969×10^{9}	3.164×10^{-10}	0.521
XeI	823.164	3.644×10^{14}	0.24	8.31532	2.452×10^{9}	3.832×10^{-10}	5.970
XeI	828.012	3.623×10^{14}	0.12	8.43653	2.437×10^{9}	3.854×10^{-10}	2.660
XeI	881.941	3.402×10^{14}	0.49	8.31532	2.288×10^{9}	4.105×10^{-10}	13.059
XeI	895.225	3.351×10^{14}	0.19	8.43653	2.254×10^{9}	4.167×10^{-10}	4.553

Table 4.2: Optical depth for $l = 1mm$, $N = 1\times10^{20}m^{-3}$ and $T = T_e = 1eV$.

Equs. 4.22 – 4.26 allow the optical depth of the HC internal plasma to be determined. Table 4.2 shows the optical depths for the spectral lines used in this investigation for typical HC operating parameters i.e. $l = 1mm$, $N = 1\times10^{20}m^{-3}$ and $T = T_e = 1eV$, the heavy particle temperature is assumed to be equal to the electron temperature. Although this may not be the case the square root relationship of the temperature and the Doppler half

width results in decreased sensitivity to temperature hence reducing the error associated with the assumption. A decrease in the electron temperature for a given set of conditions results in a decrease in the optical depth. A plasma may be described as optically thick if $\tau(\nu) >> 1$, a plasma is optically thin if $\tau(\nu) << 1$ [111]. It can be seen from Table 4.2 that the condition for an optically thin plasma is met by the internal plasma for the spectral lines of interest. This result is in agreement with the conclusions drawn from optical depth calculations performed in Ref. [2]. The optical depth of the HC plasma was determined for spectral lines in the wavelength range $\lambda = 400 - 460nm$ for neutral and singly ionised species of argon, krypton and xenon [2]. In this case the optical depth was determined for two values of the ion temperature, the first equal to the electron temperature ($T_i = 1eV$) and the second equal to the insert temperature ($T_i = 0.1eV$). For all cases the internal plasma was optically thin. This indicates that the HC plasma is optically thin over the visual and near infrared spectral range.

	τ (10^{-3})			
λ (nm)	τ_0	$\tau_{A+10\%}$	$\tau_{A-10\%}$	$\Delta\tau_{0AVE}$
823.164	5.970	6.965	5.473	0.746
828.012	2.660	25.490	20.835	20.503
881.941	13.059	7.462	6.130	6.264
895.225	4.553	1.845	1.510	2.873

Table 4.3: Calculation of optical depth with variation in transition probability τ of $\pm 10\%$.

The atomic constant f_{pq} and energy levels required in order to calculate τ_0 are typically available in atomic databases (the NIST database provides f_{pq} for Ar, Kr and E_p for Ar, the Atomic and Molecular Database lists E_p for Kr) [114, 115]. In the wavelength range of interest there are no accepted tabulated values for the oscillator strengths of the xenon line transitions. The oscillator strength f_{pq} is related to the transition probability A_{pq} by the Ladenburg formula (Equ. 4.27).

$$f_{pq} = \frac{m_e c}{8\pi^2 e^2} \frac{g_p}{g_q} \lambda^2 A_{pq} \tag{4.27}$$

Where the statistical weights for the lower and upper energy levels g_p and g_q respectively

are related to the total angular momentum quantum number J by Equ. 4.28.

$$\begin{aligned} g_p &= 2J_p + 1 \\ g_q &= 2J_q + 1 \end{aligned} \tag{4.28}$$

The values for quantum number J and the xenon energy levels of interest were obtained from Ref. [116]. Average values of theoretical and experimentally determined transition probabilities were used [117]. The maximum experimental error is 10%. Table 4.3 shows the optical depth calculated with values of A_{pq} that vary 10% from the averaged values; where $\tau_{A+10\%}$ is the optical depth calculated using a transition probability increased by 10% and $\tau_{A-10\%}$ is the optical depth calculated using a transition probability decreased by 10%. It can be seen from the values of $\Delta\tau_{0AVE}$ that some lines are more sensitive than others to variations in the transition probability but all conform to the criteria for an optically thin plasma.

4.3 Local Thermodynamic Equilibrium Model

In the LTE model it is assumed that the distribution of the electron population density is determined by collisional processes only. These collisional processes occur at such a rate that the system responds instantaneously to any changes in the plasma brought about by the collisions. Due to the principle of detailed balance each collisional process is accompanied by its inverse process (see equations 4.1 and 4.2). Hence the population densities at any point are dependent on local values of temperature and density; no knowledge of atomic cross sections is required. The population densities are described by the Boltzmann relation for the distribution of population densities due to excitation (see Equ. 4.29) and the Saha equation for ionisation (see equation 4.30) [118, 111, 107].

$$\frac{n(z,p)}{n(z,q)} = \frac{g(z,p)}{g(z,q)} \exp\left(\frac{\chi_{pq}}{kT_e}\right) \tag{4.29}$$

Where $n(z,p)$ and $n(z,q)$ are the population densities of energy levels p and q respectively, g is the statistical weight and χ_{pq} is the difference between the energy levels. T_e is the electron temperature in K.

$$\frac{n_e n(z+1,g)}{n(z,g)} = 2\frac{g(z+1,g)}{g(z,p)} \left(\frac{2\pi m_e kT_e}{h^2}\right)^{\frac{3}{2}} \exp\left(\frac{-\chi(z,g)}{kT_e}\right) \tag{4.30}$$

The population density of singly ionised atoms in the ground state is $n(z+1,g)$, $g(z+1,g)$ is the statistical weight of the ground state ion, $\chi(z,g)$ is the ionisation potential and h is Planck's constant.

The LTE model is only applicable to high density plasmas. For this model to be valid the electron density (n_e in cm^{-3}) must satisfy the criterion below as stated by McWhirter [107].

$$n_e \geq 1.6 \times 10^{12} T_e^{\frac{1}{2}} \chi_{p,q}^3 \tag{4.31}$$

Where the electron temperature T_e is in units of degrees Kelvin and the energy difference $\chi_{p,q}$ is in eV.

4.4 The Corona Model

The corona model describes low density plasmas. There are two models that may be used for this purpose, the steady state corona model or the time dependent corona model. For the steady state model it is assumed that changes in plasma parameters take place at a slow rate relative to the relaxation time of the atomic processes. The following discussion will be limited to the steady state case as this study is not concerned with rapid changes in plasma parameters or transient conditions.

Unlike the LTE model where each process is balanced by its inverse collisional process, the corona model balances collisional ionisation and excitation with radiative recombination and radiative decay. This model is critically dependent on atomic cross section data. The model begins to break down as the electron density rises to a point where collisions interfere with the radiative decay mechanisms. The criterion for the applicability of the corona model is as follows.

$$\sum_{s>p}^{g} A(p,s) \geq n_e X(T_e,p,q) \tag{4.32}$$

Where $\sum A(p,s)$ is the sum of the transition probabilities for the radiative decay of an exited atom. $X(T_e,p,q)$ is the coefficient of electron impact excitation from state p to q. This inequality may be evaluated to give the following expression in terms of T_e in degrees

Kelvin [107].

$$n_e < 5.6 \times 10^8 (z+1)^6 T_e^{\frac{1}{2}} \exp\left(\frac{1.162 \times 10^3 (z+1)^2}{T_e}\right) \tag{4.33}$$

4.5 The Collisional Radiative Model

The collisional radiative (CR) model provides an intermediate theory to describe plasmas that conform to neither the high density criterion of the LTE model or the low density corona model. The CR model considers all of the interactions described by Equs. 4.1–4.4. The essential difference between the CR and the coronal model is that the CR model considers electron collision processes that result in transitions between upper levels i.e. stepwise collisional processes. The CR model breaks down when the ion population changes significantly during the period when the quasi steady state population is being established. This breakdown of the CR model is represented by the following inequality [107].

$$\sum_{p=2}^{\infty} n(z,p) \geq n(z+1,g) \tag{4.34}$$

The complete treatment for an energy level p, in the CR regime is described by the following rate equation.

$$\begin{aligned} \frac{dn(z,p)}{dt} = -n(z,p)\{n_e S(T_e,z,p) + n_e \sum_{q \neq p} X(T_e,z,p,q) + \\ \sum_{q<p} A(z,p,q)\} n_e \sum_{q \neq p} n(z,q) X(T_e,z,q,p) + \sum_{q>p} A(z,q,p) + \\ n_e n(z+1,g)\{n_e \beta(T_e,z+1,p) + \alpha(T_e,z+1,p)\} \end{aligned} \tag{4.35}$$

Where $S(T_e,z,p)$, $\alpha(T_e,z+1,p)$ and $\beta(T_e,z+1,p)$ are the coefficients of ionisation, radiative recombination and three body recombination respectively and are represented by the empirical formulas of Equ. 4.36–Equ. 4.38 stated in Ref. [107]. $X(T_e,z,p,q)$ is the excitation coefficient and $A(z,p,q)$ are the atomic transition probabilities.

$$S(T_e,z,p) = 2.34 \times 10^{-7} \frac{\zeta_z T_e^{\frac{1}{2}}}{\chi(z,g)} \exp\left(-\frac{\chi(z,g)}{kT_e}\right) \tag{4.36}$$

$$\alpha(T_e,z+1,p) = 2.05 \times 10^{-12} \frac{\chi(z-1,g)}{T_e^{\frac{1}{2}}} \tag{4.37}$$

$$\beta(T_e, z+1, p) = 3.9 \times 10^{-28} \frac{\xi_{z+1}}{\chi(z-1, g)^{\frac{7}{4}} (kT_e)^{\frac{5}{4}}} \tag{4.38}$$

Where ζ_z is the number of electrons in the valence shell and ξ_{z+1} is the number of vacancies in the valence shell. The complete treatment of the CR model requires the rate equation (equation 4.35) to be solved for all states. This results in infinite summations over all levels. The problem may only be addressed by either using computer modelling techniques or making assumptions that reduce the rate equation to an analytical form. The assumptions made in order to apply this model to the internal plasma of a HC and carry out quantitative analysis are discussed in the following section.

4.6 Quantitative Analysis Techniques

An LTE plasma that is homogeneous (which is assumed to be the case for the small volume over which the signal from the internal plasma is recorded) and optically thin has a discrete spectral line intensity $I(p,q)$ given by Equ. 4.39; where the integration is taken over the depth of the plasma [107].

$$I(p,q) = \frac{1}{4\pi} \int n(q) A(p,q) h\nu(p,q) ds \tag{4.39}$$

This relationship may be expressed in terms of the wavelength of the transition λ_{pq} and the plasma depth l.

$$I(p,q) = \frac{ch}{4\pi} \frac{n(q)A(p,q)}{\lambda_{pq}} l \tag{4.40}$$

The line intensity is expressed in units of $Wcm^{-2}sr^{-1}$, however it is technically difficult to perform absolute intensity calibrations to the required accuracy. Under these circumstances the best option is to record the intensity in counts and use intensity ratio methods as has been done in this investigation. The ratio of discrete line intensity may be used to determine plasma parameters as shown in Equ. 4.41.

$$\frac{I(p,q)_1}{I(p,q)_2} = \frac{\lambda_{pq2} A(p,q)_1 n(q)_1}{\lambda_{pq1} A(p,q)_2 n(q)_2} \tag{4.41}$$

Using Equ. 4.29 allows the electron temperature to be determined with the use of spectral line intensities.

$$\frac{I(p,q)_1}{I(p,q)_2} = \frac{\lambda_{pq2} A(p,q)_1}{\lambda_{pq1} A(p,q)_2} \frac{g(q)_1}{g(q)_2} \exp\left(\frac{\chi_{q12}}{kT_e}\right) \tag{4.42}$$

Equ. 4.42 may be used directly to calculate the electron temperature or it may be re-arranged into an expression that has the form of a straight line ($y = mx + c$), see Equ. 4.43.

$$\ln\left(\frac{I(p,q)_1\lambda_{pq1}A(p,q)_2g(q)_2}{I(p,q)_2\lambda_{pq2}A(p,q)_1g(q)_1}\right) = \frac{\chi_{q12}}{kT_e} + \ln C \tag{4.43}$$

The log of the intensities and atomic constants may be plotted against the energy difference. In this way the electron temperature is found from the gradient of the line, $m = \frac{1}{kT_e}$ where $\ln C$ is the y intercept. This technique is known as the Boltzmann plot method and is applicable to same species transitions [119]. In order to obtain the highest possible precision for the electron temperature value the energy levels (χ_{p1}/χ_{p2}) chosen for the calculation must be spread over the widest range possible, the atomic constants must also be known accurately.

For the steady state corona case the spectral line intensity is as follows [107],

$$I(p,q) = \frac{1}{4\pi}\int n_e n(z,g)X(T_e,g,p)\frac{A(p,q)}{\Sigma_{r<q}A(q,r)}ds \tag{4.44}$$

Where the branching ratio B is defined as the ratio of the transition probability from state $p \rightarrow q$ $A(p,q)$ to the sum of all transition probabilities from state p $\Sigma_{r<p}A(p,r)$.

$$B \equiv \frac{A(p,q)}{\Sigma_{r<q}A(q,r)} \tag{4.45}$$

The excitation coefficient $X(T_e,g,p)$ in cm^3sec^{-1} is determined using the following equation,

$$X(T_e,g,p) = \frac{8.5\times10^{-4}\bar{g}f(p,q)}{T_e^{\frac{1}{2}}\chi(p,q)}\exp\left(-\frac{1.16\times10^4\chi(p,q)}{T_e}\right) \tag{4.46}$$

$f(p,q)$ is the absorption oscillator strength and is related to the mean gaunt factor $\bar{g}$. Taking the ratio of spectral lines 1 and 2 which have the required atomic data available results in Equ. 4.47, which may be used to determine the electron temperature T_e of the plasma.

$$\frac{I(p,q)_1}{I(p,q)_2} = \frac{X(T_e,g,p)_1B_1}{X(T_e,g,p)_2B_2} \tag{4.47}$$

As mentioned in Section 4.5 the use of the CR model for determining plasma parameters requires considerable simplifications to be made to the rate equation (Equ. 4.35).

An analytical form of the CR model is produced if intra–atomic processes such as collisional excitation/de–excitation and spontaneous radiative excitation/decay are ignored. This method is known as the "ladder approximation". Processes that occur between intermediate energy levels may be disregarded. Firstly, because the relaxation times of the ground state populations are orders of magnitude higher than that of the excited states. As a consequence the life time of the exited states is short compared with the observation time. Therefore processes occurring between excited states may be neglected. The second reason is due to the fact that the energy difference between levels decreases with increasing principal quantum (shell) number. As the principal quantum number increases the probability of collisional processes occurring increases whilst the probability of radiative processes decreases. There comes a point when the population of the energy level depends on collisional processes only therefore radiative processes may be ignored. As a consequence only the following processes are considered.

- Collisional ionisation from the ground state (Equ. 4.2)
- Three body recombination into the ground state (Equ. 4.2)
- Radiative recombination into the ground state (Equ. 4.4)

This results in the rate equation (Equ. 4.35) reducing to Equ. 4.48 for a steady state plasma.

$$n(z,p)n_eS(T_e,z,p) = n_en(z+1,g)\{n_e\beta(T_e,z+1,p) + \alpha(T_e,z+1,p)\} \tag{4.48}$$

Rearranging the equation above results in an expression for the number density ratio in terms of the coefficients described in Section 4.5.

$$\frac{n(z,p)}{n(z+1,g)} = \frac{n_e\beta(T_e,z+1,p) + \alpha(T_e,z+1,p)}{S(T_e,z,p)} \tag{4.49}$$

The spectral line intensity ratio for atoms of the same element but of different ionisation stages is shown in Equ. 4.50. Where $(z+1,g)$ represents the singly ionised species in the ground state and (z,p) an atom of charge z in state p [118].

$$\frac{I(z,p)}{I(z+1,g)} = \frac{\lambda(z+1,g)A(z,p)}{\lambda(z,p)A(z+1,g)}\frac{n(z,p)}{n(z+1,g)} \tag{4.50}$$

Substituting Equ. 4.49 into Equ. 4.50 results in an expression for the line intensity as a function electron temperature and electron number density, allowing either value to be determined if the other is known independently.

4.6.1 Continuum Methods

Continuum radiation may be analysed to provide further information about the plasma under investigation. This radiation may occur due to black body radiation or as the result of an electron interacting with the electric field of an atom or ion. The latter may be classified into two groups.

- Free–free radiation, also known as bremsstrahlung ("braking radiation") occurs as the electric field of the heavy particle causes the electron to accelerate. The accelerating charge emits radiation and this loss of energy results in gradual deceleration, hence the term bremsstrahlung.
- Free-bound radiation arises as a free electron is captured by a heavy particle, this is also referred to as recombination.

The intensity of continuum emissions that arise due to the interaction of electrons with heavy particles may be used to determine the electron temperature. For the case that the electron trajectory is initially a straight line and utilising Maxwell-Boltzmann statistics the emission coefficient ϵ_ν for a species of charge Z is that shown by Equ. 4.51 [108].

$$\epsilon_\nu = \frac{32\pi}{3}\left(\frac{2\pi}{3}\right)^{\frac{1}{2}}\frac{Z^2e^6}{m_e^2c^3}\left(\frac{m_e}{kT_e}\right)^{\frac{1}{2}} n_e n_i \bar{g} \exp\left(\frac{-h\nu}{kT_e}\right) \tag{4.51}$$

Where T_e is the electron temperature, $\bar{g}$ is the mean gaunt factor and ν is the photon frequency; all other constants have their usual meaning. The intensity of observed bremsstrahlung radiation is directly proportional to the emission coefficient and may be identified as the linear section of the log plot of intensity against wavelength. Taking the intensity ratio at two different wavelengths results in Equ. 4.52 [118].

$$\ln\left(\frac{I_1}{I_2}\right) = \frac{-hc}{kT_e}\left(\frac{1}{\lambda_1} - \frac{1}{\lambda_2}\right) \tag{4.52}$$

This equation has the form of a linear graph with gradient $\frac{-hc}{kT_e}$ from which the electron temperature may be determined. At high temperatures and long wavelengths i.e. in the infra red spectral range and above, free–free transitions become important [111]. However, due to the superposition of thermal and bremsstrahlung emissions electron temperature calculations are confined to the UV and visual wavelength ranges.

4.7 Summary of Methods of Analysis

The intensity of recorded spectral lines will be used to calculate the electron temperature of the internal plasma. The accuracy of the Boltzmann plot methods using the LTE and CR models are dependent on the availability of reliable atomic data and this may restrict the application of this approach to all observed discrete spectral lines. If the electron temperature is known the Saha equation can be used to estimate of the electron number density for a known ion fraction, which can be calculated using Equ. 4.50. The emission of bremsstrahlung radiation provides an independent method of calculating the electron temperature. This method relies less stringently on the plasma conforming to the LTE regime than in the case of the line intensity ratio method [119]. As stated in Chapter 3 spectra will be recorded from a small volume. This may influence the intensity of observed lines and levels of observed noise. The use of the quantitative analysis methods described to obtain accurate plasma parameter values is dependent on the quality of the recorded optical emission spectra.

Chapter 5

Experimental Results I: Characterisation and Optical Emission Spectra

5.1 Introduction to Results Chapter

The procedures outlined in Section 3.5.4 were employed in order to obtain the results presented in this chapter. Part 1 of the experimental results presents the raw data collected and the initial qualitative analysis performed. The chapter is divided into two main subject areas. The first describes HC characterisation and presents voltage current characteristics determined under various operating conditions. The second section contains example optical emission spectra accompanied by spectral line identification and a semi – quantitative analysis of the various forms of observed radiation.

5.2 Hollow Cathode Characterisation

The voltage current characteristics of the instrumented HC were investigated to ensure that the modifications made did not have an adverse effect on HC performance. The initial

HC configuration of keeper/HC separation of $3mm$ and keeper/anode separation of $60mm$ (geometry 1) was chosen as this allowed comparison with similar published work [59, 62, 56]. For the initial HC configuration used the rapid drop in anode voltage associated with the transition from plume to spot mode was not observed. In an attempt to reproduce the phenomena observed in previous investigations the keeper/anode separation was decreased by half. This caused a decrease in anode voltage at given operating parameters but as before a rapid decrease in anode voltage was not observed. There may be a number of reasons why the characteristics observed in other investigations were not reproduced in the two geometries used; mass flow rates and anode currents outside of the range used in the current investigation may be required, a further decrease in keeper/anode separation may be needed and the HC orifice geometry may be such that plume/spot transitions do not easily occur. Investigations performed on HCs with an inner dispenser diameter of $3.2mm$ and varying anode geometries show that high aspect ratios facilitate plume/spot transitions [61]. The aspect ratio is defined as the orifice length divided by its diameter, ratios of 1 to 6 were investigated. The mass flow rate required for spot to plume transition to occur was found to decrease with increasing aspect ratio. The ratio for the T6 HC used in this study is small. An orifice diameter of $0.5mm$ and length $1mm$ results in a ratio of 2, which implies that high mass flow rates are required to cause mode change to occur.

The voltage current characteristics were obtained by manually stepping up the anode current in $1A$ increments from $I_A = 2.0 - 15.0A$ at constant mass flow rate. In order to allow thermal equilibrium to be established and hence minimise hysteresis effects the anode voltage V_A and keeper voltage V_K were recorded after a two minute period (see section 6.6.2) in constant operating conditions. An average voltage was obtained from the readings recorded in two different experiments. The error bars shown in Figs. 5.1 – 5.15 were determined using the maximum variation in anode and keeper voltages observed for constant operating parameters. The propagation of determinant errors method was used to calculate the discharge voltage and power errors, using the instrument errors to represent the error associated with the discharge current. The discharge power is determined using the relation shown in Equ. 5.1 relating the keeper and anode current I_A and I_K respectively

to the keeper and anode voltages V_K and V_A.

$$P_D = I_K V_K + I_A V_A \tag{5.1}$$

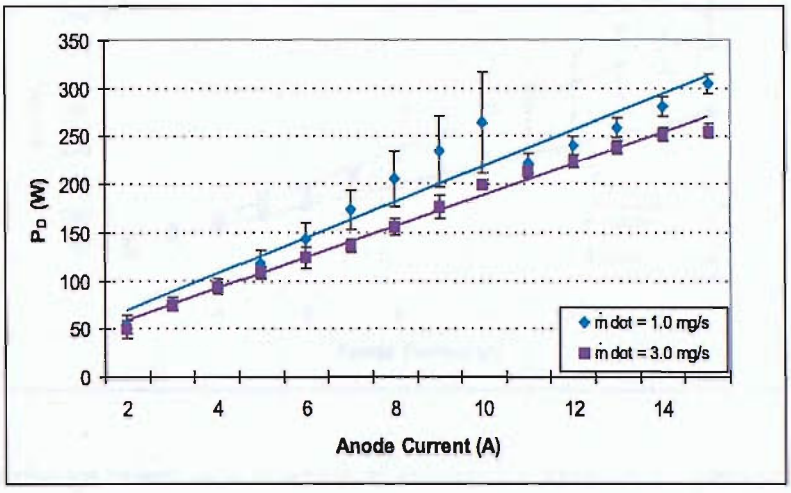

Figure 5.1: Discharge power as a function of current for argon propellant in geometry 1

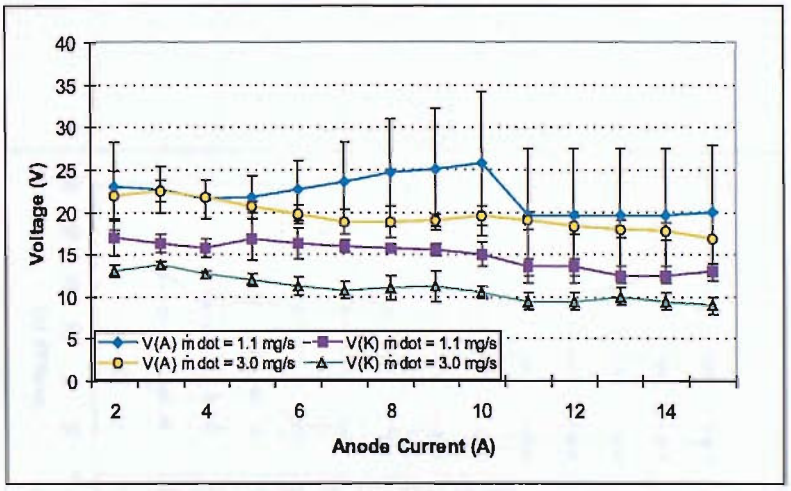

Figure 5.2: Voltage current characteristics for argon propellant in geometry 1

Figs. 5.1 – 5.6 show the voltage current characteristics for the instrumented HC operating on argon, krypton and xenon respectively with a keeper/anode separation of $60mm$ (geometry 1). There is a linear relationship between the discharge power and current. The discharge power converges to $\sim 50W$ at low anode current ($I_A = 2.0A$) for all inert

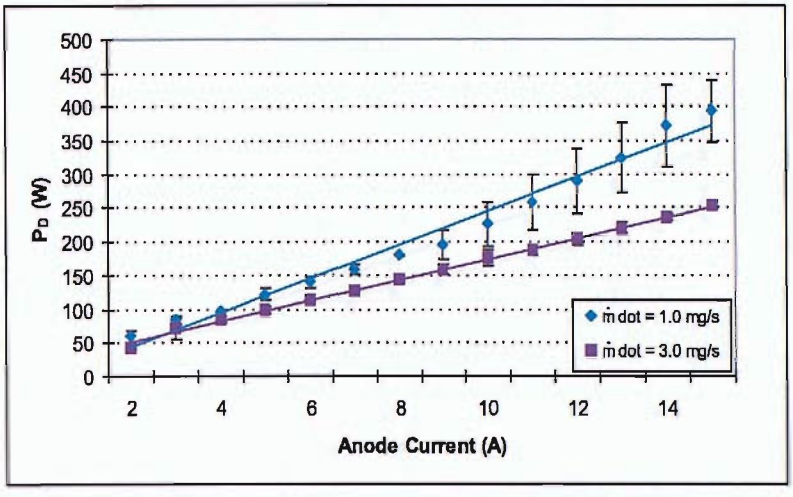

Figure 5.3: Discharge power as a function of current for krypton propellant in geometry 1

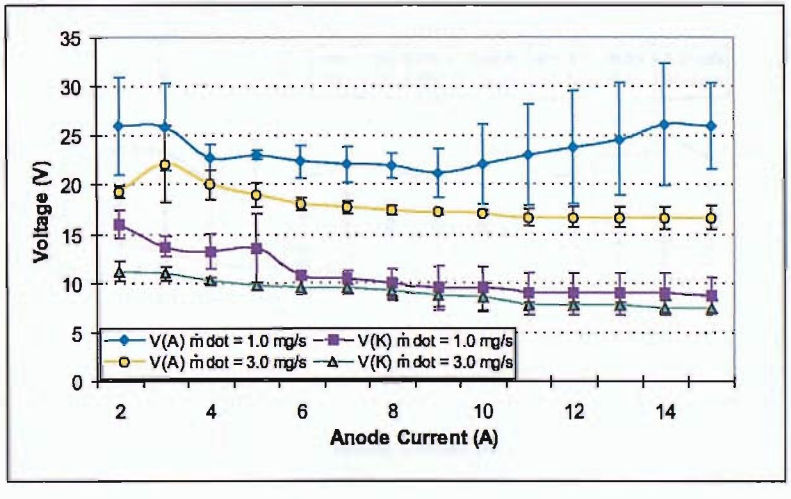

Figure 5.4: Voltage current characteristics for krypton propellant in geometry 1

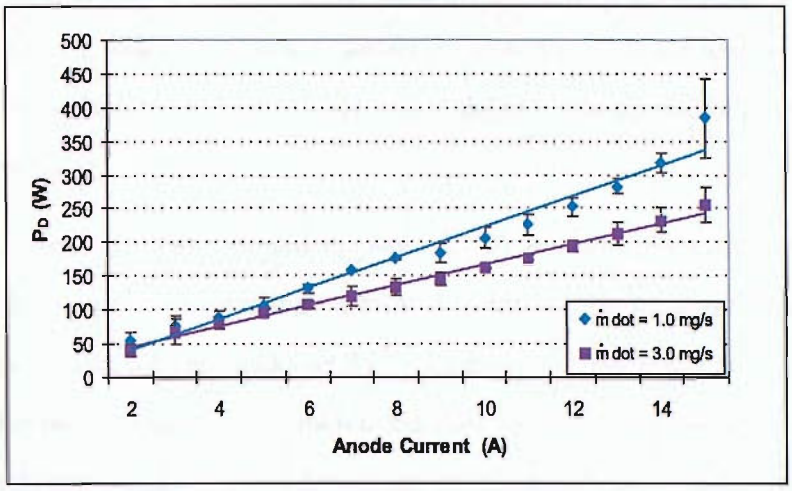

Figure 5.5: Discharge power as a function of current for xenon propellant in geometry 1

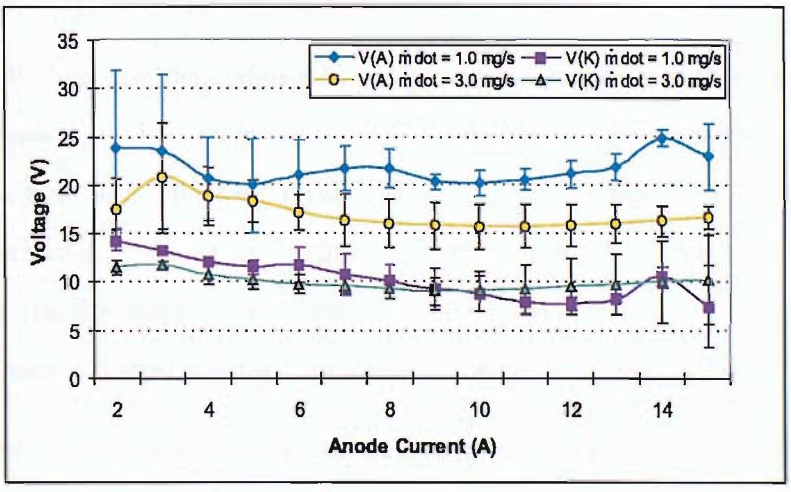

Figure 5.6: Voltage current characteristics for xenon propellant in geometry 1

gas propellants and for a given set of operating parameters increases with decreasing the atomic mass of the inert gas propellant used. The discharge voltage may decrease linearly with increasing discharge current, but the data points show a greater deviation from the line of best fit than in the case of power versus current. Fig. 5.7, 5.8 and 5.9 show that on increasing the mass flow rate from $1.0mgs^{-1}$ to $3.0mgs^{-1}$ the spread of data points about the line fit is reduced.

The keeper and anode voltages do not display a linear relationship with discharge current but typically decrease with increasing current. For the case of an argon discharge, shown in Fig. 5.2 the anode voltage peaks at $I_A = 10.0A$ and then levels at $\sim 20V$ for $I_A = 11.0 - 15.0A$ for $\dot{m} = 1.1mgs^{-1}$. On increasing the mass flow rate to $\dot{m} = 3.0mgs^{-1}$ there is no clear peak in voltage, the anode voltage decreases almost steadily with increasing current. This trend is repeated for krypton and xenon discharges shown in Figs. 5.4 and 5.6, where the variability of the anode voltage with current is reduced when mass flow rate is increased i.e. peaks and troughs are not observed for $\dot{m} = 3.0mgs^{-1}$. The sensitivity of the keeper voltage on mass flow rate decreases with increasing atomic mass. Comparing Fig. 5.2 for argon and Fig. 5.6 for xenon, the keeper voltages for $\dot{m} = 1.1$ and $3.0mgs^{-1}$ differ by at least $2V$ for the HC operating on argon propellant whereas for the xenon case the voltages for both mass flow rates are similar.

Figs. 5.7 – 5.9 show the dependence of discharge power on mass flow rate. It can be seen that increasing anode current results in an increase in the sensitivity of the discharge power to mass flow rate with larger variations in the difference between maximum and minimum power for a given set of conditions. For example, the argon discharge shown in Fig. 5.7 shows the discharge power decreasing by $\sim 50W$ for $I_A = 15.0A$ and by $\sim 10W$ for $I_A = 2.0A$ over a $2Aequiv$ range from $2.7 - 4.7Aequiv$.

The voltage current characteristics for the HC in geometry 2 (keeper/anode separation of $30mm$) are shown in Figs. 5.10 – 5.15. The discharge powers determined for geometry 1 and geometry 2 are similar at low mass flow rates for argon and krypton plasmas. At high flow rate ($\dot{m} = 3.0mgs^{-1}$) the discharge power in geometry 2 is decreased relative to that observed in geometry 1 for the same operating conditions. For the case of the HC

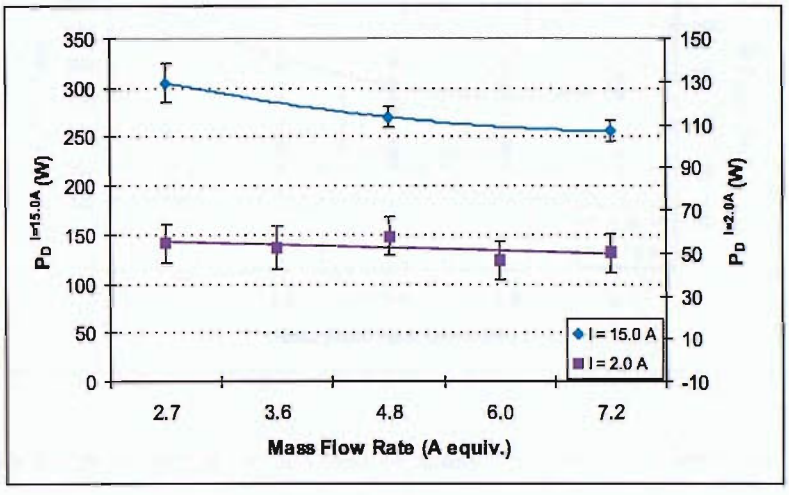

Figure 5.7: Discharge power as a function of mass flow rate at minimum and maximum currents for argon propellant in geometry 1

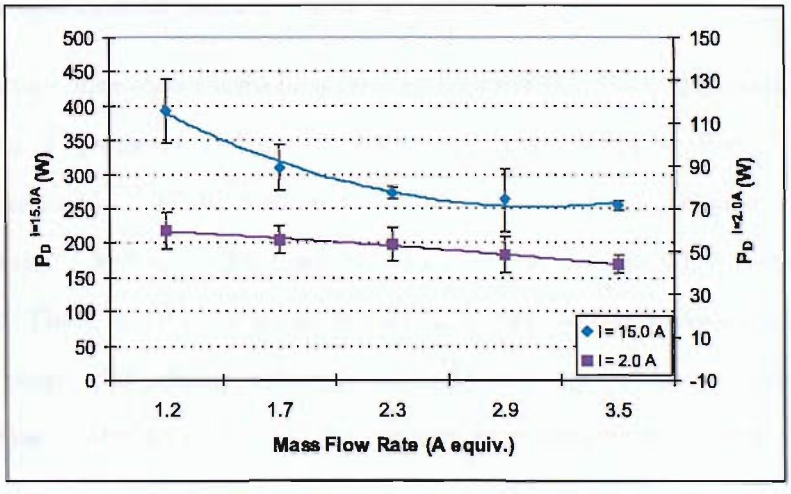

Figure 5.8: Discharge power as a function of mass flow rate at minimum and maximum currents for krypton propellant in geometry 1

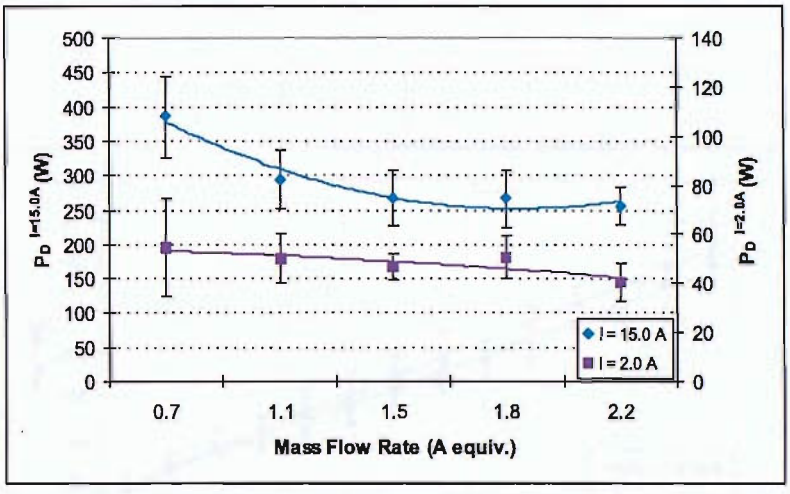

Figure 5.9: Discharge power as a function of mass flow rate at minimum and maximum currents for xenon propellant in geometry 1

operating on argon propellant a $\sim 10W$ decrease is observed and for krypton the discharge power decreases by approximately $20W$ at maximum current. For a xenon plasma (see Fig. 5.5 and Fig. 5.14) the discharge power in geometry 1 is higher than that determined for geometry 2 for all mass flow rates; the discharge power is decreased in geometry 2 by $\sim 20W$ and $\sim 15W$ for $\dot{m} = 1.0mgs^{-1}$ and $\dot{m} = 3.0mgs^{-1}$ respectively. The relationship between power and current remains linear for both geometries.

The keeper voltage also shows a marked decrease compared to voltages recorded under the same conditions in geometry 1. For example, an argon discharge with $\dot{m} = 1.1mgs^{-1}$ and $I_D = 2.5A$ achieves $V_K = 17.0V$ compared to $13.5V$ in geometry 2, while a xenon discharge with $\dot{m} = 1.0mgs^{-1}$ and $I_D = 2.5A$ achieves $V_K = 14.3V$ in geometry 1 and $V_K = 11.0V$ in geometry 2. There is little variation in the discharge voltage or anode voltage over the experimental range of discharge currents used. Decreasing the keeper/anode separation causes a decrease in the sensitivity of the voltages to variations in current.

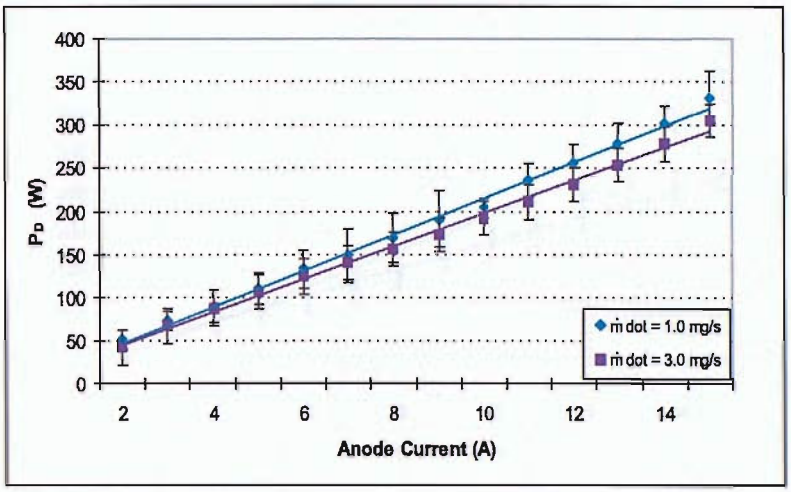

Figure 5.10: Discharge power as a function of current for argon propellant in geometry 2

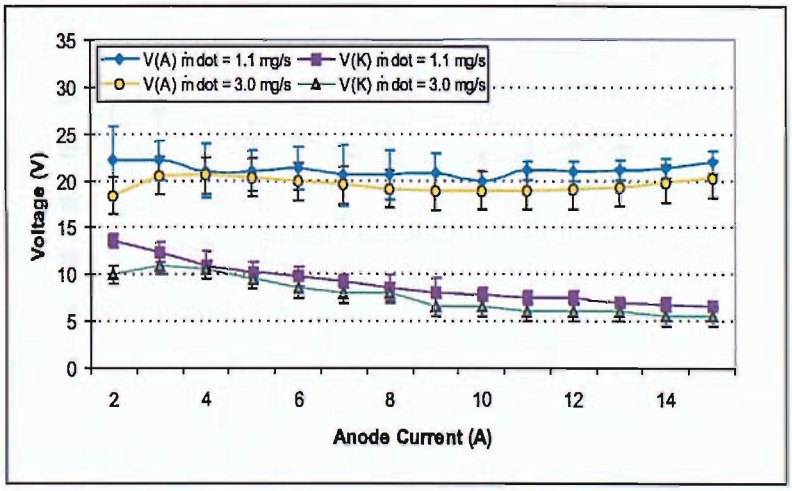

Figure 5.11: Voltage current characteristics for argon propellant in geometry 2

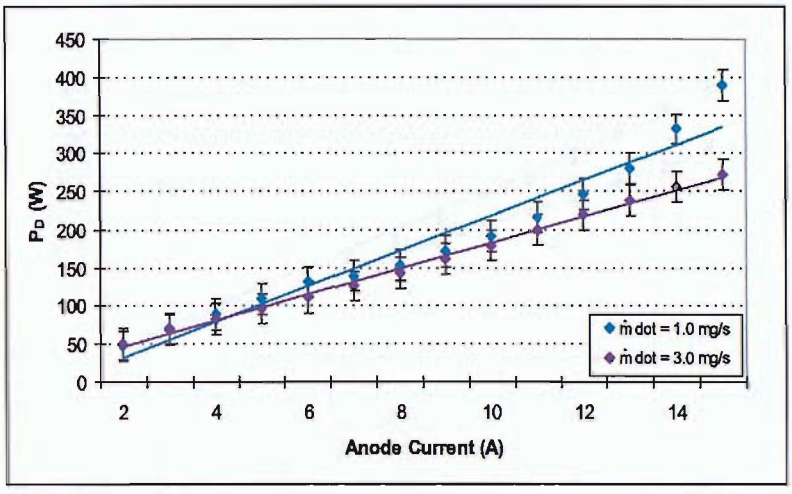

Figure 5.12: Discharge power as a function of current; krypton propellant in geometry 2

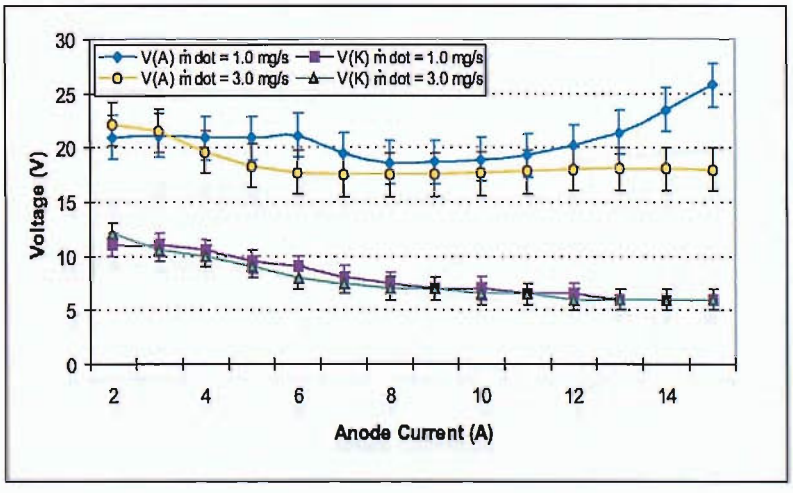

Figure 5.13: Voltage current characteristics for krypton propellant in geometry 2

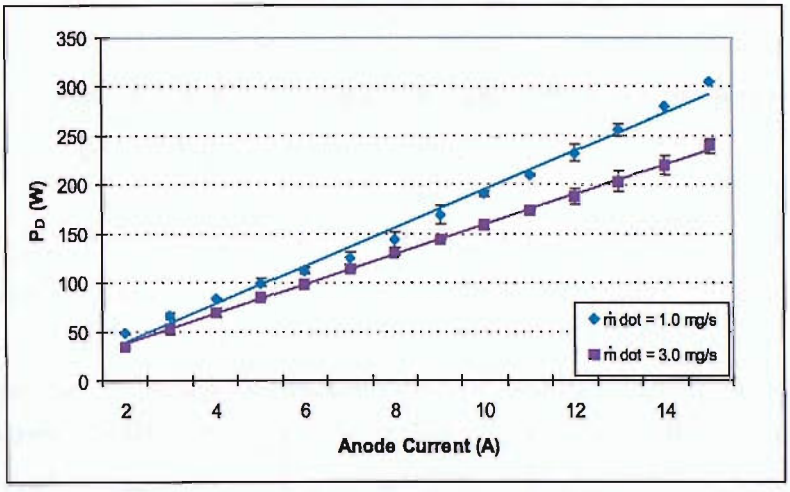

Figure 5.14: Discharge power as a function of current for xenon propellant in geometry 2

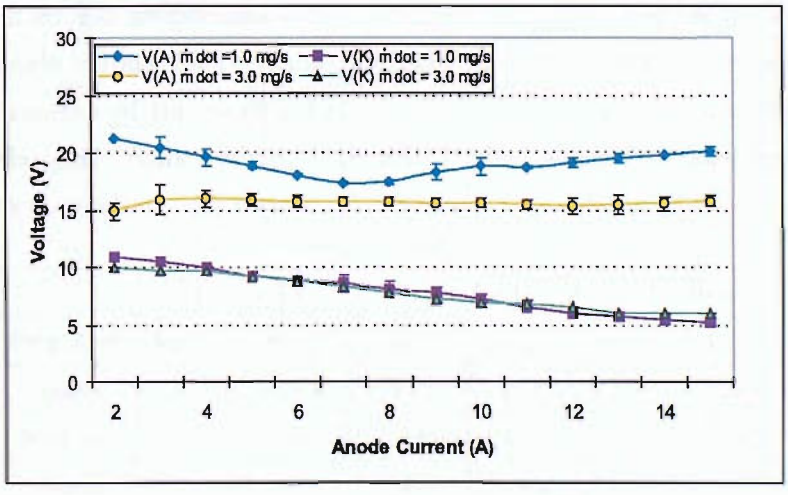

Figure 5.15: Voltage current characteristics for xenon propellant in geometry 2

HCs consisting of tantalum tubes with no dispenser studied by Delcroix and Trindade were said to be operating in the "N–Regime" or normal regime (spot mode in electric propulsion applications) if the following generic trends were adhered to [40],

- For a given mass flow rate, increasing the anode current causes a decrease in anode voltage and keeper voltage.
- For a given anode current, increasing the mass flow rate results in a decrease in anode and keeper voltages.

The voltage current characteristics for the instrumented HC are in agreement with these trends. Comparing the HC performance with that of standard T6 HC models demonstrates that the observed voltages are within accepted bounds for normal operation [59]. The characterisation performed on a T6 HC with orifice diameter of $1.3mm$ operating on xenon propellant produced anode voltages that ranged from $20V - 13V$ for anode currents of $5A - 30A$ with $\dot{m} = 2.26mgs^{-1}$ [62]. Discharge voltages presented in Ref. [56] decreased linearly with currents of $5 - 10A$ from $15 - 32V$ for $\dot{m} = 5ccmin^{-1}$ $(0.5mgs^{-1})$, with keeper voltages of $12 - 17V$. There is little published work on the characterisation of the T6 HC operating on alternative propellants such as argon or krypton. However, the HC characteristics obtained in this investigation for argon and krypton compare well with the values achieved by xenon propellant. As shown by Table 5.1 the voltages obtained are similar for all inert gas propellants with a maximum difference in keeper voltage of $1.7V$ and $4.4V$ in anode voltage for the same discharge current. Therefore, it is fair to assume that the performance of the modified HC conforms to the normal criteria of operation (dictated by the performance of the standard T6 HC where V_D does not exceed $50V$) regardless of the propellant gas used.

	$I_A = 2.0A$		$I_A = 5.0A$		$I_A = 10.0A$	
Propellant	V_K (V)	V_A (V)	V_K (V)	V_A (V)	V_K (V)	V_A (V)
Argon	13.0	21.9	12.0	20.6	10.5	19.6
Krypton	11.3	19.3	9.8	19.0	8.5	17.2
Xenon	11.5	17.5	10.3	18.3	9.0	15.7

Table 5.1: Comparison of keeper and anode voltages for $\dot{m} = 3.0mgs^{-1}$ in geometry 1.

5.3 Optical Emission Spectra

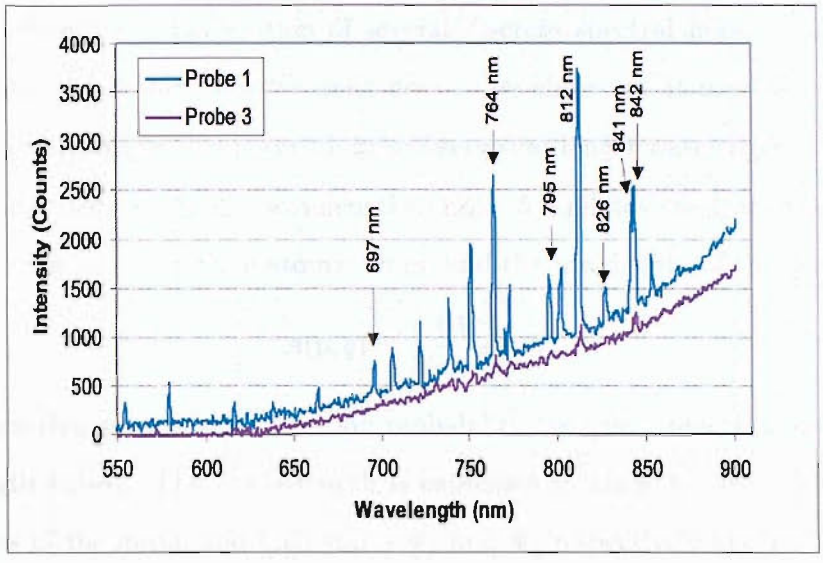

Figure 5.16: Comparison of argon spectra from two extreme axial positions for a cathode/anode separation of 60mm, $\dot{m} = 1.1mgs^{-1}$ and $I_A = 5.0A$

Fig. 5.16 shows the spectra recorded from optical probes in the two extreme positions nearest to the HC tip (probe 1) and in the furthest upstream probe position (probe 3), (see Chapter 3). The spectra were recorded under the conditions of $\dot{m} = 1.1mgs^{-1}$ and $I_A = 5.0A$. It can be seen that the spectrum obtained from the probe in the furthest downstream position (probe 1) display discrete spectral lines. Weak discrete spectral lines were observed in the probe 3 position compared to those observed in the Probe 1 and 2 positions; there is also a decrease in the intensity of the continuum thermal emissions. This is the case for all inert gas propellants used. The plasma was found to emit strongly in the near infrared region of the spectrum i.e. $\lambda > 600nm$ for both continuum and discrete radiation. Few discrete spectral lines were observed in the ultra violet and visual regions of the spectrum. This is in stark contrast to the spectra recorded in previous studies from an external vantage point [2, 3]. In the current investigation the spectral lines observed in this wavelength range not only have decreased intensity relative to the lines observed at longer wavelengths but also appear to have a larger line width or FWHM (full width half maximum) (see Figs. 5.18, 5.20 and 5.22). There are two possible reasons for the

lack of well defined spectral lines at shorter wavelengths; 1) The spectrograph resolution of $1.7nm$ may be unable to provide adequate separation of adjacent lines, therefore the spectra may show the superposition of several discrete spectral lines, 2) The signal to noise ratio may not be sufficient for weak lines to be observed. It may be expected from theoretical considerations that spectral lines observed at longer wavelengths display higher intensities than those at shorter wavelengths. Equ. 5.2 relates the transition probability $A(p,q)$ to the line strength S (in atomic units) and the wavelength of the transition [120].

$$A(p,q) = \frac{64\pi^4}{3hg(q)\lambda^3}S \tag{5.2}$$

It can be seen that for a given transition probability the line strength is proportional to the wavelength cubed. The line strength is expressed in Dirac notation in terms of the wavefunctions of the initial and final states Ψ_p and Ψ_q respectively and the length dipole operator r^1 as shown in Equ. 5.3.

$$S = |\langle \Psi_p | r^1 | \Psi_q \rangle|^2 \tag{5.3}$$

The transition probability typically increases as wavelength increases but is dependent on the line in question. For the case of neutral argon spectra $A(p,q) \sim 10^4 - 10^5 s^{-1}$ for $\lambda < 500nm$, $A(p,q) \sim 10^6 - 10^7 s^{-1}$ for $\lambda > 500nm$ as shown in Table 5.2; for singly ionised species $A(p,q)$ is typically of the order of $10^7 s^{-1}$. This implies that neutral lines at longer wavelengths will have a larger line strength / intensity than those at shorter wavelengths. Transition probabilities for ionised species tend to be higher than those of neutral species at shorter wavelengths and do not vary with increasing wavelength to the degree observed for neutral line species. Therefore ionised species may be expected to produce higher intensity lines than neutral species in the UV and visual spectral range. However, this is in contradiction with listed relative intensities, which show that intensities for neutral lines are considerably higher (typically approaching values of tens of thousands) than those of ionised species which do not exceed 3000 [114]. On considering the transition probabilities, relative intensities (a qualitative description of what the emission spectrum of a low density plasma may be expected to look like) and the relationship expressed by Equ. 5.2 we may expect that lines produced in the near infra region of the spectrum will be of a higher intensity than those observed at shorter wavelengths.

Atomic Species	$\lambda(nm)$	Relative Intensity	$A(p,q)$ (s^{-1})
Ar I	452.2323	20	8.94×10^4
	696.5431	10,000	6.39×10^6
	738.3980	10,000	8.47×10^6
	772.407	10,000	1.17×10^7
	826.4522	10,000	1.53×10^7
Ar II	453.0552	20	2.1×10^6
	738.0426	20	5.6×10^6
Kr I	450.2353	600	9.2×10^5
	690.4078	100	1.3×10^6
	722.4104	100	1.4×10^6
	829.8107	5,000	3.2×10^7
Kr II	458.2978	300	7.6×10^7
	740.702	400	7.0×10^6
Xe I	452.46805	-	2.1×10^5
	796.7342	-	3.0×10^5
	840.91894	-	1.0×10^6
Xe II	460.303	600	2.8×10^7
	699.088	2000	2.7×10^7

Table 5.2: Comparison of spectral line transition probabilities and relative intensities.

The spectral lines observed in the near infra red region of the spectrum are in most cases the result of same n (principal quantum number) transitions that correspond to lower energy interactions. Spectral lines in the ultra violet and visual wavelength range occur as a consequence of higher energy excitations that correspond to jumps in the quantum number n. The free electrons within the HC internal plasma may not possess sufficient energy to produce these transitions. For example the energy required to produce the transitions responsible for the spectra lines $\lambda_{Ar} = 763.511nm$, $\lambda_{Kr} = 760.154nm$ and $\lambda_{Xe} = 895.225nm$ are $\chi_{pq} = 1.623$, $\chi_{pq} = 1.631$ and $\chi_{pq} = 1.385eV$ respectively compared to the $\chi_{pq} = 3.487$, 3.460 and $3.486eV$ required to produce the transitions $\lambda_{Ar} = 355.431nm$, $\lambda_{Kr} = 358.360nm$ and $\lambda_{Xe} = 355.592nm$ respectively, which arise due to changes in quantum number n. On inspection of the spectral lines observed in the recorded optical emission spectra the critical factor dictating which intense lines are produced is the energy needed to produce such a transition. High energy interactions requiring

transitions through orbitals with energy differences exceeding $\sim 2eV$ are not observed.

5.3.1 Spectral Line Identification

Optical emission spectra are recorded as data files of two column arrays that correspond to the radiation intensity and its associated wavelength (λ_{obs}), with spectral lines identified as peaks in intensity occurring above the threshold noise level. Spectral lines are assigned tabulated / accepted wavelengths that correspond to transitions between specified atomic states. The uncertainty associated with spectral line identification is due to the error associated with the spectrograph wavelength calibration and spectral resolution. The spectral resolution may be defined as the wavelength difference between two adjacent peaks of the same intensity close to each other in the spectrum that can be separated. In this case the spectral resolution is 1.7 nm. If the observed wavelength of a spectral line is in the region of a tabulated value that has no other lines within $\pm 1.7nm$ of it, the observed discrete line may be positively identified. These lines are assigned "P" in the line identification tables. In the case where lines are within 1.7 nm of each other the relative intensities of the tabulated lines are considered as well as the proximity of the line to the observed wavelength. After considering these factors a tentative identification may be made, assigned "T" in the line identification tables.

Example optical emission spectra are shown in Figs. 5.17 – 5.22. The observed continuum radiation has been subtracted from the spectra in order to display discrete radiation alone. The spectra are dominated by transitions of neutral species. The spectra show several discrete lines in the near infrared region of the spectrum with fewer in the visual range. The argon spectra (see Fig 5.17) are dominated by transitions occurring for wavelengths greater than $700nm$; there are few listed ionised species in this wavelength range. Out of a total of 261 neutral and singly ionised species listed in the wavelength range $\lambda = 250 - 900nm$ only 13 lines are observed for wavelengths greater than 600nm for ionised species [114]. Fig. 5.18 focusses on the visual region. There is a noise level of approximately 25 counts with peaks approaching 100 counts. Separating adjacent spectral lines is problematic due to the fact that lines may be superimposed on one another. This not only effects the line

intensity but the position of peak intensity may also be shifted, therefore line identification is prohibited.

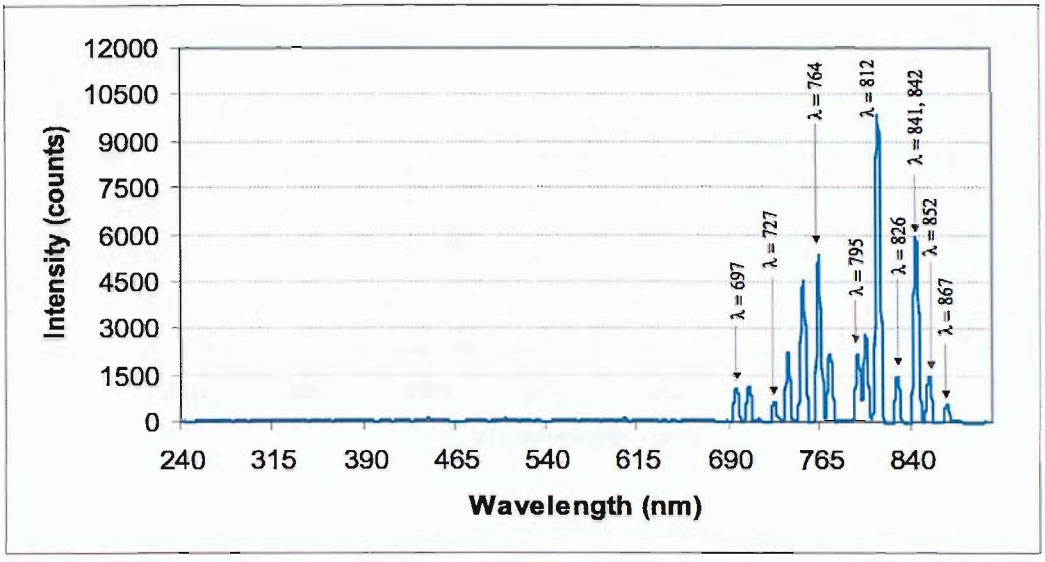

Figure 5.17: Argon optical emission spectrum obtained in the probe 2 position in geometry 1 for $\dot{m} = 1.1mgs^{-1}$ and $I_A = 2.0A$, corrected for continuum radiation

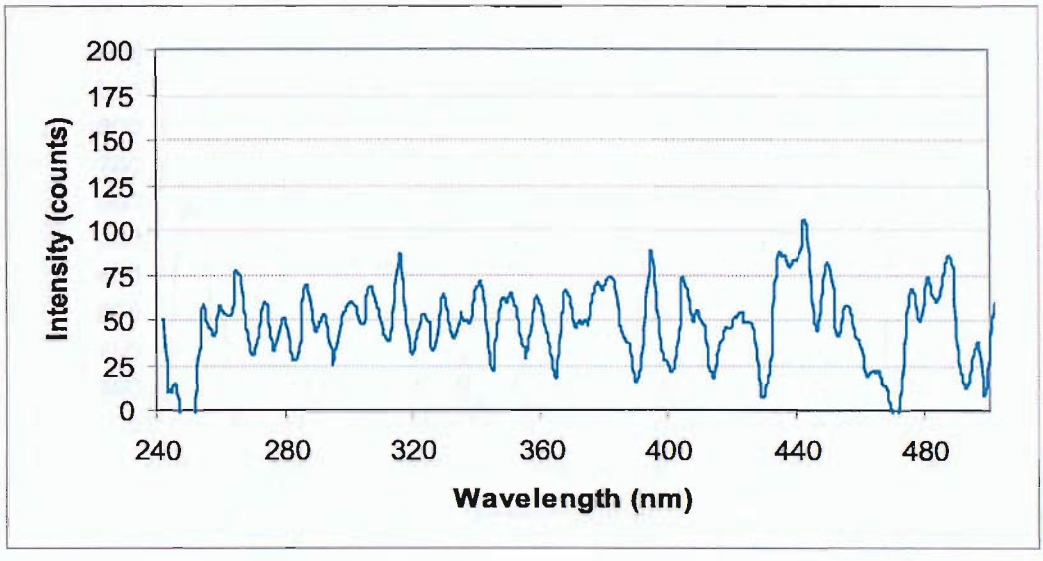

Figure 5.18: Argon optical emission spectrum for the UV - visual region obtained in the probe 2 position in geometry 1 for $\dot{m} = 1.1mgs^{-1}$ and $I_A = 2.0A$, corrected for continuum radiation

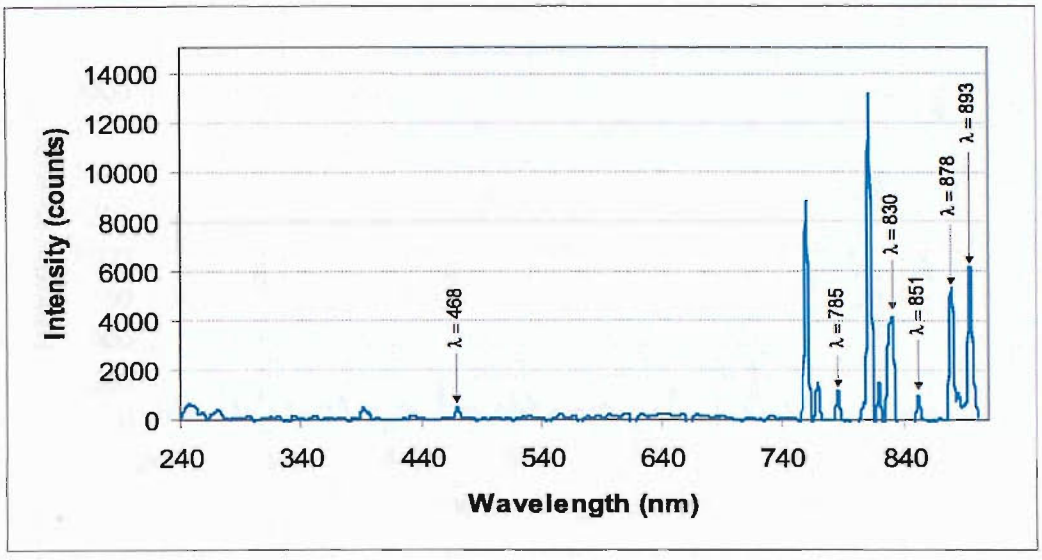

Figure 5.19: Krypton spectrum from the furthest downstream position (Probe 1) in geometry 1 for $\dot{m} = 1.0mgs^{-1}$ and $I_A = 2.0A$, corrected for continuum radiation.

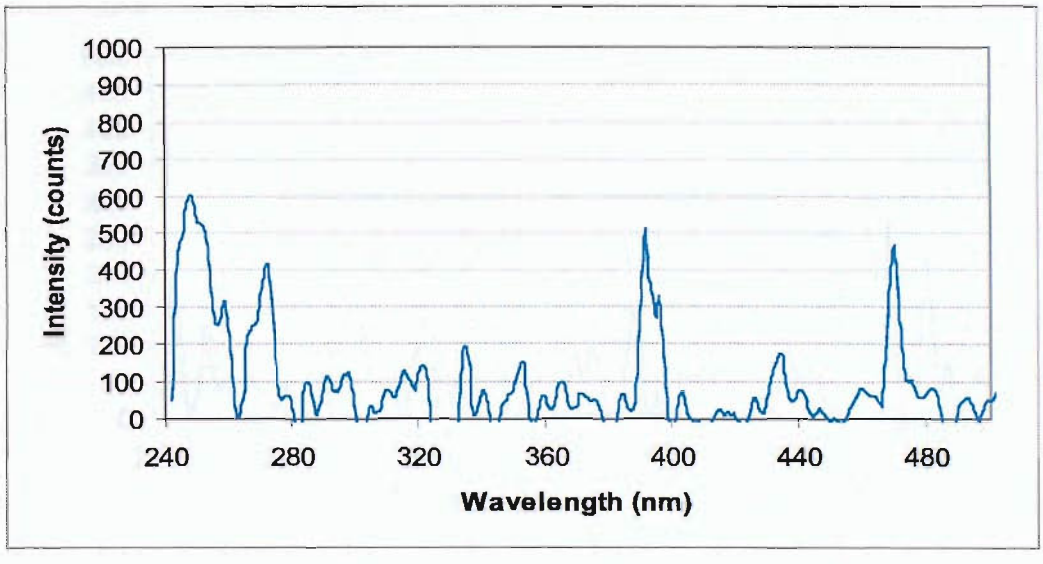

Figure 5.20: Krypton spectrum from the furthest downstream position (Probe 1)in geometry 1 for the UV - visual region with $\dot{m} = 1.0mgs^{-1}$ and $I_A = 2.0A$, corrected for continuum radiation.

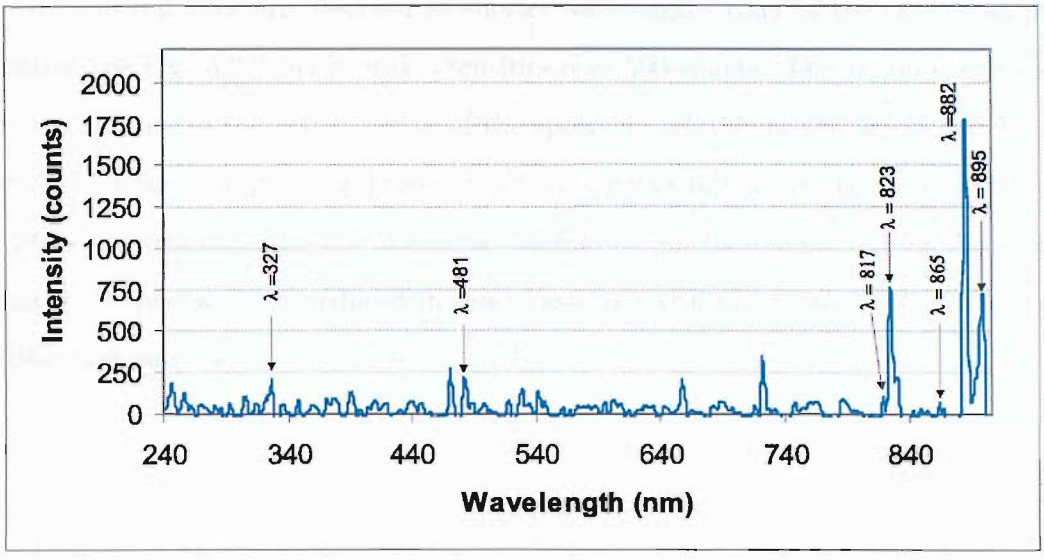

Figure 5.21: Xenon spectrum from the furthest downstream position (Probe 1) in geometry 1 for $\dot{m} = 1.0mgs^{-1}$ and $I_A = 2.0A$, corrected for continuum radiation.

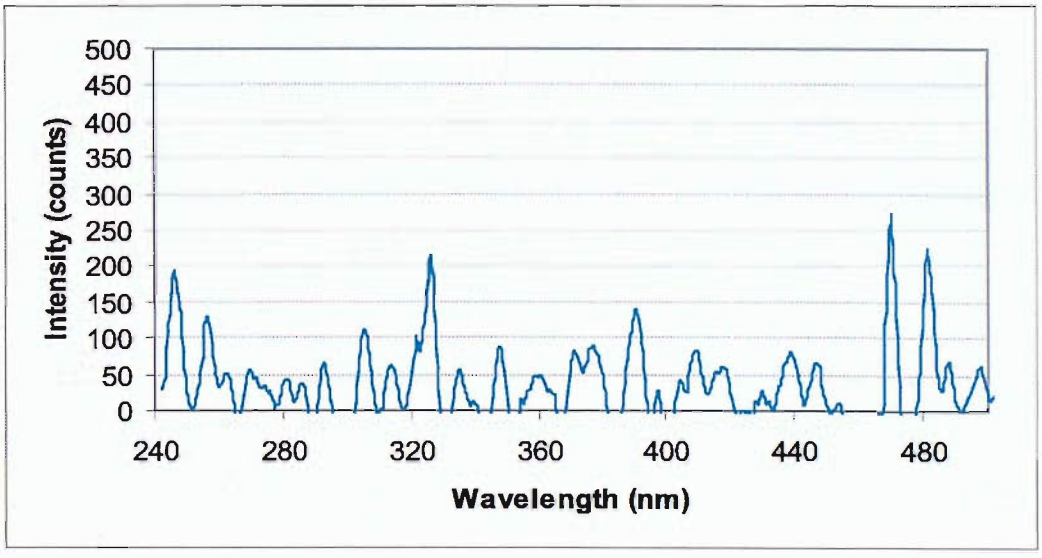

Figure 5.22: Xenon spectrum from the furthest downstream position (Probe 1) in geometry 1 for the UV - visual region with $\dot{m} = 1.0mgs^{-1}$ and $I_A = 2.0A$, corrected for continuum radiation.

The krypton spectra display intense lines for wavelengths longer than $740nm$ and higher intensity spectral lines are observed at shorter wavelengths than in the case of an argon discharge (see Fig. 5.20), with peak intensities over 500 counts. The xenon spectra show increased activity in the visual region of the spectrum relative to the argon and krypton spectra, as shown in Fig. 5.22. There are a high number of lines in the wavelength range $\lambda = 240 - 500nm$, although the intensities are lower than those observed for the krypton discharge the line width is reduced in most cases but still not to the level necessary for identification purposes.

Atomic Species	$\lambda_{obs}(nm)$	$\lambda(nm)$	Relative Intensity	Confidence
Ar I	896.65	896.2147	-	P
Ar I	869.25	866.7943	4500	P
Ar I	853.94	852.1441	1500	P
Ar I	844.37	842.4647	20000	P
Ar I	842.46	840.8209	15000	P
Ar I	827.78	826.4521	10000	P
Ar I	813.09	811.5311	35000	P
Ar II	-	801.7528	-	-
Ar I	802.86	801.4785	25000	T
Ar I	-	800.6156	20000	-
Ar I	795.83	794.8176	20000	P
Ar I	-	772.4207	10000	-
Ar I	773.45	772.3760	15000	T
Ar I	764.49	763.5105	25000	P
Ar I	-	751.4651	15000	-
Ar I	751.69	750.3868	20000	T
Ar I	-	739.2980	20	-
Ar I	739.52	738.3980	10000	T
Ar II	-	738.0423	20	-
Ar I	727.34	727.2935	2000	T
Ar I	-	727.0664	7	-
Ar I	707.47	706.7217	10000	T
Ar I	-	706.8735	100	-
Ar I	695.92	696.5430	10000	T
Ar I	-	696.0205	7	-

Table 5.3: Argon spectral line identification using NIST atomic spectra data base

Atomic Species	$\lambda_{obs}(nm)$	$\lambda(nm)$	Relative Intensity	Confidence
Kr I	894.74	892.8692	2000	P
Kr I	879.45	877.6748	6000	P
Kr I	852.67	850.8870	3000	P
Kr I	830.97	829.8107	5000	P
Kr I	827.78	827.2353	100	-
Kr I	-	826.3240	3000	T
Kr II	820.11	820.270	200	-
Kr I	-	819.0054	3000	T
Kr I	812.45	811.2899	6000	T
Kr I	-	810.4364	4000	-
Kr I	807.34	805.9503	1500	P
Kr I	786.24	785.4821	800	P
Kr I	769.61	769.4538	1200	T
Kr I	-	768.5244	1000	-
Kr I	760.65	760.1544	2000	P
Kr I	759.37	758.7411	1000	P
Kr I	524.73	520.832	500	T
Kr II	470.45	469.4360	200	T
Kr II	-	469.1301	100	-
Kr II	469.16	468.0406	500	P
Kr IV	395.97	393.429	5	P
Kr II	392.07	392.0081	200	T
Kr II	-	390.6177	150	-
Kr II	272.48	271.240	80w	P

Table 5.4: Identified krypton spectral lines from the probe 1 position

Atomic Species	$\lambda_{obs}(nm)$	$\lambda(nm)$	Relative Intensity	Confidence
Xe I	896.65	895.225	1000	P
Xe I	883.27	881.941	5000	P
Xe I	863.51	864.854	250	P
Xe I	829.05	828.0116	7000	P
Xe I	823.94	823.1635	10000	P
Xe I	818.20	817.102	100	P
Xe I	806.70	806.134	150	T
Xe I	-	805.726	200	
Xe II	716.45	716.483	500	P
Xe I	657.40	659.556	100	
Xe II	-	659.501	1000	T
Xe II	546.03	546.039	400	T
Xe I	-	545.045	200	
Xe II	527.96	526.195	500	T
Xe II	-	526.044	500	
Xe I	481.44	480.702	500	P
Xe III	470.45	472.360	30	
Xe III	-	468.357	60	T
Xe III	326.41	326.898	80	P

Table 5.5: Xenon spectral line identification

5.3.2 Qualitative Analysis of Continuum Radiation

The observed intensity of the radiation emitted by the plasma discharge is dependent on the HC operating parameters. The continuum radiation observed in the near infrared region of the spectrum increases with increasing anode current and hence increasing discharge power for all inert gas propellants. Figs. 5.23 – 5.25 show the dependence of the intensity of continuum radiation that arises due to thermal emissions from the insert on discharge power. The intensity was taken at $\lambda = 800nm$ as this lies near the central wavelength of the near infra red wavelength range. The continuum intensity is not distorted by the presence of discrete lines at this wavelength. The intensity values are normalised with the intensity

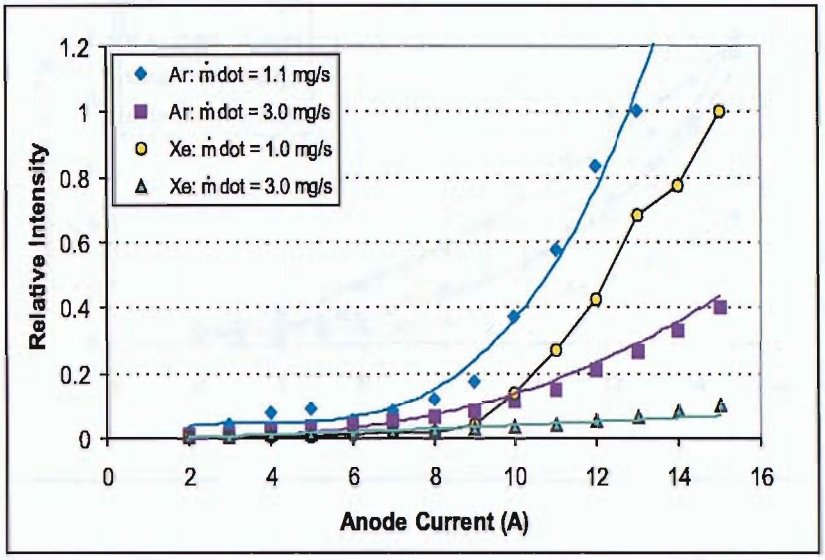

Figure 5.23: Intensity of continuum radiation recorded at $\lambda = 800nm$ in the probe 1 position in geometry 1

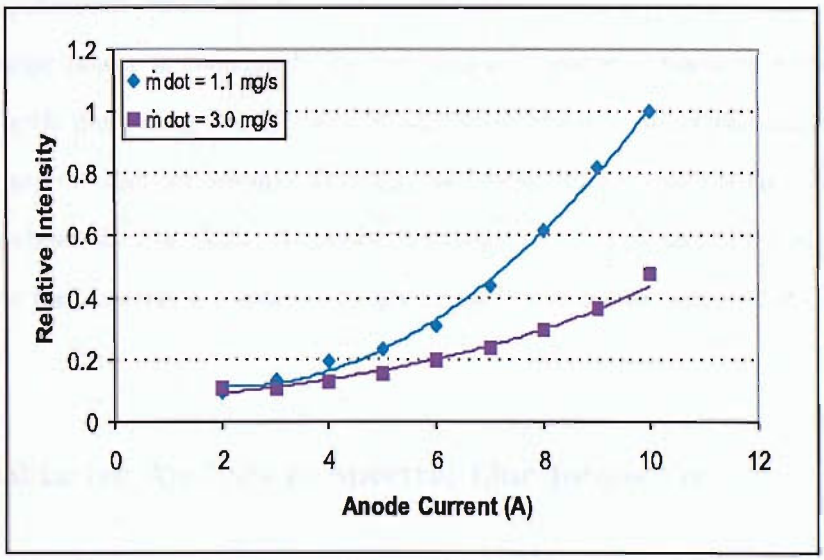

Figure 5.24: Intensity of continuum radiation recorded at $\lambda = 800nm$ for argon propellant in the probe 2 position in geometry 1

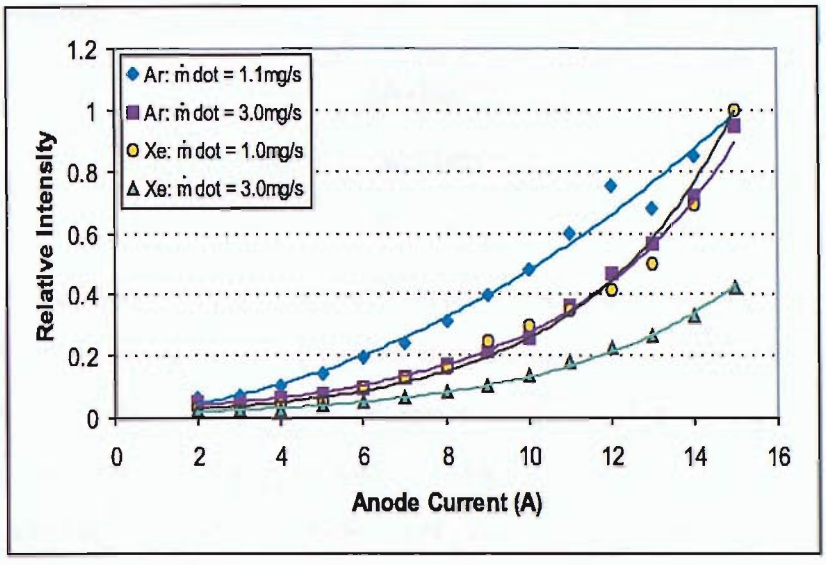

Figure 5.25: Intensity of continuum radiation recorded at $\lambda = 800nm$ in the probe 3 position in geometry 1

recorded at maximum discharge current with $\dot{m} = 1.1mgs^{-1}$ for argon or $\dot{m} = 1.0mgs^{-1}$ for xenon. There is an exponential increase in continuum radiation intensity with increasing discharge power, a correlation coefficient of $R^2 > 0.93$ is obtained in all cases. This increase in continuum emissions may be attributed to a rise in the insert temperature as the discharge power is increased. In the region of probe 1 there is a steeper fall off in intensity with increasing atomic weight and higher levels of continuum radiation are recorded for argon than for xenon. The relative intensity decreases with increasing mass flow rates as shown in Fig. 5.23. At probe positions 2 and 3 there is little dependence on mass flow rate particularly for argon but again a decrease in intensity occurs for increasing atomic mass.

5.3.3 Qualitative Analysis of Spectral Line Intensities

A comparison of the plasma characteristics of HCs operating on different inert gas propellants may be made by identifying equivalent spectral lines that arise as a result of similar atomic processes. The atomic configurations for the ground states of argon, krypton and

xenon are as follows;

$$\begin{aligned} &[Ne]3s^2 3p^6 \\ &[Ar]3d^{10}4s^2 4p^6 \\ &[Kr]4d^{10}5s^2 5p^6 \end{aligned} \tag{5.4}$$

Where the atomic configurations are represented as the nearest complete inert gas atom plus the additional orbitals required to provide a complete description of argon, krypton and xenon respectively. The letters s, p and d represent atomic orbitals. In order to identify equivalent lines the spectroscopic term that describes the excitation process must be know. Spectroscopic notation identifies configuration using a letter code in the form of $^{2S+1}L_J$ as shown in the third column of Table 5.6, where the letters represent quantum numbers; $S = \pm\frac{1}{2}$ is the total spin number, L is the orbital angular momentum number and the total angular momentum is $J = S + L$; for any given L value there are $2S + 1$ J values. The spectroscopic term may be represented as $^{2S+1}[J]^{Parity}$, as shown in the second column of Table 5.6. The parity is denoted by a 0 for odd parity. The number 1 represents even parity but is typically omitted. Table 5.6 shows the identified equivalent lines in the spectra of Ar, Kr and Xe plasmas along with the configurations and associated terms.

$\lambda\ nm$	Configuration	Term
$\lambda_{Ar} = 763.511$	$3p^5(^2P^0_{3/2})4s \longrightarrow 3p^5(^2P^0_{3/2})4p$	$^2[\frac{3}{2}]^0 -^2 [\frac{3}{2}]$
$\lambda_{Kr} = 760.154$	$4p^5(^2P^0_{3/2})5s \longrightarrow 4p^5(^2P^0_{3/2})5p$	
$\lambda_{Xe} = 895.225$	$5p^5(^2P^0_{3/2})6s \longrightarrow 5p^5(^2P^0_{3/2})6p$	
$\lambda_{Ar} = 852.144$	$3p^5(^2P^0_{1/2})4s \longrightarrow 3p^5(^2P^0_{1/2})4p$	$^2[\frac{1}{2}]^0 -^2 [\frac{3}{2}]$
$\lambda_{Kr} = 805.950$	$4p^5(^2P^0_{\frac{1}{2}})5s \longrightarrow 4p^5(^2P^0_{\frac{1}{2}})5p$	
$\lambda_{Ar} = 842.465$	$3p^5(^2P^0_{3/2})4s \longrightarrow 3p^5(^2P^0_{3/2})4p$	$^2[\frac{3}{2}]^0 -^2 [\frac{5}{2}]$
$\lambda_{Xe} = 881.941$	$5p^5(^3P^0_{3/2})6s \longrightarrow 5p^5(^2P^0_{3/2})6p$	

Table 5.6: Terms and configurations for equivalent lines of the HC internal plasma

Fig. 5.26 shows keeper/anode separation does not greatly influence line intensity and its dependence on anode current particularly for an argon discharge. On increasing the atomic

mass of the propellant gas line intensity is not effected by increasing anode current for large keeper/anode separations. Decreasing the keeper/anode separation causes line intensity to increase with increasing current, this is confirmed by the comparison of the intensity ratio of the argon and krypton lines shown in Fig. 5.27. The dependence of line intensity on anode current increases moving upstream as shown in Fig. 5.29.

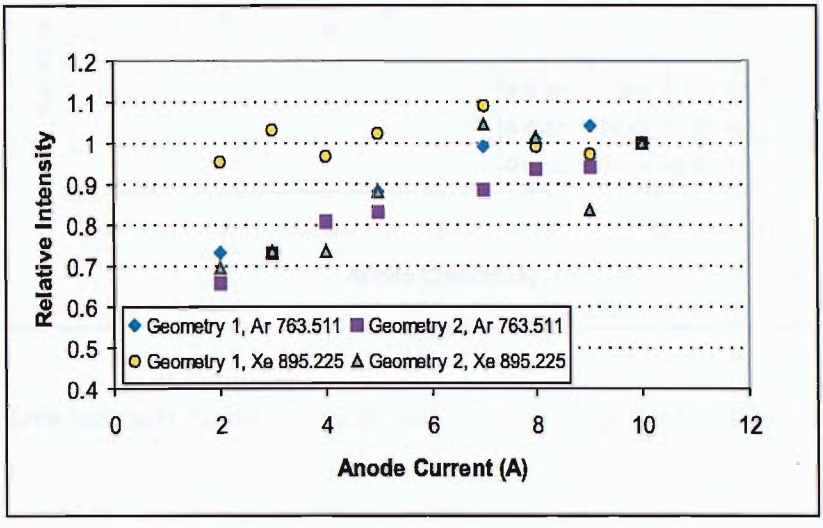

Figure 5.26: Comparison of line intensity ratios in the probe 1 position for $\dot{m} = 1.1mgs^{-1}$ for argon and $\dot{m} = 1.0mgs^{-1}$ for xenon

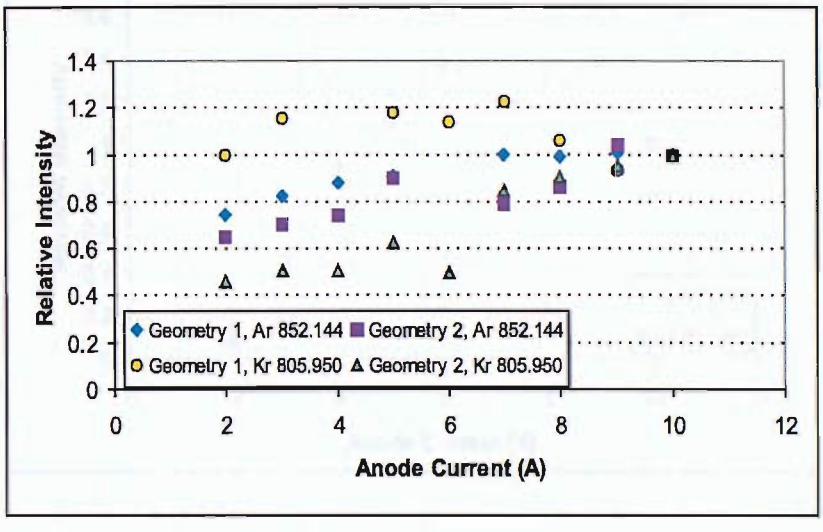

Figure 5.27: Line intensity ratios in the probe 1 position for $\dot{m} = 1.1mgs^{-1}$ for argon and $\dot{m} = 1.0mgs^{-1}$ for krypton

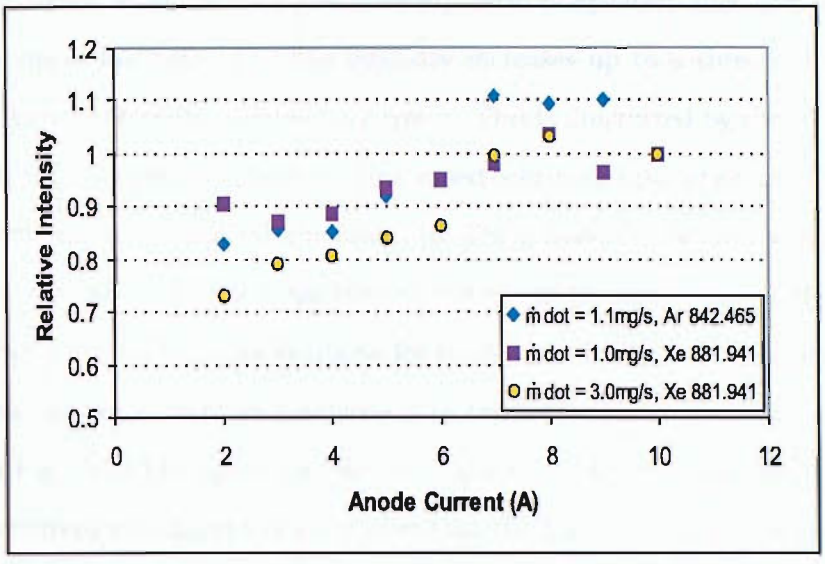

Figure 5.28: Line intensity ratios for argon and krypton propellant in the probe 1 position in geometry 1

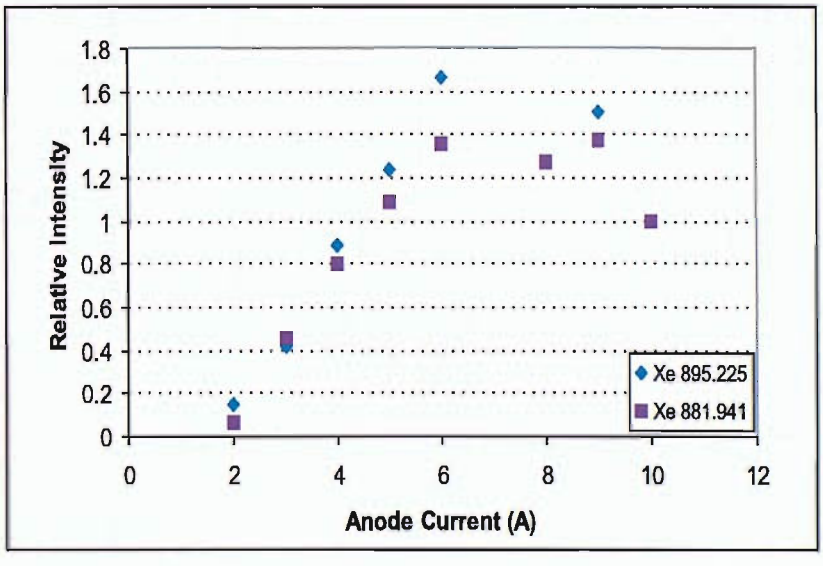

Figure 5.29: Line intensity ratios for xenon propellant in the probe 2 position in geometry 1 $\dot{m} = 1.0mgs^{-1}$.

The neutral line intensity is not highly sensitive to anode current in the region of probe 1 and no clear trends exist between the intensity ratio of spectral lines and varying anode geometry or mass flow rate. The line intensity increases up to a threshold value ($\sim 6A$) after which there is little dependence on current. This is illustrated by the trends displayed in Figs. 5.26 and 5.27 and may be due to increased continuum radiation at higher discharge currents interfering with spectral line intensity. There may also be a maximum achievable line intensity related not to discharge current but to the characteristics of the plasma such as the number density of species available for excitation. In the region of probe 2 spectral lines are weak at low current in comparison to the intensities achieved at higher current as shown in Fig. 5.29 but again decrease for $I_A > 6A$. The increased dependence of line intensity on current moving upstream implies that the plasma in this region requires higher power to produce a sufficient number of atomic transitions that result in intense spectral lines.

Chapter 6

Experimental Results II: Plasma Parameters and Thermal Characterisation

This chapter describes the analysis methods used to extract plasma parameter values and the insert temperature from the raw data. The results are presented in two main sections. The first addressing the calculation of the electron temperature, ion fraction and electron number density. The final section describes the thermal characterisation of the HC. The results obtained from three independent methods of determining the insert temperature will be presented.

6.1 Boltzmann Plot: LTE Electron Temperature

The Boltzmann plot method as described in Chapter 4 was used to provide an estimate of the electron temperature. This technique requires the internal plasma to conform to the LTE regime and its accuracy is dependent on the precision with which the transition probabilities of the spectral lines are known. Unfortunately the transition probabilities for all spectral lines, particularly those of the heavier elements remain unknown. As research

into the determination of atomic constants requires further work. This is the case for the majority of xenon spectral lines in the wavelength range of interest and a large number of the krypton lines. This limits the spectral lines available for use with this technique. For the case of krypton spectra the required atomic data were obtained for 5 lines from the atomic and molecular database [115] and where possible cross referenced with NIST data [114]. Atomic transition probabilities for xenon lines in the near infra red region of the spectrum were not listed in the atomic databases so experimental values stated in Ref. [117] with a typical error of $\pm 10\%$ were used. The atomic constants stated in Table 6.1 were used in conjunction with Equ. 6.1 in order to calculate the electron temperature.

Atomic Species	$\lambda\ (m)$	$A(p,q)\ (s^{-1})$	$\chi_q\ (eV)$	g_q
ArI	7.63511×10^{-07}	2.45×10^{07}	13.17178	5
	7.94818×10^{-07}	1.86×10^{07}	13.28264	3
	8.26452×10^{-07}	1.53×10^{07}	13.32786	3
	8.40821×10^{-07}	2.23×10^{07}	13.30223	5
	8.42465×10^{-07}	2.15×10^{07}	13.09487	5
	8.52144×10^{-07}	1.39×10^{07}	13.28264	3
KrI	7.601544×10^{-07}	3.10×10^{07}	11.54583	5
	7.854821×10^{-07}	2.30×10^{07}	12.14043	3
	8.059503×10^{-07}	1.90×10^{07}	12.10034	3
	8.508870×10^{-07}	2.40×10^{07}	12.10034	3
	8.928692×10^{-07}	3.70×10^{07}	11.30352	3
XeI	8.231635×10^{-07}	2.39×10^{07}	9.82110	5
	8.280116×10^{-07}	3.40×10^{07}	9.93349	1
	8.819410×10^{-07}	3.00×10^{07}	9.72074	7
	8.952250×10^{-07}	0.965×10^{07}	9.82110	5

Table 6.1: Atomic constants and energy levels used for determining T_e via the Boltzmann Plot method

$$\underbrace{\ln\left(\frac{I(p,q)_1\lambda_{pq1}A(p,q)_2g(q)_2}{I(p,q)_2\lambda_{pq2}A(p,q)_1g(q)_1}\right)}_{y} = \underbrace{\frac{\chi_{q12}}{kT_e}}_{mx} + \underbrace{\ln C}_{c} \tag{6.1}$$

Fig. 6.1 shows Boltzmann plots generated for the HC discharge operating on argon propellant at probe position 1 (1.3mm from the HC tip) and probe position 2 (3.7mm from the tip). The equations for the lines of best fit are obtained by linear regression analysis using the "least squares" method to fit the line through the data points. The deviation of the data points from the line of best fit is represented by the correlation coefficient R^2 where high values (approaching $R^2 = 1$) indicate a good fit. The correlation coefficient estimates the percentage error of the gradient of the line of best fit. The propagation of errors method is used to obtain the error on the T_e value. The error bars on the following figures were determined using the relation, $error = \pm(1 - R^2)T_e$. The resulting electron temperature values are presented in Fig. 6.2 - Fig. 6.6.

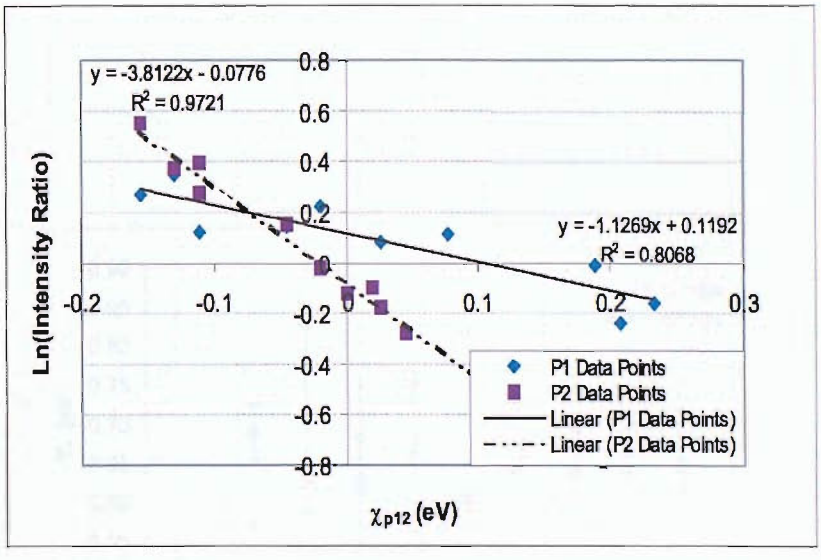

Figure 6.1: Example Boltzmann plots for argon propellant with a keeper/anode separation of $60mm$ (geometry 1), $\dot{m} = 1.1mgs^{-1}$ and $I_A = 2.0A$.

The electron temperatures determined for a xenon discharge are shown in Fig. 6.2, T_e ranges from $0.5-1.2eV$ and shows the largest variability with I_A of all inert gas propellants. The HC operating on krypton propellant displays the lowest variation in T_e of $0.2eV$ for the range of operating conditions investigated and there is no clear trend between T_e and

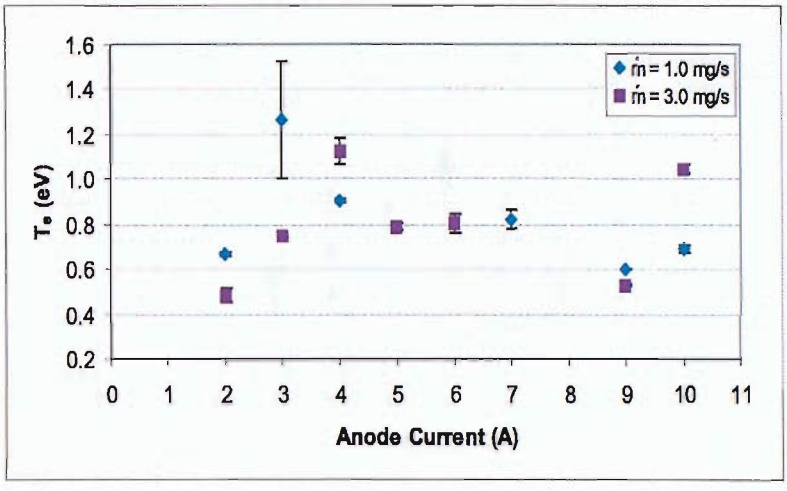

Figure 6.2: Electron temperature as a function of anode current at probe 1 for a xenon discharge in geometry 1

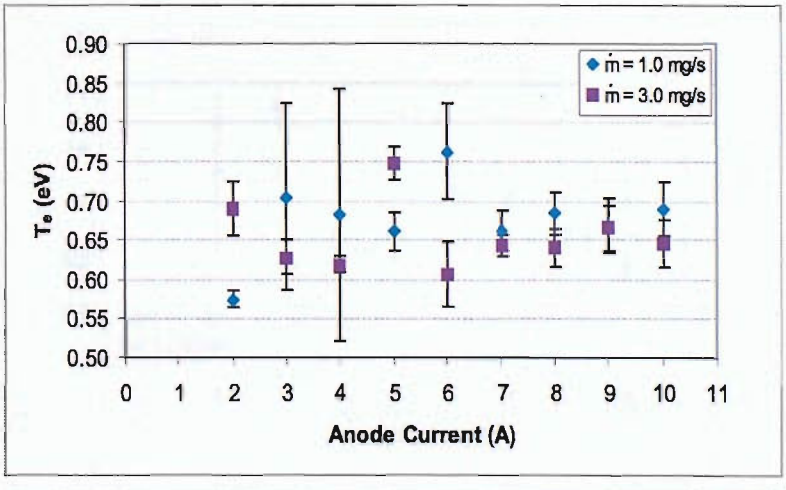

Figure 6.3: Electron temperature as a function of anode current at probe 1 for a krypton discharge in geometry 1

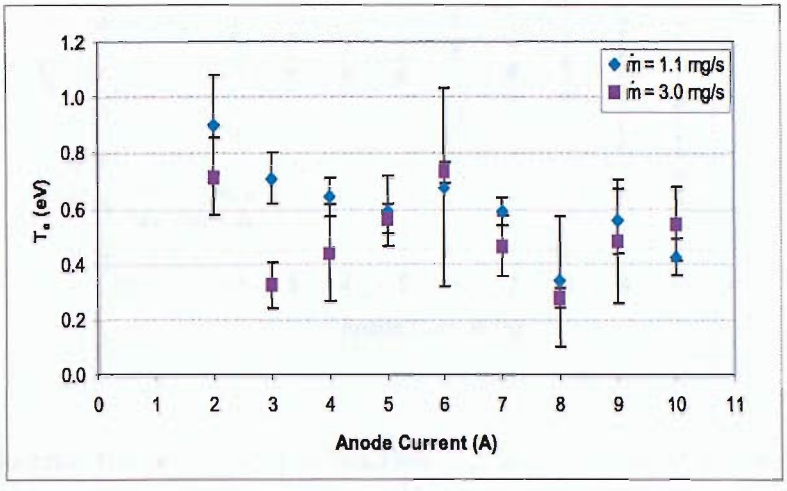

Figure 6.4: Electron temperature as a function of anode current at probe 1 for an argon discharge in geometry 1

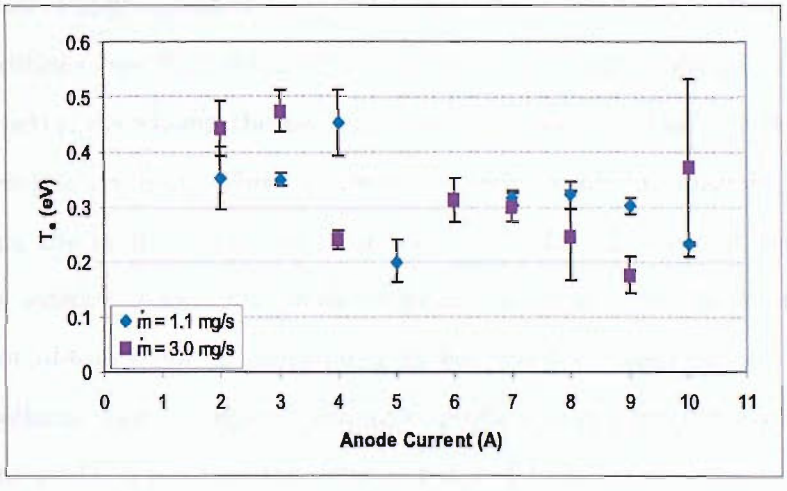

Figure 6.5: Electron temperature as a function of anode current at probe 1 for an argon discharge in geometry 2

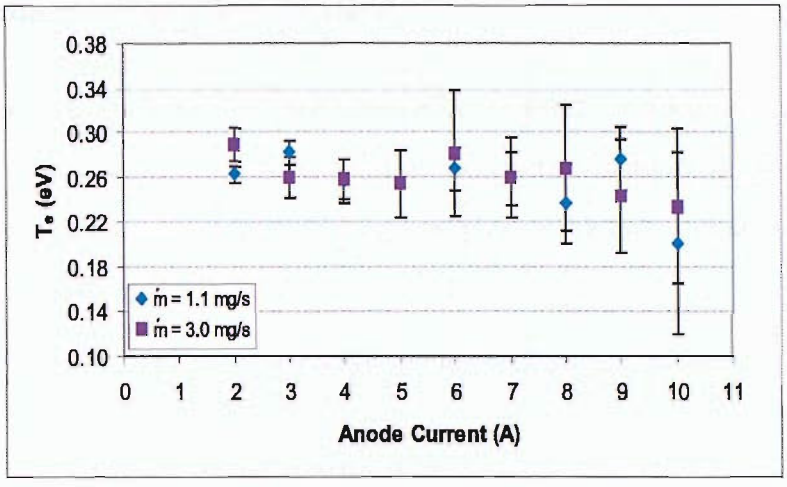

Figure 6.6: Electron temperature as a function of anode current at probe 2 for an argon discharge in geometry 1

I_A. Increasing mass flow rate causes a decrease in T_e. The argon plasma T_e shows a large variation with varying I_A in probe position 1 and geometry 1 ($T_e = 0.3 - 0.9eV$ for $\dot{m} = 1.1mgs^{-1}$ and $T_e = 0.3 - 0.7eV$ for $\dot{m} = 3.0mgs^{-1}$). There appears to be no dependence on mass flow rate; however, increasing mass flow rate results in a decreased spread of the T_e values obtained. Moving upstream to probe position 2 there is a dramatic decrease in T_e, in some cases of approximately two thirds the value determined at probe 1 for the same operating conditions (see Fig. 6.6). The electron temperature appears to be dependent on anode geometry; decreasing the keeper/anode separation by half results in a decrease in T_e by approximately half. There is also a dependence on the mass of the propellant used, increasing the atomic mass causes an increase in T_e. However, it becomes difficult to state trends with confidence due to the error associated with the T_e measurement. The maximum error obtained for T_e at probe 1 in geometry 1 is approximately 25% for all inert gas propellants. For an argon discharge at probe 1 in geometry 2 errors are less than 30% and in the probe 2 position the error is reduced to less than 20% for all operating conditions. A possible source of error may be the use of the LTE model to calculate the electron temperature when the discharge may not conform to this regime. Also the errors of the atomic constants (particularly in the case of xenon) may be large enough to prevent the stating of T_e to a precision necessary for the trends to manifest themselves.

6.1.1 Plasma Regime Classification

The electron temperature values determined in Section 6.1 may be used in conjunction with the Saha Equ. to provide an estimate of the electron number density. Once n_e is known the criteria stated in Chapter 4 may be applied to identify the appropriate regime for the HC internal plasma.

$$\frac{n_e n(z+1,g)}{n(z,g)} = 2\frac{g(z+1,g)}{g(z,p)}\left(\frac{2\pi m_e k T_e}{h^2}\right)^{\frac{3}{2}} \exp\left(\frac{-\chi(z,g)}{kT_e}\right) \tag{6.2}$$

It is assumed that the ratio of the statistical weights $\frac{g(z+1,g)}{g(z,p)} \approx 1$. The electron number density has been calculated for different ionisation fractions α_{ion} as shown in Figs. 6.7 – 6.9. An ionisation fraction of $\alpha_{ion} = 1$ is for a fully ionised plasma and $\alpha_{ion} = 0.5$ implies that there are double the number of neutral atoms to ions.

$$\alpha_{ion} = \frac{n(z+1,g)}{n(z,g)} \tag{6.3}$$

The boundaries for the plasma regimes determined using Equ. 6.4 and Equ. 6.5 are shown on Figs. 6.7 – 6.9 for the first ionisation potentials of Ar, Kr and Xe which are 15.8 ,14.0 and $12.1V$ respectively. This allows the plasma regime applicable to the HC internal plasma with ionic charge $z+1 = 1$ to be identified.

$$n_e \geq 1.6 \times 10^{12} T_e^{\frac{1}{2}} \chi(p,q)^3 \tag{6.4}$$

$$n_e < 5.6 \times 10^8 (z+1)^6 T_e^{\frac{1}{2}} \exp\left(\frac{1.162 \times 10^3 (z+1)^2}{T_e}\right) \tag{6.5}$$

For a HC operating on Ar propellant the internal plasma conforms to the CR regime with n_e in the range of $6 \times 10^{16} - 7 \times 10^{23} m^{-3}$, this typically applies to the plasma in the region of probe 1 for a keeper/anode separation of $60mm$. For $T_e < 0.6eV$ found in the region of probe 1 for keeper/anode separations of $30mm$ or in the vicinity of probe 2, the plasma lies in the corona range with $n_e < 6 \times 10^{16} m^{-3}$. When operating the HC on Kr propellant the CR regime lies in the range of $n_e \approx 6 \times 10^{16} - 5 \times 10^{23} m^{-3}$ corresponding to $T_e \approx 0.6 - 1.1eV$ obtained in the probe 1 position for a keeper/anode separation of $60mm$. The upper limit for CR regime is $n_e \sim 3 \times 10^{23} m^{-3}$ for Xe propellant with a lower limit of $n_e \sim 5 \times 10^{16} m^{-3}$ after which the plasma falls into the corona regime for $T_e < 0.5eV$.

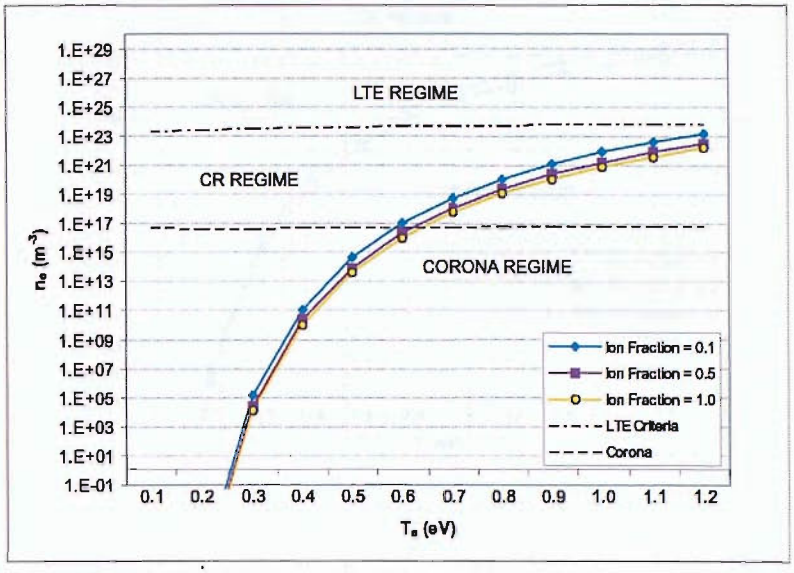

Figure 6.7: Electron number density for T_e values of interest for various ionisation fractions with regime boundaries for argon

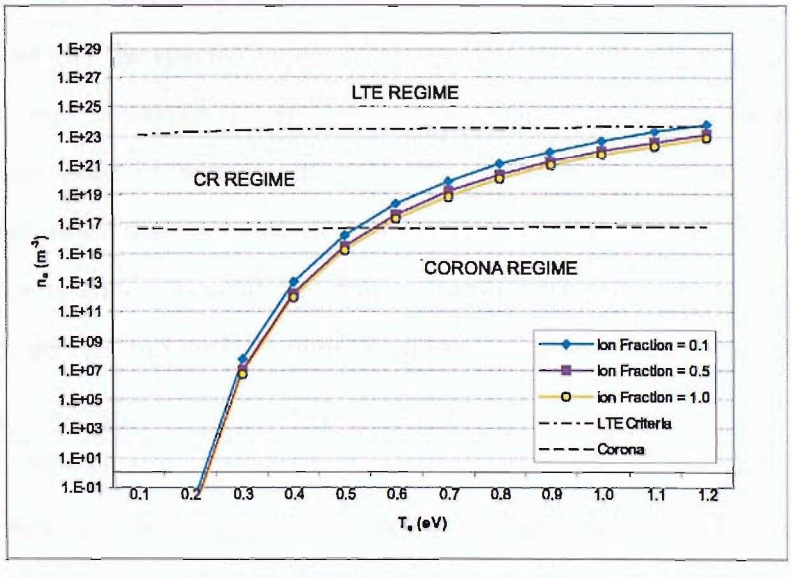

Figure 6.8: Electron number density for T_e values of interest for various ionisation fractions with regime boundaries for krypton

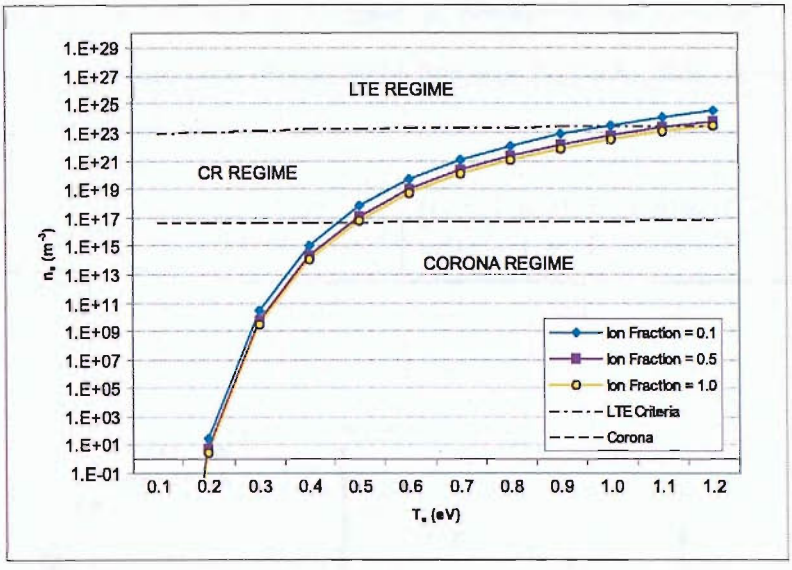

Figure 6.9: Electron number density for T_e values of interest for various ionisation fractions with regime boundaries for xenon

6.2 Collisional Radiative Electron Temperature

The ladder approximation for the CR model is used in order to calculate the electron temperature [2, 107]. This model takes advantage of the fact that with increasing principal quantum number (n) the spacing between energy levels becomes closer, the probability of collisional processes occurring becomes greater and the probability of radiative processes decreases (as discussed in Section 4.6). As a consequence there is a level above which all radiative processes may be neglected, referred to as the thermal level. Under these circumstances a modified form of the Saha equation may be used to estimate the ion fraction for known electron number density and temperature (see Equ. 6.6)[107].

$$\frac{n(z+1,g)n_e}{n(z,q)} = 2\frac{g(z+1,g)}{g(z,q)}\left(\frac{2\pi m_e kT_e}{h^2}\right)^{\frac{3}{2}}\exp\left(\frac{\chi(q)-\chi(z,g)}{kT_e}\right) \tag{6.6}$$

The modified Saha equation may be substituted into the intensity ratio equation for lines of differing ionisation stages (**Equ. 4.50**). In this way an expression is obtained that relates line intensity to the electron temperature.

$$\frac{I(z+1,g)\lambda(z+1,g)A(z,q)}{I(z,q)\lambda(z,q)A(z+1,g)} = \frac{2g(z+1,g)}{n_e g(z,q)}\left(\frac{2\pi m_e kT_e}{h^2}\right)^{\frac{3}{2}}\exp\left(\frac{\chi(q)-\chi(z,g)}{kT_e}\right) \tag{6.7}$$

The Boltzmann plot technique may be used to determine the electron temperature by arranging Equ. 6.7 into the form of a straight line (see Equ 6.8), this method was used in the PhD thesis of Rudwan [2].

$$\underbrace{\ln\left(\frac{A(z,q)g(z,q)}{I(z,q)\lambda(z,q)}\right)}_{y} = \underbrace{\frac{\chi(q)}{kT_e}}_{mx} \underbrace{- \left\{\frac{\chi(z,g)}{kT_e} + \ln\left[\frac{I(z+1,g)\lambda(z+1,g)n_e}{2A(z+1,g)g(z+1,g)}\left(\frac{2\pi m_e kT_e}{h^2}\right)^{-\frac{3}{2}}\right]\right\}}_{c} \tag{6.8}$$

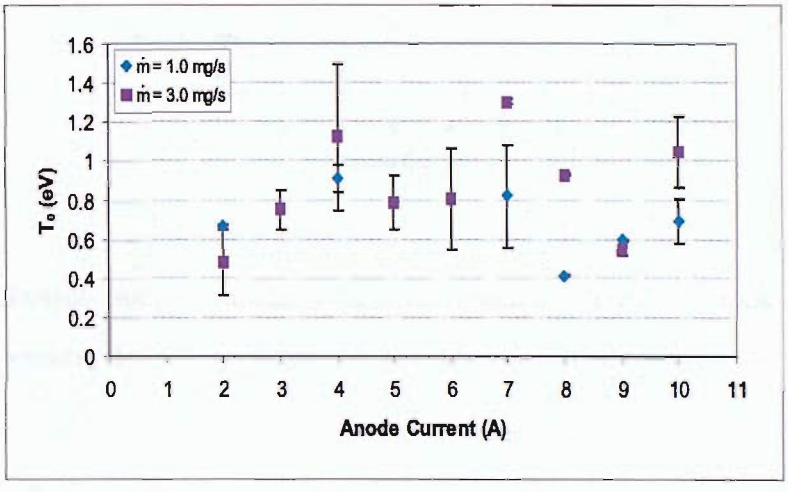

Figure 6.10: Electron temperature as a function of anode current at probe 1 for the HC operating on xenon propellant in geometry 1

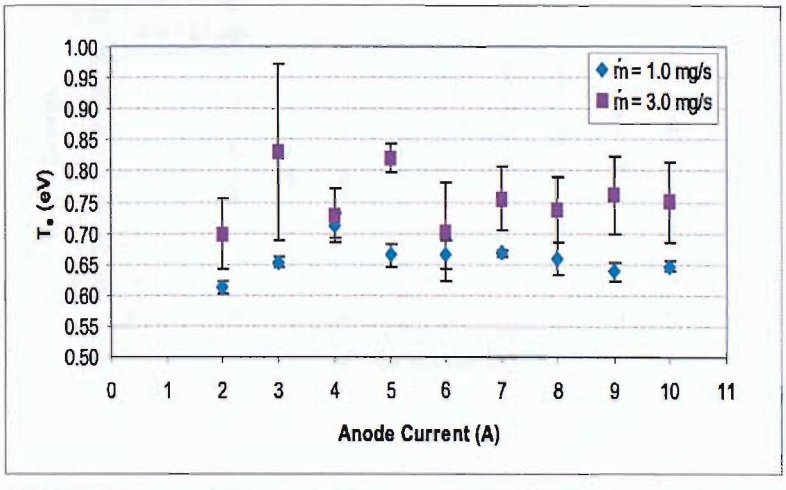

Figure 6.11: Electron temperature as a function of anode current at probe 1 for a krypton discharge in geometry 1

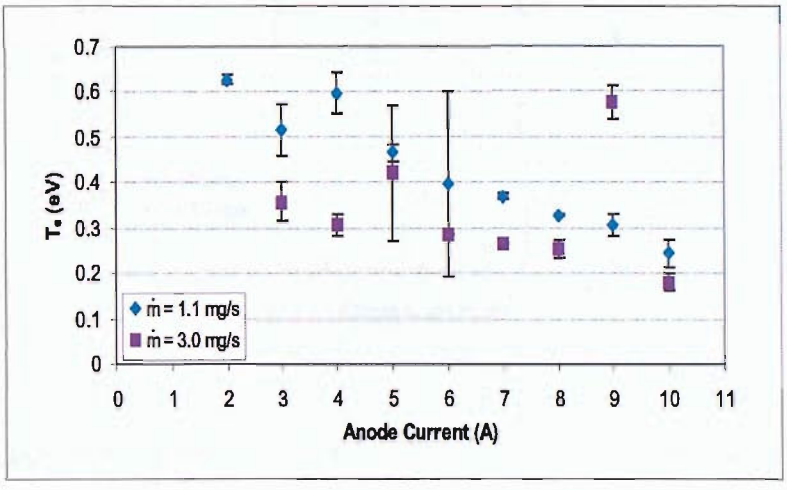

Figure 6.12: Electron temperature as a function of anode current at probe 1 for an argon discharge in geometry 1

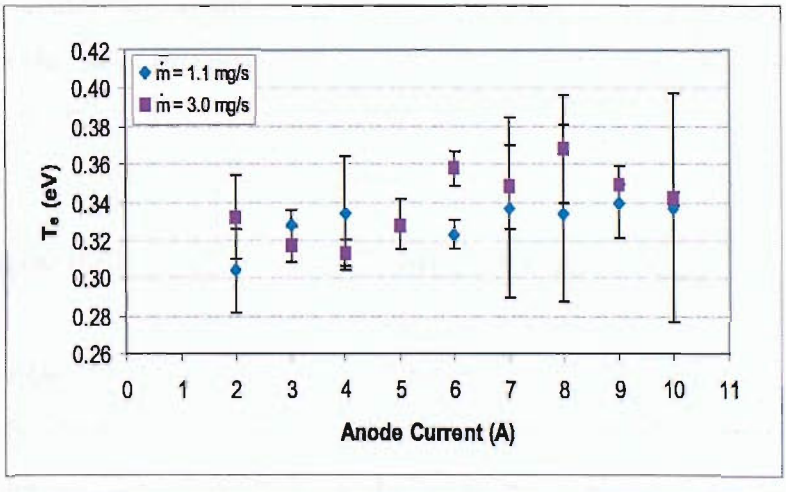

Figure 6.13: Electron temperature as a function of anode current at probe 2 for an argon discharge in geometry 1

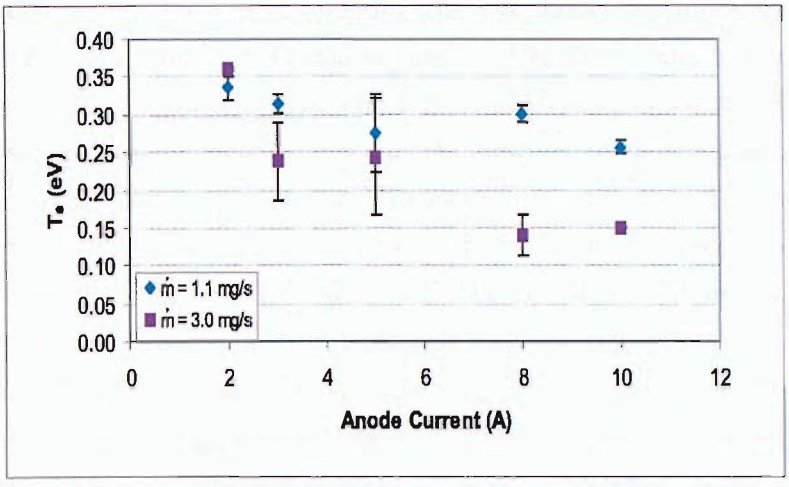

Figure 6.14: Electron temperature as a function of anode current at probe 1 for an argon discharge in geometry 2

The CR T_e are similar to the LTE results particularly for a xenon discharge (see Fig. 6.10). The variation in T_e with I_A is reduced compared to the LTE model and the error associated with the calculation is also reduced. The dependence of T_e on $\dot{m}$ is reversed for the case of krypton and argon at probe 2, with T_e increasing with increasing $\dot{m}$. Ideally the corona model should be used for the T_e calculation at probe 1 in geometry 2 and in the region of probe 2. Unfortunately the atomic constants required for the calculation are not available which prohibits the use of this model. For a full discussion of the corona model and atomic data see Appendix B.

6.3 Comparison of Electron Temperatures

The electron temperature values determined using the LTE and CR models are compared in Tables 6.2 – 6.6. The tables state T_e values with the corresponding correlation coefficients R^2 and the difference between the LTE and CR electron temperatures determined under the same conditions.

For the case of the HC operating on argon propellant in geometry 1 with spectra recorded from probe 1 the average difference in electron temperature with $\dot{m} = 1.1 mgs^{-1}$ and $\dot{m} = 3.0 mgs^{-1}$ is $\Delta T_e^{1.1} = 0.194eV \pm (\sigma_{sd} = 0.075eV)$ and $\Delta T_e^{3.0} = 0.208eV \pm (\sigma_{sd} = 0.165eV)$

respectively. The results show that applying the CR model produces a decrease in T_e relative to the LTE values. The R^2 values for the CR model are higher than that of the LTE model indicating an improved line fit through the data points. Decreasing the anode/keeper separation causes a decrease in ΔT_e compared to the geometry 1 results; again R^2 values show improvement in the CR case compared to the LTE model (see Table 6.3) and T_e typically decreases using the CR model. The results presented in Table 6.4 for probe 2 again show improved R^2 values with the use of the CR model. The krypton discharge shows little difference in the LTE and CR results particularly at low $\dot{m}$ (see Table 6.5). The R^2 values are also similar with average values of $R^2 = 0.916 \pm 0.079$ and $R^2 = 0.959 \pm 0.019$ for the LTE case with $\dot{m} = 1.0 mgs^{-1}$ $\dot{m} = 3.0 mgs^{-1}$ respectively, compared to $R^2 = 0.977 \pm 0.012$ and $R^2 = 0.915 \pm 0.039$ for the CR results.

	LTE				CR					
	$\dot{m} = 1.1 mgs^{-1}$		$\dot{m} = 3.0 mgs^{-1}$		$\dot{m} = 1.1 mgs^{-1}$		$\dot{m} = 3.0 mgs^{-1}$			
I_A (A)	R^2	T_e	R^2	T_e	R^2	T_e	R^2	T_e	$\Delta T_e^{1.1}$	$\Delta T_e^{3.0}$
2.0	0.807	0.903	0.808	0.716	0.983	0.628	0.641	1.148	0.275	0.432
3.0	0.867	0.708	0.743	0.323	0.889	0.517	0.878	0.358	0.191	0.035
4.0	0.889	0.641	0.600	0.44	0.925	0.599	0.920	0.306	0.042	0.134
5.0	0.809	0.588	0.906	0.562	0.963	0.465	0.643	0.421	0.123	0.141
6.0	0.763	0.532	0.950	0.734	0.483	0.396	1.000	0.285	0.136	0.449
7.0	0.916	0.589	0.753	0.463	0.982	0.370	0.997	0.266	0.219	0.197
8.0	0.911	0.516	0.881	0.278	0.995	0.329	0.916	0.254	0.187	0.024
9.0	0.792	0.554	0.954	0.481	0.917	0.307	0.936	0.579	0.247	0.098
10.0	0.847	0.426	0.753	0.543	0.867	0.244	0.897	0.182	0.182	0.361
Ave.	0.845		0.817		0.890		0.870		0.178	0.208
σ_{sd}	0.0549		0.117		0.157		0.135		0.0702	0.165

Table 6.2: Argon plasma electron temperature at probe 1 and geometry 1

	LTE				CR					
	$\dot{m} = 1.1mgs^{-1}$		$\dot{m} = 3.0mgs^{-1}$		$\dot{m} = 1.1mgs^{-1}$		$\dot{m} = 3.0mgs^{-1}$			
I_A (A)	R^2	T_e	R^2	T_e	R^2	T_e	R^2	T_e	$\Delta T_e^{1.1}$	$\Delta T_e^{3.0}$
2.0	0.839	0.353	0.888	0.442	0.956	0.335	0.992	0.361	0.018	0.081
3.0	0.969	0.351	0.919	0.474	0.962	0.314	0.783	0.238	0.037	0.236
4.0	0.866	0.453	0.934	0.240	0.999	0.373	0.797	0.107	0.08	0.133
8.0	0.922	0.323	0.669	0.248	0.964	0.300	0.807	0.139	0.023	0.109
9.0	0.948	0.302	0.817	0.177	0.948	0.326	0.930	0.117	0.024	0.060
10.0	0.985	0.233	0.565	0.373	0.969	0.256	1.00	0.150	0.023	0.223
Ave.	0.912		0.840		0.945		0.871		0.0353	0.156
σ_{sd}	0.0650		0.138		0.0564		0.112		0.0262	0.0708

Table 6.3: Argon plasma electron temperature at probe 1 and geometry 2

	LTE				CR					
	$\dot{m} = 1.1mgs^{-1}$		$\dot{m} = 3.0mgs^{-1}$		$\dot{m} = 1.1mgs^{-1}$		$\dot{m} = 3.0mgs^{-1}$			
I_A (A)	R^2	T_e	R^2	T_e	R^2	T_e	R^2	T_e	$\Delta T_e^{1.1}$	$\Delta T_e^{3.0}$
2.0	0.972	0.262	0.947	0.289	0.927	0.304	0.994	0.332	0.042	0.043
3.0	0.963	0.282	0.930	0.259	0.979	0.328	0.971	0.317	0.046	0.058
4.0	0.924	0.256	0.928	0.258	0.909	0.334	0.977	0.313	0.078	0.055
5.0	-	-	0.884	0.254	-	-	0.959	0.328	0	0.074
6.0	0.932	0.267	0.799	0.281	0.976	0.323	0.974	0.358	0.056	0.077
7.0	0.908	0.259	0.863	0.260	0.858	0.337	0.937	0.348	0.078	0.088
8.0	0.853	0.236	0.791	0.268	0.859	0.334	0.923	0.368	0.098	0.100
9.0	0.897	0.276	0.790	0.243	0.943	0.340	0.999	0.349	0.064	0.106
10.0	0.593	0.201	0.706	0.234	0.821	0.337	0.989	0.342	0.136	0.108
Ave.	0.880		0.849		0.909		0.969		0.0664	0.0788
σ_{sd}	0.122		0.0819		0.0582		0.0256		0.0382	0.0235

Table 6.4: Argon plasma electron temperature at probe 2 and geometry 1

	LTE				CR					
	$\dot{m} = 1.0mgs^{-1}$		$\dot{m} = 3.0mgs^{-1}$		$\dot{m} = 1.0mgs^{-1}$		$\dot{m} = 3.0mgs^{-1}$			
I_A (A)	R^2	T_e	R^2	T_e	R^2	T_e	R^2	T_e	$\Delta T_e^{1.1}$	$\Delta T_e^{3.0}$
2.0	0.982	0.575	0.930	0.650	0.983	0.612	0.920	0.699	0.037	0.0490
3.0	0.801	0.704	0.962	0.628	0.986	0.653	0.830	0.831	0.0510	0.203
4.0	0.764	0.682	0.984	0.619	0.973	0.712	0.939	0.729	0.0300	0.110
5.0	0.964	0.661	0.972	0.747	0.973	0.665	0.97	0.822	0.004	0.075
6.0	0.915	0.762	0.931	0.607	0.966	0.665	0.885	0.702	0.097	0.095
7.0	0.962	0.662	0.978	0.643	0.992	0.668	0.932	0.756	0.00600	0.113
8.0	0.961	0.684	0.963	0.640	0.959	0.658	0.927	0.739	0.026	0.099
9.0	0.948	0.668	0.957	0.666	0.978	0.638	0.918	0.763	0.03	0.097
10.0	0.95	0.689	0.953	0.645	0.987	0.647	0.915	0.751	0.0420	0.106
Ave.	0.916		0.959		0.977		0.915		0.0359	0.105
σ_{sd}	0.0785		0.0189		0.0107		0.0390		0.0276	0.0417

Table 6.5: Krypton plasma electron temperature at probe 1 and geometry 1

	LTE				CR					
	$\dot{m} = 1.0mgs^{-1}$		$\dot{m} = 3.0mgs^{-1}$		$\dot{m} = 1.0mgs^{-1}$		$\dot{m} = 3.0mgs^{-1}$			
I_A (A)	R^2	T_e	R^2	T_e	R^2	T_e	R^2	T_e	$\Delta T_e^{1.1}$	$\Delta T_e^{3.0}$
2.0	0.992	0.666	0.942	0.480	0.983	0.662	0.642	0.480	0.004	0
3.0	0.792	1.264	0.983	0.750	0.297	1.264	0.865	0.750	0	0
4.0	0.991	0.907	0.947	1.123	0.927	0.907	0.666	1.123	0	0
5.0	0.977	0.788	0.977	0.789	0.822	0.788	0.824	0.789	0	0
7.0	0.950	0.819	0.999	1.300	0.680	0.819	0.990	1.300	0	0
9.0	1.000	0.598	0.992	0.528	0.998	0.598	0.932	0.548	0	0.02
10.0	0.979	0.691	0.977	1.047	0.839	0.691	0.827	1.047	0	0
Ave.	0.954		0.974		0.792		0.821		0.000444	0.00222
σ_{sd}	0.0734		0.0216		0.244		0.128		0.00133	0.0667

Table 6.6: Xenon plasma electron temperature at probe 1 and geometry 1

The CR model reduces to the LTE case at high densities. McWhirter states in Ref. [107], "...in the limit of very high density the CR model must reduce to the LTE model." This implies that the level above which radiative processes do not contribute to population densities and therefore may be neglected is the ground state. This is demonstrated by the results obtained for the xenon discharge. There is no significant difference between

the LTE and CR electron temperatures. It can also be seen that the R^2 values for the CR case are significantly lower than the LTE values. The increased spread in data points implies that the modified Saha equation is not applicable and the most appropriate model for use is the LTE model. The electron temperatures determined for the HC operating on xenon propellant are higher than those determined for argon and krypton propellants under the same operating conditions. Due to the exponential dependence of electron density on temperature, the electron density for the xenon discharge may be expected to be significantly higher than that obtained for the alternative propellants, resulting in a high density discharge that tends to the LTE regime.

The general trends in the results presented show that T_e is insensitive to variations in anode current and hence discharge power. In the region of probe 1 in geometry 1 T_e increases with increasing atomic mass. There is no clear relationship between $\dot{m}$ and T_e. For krypton propellant T_e increases with increasing $\dot{m}$ but this cannot be said for the remaining two propellants. It becomes difficult state trends with confidence if the differences between the data points are of the same order as the error associated with the value. Although the HC internal plasma does not strictly conform to the LTE regime, the model provides a good estimate for the electron temperature that agrees well with the values obtained using the CR approach.

6.4 Ionisation Fraction and Electron Number Density

In order to provide an accurate value of the electron number density the ionisation fraction must be determined. The ion fraction states the degree of ionisation of the plasma and may be determined using Equ. 4.50, which relates the ionisation fraction to the intensity ratio of lines of different ionisation stages. Using this method we obtain the ratio of ionised species to neutral species. Although this approach is specific to the line species used it allows an estimate of the degree of ionisation to be determined. Table 6.7 shows the ion fraction for a krypton discharge at probe 1 calculated using the ionised line $\lambda = 468.041nm$ with a variety of neutral lines. This demonstrates the variability of the ion fraction with changing spectral lines and the influence this has on the electron number density. The

ionisation fraction α_{ion} varies from 3% to 15% for $\dot{m} = 1.0mgs^{-1}$ and 1% to 5% for $\dot{m} = 3.0mgs^{-1}$ depending on the combination of lines used. The electron number densities were determined using the LTE Saha Equ. as discussed below.

	$\dot{m} = 1.0mgs^{-1}$		$\dot{m} = 3.0mgs^{-1}$	
λ (nm)	α_{ion}	n_e (m^{-3})	α_{ion}	n_e (m^{-3})
760.154	0.0271	6.989×10^{17}	0.0089	5.730×10^{19}
785.482	0.1332	8.959×10^{16}	0.0385	9.426×10^{18}
805.950	0.1323	9.628×10^{16}	0.0468	8.202×10^{18}
850.887	0.1511	8.429×10^{16}	0.0502	7.650×10^{18}
892.869	0.0373	1.256×10^{18}	0.0146	8.323×10^{19}
Average	0.0962	4.450×10^{17}	0.0318	3.298×10^{19}
σ_{sd}	0.0590	5.245×10^{17}	0.0189	3.477×10^{19}

Table 6.7: Ion fractions and electron number densities for krypton propellant at probe 1 in geometry 1, $I_A = 2.0A$, $\dot{m} = 1.0mgs^{-1}$ with $T_e = 0.612eV$ and $\dot{m} = 3.0mgs^{-1}$ with $T_e = 0.699eV$

The ion fraction is highly dependent on mass flow rate and anode current (particularly at high $\dot{m}$) as shown in Fig. 6.15 and Fig. 6.16. For the xenon discharge an ionised species with $\lambda = 716.483nm$ was used for the calculation. Increasing atomic mass increases the ionisation fraction and it becomes less sensitive to mass flow rate; variations with anode current are also less pronounced with similar fractions achieved for $I_A > 6.0A$ (see Figs. 6.17 – 6.18). Increasing the anode current causes the ion fraction to decrease, particularly at high mass flow rate. This may be due to an increase in pressure caused by increased current. A maximum ion fraction of 15% is achieved for $\dot{m} = 1.0mgs^{-1}$ compared to 5% for $\dot{m} = 3.0mgs^{-1}$ for the krypton discharge. The ion fraction shows reduced sensitivity with a xenon discharge, achieving maxima of 22% and 19% for $\dot{m} = 1.0mgs^{-1}$ and $\dot{m} = 3.0mgs^{-1}$ respectively. The ionisation fraction could not be determined for an argon discharge because no ionised species were positively identified.

The dependence of the ion fraction on the atomic mass of the propellant gas is due to variations in the ionisation cross sections of different gases. Increasing atomic mass causes

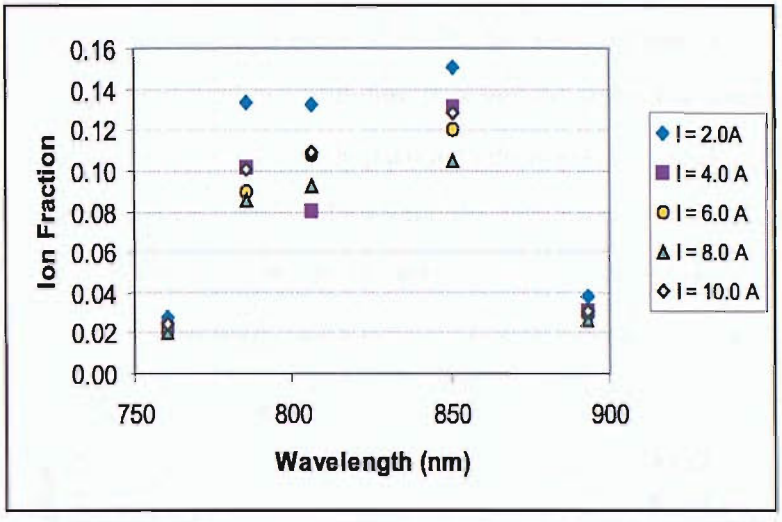

Figure 6.15: The dependence of ionisation fraction on spectral line species and anode current for krypton propellant at probe 1 in geometry 1 with $\dot{m} = 1.0mgs^{-1}$

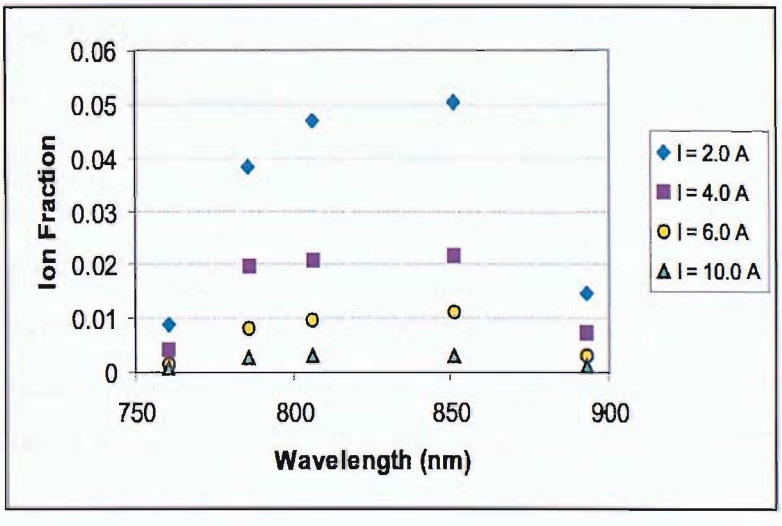

Figure 6.16: The dependence of ionisation fraction on spectral line species and anode current for krypton propellant at probe 1 in geometry 1 with $\dot{m} = 3.0mgs^{-1}$

an increase in the broad features i.e. the generic curve of the cross section, but it is impossible to make comparisons regarding fine structure features of the cross sections. The opacity of the plasma to neutrals is also a factor that influences ion fraction. The distance a neutral atom is able to travel before it is ionised will influence the length of the active region of the plasma. The mean free path for ionisation λ_{ion} is inversely proportional to the ionisation cross section [121]. Therefore, the ion fraction not only increases with increasing atomic mass but the scale length of the plasma also increases.

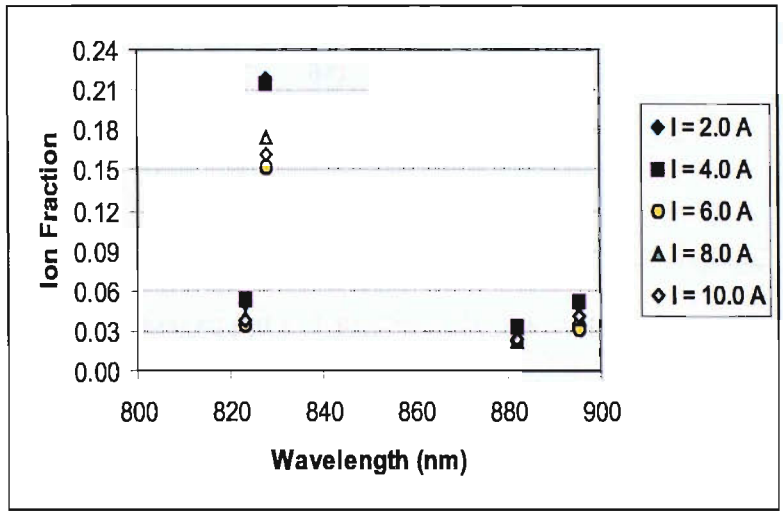

Figure 6.17: The dependence of ionisation fraction on spectral line species and anode current for xenon propellant at probe 1 in geometry 1 with $\dot{m} = 1.0mgs^{-1}$

Fig. 6.20 shows the dependence of the ionisation fraction on electron temperature for a krypton discharge. The ion fraction decreases with increasing T_e and mass flow rate. This is expected as increasing $\dot{m}$ will increase the neutral density and in the case of the krypton discharge T_e displayed a dependence on $\dot{m}$. The dependence is less pronounced for a xenon discharge and the dominant factor in dictating ionisation fraction is the propellant flow rate.

It has been shown in Ref. [2] that the most appropriate method for determining the electron number density of a HC discharge is the LTE Saha relation (see Equ. 6.9); the

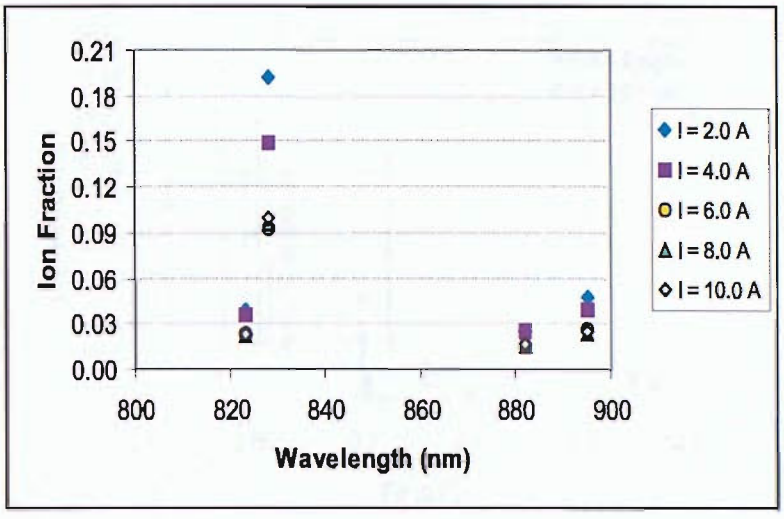

Figure 6.18: The dependence of ionisation fraction on spectral line species and anode current for xenon propellant at probe 1 in geometry 1 with $\dot{m} = 3.0mgs^{-1}$

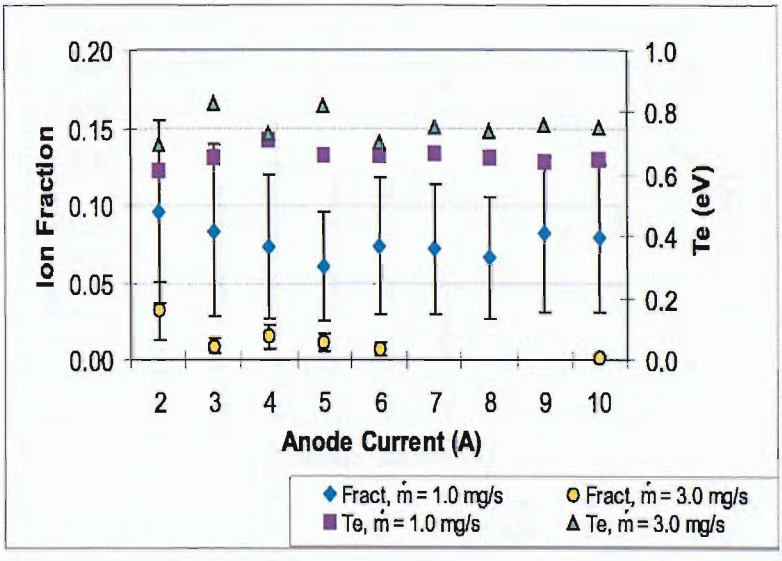

Figure 6.19: Average ionisation fraction as a function of anode current for krypton propellant at probe 1 in geometry 1

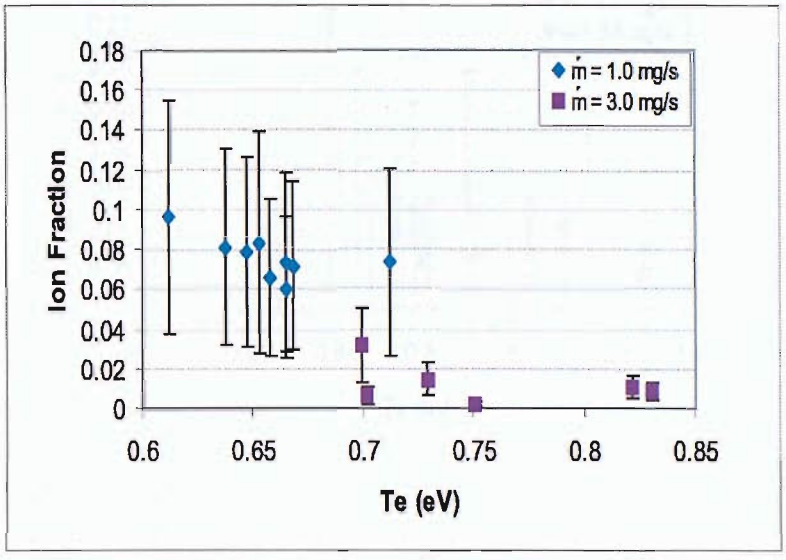

Figure 6.20: Average ionisation fraction as a function of electron temperature for krypton propellant at probe 1 in geometry 1

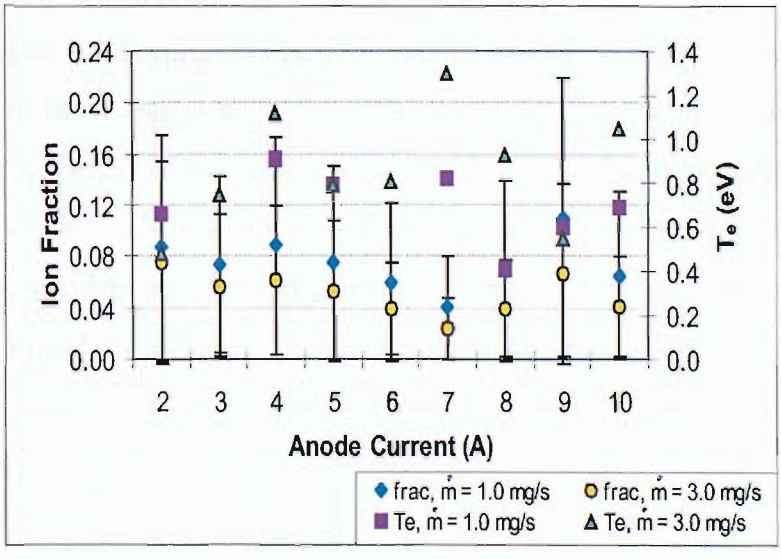

Figure 6.21: Average ionisation fraction as a function of anode current for xenon propellant at probe 1 in geometry 1

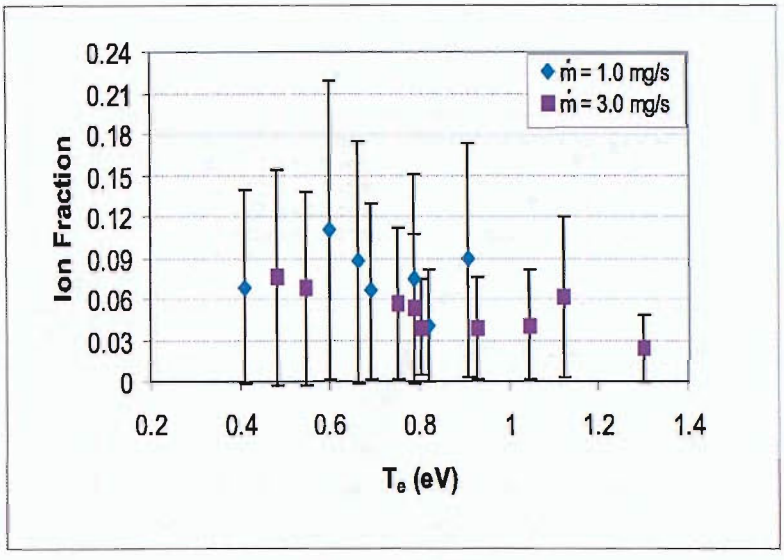

Figure 6.22: Average ionisation fraction as a function of electron temperature for xenon propellant at probe 1 in geometry 1

CR model may only be used under certain operating conditions [2].

$$n_e = \frac{2g(z+1,q)}{\alpha_{ion} g(z,q)} \left(\frac{2\pi m_e k T_e}{h^2}\right)^{\frac{3}{2}} \exp\left(\frac{\chi(z,g) - \chi(z,q) - \chi(z+1,q)}{kT_e}\right) \tag{6.9}$$

Equ. 6.9 was used to determine the electron number density using the CR electron temperature for argon and krypton plasmas and the LTE electron temperature for xenon, in conjunction with the average ion fractions. The ionisation fraction for an argon discharge in the region of probe 1 is assumed to be 10% for $\dot{m} = 1.1 mgs^{-1}$ and 5% for $\dot{m} = 3.0 mgs^{-1}$. The energy of upper levels of singly ionised argon species is $\approx 20eV$ whilst the energy of the observed excited species is $\approx 13eV$; this results in the denominator of the exponential term $\chi(z,g) - \chi(z,q) - \chi(z+1,q) = -17.2eV$. The values of electron number density as a function of T_e are presented in Figs. 6.23 – 6.25 along with the reclassification of the HC plasma regime.

The internal plasma of a HC operating on argon propellant lies in the corona regime for all operating conditions(see Fig. 6.23). The HC internal plasma in the region of probe 1 lies in the CR regime for a krypton discharge for all mass flow rates and discharge currents. The xenon plasma shows the highest variability in electron temperature over the range of operating conditions investigated. In the region of probe 1 the plasma may conform to

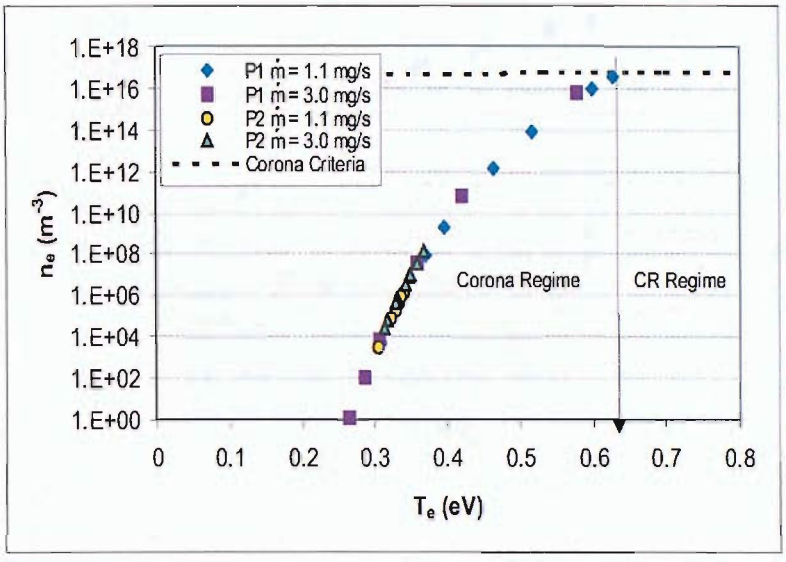

Figure 6.23: Average electron density as a function of electron temperature for argon propellant at probe 1 in geometry 1

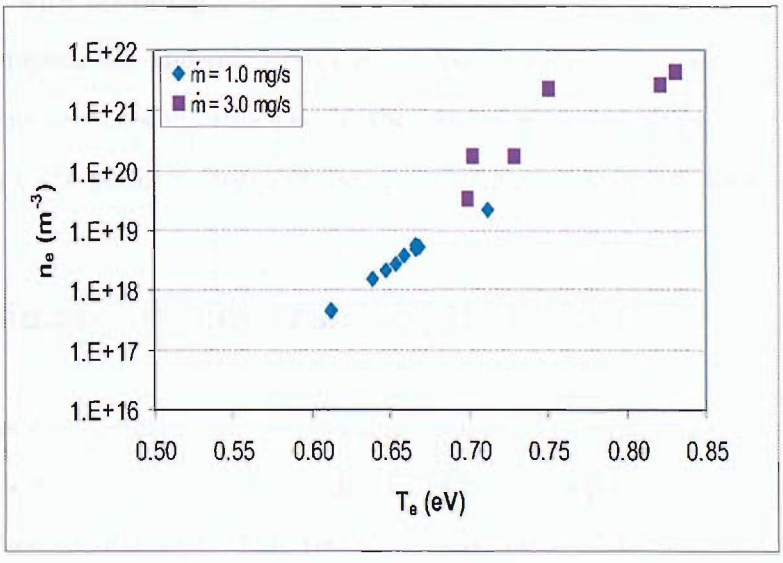

Figure 6.24: Average electron density as a function of electron temperature for krypton propellant at probe 1 in geometry 1

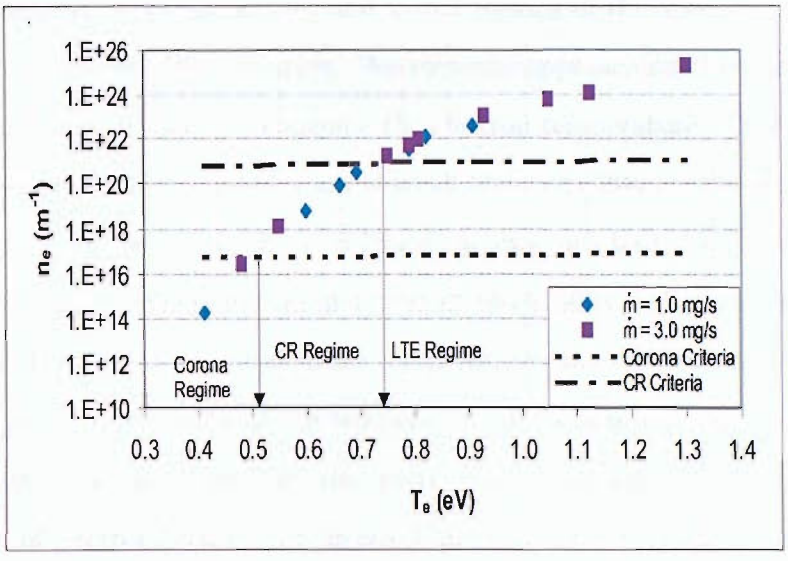

Figure 6.25: Average electron density as a function of electron temperature for xenon propellant at probe 1 in geometry 1

any of the three plasma models depending on the operating parameters. For $T_e \geq 0.75eV$ the internal plasma lies in the LTE regime, for $T_e \leq 0.52eV$ the internal plasma lies in the corona regime. In order to assess the characteristics of the internal plasma and how they vary with operating parameters the emphasis must be placed on determining the electron temperature and number density. The plasma regime to which the internal plasma conforms provides information on the general characteristics of the plasma only and must be used to perform more detailed calculations as has been done in this chapter.

6.5 Continuum Bremsstrahlung Radiation

The intensity of continuum radiation resulting from an electron decelerating in the field of a heavy particle may be used to determine the electron temperature of the plasma under investigation (see section 4.6). This technique was intended to provide an independent method of determining the electron temperature that could be used to verify the values obtained from line intensity ratio methods. However, this method requires the judicial identification of linear sections of log plots of intensity against wavelength. This is a highly subjective process. Also, the wavelength range available for the electron temperature

calculation is limited to the ultraviolet and visual regions of the spectrum that have not been distorted by discrete line radiation. Wavelengths approaching the infrared region of the spectrum can not be used to determine the electron temperature. This is because the wavelength range used for the calculation is small (typically 20nm), therefore $\Delta\lambda \rightarrow 0$ i.e $\lambda_1/\lambda_2 \sim 1$. As can be seen from Equ. 6.10 for the case of small $\Delta\lambda$ the expressions for the ratio of bremsstrahlung radiation and that of black body radiation (see section 6.6) are approximately equal. As a consequence temperature values determined in the range of $\lambda > 600nm$ provide an estimate of the temperature of the insert surface as this region is dominated by thermal emissions from the insert. The use of bremsstrahlung radiation in the calculation of electron temperature is also limited to use on high temperature plasmas only.

$$\begin{aligned} \ln\left(\frac{I_1}{I_2}\right) &= \frac{-hc}{kT_e}\left(\frac{1}{\lambda_1} - \frac{1}{\lambda_2}\right) \\ \ln\left(\frac{B_{\lambda 1}(T)}{B_{\lambda 2}(T)}\frac{\lambda_1^5}{\lambda_2^5}\right) &= \frac{-hc}{kT}\left(\frac{1}{\lambda_1} - \frac{1}{\lambda_2}\right) \end{aligned} \tag{6.10}$$

Initial calculations for the HC operating on argon propellant yield values of the electron

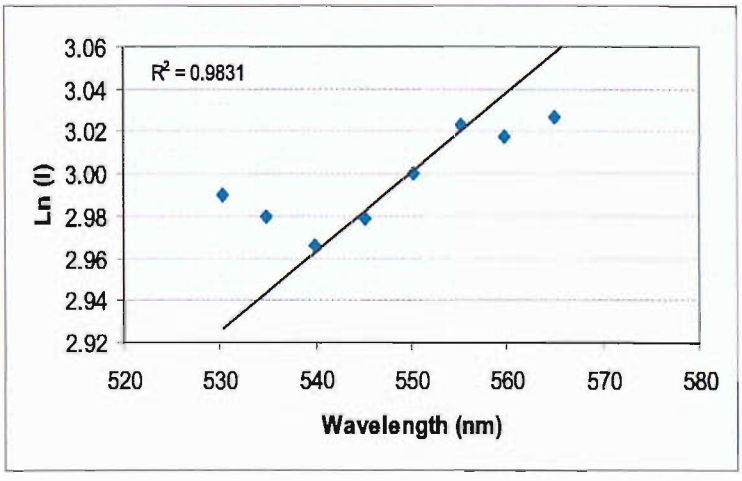

Figure 6.26: Identification of bremsstrahlung radiation for the case of argon propellant in geometry 1 at probe position 1, $\dot{m} = 1.1mgs^{-1}$, $I_A = 10.0A$

temperature that agree with the values determined using line intensity ratio methods. In the region of probe 1 bremsstrahlung radiation was observed in the wavelength range of $\lambda = 540 - 555nm$ (see Fig. 6.26) and the electron temperature obtained was $T_e = 0.491eV$

with a correlation coefficient of $R^2 = 0.894$ compared to an LTE value of $T_e = 0.426eV$ and the CR result of $T_e = 0.244eV$. In the region of probe 2 $T_e = 0.227eV$ with $R^2 = 0.923$ for $\lambda = 255 - 265nm$, the LTE $T_e = 0.201eV$ and CR $T_e = 0.337eV$; in both cases data were collected in geometry 1 with an anode current of $I_A = 10.0A$ and $\dot{m} = 1.1mgs^{-1}$.

6.6 Thermal Characterisation

6.6.1 Temperature Measurement Technique

Planck's distribution law states that a body at temperature T in degrees Kelvin emits radiation with a spectral distribution or intensity $B_\lambda(T)$ given by Equ. 6.11 [122].

$$B_\lambda(T) = \epsilon(\lambda, T)\frac{2hc}{\lambda^5(e^{\frac{hc}{\lambda kT}} - 1)} \tag{6.11}$$

Where λ is the wavelength, h is Plank's constant, k is Boltzmann's constant, c is the speed of light in vacuo and $\epsilon(\lambda, T)$ is the emissivity of the surface. Materials do not behave as perfect black–bodies that emit isotropic, homogeneous and unpolarised radiation. The emissivity is a correction function that is applied to account for this. For simplicity the insert surface is treated as a grey–body i.e. the emissivity is constant and therefore not a function of wavelength. Over a wavelength range of $600-900nm$ the emissivity of tungsten varies by 0.042 from 0.455 to 0.413 for $T = 1600K$ and by 0.045 from 0.452 to 0.407 for $T = 1800K$ [123]. This constitutes a change in emissivity of approximately 10% from the minimum to maximum wavelengths; this may influence the temperature determined using the two extreme wavelength by a maximum of 200^o. As an average temperature will be calculated using intensity wavelength pairs over the entire wavelength range this error will be considerably reduced. These values of emissivity are not for impregnated tungsten. There is no available data on the effect of impregnate materials on emissivity, therefore we assume that the thermal properties of the material do not deviate widely from the un-impregnated material. As $\lambda \longrightarrow 0$ the exponential term in Plank's law is much larger than 1, as a result Equ. 6.11 reduces to the following expression,

$$B_\lambda(T) = \epsilon(\lambda, T)\frac{2hc^2}{\lambda^5}\exp\left(\frac{-hc}{\lambda kT}\right) \tag{6.12}$$

The optical emission spectra recorded displayed an increase in the intensity of continuum radiation with increasing anode current for wavelengths in the near infra red region of the spectrum, as shown in Section 5.3.2. This increase in radiation is due to thermal emissions that arise as a consequence of the heating of the insert surface. The following assumptions have been made for the treatment of continuum radiation in order to calculate the insert surface temperature:

- The insert is a grey body.
- The insert surface and the internal plasma are considered as two systems at two different temperatures.
- The insert surface achieves thermal equilibrium i.e. is at constant temperature with respect to time.

The insert temperature was determined using the continuum data collected in the near infra red region of the spectrum. A polynomial curve of order 3 was fitted to continuum data for $\lambda > 500nm$. This enables a smooth curve to be produced and hence minimizes the influence of noise on the results obtained. The equation of this curve was used to calculate thermal radiation intensities for a given wavelength. These intensities and corresponding wavelengths were used to create the input data files (see appendix D) for the programme described in appendix C. The input files are a (392,2) array, i.e. 392 intensity wavelength pairs were used as input data. This was the number of data points recorded by the spectrograph over the wavelength range of interest. Therefore the intensity is calculated in wavelength intervals of $0.64nm$. The programme utilises an intensity ratio method, as shown by equation 6.13

$$T = \frac{\frac{hc}{k}\left(\frac{\lambda_1-\lambda_2}{\lambda_1\lambda_2}\right)}{ln\left(\frac{B_{\lambda 1}(T)}{B_{\lambda 2}(T)}\frac{\lambda_1^5}{\lambda_2^5}\right)} \tag{6.13}$$

The temperature is calculated for all possible combinations of intensity and wavelength over a wavelength range of $\lambda \approx 650nm$ to $\lambda \approx 900nm$. This results in the determination of 76636 temperature values. These values are averaged to produce an estimate of the insert surface temperature. The standard deviation calculated provides the error associated with the measurement and is shown as the error bars on the figures below. The standard deviations are small with typical values of $\sim 5\% - 10\%$.

The small standard deviations imply that the continuum intensity curve is characterised by one temperature and the emissivity is not a function of wavelength. The standard deviations are typically larger for lower anode currents. At lower anode currents more noise is observed on the spectra. This may be due to the stability of the discharge and/or the signal to noise ratio. These factors have a detrimental effect on the curve fit for the

continuum radiation resulting in a larger error for the temperature measurement. At higher anode currents ($I_A > 5A$) the noise on the signal disappears and the standard deviations are similar for all temperature values beyond this point.

6.6.2 Insert Temperature Results

The time taken for the discharge to stabilise and thermal equilibrium to be established was investigated under the operating conditions of $\dot{m} = 1.5mgs^{-1}$ and $I_A = 5.0A$ for an argon discharge. The process of recording spectra began immediately after the operating parameters were set, an integration time of 60s with one exposure was used and recording of subsequent spectra commenced as soon as the previous spectra had been saved, with the exception of $t = 320s$ and $t = 485s$. The discharge power values shown in Fig. 6.27 represent values taken at the beginning of each spectra recording. It can be seen that

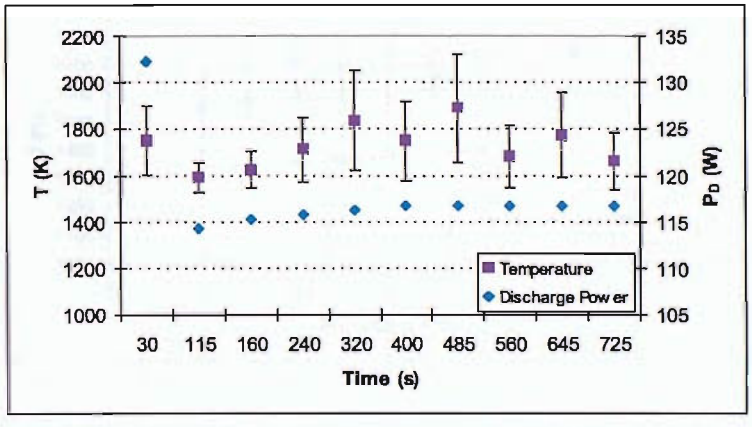

Figure 6.27: Argon Geometry 1: Insert temperature as a function of time and discharge power in the furthest upstream probe position (probe 3)

P_D requires a finite amount of time to stabilise on changing the operating parameters. It appears that the insert temperature is not highly dependent on the time spent under set conditions. Increases in temperature tend to coincide with increases in the discharge power caused by fluctuations in the keeper and anode voltages. There is little variation in the temperatures determined over a 13 minute period, with an average temperature of $T = 1691.9K$ and standard deviation of $\sigma_{sd} = 64.0K$. This implies that thermal equilibrium is rapidly established in under 60s of changing HC operating parameters.

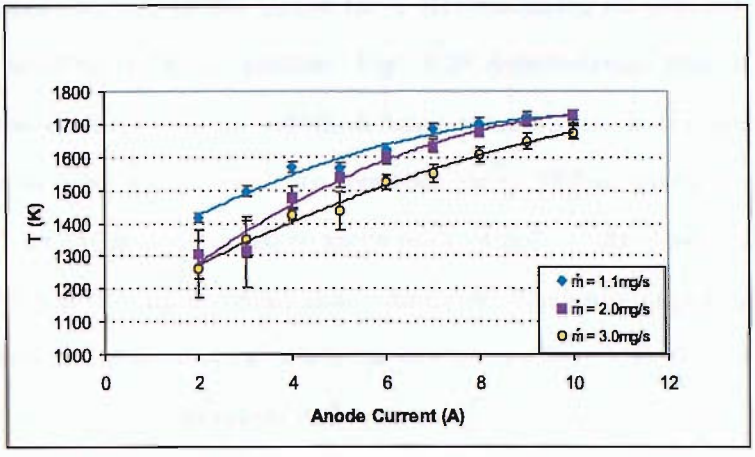

Figure 6.28: Argon Geometry 1: Insert temperature as a function of anode current for probe position 2

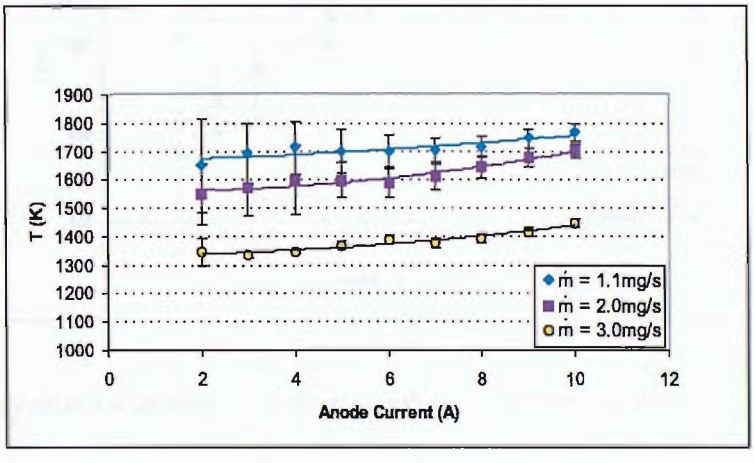

Figure 6.29: Argon Geometry 1: Insert temperature as a function of anode current for probe position 3

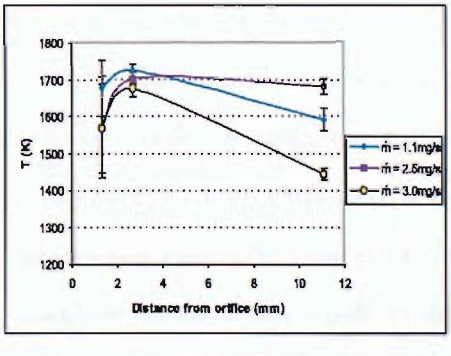

Figure 6.30: Insert temperature as a function of position for argon, geometry 1, $I_A = 10.0A$

The thermal characteristics of the insert for a HC operating on argon propellant varies dramatically depending on axial position. Fig. 6.28 demonstrates that when the HC tip is approached the dominant factor which dictates temperature is the anode current. At constant mass flow rate the temperature increases by $\sim 300^o$ at probe 2 as the current is increased from 2.0 to $10.0A$ compared to an increase of $\Delta T \sim 100^o$ observed at probe 3 (see Fig. 6.29). Moving upstream the mass flow rate becomes equally important in influencing temperature; there is a difference of $\sim 300^o$ as $\dot{m}$ changes from $1.1 - 3.0mgs^{-1}$ at constant current. At probe 2 the a temperature difference of $\Delta T \sim 150^o$ occurs for an anode current of $2.0A$ and $\Delta T \sim 50^o$ at $I_A = 10.0A$.

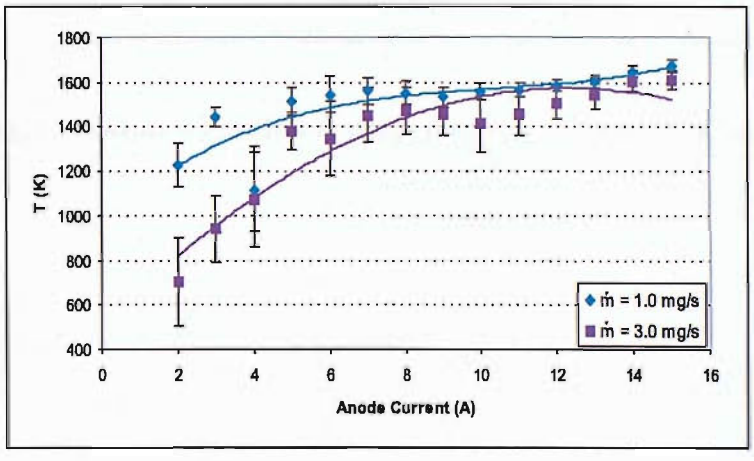

Figure 6.31: Krypton Geometry 1: Insert temperature as a function of anode current for probe position 1

Fig. 6.32 shows the dependence of insert temperature on current for geometry 2. Comparing these results with the temperatures determined in geometry 1, shown in Fig. 6.31 demonstrates that decreasing the separation between the keeper electrode and anode results in a decrease in temperature. For example, for a mass flow rate of $3.0mgs^{-1}$ temperatures of $T \approx 1400K$ and $T \approx 1600K$ are obtained for anode currents of $I_A = 5.0A$ and $I_A = 15.0A$ respectively compared to $T \approx 900K$ and $T \approx 1400K$ in geometry 2. Fig. 6.34 also demonstrates that decreasing electrode separation decreases the insert temperature. Reducing the keeper / anode separation may result in increased bombardment of the HC tip by ions due to an increase in the electric field. This increased ion bombardment will cause an increase in the temperature of the HC causing increased electron extraction,

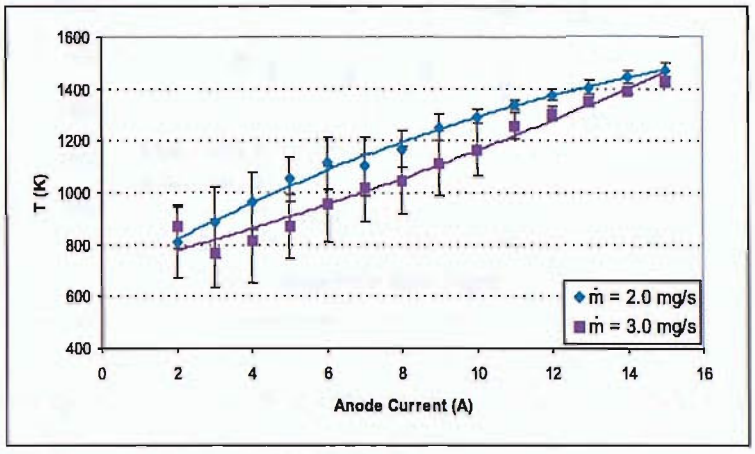

Figure 6.32: Krypton Geometry 2: Insert temperature as a function of anode current for probe position 1

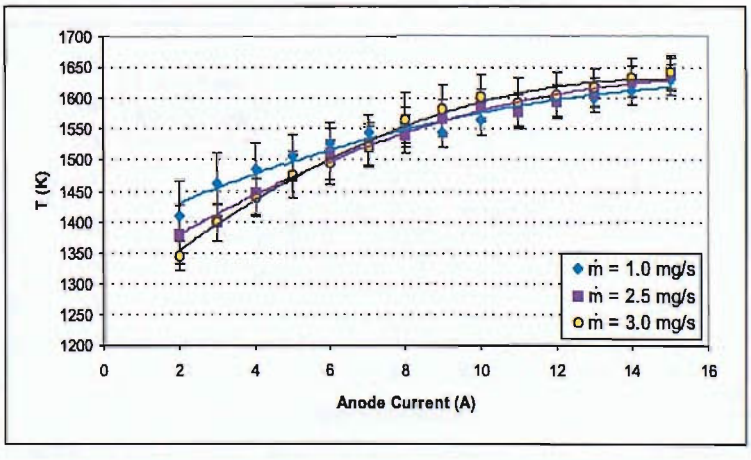

Figure 6.33: Krypton Geometry 1: Insert temperature as a function of anode current for probe position 3

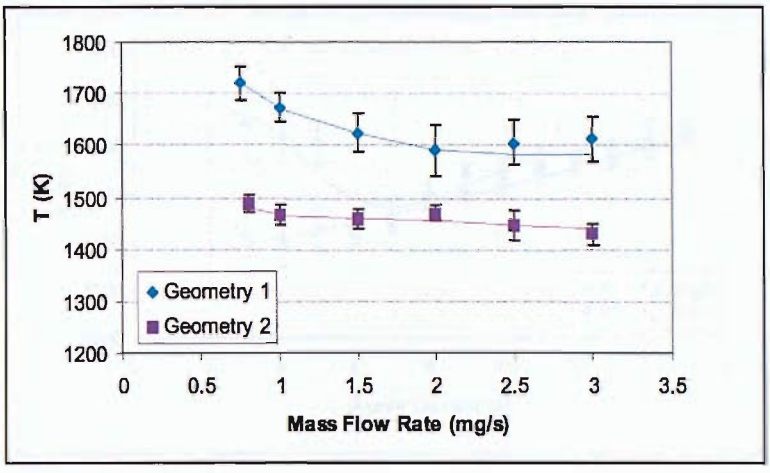

Figure 6.34: The influence of mass flow rate on temperature for geometries 1 and 2 in the probe 1 position with $I_A = 15A$ for krypton propellant

which may result in a decrease in the insert temperature.

When the atomic mass of the propellant gas is increased the dependence of temperature on $\dot{m}$ is reduced compared to the case of argon propellant. This is demonstrated by Fig. 6.33 for the HC operating on krypton, where $\Delta T \sim 50^o$ for a change in $\dot{m}$ of $1.0 - 3.0 mgs^{-1}$ compared to an increase in temperature of $\sim 200^o$ as current is increased from 2.0 to $10.0A$. Similar trends are observed for xenon.

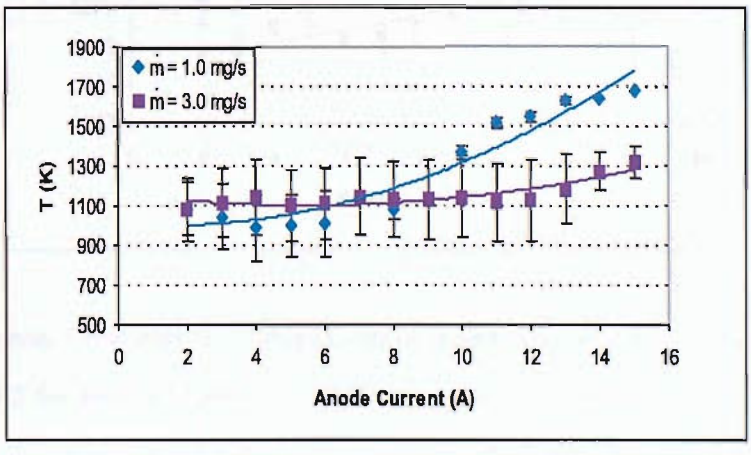

Figure 6.35: Xenon Geometry 1: Insert temperature as a function of anode current for the furthest downstream probe position (probe 1)

Fig. 6.37 compares the insert temperature probe 1, $1.3mm$ from the HC tip and probe

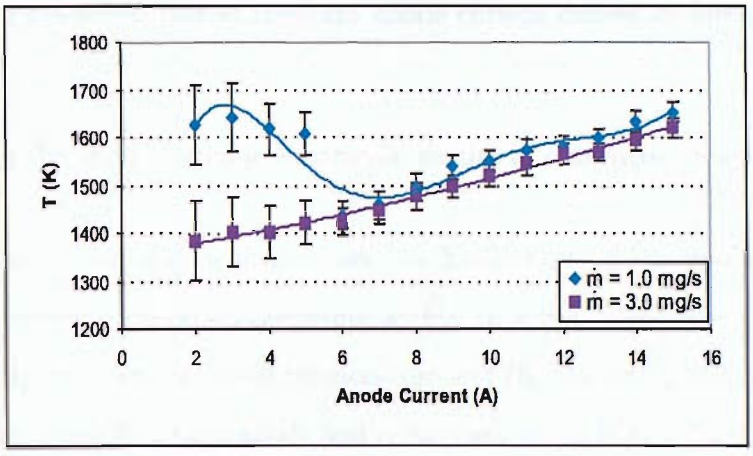

Figure 6.36: Xenon Geometry 1: Insert temperature as a function of anode current for the furthest upstream probe position (probe 3)

2, 2.7mm from the tip. The figure shows that between the two probe positions the insert temperature decreases by approximately 150° as the tip is approached. This is in agreement with the results obtained for argon propellant shown in Fig. 6.30.

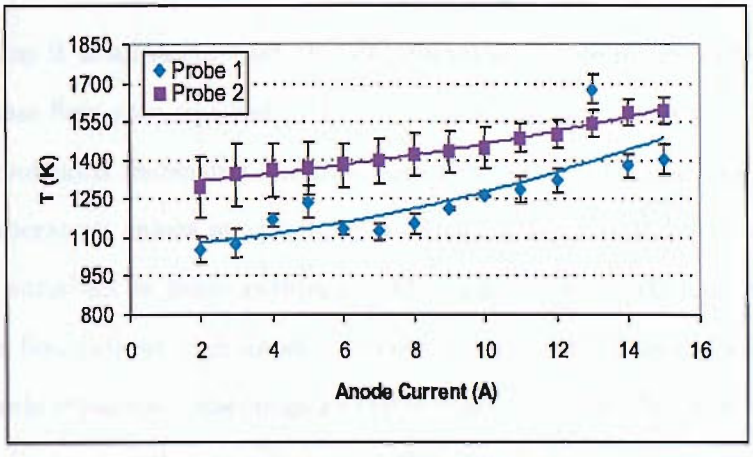

Figure 6.37: Xenon Geometry 2: Comparison of insert temperatures obtained from probe positions 1 and 2 for $\dot{m} = 1.5mgs^{-1}$

The following general trends are apparent from the results presented in figures 6.28–6.37:

- Increasing anode current at constant mass flow rate causes an increase in temperature.

- Decreasing mass flow rate at constant anode current causes an increase in temperature.
- Decreasing the anode/cathode separation results in a decrease in temperature.

The thermal balance equation stated in section 2.4.3 (Equ. 2.13) provides a crude description of the thermal processes occurring within HCs but offers no explanation of the direct relationship between the insert temperature and HC operating parameters including discharge current, mass flow rate, anode and orifice geometry. Equ. 6.14 describes laminar flow through a cylindrical tube. It has been stated that the gas temperature within the HC differs from the insert surface temperature by $10 - 20\%$, therefore the insert temperature is assumed to be approximately equal to the gas/discharge temperature [41]. Using this expression allows the insert temperature to be related to the mass flow rate, HC internal radius r, the pressure within the HC P_C and the propellant gas used.

$$P_C = \frac{\dot{m}}{\pi r^2}\left(\frac{RT}{\gamma m}\right)^{\frac{1}{2}} \tag{6.14}$$

From this relation it is apparent that the HC operating temperature is inversely proportional to the mass flow rate squared ($\sqrt{T} \propto 1/\dot{m}$) at constant pressure. However, under experimental conditions increasing the flow rate through the HC increases the pressure. Comparing temperature values at various mass flow rates shows that the relationship between the two variables is more complex. The temperature becomes less sensitive to changes in mass flow rate at high anode current and as the tip is approached. Decreasing the cathode/anode separation also negates the influence of mass flow rate on temperature (see Fig. 6.34). Increasing the atomic mass of the propellant gas used results in decreased sensitivity to changes in mass flow rates. The results show that complex processes occurring within the HC cause shifts in the influence of certain operating parameters on HC operating temperature. Equ. 6.14 does not consider a plasma flow but an idealised gas flow. Therefore, it cannot be expected to provide exact agreement with the experimental results obtained. The dependence of the insert temperature on mass flow rate depends on the axial position in question, the propellant, anode geometry and current.

The insert temperature shows a strong dependence on anode current under most con-

ditions. The relationship between temperature and increasing current is intuitive, one expects temperature to increase with increasing discharge current. Increasing discharge current increases the discharge power, which increases the energy to the plasma which is transferred to the HC insert. Increasing current increases the contribution of Joule heating as the plasma resistivity is proportional to temperature.

$$\rho_p = \rho_0(1 + \alpha\Delta T) \tag{6.15}$$

Where ρ_0 is the resistivity at some reference temperature and α is the temperature coefficient. The discharge current also influences the plasma potential, ($I_D \propto V_P$). The electric field adjacent to the HC wall is proportional to the square root of the plasma potential [39]. Therefore, increased current causes an increase in the electric field strength, as a consequence ions bombard the insert surface with increased energy thus causing more heating. However, this may be accompanied by increased electron extraction which may counteract this effect.

The weakest relation between temperature and current occurs at the furthest upstream position (probe 3) especially for argon propellant. As stated above increasing the discharge current increases the electric field strength causing ion bombardment to occur with increased energy. In the furthest downstream position ion densities may not be sufficient to cause an appreciable increase in temperature. This is supported by the observation of weak lines in optical emission spectra which provide an indication of the abundances of species. A gradient in the electric field may also exist, therefore the field strength that the ions are exposed to is reduced in the furthest upstream position, as a consequence the dependence of the insert temperature on the discharge current is reduced moving away from the HC tip.

6.7 Alternative Methods for Temperature Measurement

6.7.1 Wien's Law

Wien's displacement law (Equ. 6.16) predicts the wavelength λ_{max} at which maximum emission from a black body occurs [122]. This corresponds to the maximum emission

intensity dictated by the Planck formula.

$$T = \frac{2.898 \times 10^{-3}}{\lambda_{max}} \tag{6.16}$$

The use of Wien's law provides an alternative method for the calculation of the insert temperature and the values obtained can be used to verify the results presented in Section 6.6.2. In order to determine the characteristic temperature of the spectral distribution under investigation the wavelength at which maximum emission occurs must be found. To this end the intensity of thermal radiation described by Planck's formula which has the form of Equ. 6.17 is differentiated to locate the maximum.

$$B_\lambda(T) = \frac{a}{\lambda^5} \exp\left(\frac{-b}{\lambda}\right) \tag{6.17}$$

Where the coefficients a and b are dependent on the characteristics of the curve in question. By differentiating Equ. 6.17 we obtain the maximum.

$$B'_\lambda(T) = \frac{ab}{\lambda^7} \exp\left(\frac{-b}{\lambda}\right) - \frac{5a}{\lambda^6} \exp\left(\frac{-b}{\lambda}\right) \tag{6.18}$$

$$B'_\lambda(T) = 0 \longrightarrow \lambda_{max} = \frac{b}{5} \tag{6.19}$$

The expression for λ_{max} is for a true maximum provided that $B''_\lambda(T) < 0$ which is the case for all data used in the current investigation. The value of coefficient b may be found by taking the ratio of Equ. 6.17 at two different wavelengths.

$$b = \ln \frac{I_2 \lambda_2^5}{I_1 \lambda_1^5} \left(\frac{1}{\frac{1}{\lambda_1} - \frac{1}{\lambda_2}}\right) \tag{6.20}$$

Intensity wavelength pairs were taken over a wavelength range of $650 - 900nm$ in $50nm$ intervals. The intensity data were the same as that used for the calculations using the Planck formula. All possible combinations of these intensity wavelength pairs were used to calculate the value of the coefficient b resulting in 15 b values that were then averaged and used to determine λ_{max}. This wavelength value was then used to determine the insert temperature; the results are shown in Tables 6.8 – 6.10.

6.7.2 Identification of Thermal Emission from Logarithmic Plots

When attempting to identify regions of bremsstrahlung emission by selecting linear sections of log plots of intensity against wavelength, it was observed that if the wavelength ranges

selected were in the near infra red region of the spectrum the temperatures obtained were similar to those of the insert surface temperature. This implies that thermal emissions may be identified using the same method which isolates regions of bremsstrahlung radiation. By comparing Equs. 4.52 and 6.13 it is clear that the expressions are approximately equal if $\lambda_1 \approx \lambda_2$. Therefore the gradient of the log of intensity plotted against the inverse of the wavelength difference provides a value of the insert temperature. This provides an alternative independent method for the determination of the insert temperature. The results are presented in Figs. 6.41–6.45.

6.7.3 Comparison of Temperature Values

	$\dot{m}$		Argon			
	(mgs^{-1})	I_A (A)	λ_{max} (μm)	T_{Wien} (K)	T_{Planck} (K)	ΔT
P1	1.1	2.0	5.19999 ± 3.842	557 ± 361	1015 ± 581	460
G1		5.0	2.36740 ± 0.219	1224 ± 104	1129 ± 226	95
		10.0	1.71775 ± 0.0852	1687 ± 85	1676 ± 75	11
		15.0	1.70695 ± 0.0195	1698 ± 19	1693 ± 19	5
P1	1.1	2.0	1.84620 ± 0.231	1570 ± 226	1559 ± 196	11
G2		5.0	1.99384 ± 0.0602	1453 ± 44	1443 ± 39	10
		10.0	1.90709 ± 0.0284	1520 ± 22	1515 ± 22	5
		15.0	1.73893 ± 0.0263	1667 ± 25	1661 ± 24	5
	3.0	2.0	2.40952 ± 0.0769	1203 ± 41	1186 ± 33	17
		5.0	2.15108 ± 0.0941	1347 ± 62	1333 ± 52	14
		10.0	2.01607 ± 0.0561	1437 ± 40	1427 ± 35	10
		15.0	1.80255 ± 0.0253	1608 ± 22	1602 ± 22	6
P3	1.1	2.0	1.74508 ± 0.187	1661 ± 193	1651 ± 169	10
G1		5.0	1.69371 ± 0.120	1711 ± 125	1698 ± 110	12
		10.0	1.72092 ± 0.334	1684 ± 203	1765 ± 22	81
		15.0	1.69120 ± 0.0217	1714 ± 22	1708 ± 21	6
	3.0	2.0	2.13284 ± 0.0843	1359 ± 56	1345 ± 47	13
		5.0	2.10681 ± 0.0178	1376 ± 12	1370 ± 11	6
		10.0	2.00399 ± 0.0253	1446 ± 18	1445 ± 16	2
		15.0	1.77734 ± 0.0207	1631 ± 19	1626 ± 19	4

Table 6.8: Comparison of argon insert temperature results obtained using Wien's Law and Planck's formula

	$\dot{m}$		Krypton			
	(mgs^{-1})	I_A (A)	λ_{max} (μm)	T_{Wien} (K)	T_{Planck} (K)	ΔT
P1	1.0	2.0	2.12740 ± 0.579	1119 ± 206	1227 ± 99	108
G1		5.0	2.17387 ± 0.397	1333 ± 210	1512 ± 63	178
		10.0	1.86569 ± 0.0564	1553 ± 45	1558 ± 37	5
		15.0	1.73305 ± 0.0358	1672 ± 34	1673 ± 28	0.7
	3.0	2.0	2.36228 ± 1.735	816 ± 212	703 ± 200	112
		5.0	2.53409 ± 0.643	1347 ± 122	1381 ± 83	35
		10.0	2.22271 ± 0.435	1304 ± 213	1416 ± 129	112
		15.0	1.80337 ± 0.0623	1607 ± 53	1613 ± 44	6
P1	1.0	2.0	6.94475 ± 4.754	600 ± 344	868 ± 105	268
G2		5.0	3.30117 ± 0.601	901 ± 153	874 ± 174	27
		10.0	2.34845 ± 0.151	1234 ± 74	1257 ± 49	23
		15.0	1.96749 ± 0.0238	1473 ± 18	1467 ± 18	6
	3.0	2.0	4.65241 ± 1.807	698 ± 238	870 ± 85	173
		5.0	3.30812 ± 0.517	893 ± 131	869 ± 152	24
		10.0	2.73699 ± 0.605	1059 ± 189	1169 ± 101	111
		15.0	2.02351 ± 0.0230	1432 ± 16	1430 ± 16	2
P3	1.0	2.0	2.03768 ± 0.0938	1422 ± 68	1408 ± 58	14
G1		5.0	1.91159 ± 0.0480	1516 ± 38	1507 ± 34	9
		10.0	1.84330 ± 0.0319	1572 ± 27	1566 ± 26	6
		15.0	1.77024 ± 0.0283	1637 ± 26	1631 ± 25	6
	3.0	2.0	2.13930 ± 0.0433	1355 ± 28	1345 ± 24	10
		5.0	1.95073 ± 0.0551	1486 ± 42	1476 ± 38	9
		10.0	1.79789 ± 0.0420	1612 ± 37	1604 ± 35	8
		15.0	1.75849 ± 0.0336	1648 ± 31	1642 ± 29	6

Table 6.9: Comparison of krypton insert temperature results obtained using Wien's Law and Planck's formula

	$\dot{m}$		Xenon			
	(mgs^{-1})	I_A (A)	λ_{max} (μm)	T_{Wien} (K)	T_{Planck} (K)	ΔT
P1	1.0	2.0	2.97455 ± 0.795	974 ± 205	1083 ± 137	108
G1		5.0	3.71181 ± 1.773	781 ± 278	997 ± 157	217
		10.0	2.13774 ± 0.107	13556 ± 63	1367 ± 50	11
		15.0	1.72205 ± 0.0191	1683 ± 19	1680 ± 17	3
	3.0	2.0	3.40685 ± 1.575	851 ± 288	1079 ± 157	228
		5.0	3.45233 ± 1.778	839 ± 316	1100 ± 179	261
		10.0	3.37826 ± 1.828	858 ± 344	1142 ± 204	284
		15.0	2.25487 ± 0.200	1285 ± 102	1312 ± 79	27
P1	1.0	2.0	3.00316 ± 0.317	965 ± 97	940 ± 127	25
G2		5.0	2.17907 ± 0.277	1330 ± 208	1288 ± 142	41
		10.0	2.00070 ± 0.120	1448 ± 92	1422 ± 67	26
		15.0	1.61468 ± 0.0606	1795 ± 65	1787 ± 65	8
	3.0	2.0	2.27621 ± 0.315	1273 ± 213	1230 ± 248	43
		5.0	2.07169 ± 0.338	1399 ± 271	1373 ± 219	25
		10.0	2.00717 ± 0.152	1444 ± 117	1417 ± 91	27
		15.0	1.86087 ± 0.128	1557 ± 115	1526 ± 82	31
P3	1.0	2.0	1.86938 ± 0.161	1550 ± 143	1537 ± 125	13
G1		5.0	1.85244 ± 0.100	1564 ± 87	1552 ± 76	12
		10.0	1.87251 ± 0.0265	1548 ± 22	1543 ± 21	5
		15.0	1.75001 ± 0.0255	1656 ± 24	1651 ± 23	5
	3.0	2.0	2.06887 ± 0.134	1401 ± 98	1385 ± 83	16
		5.0	2.02273 ± 0.0719	1433 ± 51	1422 ± 45	11
		10.0	1.89920 ± 0.0295	1526 ± 23	1520 ± 22	6
		15.0	1.78245 ± 0.0237	1626 ± 21	1621 ± 21	5

Table 6.10: Comparison of xenon insert temperature results obtained using Wien's Law and Planck's formula

The insert temperatures calculated using Wien's law shows good agreement with that determined using Planck's formula. The difference in the temperature values obtained using these two techniques ΔT is not highly dependent on mass flow rate or anode geometry, ΔT generally decreases with increasing anode current. The data shown in tables 6.8 – 6.10 are graphically represented in Fig. 6.41 – 6.45.

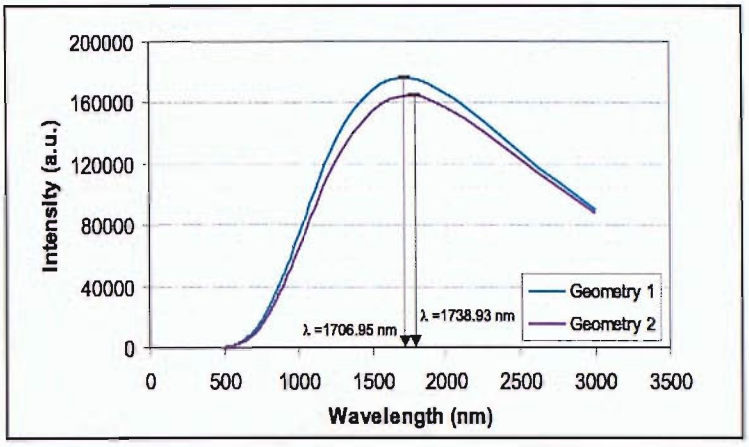

Figure 6.38: Probe 1, argon spectral distribution curve for $I_A = 15.0A$ and $\dot{m} = 1.1mgs^{-1}$

Figs. 6.38 – 6.40 show the theoretical spectral distribution for argon, krypton and xenon plasmas respectively. The spectral distributions were calculated using Equ. 6.17 and the values for the coefficients a and b determined for the temperature calculations. As expected, higher temperature plasmas produce higher intensity thermal radiation as shown in Fig. 6.38. Increasing mass flow rate causes an increase in thermal emissions.

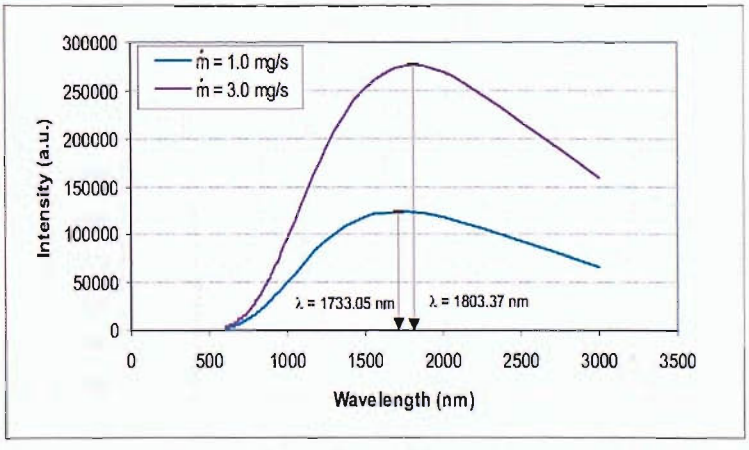

Figure 6.39: Krypton spectral distribution curve for probe 1 in geometry 1 with $I_A = 15.0A$

For comparison the insert temperature determined using the logarithmic plot method for $I_A = 10.0A$ has been included in Figs. 6.41 – 6.45. Data were collected from the following wavelength ranges: $\lambda = 875 - 901nm$ with $R^2 = 0.977$ for argon with $\dot{m} = 1.1mgs^{-1}$, $\lambda = 690 - 705nm$ with $R^2 = 0.901$ for $\dot{m} = 1.0mgs^{-1}$ and $\lambda = 680 - 705nm$ with

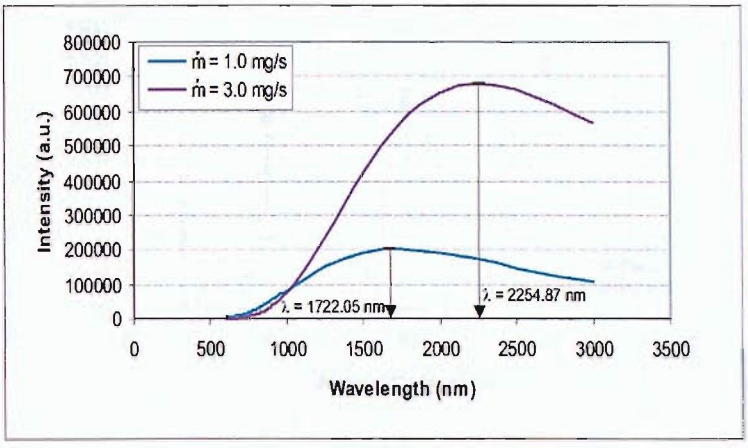

Figure 6.40: Xenon spectral distribution curve for probe 1 in geometry 1 with $I_A = 15.0A$

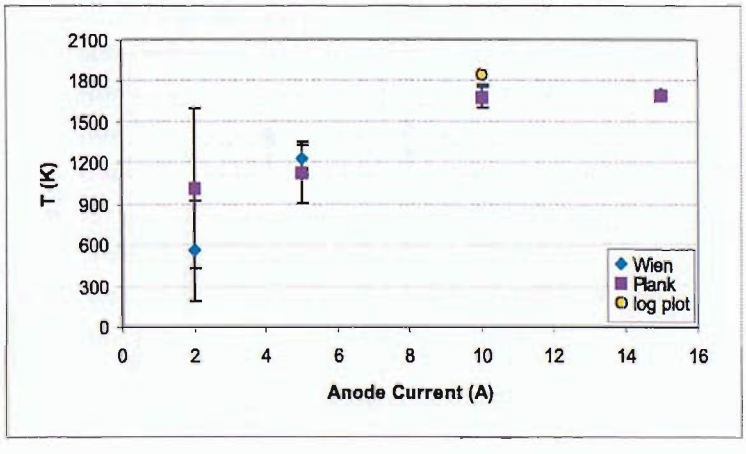

Figure 6.41: Comparison of temperature results obtained using different techniques for argon propellant $\dot{m} = 1.1mgs^{-1}$ at probe 1 and geometry 1

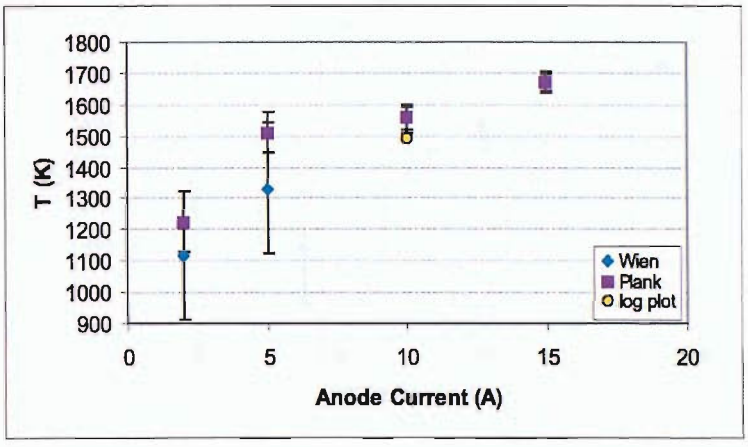

Figure 6.42: Comparison of temperature results obtained using different techniques for krypton propellant $\dot{m} = 1.0mgs^{-1}$ at probe 1 and geometry 1

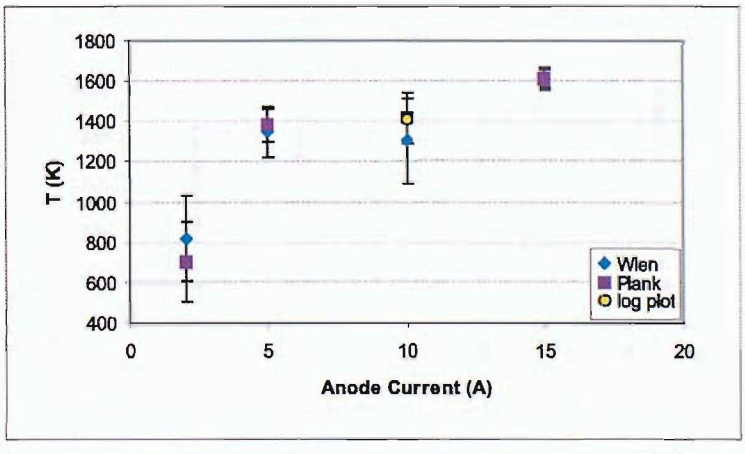

Figure 6.43: Comparison of temperature results obtained using different techniques for krypton propellant $\dot{m} = 3.0mgs^{-1}$ at probe 1 and geometry 1

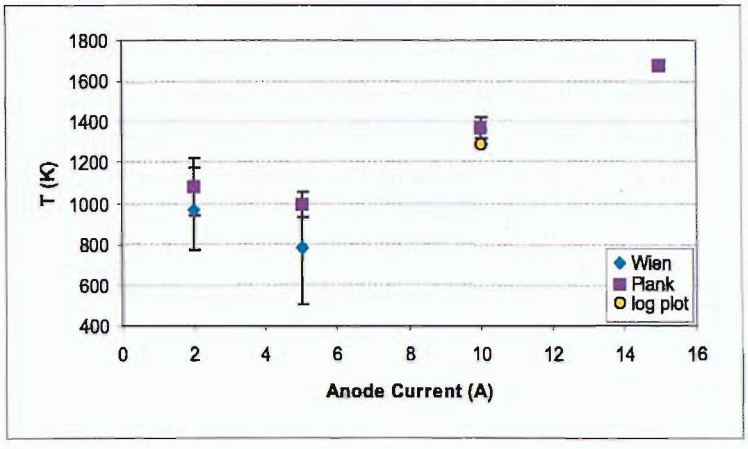

Figure 6.44: Comparison of temperature results obtained using different techniques for xenon propellant $\dot{m} = 1.0mgs^{-1}$ at probe 1 and geometry 1

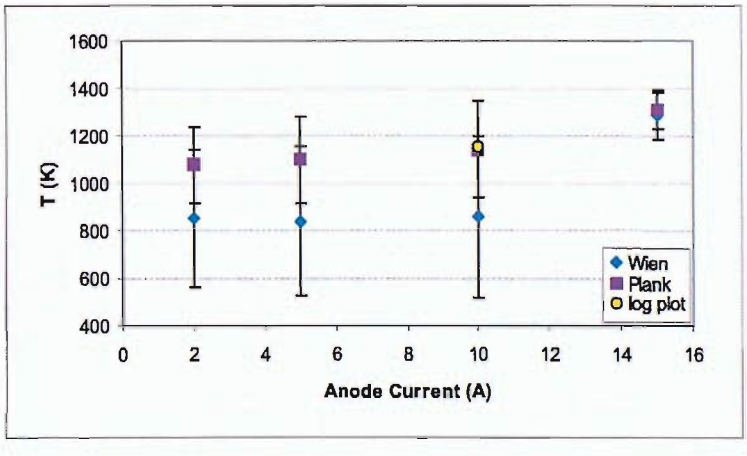

Figure 6.45: Comparison of temperature results obtained using different techniques for xenon propellant $\dot{m} = 3.0mgs^{-1}$ at probe 1 and geometry 1

$R^2 = 0.878$ for $\dot{m} = 3.0mgs^{-1}$ for krypton propellant, $\lambda = 565 - 555nm$ with $R^2 = 0.996$ for $\dot{m} = 1.0mgs^{-1}$ and $\lambda = 570 - 565nm$ with $R^2 = 0.966$ for $\dot{m} = 3.0mgs^{-1}$ for xenon propellant. All methods for the determination of insert temperature show good agreement.

Chapter 7

Discussion

7.1 Comparisons of Optical Emission Spectra from Previous Investigations

The optical emission spectra recorded in different investigations show differences in regions of activity. The spectra obtained in Ref. [2] from an external vantage point shows intense discrete lines in the visual region of the spectrum with no highly defined high intensity spectral lines recorded for wavelengths shorter than $\lambda \sim 400nm$. In contrast the spectra obtained in Ref. [3] from the rear of the HC shows discrete lines of similar intensities in the UV and visual regions; neither investigation collected spectra extending to the infra red region of the spectrum. On comparing the spectra of Fig. 7.1 with that of Fig. 7.2 it is evident that the plasma produced in the insert region does not produce intense spectral lines in the visual region of the spectrum. Thus the interactions responsible for these lines must occur within the orifice and/or the region between the HC and electrodes. The spectrum shown in Fig. 7.1 also shows discrete lines due to transitions of contaminant species such as barium, aluminum and oxygen. Barium lines were identified tentatively in Ref. [2]. The species Ba II $\lambda = 455.403nm$ is a strong line with relative intensity 9300 and was possibly observed in all discharges; Ba II $\lambda = 426.795nm$ is weak line with a relative intensity of 8 observed only for the HC operating on xenon propellant. Malik observed species Ba II $\lambda = 192.47nm$, Al I $\lambda = 237.33nm$, O II $\lambda = 253.03nm$. The

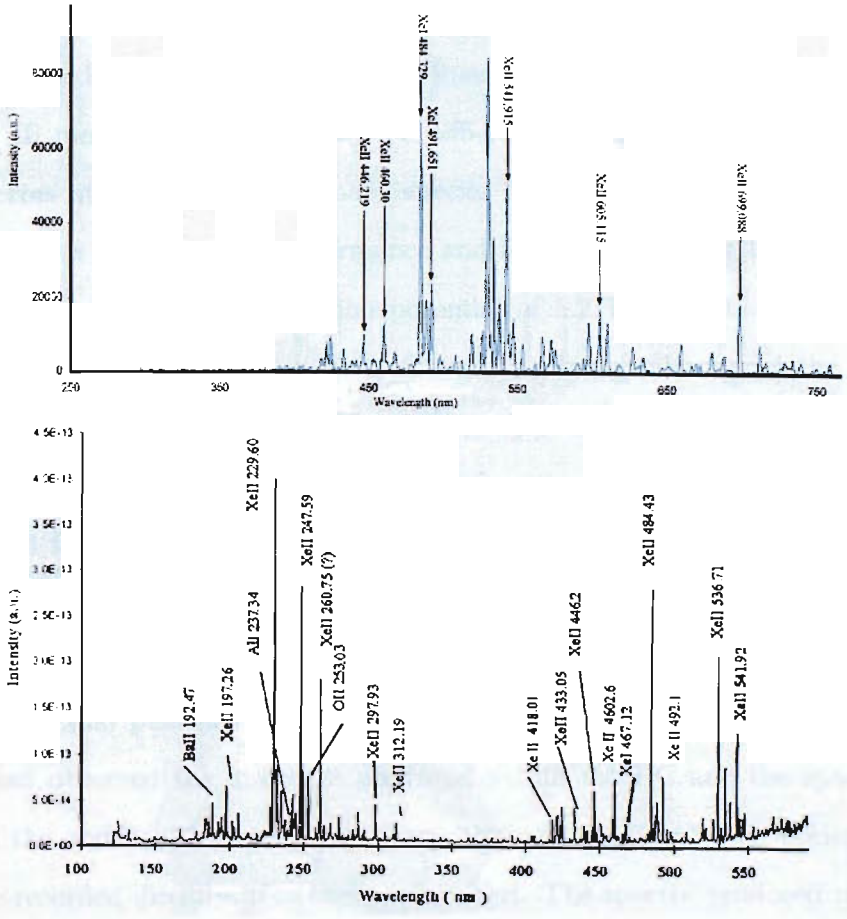

Figure 7.1: Comparison of the spectra recorded by Rudwan with $\dot{m} = 1.0mgs^{-1}$, $I_D = 5.0A$ (top)[2] and Malik (bottom)[3]

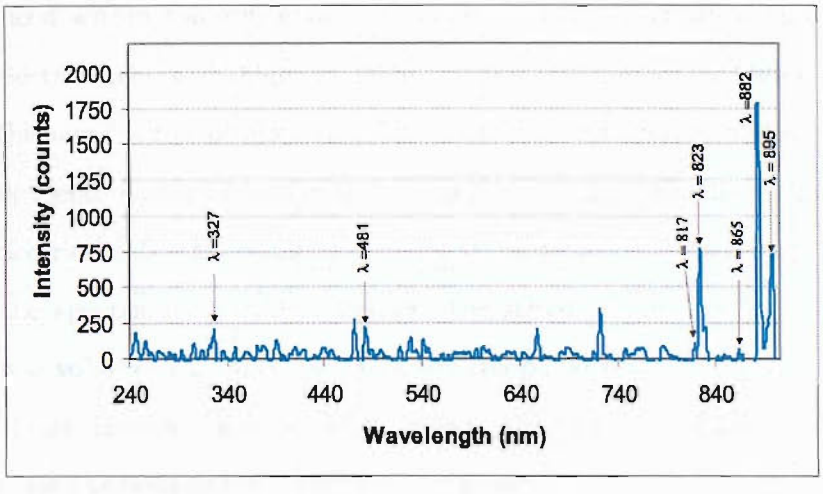

Figure 7.2: Xenon spectra from the current investigation, furthest downstream position in geometry 1 for $\dot{m} = 1.0mgs^{-1}$ and $I_A = 2.0A$, corrected for continuum radiation.

spectral lines of these transitions were outside of the spectral range of this investigation and that performed by Rudwan [2], also the lines listed have low relative intensities of the order of 10 meaning that they may be difficult to identify due to signal to noise issues. In terms of observed contaminant species barium is the element of interest as its concentration is linked to HC performance and life. The fact that barium is released from the insert and has a low ionisation potential of $5.21V$ suggests that the element and its ions may be expected to appear in spectra in a higher abundance than recorded; no spectral lines due to contaminants were positively identified in this study. This may be due to barium emitting strongly in the visual region of spectrum where lines could not be resolved to the accuracy required to allow identification. Comparing the spectra recorded from T6 HCs at different vantage points with differing experimental facilities shows that the resulting spectra are dependent on the plasma under observation. Malik observed the internal plasma through a neutral column of xenon gas at the HC's rear, whilst Rudwan observed the discharge produced within the HC and the space between the HC and the anode. This study represents the only occasion when optical emission spectra were recorded directly from the insert region. The spectra produced in each case is different; factors such as vacuum chamber pressure may also influence the appearance of resulting spectra. Most importantly the comparison of these spectra shows that the plasma created in the insert differs significantly from the plasma in the orifice region. The plasma produced within the orifice and the inter electrode space displays an abundance of discrete spectral lines with high intensities in the UV and visual range that are not observed to the same degree of intensity when observing the internal plasma alone. There is considerable electron acceleration within the orifice and inter electrode space due to the presence of electric fields, this results in enhanced excitation and ionisation. The volume from which the spectra is recorded influences the signal to noise ratio. Data has been collected from a volume of $2.7mm^3$ in this study compared to a volume of $\sim 63mm^3$ used in Refs. [2, 3], therefore we may expect to observe spectral lines of lower intensity under similar integration periods in the current investigation.

There are no experimental spectra available for comparison with the HC internal plasma in the near infrared region of the spectrum. Theoretical spectra determined using the

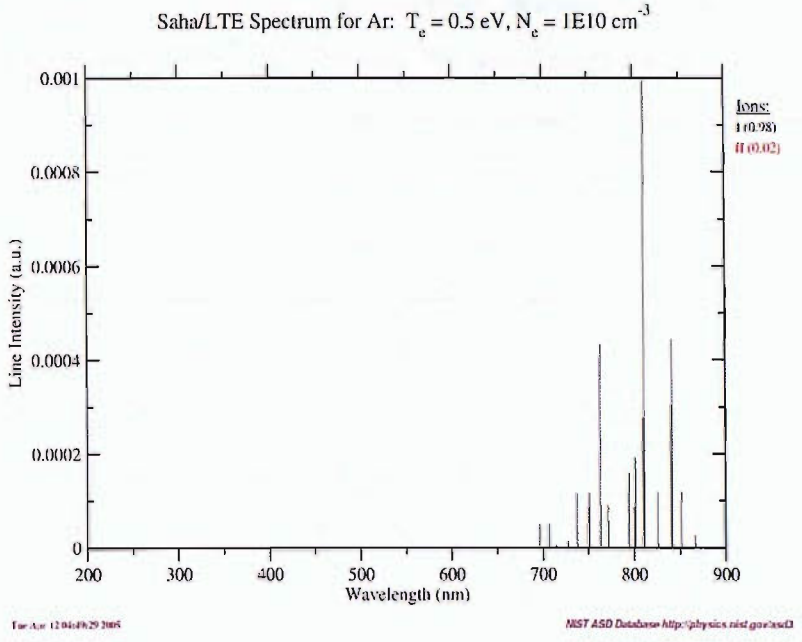

Figure 7.3: Theoretical argon spectra

Saha LTE equilibrium model, accepted transition probabilities and relative intensities are provided by the NIST database [114]. The spectra for an argon plasma with plasma parameters typical of those found in this investigation i.e. $T_e = 0.5eV$ show good agreement with the spectrum shown in Fig. 5.17. The relative intensities of all observed lines are comparable and both spectra are dominated by the transitions of neutral species with $\lambda > 650nm$. For example the spectral line present at $\lambda = 811.5311nm$ is the most intense for both experimental and theoretical spectra and in both spectra a pair of lines of equal intensity occur at $\lambda \approx 700nm$. In fact all of the observed spectral lines are mirrored in the theoretical spectrum. For the case of the spectrum shown in Fig. 7.3 discrete lines due to neutral transitions account for 98% of the spectral lines with singly ionised species responsible for the remaining 2% of lines.

7.2 Plasma Parameters and the Active Region Theory

The optical emission spectra recorded at different axial positions show different characteristics. From the flange to half way along the insert the propellant may be characterised as a hot gas; only weak spectral lines were observed 11.1mm from the orifice at probe position

3. As the tip is approached the insert temperature increases and electron extraction increases causing increased interactions between the heavy particles and electrons but not at sufficient levels to cause high degrees of ionisation as shown by the ion fractions determined in Chapter 6. On entering the orifice the plasma is restricted within a volume of radius a quarter that of the insert. In this region plasma density increases causing increased resistive heating resulting in a more energetic plasma with rapid collisions occurring between electrons and heavy particles. This results in increased ionisation and a plasma which is dominated by the spectral lines of ionised species and emissions in the UV and visual regions of the spectrum. The plasma then expands into the chamfered region and is extracted (electrons are accelerated) by the presence of the electric field of the keeper electrode.

The results obtained from this investigation imply that the real "ion production zone" alluded to by Siegfried in Ref. [39] is actually located within the HC orifice and not in the insert region adjacent to the orifice. The results obtained in this investigation for an argon discharge show strong gradients in the axial direction for electron temperature and number density. For example, a decrease of $\sim 0.2eV$ occurs for T_e and a decrease of six orders of magnitude in n_e is observed over a distance of $1.4mm$ from probe 1 to probe 2 (see sections 6.3 and 6.4). Despite this rapid increase in electron density as the HC tip is approached the spectra recorded are dominated by neutral line species. The ion fractions calculated for xenon and krypton plasmas show that a maximum ion fraction of $\sim 20\%$ and $\sim 15\%$ respectively may be achieved at low mass flow rates ($\dot{m} = 1.0mgs^{-1}$), as shown in section 6.4. Therefore, more than 80% of ions produced by the internal plasma discharge are generated within the orifice and the keeper region.

The only other experimental investigations performed on the T6 HC operating on inert gas propellants that utilised emission spectroscopy were carried out by Malik et. al. and Rudwan [3, 2]. Although the spectra that were recorded show differences (discussed in the previous section) the plasma parameters calculated from them show good agreement. Malik calculated an electron temperature of $T_e = 1.1eV$ using the ratio of bremsstrahlung radiation for a xenon discharge with $\dot{m} = 1.27mgs^{-1}$ and $n_e \sim 10^{14}cm^{-3}$. Rudwan

completed an extensive study on the HC internal plasma using a variety of inert gas propellants; the results obtained for a xenon discharge produced $T_e \approx 1eV$ and $n_e \approx 1 \times 10^{16} cm^{-3}$ for $\dot{m} = 1 - 1.6 mgs^{-1}$. The plasma parameter results are summarised in Table 7.1. Increasing the mass flow rate of the propellant gas causes an increase in T_e for argon and krypton, although no clear trend exists between T_e and atomic mass.

Table 7.1 compares the results presented in Ref. [2] and those obtained in this investigation. The table shows the electron temperature calculated using the CR Boltzmann plot method in column 5 and the electron number density was determined using the LTE Saha equation and the average ionisation fraction determined in section 6.4; the complete results are presented in Chapter 6. The electron number densities determined by Rudwan are orders of magnitude greater that calculated in this investigation. For the HC operating on xenon propellant n_e is two orders of magnitude greater than the value obtained by Malik. Theoretical calculations performed for the neutraliser of NASA's Solar Electric Propulsion Readiness Application (NSTAR) ion thruster showed that a third of electrons contributing to the total discharge current are generated by ionisation in the orifice [69]. But this does not account for the large differences in n_e obtained from the different studies. The high electron densities achieved by Rudwan may be explained by the fact that a HC with an enclosed keeper was used. It has been stated that the use of an enclosed keeper increases electron emission by up to 70% [25]. By reducing Rudwan's n_e value by 70% and reducing it further by a third we obtain n_e corrected for increased electron production due the enclosed keeper and orifice production. This allows direct comparison with the results found in this investigation for an open keeper configuration and compensates for the fact that the plasma within orifice is outside of the field of view of the optical probe, therefore orifice processes cannot be observed. For the case of xenon a revised value of $n_e = 5.41 \times 10^{15} cm^{-3}$ is obtained that compares well with $n_e = 3.73 \times 10^{15} cm^{-3}$. Decreasing the atomic mass of the propellant gas results in an increase in the difference between the electron densities determined by Rudwan and those of the current investigation. For a xenon discharge the difference between the n_e values is 1 order of magnitude; this increases to 3 orders of magnitude for krypton and 8 for argon.

		Rudwan Plasma Parameters		Current Investigation	
Propellant	$\dot{m}$ (mgs^{-1})	T_e (eV)	n_e (cm^{-3})	T_e (eV)	n_e (cm^{-3})
Argon	1.0	1.12 ± 0.05	3.10×10^{14}	0.465 ± 0.0017	1.61×10^{6}
	2.0	1.38 ± 0.05	3.62×10^{17}	-	-
Krypton	1.0	1.19 ± 0.14	4.20×10^{15}	0.665 ± 0.018	5.46×10^{12}
	2.1	1.31 ± 0.14	2.05×10^{17}	-	-
Xenon	1.0	1.05 ± 0.17	1.38×10^{16}	0.788 ± 0.024	3.73×10^{15}
	1.56	0.954 ± 0.19	1.09×10^{16}	-	-

Table 7.1: Summary of plasma parameter results obtained for a T6 HC with enclosed keeper in plume mode with $I_A = 5A$ [2] compared to results of the current investigation, argon results have $\dot{m} = 1.1mgs^{-1}$ for the current investigation.

Table 7.1 shows that the electron density decreases with decreasing atomic mass for $\dot{m} = 1.0mgs^{-1}$. The emission mechanism for primary electrons, field enhanced thermionic emission is independent of atomic mass (see Equ. 2.2). The emission of secondary electrons may be responsible for variations in electron number densities with changing propellant gas. The ionisation potential of the gas increases with decreasing atomic mass and the ionisation cross section is reduced. Therefore, the ease with which electrons may be liberated from atoms is reduced. As a consequence ionisation in the bulk plasma may decrease resulting in an overall reduction in electron density. The dependence of n_e on the propellant gas is highlighted when orifice processes are not observed as is the case with this investigation. There is a decrease in electron density of 9 orders of magnitude from xenon to argon discharges compared to 2 orders of magnitude observed for the results of Rudwan. This implies that the length of the active region decreases with decreasing mass of the propellant gas and as this occurs orifice and inter electrode processes become more significant.

As with the electron number density the difference between T_e determined in this investigation and that of Ref. [2] increases with decreasing atomic mass. The observed trends of the electron temperature results will be discussed in detail in section 7.4.

7.3 Comparisons with Theoretical Investigations

The model developed by Siegfried states the energy balance in the active region [39]. The rate of energy input to the plasma from primary electrons is balanced by energy losses from ions leaving the active region and convection due to the loss of Maxwellian electrons and ions (see Equ. 7.1).

$$V_p j_e A s = \chi(z,g) j_i A_s + \frac{5kT_e}{2e}(j_e + j_i)A_s \tag{7.1}$$

Where V_p is the plasma potential, $\chi(z,g)$ is the first ionisation potential, j_e is the electron current density due to field enhanced thermionic emission with an effective work function of $\phi_{eff} = 2.1eV$ as stated in Equ. 2.2, A_s is the total surface area of ion production, and j_i is the ion current density determined using the Bohm criterion (see Equ. 7.2).

$$j_i = en_e \left(\frac{kT_e}{m_i}\right)^{\frac{1}{2}} \tag{7.2}$$

A model was later developed by Salhi from first principles; unlike previous models there was no reliance on empirical formulae [124]. An expression for the electric field at the insert surface was obtained from a double sheath analysis governed by Poisson's equation for a charge density ρ^c ($\nabla^2 V = \frac{-\rho^c}{\epsilon_0}$). An expression for the electric field E is obtained in terms of the solution to Poisson's equation ε_c, in the presence of a double sheath.

$$E = \frac{\varepsilon_c kT_e}{e\lambda_D} \tag{7.3}$$

$$\varepsilon_c = \left\{ 4\nu\eta_o \left[\left(1 + \frac{\eta_c}{\eta_o}\right)^{\frac{1}{2}} - 1 \right] - 8J_b\eta_c^2 + 2\exp -\eta_c - 2 \right\}^{\frac{1}{2}} \tag{7.4}$$

Where the dimensionless parameters ν, η_o, η_c and J_b are the ion to electron number density ratio, normalised ion energy at sheath edge, normalised fall voltage and normalised thermionic emission current density respectively.

$$\eta_c = \frac{eV_p}{kT_e} \tag{7.5}$$

$$\eta_o = \frac{1 + 2\eta_c J_b}{2(1 - J_b)} \tag{7.6}$$

$$\nu = 1 + 2\eta_c J_b \tag{7.7}$$

$$J_b = \frac{j_e}{en_e \left(\frac{kT_e}{m_e}\right)^{\frac{1}{2}} (2\eta_c)^{\frac{3}{2}}} \tag{7.8}$$

Input Plasma Parameters				Predicted Plasma Parameters				
Propellant	T_e (eV)	T (K)	n_e (m^{-3})	j_e (Am^{-2})	j_i (Am^{-2})	I_D (A)	V_p (V)	E (Vm^{-1})
Krypton	0.665	1512	5.46×10^{18}	2.73×10^5	7.652×10^2	3.44	1.71	3.50×10^5
Xenon	0.98	1482	6.99×10^{20}	1.89×10^5	9.50×10^4	3.57	9.77	9.25×10^6

Table 7.2: Theoretical calculations with input data for a krypton discharge, $\dot{m} = 1.0mgs^{-1}$ and $I_D = 5.5A$ (top) compared with a xenon discharge in spot mode, $\dot{m} = 3.29mgs^{-1}$ [2]

Equs. 7.1 – 7.8 were used to determine plasma parameters (electron and ion density, discharge current, plasma potential and electric field strength) using experimentally determined parameters i.e. electron temperature and density and the insert surface temperature. The results are shown in Table 7.2 for a krypton discharge with input parameters determined in this investigation compared to the results obtained for a xenon plasma stated in Ref. [2]. The length of the ion production zone and the electron emission length L_e are assumed to be equal with $L_e = 2mm$. The discharge current is determined from the contribution of the ion and primary electron current $I_D = A_s(j_e+j_i)$. There is an $\approx 2A$ difference between the calculated discharge current shown in Table 7.2 and the experimental value. Taking the percentage of the calculated discharge current with the experimental value of $5.5A$ we find that electrons released by volume ionisation in the bulk plasma contribute $\approx 37\%$ to the overall current. The value of the electron current density, $j_e = 2.73 \times 10^5$ is well within the range of 2×10^5 to $8 \times 10^5 Am^2$ stated in literature [66]. When space averaged plasma parameters are used as inputs a higher ion current, plasma potential and electric field are observed. The difference is due to the use of an electron temperature that is $0.3eV$ greater than the localised T_e value determined in the current investigation and an electron density that is two orders of magnitude greater. These calculations show that the plasma parameters determined from experimental data are consistent with the existing theory for HC operation.

The results obtained for a xenon discharge compare well to the theoretical results of Salhi for a HC with a discharge current of $5A$, $\dot{m} = 92mAequiv$ $(0.125mgs^{-1})$ and a surface workfunction of $2.25eV$ [124]. An electron temperature of $T_e = 0.7eV$ was obtained with $n_e \approx 10^{20}m^{-3}$ and $V_p = 9V$. These results were obtained for a HC with internal diameter of

$4mm$ and orifice diameter of $0.76mm$. Calculations were not performed for a HC operating on krypton propellant, therefore direct comparisons cannot be made.

7.4 Discussion of Observed Plasma Parameter Trends

The following observations may be made from the experimental results obtained in this study:

- The electron temperature increases with increasing atomic mass of the propellant gas.
- The electron temperature increases with increasing electrode separation.
- The electron temperature decreases moving upstream.
- The electron temperature is not dependent on discharge power or mass flow rate.

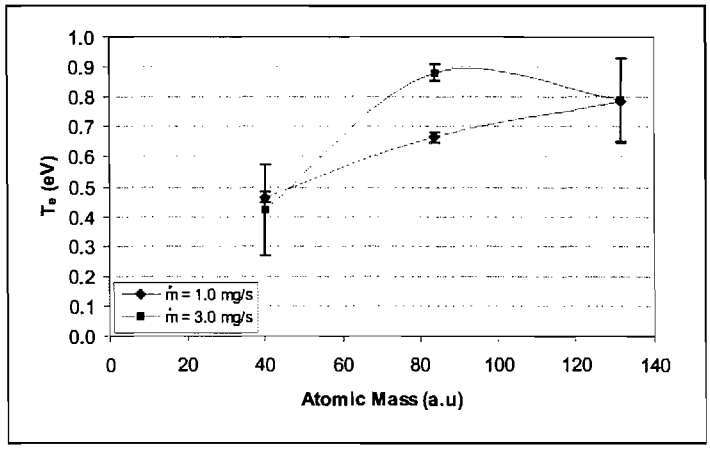

Figure 7.4: Comparison of T_e at probe 1 geometry 1 with $I_A = 5.0$ for different mass flow rates

The T_e values calculated using line intensity ratio methods show a dependence on the atomic mass m_A which, has the form $T_e = 0.09\sqrt{m_A}$ with $R^2 = 0.996$ for $\dot{m} = 1mgs^{-1}$ as shown in Fig. 7.4.

From consideration of the electron–ion collision cross sections for various inert gas plasmas it is evident that the electron–ion collision frequency increases with decreasing atomic mass

[42]. This is supported by the fact that increasing the atomic mass of the propellant gas causes increased electron shielding of the positive nucleus of the heavy particles. Increased shielding causes a decrease in the Coulomb attraction between electrons and the constituent particles of the plasma, resulting in a decreased collision frequency. The electron–ion collision frequency for a fully ionised gas determined using the Lorentz gas approximation (a plasma in which electrons collide with fixed ions and not other electrons) is shown in Equ. 7.9 [121].

$$\nu_{ei} = \frac{4\pi n_e e^4 \ln \Lambda}{3\sqrt{m_e}(kT_e)^{\frac{3}{2}}} \tag{7.9}$$

Where $\ln \Lambda$ is the Coulomb logarithm. The quantity Λ is the ratio of the maximum impact parameter to the impact parameter for scattering at 90° but may be related to the plasma parameters via Equ. 7.10.

$$\Lambda = 1.24 \times 10^7 \left(\frac{T_e^3}{n_e}\right)^{\frac{1}{2}} \tag{7.10}$$

The ratio of impact parameters is a function of electron density and temperature but its logarithm is insensitive to these variables. Typical values of $\ln \Lambda$ are stated in tables; it is evident that the function varies not more than a factor of two as the plasma parameters vary over orders of magnitude. It is sufficient to use the stated value for a gas discharge of $\ln \Lambda \approx 12$ to provide a description of the collision processes occurring within the HC internal plasma. Equ. 7.9 shows that the electron–ion collision frequency, $\nu_{ei} \propto T_e^{-\frac{3}{2}}$. As the collision frequency decreases with increasing atomic mass, the electron temperature may be expected to increase with increasing atomic mass of the propellant gas.

The electron temperature has shown a dependence on electrode separation, the reason for this may be explained in terms of the magnitude of the resulting electric field that the electrons are exposed to. The total current density $\mathbf{J}$ is directly proportional to the applied electric field $\mathbf{E}$ with the electrical conductivity being the constant of proportionality.

$$\mathbf{J} \equiv \sigma_p \mathbf{E} \tag{7.11}$$

Although Equ. 7.11 refers to the electric field external to the HC it is fair to assume that the electric field strength influences the plasma discharge of the HC. This is supported by the observed differences of plasma parameter results at constant mass flow rate and current

with changing electrode separation. Utilising the relationship between the conductivity and electron temperature the reliance of current density on T_e and the electric field is obtained, $\mathbf{J} \propto T_e^{\frac{3}{2}}\mathbf{E}$. If the applied electric field is increased whilst maintaining the current drawn from the HC the external electron temperature will decrease. From the relation $E = V/d$ it is clear that decreasing the electrode separation results in an increase in electric field strength. The V–I characteristics presented in Chapter 5 show that the discharge voltage decreases with a decrease in electrode separation. However, a decrease in separation of $30mm$ more than compensates for the decreased discharge voltage. Hence, for a given discharge current the T_e values determined for geometry 1 are greater than those obtained with the reduced electrode separation of geometry 2.

The axial electron temperature distribution may be estimated using Equ. 7.12. Neglecting the energy loss due to the creation of ions and only considering one dimension results in the expression shown in Equ. 7.13. This is a modified form of the Salhi model where only conduction and resistive heating were considered [125].

$$\nabla \cdot \left\{ \frac{5}{2} j_e T_e + \kappa \nabla T_e \right\} + \dot{n}\chi(z,g) = \frac{j_e^2}{\sigma_p} \tag{7.12}$$

$$\frac{d}{dx}\left\{ \frac{5}{2} j_e T_e + \kappa \frac{dT_e}{dx} \right\} = \frac{j_e^2}{\sigma_p} \tag{7.13}$$

Using the following expressions for thermal conductivity, electrical conductivity and collision frequency [125],

$$\begin{aligned} \kappa &= \frac{3.203 n_e k^2 T_e}{m_e \nu_{ei}}, \\ \sigma_p &= \frac{1.975 n_e e^2}{m_e \nu_{ei}}, \\ \nu_{ei} &= \frac{3.64 \times 10^{-6} n_i \ln\Lambda}{T_e^{\frac{3}{2}}} \end{aligned} \tag{7.14}$$

$$\frac{d}{dx}\left\{ \frac{5}{2} j_e T_e + \frac{3.203k^2}{3.64 \times 10^{-6} m_e \ln\Lambda} T_e^{\frac{5}{2}} \frac{dT_e}{dx} \right\} = \frac{3.64 \times 10^{-6} m_e \ln\Lambda}{1.975 e^2} \frac{j_e^2}{T_e^{\frac{3}{2}}} \tag{7.15}$$

$$\int \frac{d}{dx}\frac{5}{2} j_e T_e dx + \frac{3.203k^2}{3.64 \times 10^{-6} m_e \ln\Lambda} \left\{ \int \frac{5}{2} T_e^{\frac{3}{2}} \frac{dT_e}{dx} dx + \int T_e^{\frac{5}{2}} \frac{d^2 T_e}{dx^2} dx \right\} = \frac{3.64 \times 10^{-6} m_e \ln\Lambda}{1.975 e^2} \frac{j_e^2}{T_e^{\frac{3}{2}}} \int dx \tag{7.16}$$

$$\int \frac{5}{2} j_e T_e dx + \frac{3.203k^2}{3.64 \times 10^{-6} m_e \ln \Lambda} \left\{ \int \frac{5}{2} T_e^{\frac{5}{2}} dx + \int T_e^{\frac{5}{2}} \frac{dT_e}{dx} dx \right\} = \frac{3.64 \times 10^{-6} m_e \ln \Lambda}{1.975 e^2} \frac{j_e^2}{T_e^{\frac{3}{2}}} \int x dx \tag{7.17}$$

$$\frac{5}{2}(T_{e1} - T_{e2})\Delta x + \frac{3.203k^2}{3.64 \times 10^{-6} m_e \ln \Lambda} \left\{ \frac{5}{2}(T_{e1}^{\frac{5}{2}} - T_{e2}^{\frac{5}{2}})\Delta x + (T_{e1}^{\frac{7}{2}} - T_{e2}^{\frac{7}{2}}) \right\} = \frac{3.64 \times 10^{-6} m_e \ln \Lambda j_e^2}{2(1.975) e^2} \frac{\Delta x^2}{(T_{e1}^{\frac{3}{2}} - T_{e2}^{\frac{3}{2}})} \tag{7.18}$$

The electron temperature corresponding to the root of Equ. 7.18 was determined for Δx values of 1mm intervals for an initial $T_{e1} \approx 0.5eV$ and $x_1 = 1.3mm$ with $j_e \approx 1 \times 10^5 Am^{-3}$, for simplicity it was assumed that there are no axial variations in the insert temperature. The results shown in Fig. 7.5 are compared to the experimental CR argon results for the case $I_A = 3.0$ and $\dot{m} = 1.1mgs^{-1}$ in geometry 1. This model provides a crude estimate of the electron temperature profile. The variations that may arise due to changing the HC operating parameters cannot be determined and this method is reliant upon the use of experimental data for initial inputs.

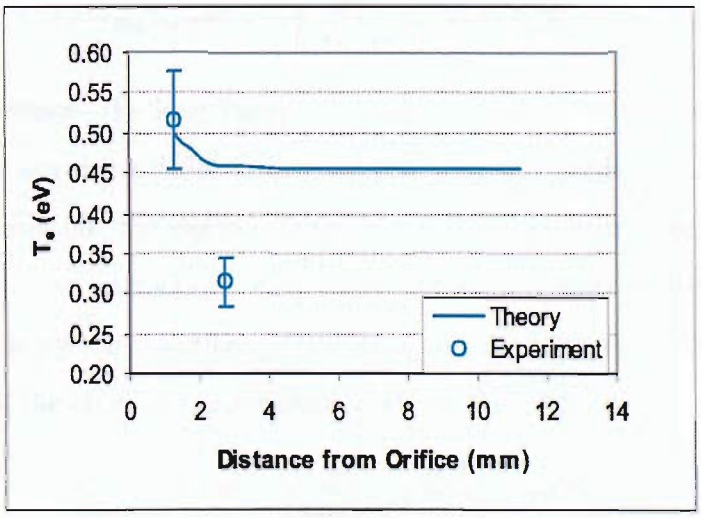

Figure 7.5: Electron temperature profile compared with argon experimental results

It can be seen that the theoretical profile does not fall off as rapidly as expected. This may be due to the neglect of the energy loss term for ion production, also assumptions made regarding a uniform insert temperature distribution and hence electron current density

may cause further discrepancies between theoretical and experimental results. The conductivities used in these calculations were formulated for fully ionised plasmas. The rapid increase in current density as the orifice is approached demonstrated in literature indicates that the ion fraction will also vary considerably along the HC axis and that the majority of ionisation occurs in the orifice (supported in this investigation) [69, 66]. As a consequence it may not be appropriate to assume that the HC internal plasma is uniformly fully ionised for all axial coordinates for the case of localised plasma parameter calculations.

The mass flow rate through the HC may be expected to influence the electron temperature of the plasma discharge as increasing $\dot{m}$ increases the heavy particle density thus increasing the rate of collisions between electrons and heavy particles. This results in an increased collision frequency causing a decrease in the plasma conductivity and the electron temperature. However, experimental results have shown T_e has little dependence on $\dot{m}$. This is explained by considering the relative importance of electron collisions with neutrals compared to interactions with ions. The cross section σ_n for elastic scattering of electrons off neutrals with Bohr radius a_0 is shown in Equ. 7.19 [121].

$$\sigma_n \sim \pi a_0^2 \sim \pi \left(\frac{h^2 \epsilon_0}{\pi m_e e^2} \right)^2 \sim 10^{-20} m^2 \tag{7.19}$$

An electron experiences the long range Coulomb force at any distance r from a singly charged ion. This attraction deflects the electrons motion towards the ion; if the angle of deflection approaches 90^o the electron looses its initial momentum, therefore in terms of momentum exchange an interaction / close encounter with an ion is equivalent to a collision. The effective Coulomb cross section σ_c is related to the distance of closest approach for the electron b and the electron temperature in eV by Equ. 7.20.

$$\sigma_c \sim \pi b^2 \sim \frac{\pi e^4}{(4\pi\epsilon_0)^2 T_e^2} \sim \frac{10^{-17}}{T_e^2} m^2 \tag{7.20}$$

From Equ. 7.19 and Equ. 7.20 it is clear that Coulomb collisions dominate over collisions with neutrals for any plasma with $T_e < 10eV$. Therefore the neutral density and hence the mass flow rate has little influence on collisional processes occurring within the HC compared to ionised species. As a consequence the electron temperature is not highly dependent on neutral density and mass flow rate.

The electron temperature has also demonstrated little dependence on discharge current. The total discharge current is formed from contributions from thermionic electrons, the ion current and electrons liberated via volume ionisation in the bulk plasma. Equ. 7.21 provides an approximate estimate of the discharge current for an electron emission area A_e and ion production area of A_s ignoring contributions from bulk ionisation.

$$I_D \approx \left\{ A_o T^2 \exp\left(-\frac{e\phi_{eff}}{kT}\right) \right\} A_e + \left\{ en_e \left(\frac{kT_e}{m_i}\right)^{\frac{1}{2}} \right\} A_s \tag{7.21}$$

Equ. 7.21 shows that the contribution to the total discharge current from the Bohm current is directly proportional to the electron density and the square root of the electron temperature. This expression shows that the electron temperature may be expected to increase with increasing discharge current at constant operating temperature. But increasing the current increases the electron density therefore increasing the number of charge carriers per unit volume. As a consequence there is an increase in the rate of collisions occurring between constituent particles of the plasma. This results in an increase in the electron–ion collision frequency ($\nu_{ei} \propto T_e^{-\frac{3}{2}}$) which in turn causes a decrease in the electron temperature. Therefore the effect of increased current density is cancelled out by the effect of increased collision frequency resulting in T_e displaying little dependence on discharge current.

7.5 Insert Temperature, Barium Depletion and HC Lifetime

This is the first experimental investigation where the temperature of an impregnated tungsten insert has been determined at different axial positions for a variety of operating parameters. Therefore there are no data available (theoretical or experimental) for direct comparison. For this reason the validity of the results obtained in this investigation will be assessed via comparisons with studies performed on alternative inserts e.g. tantalum inserts coated in carbonate mixtures; comparisons will also be made with theoretical calculations and tip temperature measurements.

The temperature profile shown in Fig. 7.6 was obtained for a HC with an insert consisting of a single layer of tantalum foil coated in a double carbonate mixture of $BaSrCO_3$ with an

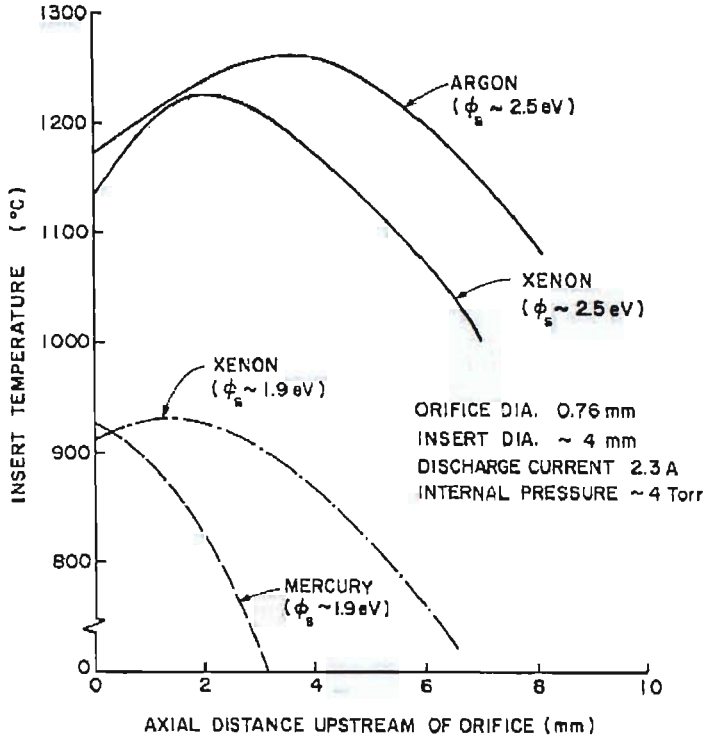

Figure 7.6: Temperature profiles argon and xenon [4]

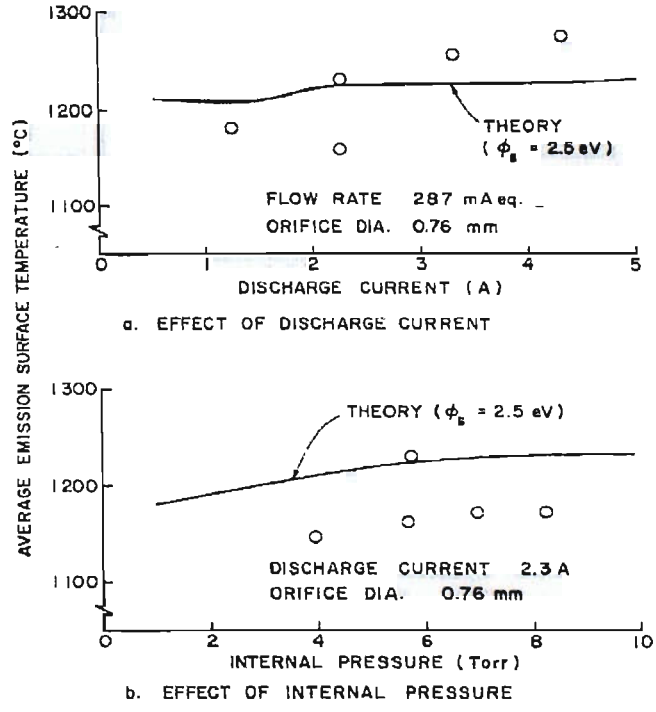

Figure 7.7: Dependence of temperature operating parameters for argon propellant [4]

insert length of $\sim 20mm$ and diameter $3.8mm$ [4]. In spite of the differences in HC design the temperature values compare well with those obtained in the current investigation; unfortunately the temperature profile was not related to the propellant flow rate. An empirical formula that relates HC pressure P to the orifice diameter d_o and $\dot{m}$ has been used to estimate $\dot{m}$ (see Equ. 7.22) [39]. For an internal pressure of $P = 4Torr$ we obtain $\dot{m} \sim 0.1mgs^{-1}$ for xenon and $\dot{m} \sim 0.03mgs^{-1}$ for argon.

$$P(Torr) = \frac{\dot{m}(Aequiv)}{d_o(mm)}(13.7 + 7.82I_D) \tag{7.22}$$

The theoretical investigation (see Fig. 7.6) produced peak temperatures of $\sim 1550K$ for argon with a surface workfunction of $2.5eV$ compared to $1400K$ found in the current study for $I_D = 2.5A$ and $\dot{m} = 1.1mgs^{-1}$. For a workfunction of $1.9eV$ for a xenon discharge a peak temperature of $\sim 1173K$ occurring $\sim 2mm$ from the tip is obtained; this compares well to experimental values of $T = 1083K$. The theoretical profile shows that the maximum insert temperature is achieved at some point upstream of the tip with the location moving further upstream as the atomic mass of the propellant gas is decreased. This agrees well with the results presented for the temperature distribution for the HC operating on argon propellant (see Fig 6.30) and the findings of other investigations, although the temperature is overestimated in these cases (see Fig. 2.11 and Fig. 2.13) [41, 57, 46]. As shown in Fig. 7.7 the insert temperature shows little dependence on mass flow rate (pressure). The experimental temperature increases by $\sim 100^o$ for an increase in current of $5A$ which compares well with the argon results of this study, for example $T = 1400K$ with $I_D = 2.5A$ and increases to $T = 1550K$ with $I_D = 5.5A$ for $\dot{m} = 1.1mgs^{-1}$ at probe 2.

7.5.1 Temperature Calculation

Theoretical values of the insert temperature may be determined as a method of performing a consistency check on the experimental results obtained. Integrating the one dimensional steady state heat conduction equation and including a term for radiation results in Equ. 7.23; this relates the power loss due to conduction through the HC to the loss caused by radiation from the tip [122].

$$\dot{Q} = \frac{\kappa A_1}{\Delta x}(T_1 - T_2) + \varepsilon\sigma_{SB}A_2(T_1^4 - T_3^4) \tag{7.23}$$

Where $\dot{Q}$ is the total thermal power loss, σ_{SB} is the Steffan Boltzmann constant, κ and ε are the thermal conductivity and emissivity of the material respectively, for tantalum $\kappa = 57.5Wm^{-1}K^{-1}$ and $\varepsilon = 0.21$. The axial distance from the tip $\Delta x = 1.3mm$ i.e at probe 1, the area A_1 is the cross sectional area of the T6 HCs tantalum tube with outer radius $3.5mm$ and inner radius $2.25mm$, A_2 is the surface area of the tip. The temperature T_1 is the insert temperature, $T_2 = 773K$ is the heat sink at the HC flange obtained using an imaging radiometer in Ref. [61] and $T_3 = 300K$ is the ambient temperature. The expression for the power conducted and radiated from the insert surface stated in Ref. [39] has been modified to include thermal input from ohmic heating and convection losses, with the remaining terms presenting power losses from electron emission and gains from ion bombardment, plasma radiation and the de–excitation of plasma species (see Equ. 7.24) [124]. Equating the expressions for $\dot{Q}$ (Equs. 7.23 and Equ. 7.24) and solving for T_1 we obtain the results shown in Table 7.3 for a krypton discharge.

$$\begin{aligned}\dot{Q} = 2j_i A_c \phi_{eff} + j_i A_e \phi_{eff} + j_i(V_p + \chi(z,g) - \phi_s) + \frac{j_i^2}{\sigma_p} \\ -j_i I_D \phi_{eff} - \frac{5k}{2e} T_e \{(j_i + j_e)A_e\}^2\end{aligned} \tag{7.24}$$

Where A_c is the area of the end boundary of the ion production region with radius $1mm$ (taken as the dispenser inner radius), all other variables have their usual meaning. For the purposes of this calculation the effective work function is assumed to be approximately equal to the surface work function $\phi_s = 2.1eV$.

Propellant	T_e (eV)	j_i (Am^{-1})	V_p (V)	σ_p (Sm^{-1})	T (K)	T_{Plank} (K)
Krypton	0.665	765.2	1.71	864.071	2589.670	1558.348 ± 36.573
Argon	0.465	2.7328×10^{-4}	1.71	505.239	489.165	1129.180 ± 225.941

Table 7.3: Theoretical calculations for the insert temperature with a krypton discharge at probe position 1 and geometry 1 with $\dot{m} = 1mgs^{-1}$ and $I_D = 5.5A$

The theoretical values of the insert temperature presented in Table 7.3 do not show good agreement with the experimentally determined values. For the case of argon the theoretical value is half that of the experimental value and twice the experimental value for the case of a krypton discharge. The discrepancy may arise due to the use of the Spitzer formula ($T_e = (5.23 \times 10^{-5} z \sigma_p \ln\Lambda)^{\frac{2}{3}}$) in calculating the plasma conductivity [121]. The

formula is applicable to fully ionised gases and the HC internal plasma is a partially ionised gas. On increasing the conductivity to $\sigma_p = 1475Sm^{-1}$ ($\approx 60\%$ increase) which corresponds to an electron temperature of $T_e = 0.95eV$ whilst keeping the remainder of parameters the same a theoretical value of $T = 1628.178K$ for krypton is obtained. This implies that calculating the total thermal power loss using plasma parameters determined from the insert region may not be appropriate. The use of electron temperature values approximately equal to the space averaged values determined by Rudwan results in a theoretical temperature value that shows a better agreement with the experimental values determined in this investigation. The theory indicates that the main contribution to HC heating comes from ion bombardment and ohmic / resistive heating whilst the dominant heat loss processes are electron extraction and conduction.

7.5.2 Life Time Considerations

The main limiting factor for HC lifetime is barium depletion. The rate of Ba depletion is dependent on the operating temperature of the HC, therefore the optimisation of temperature with desired charge current is required for long life. Investigations relating lifetime t in hours, to temperature and the depleted depth of barium e, have resulted in the expressions shown by Equ. 7.25 and 7.26 and demonstrate that Ba loss occurs via simple diffusion through the pores with a Arrhenius [1] dependence on temperature [81, 82].

$$\ln t_{ref} = \frac{eE_{evap}}{kT} + A_1 \tag{7.25}$$

Previous investigations into Ba depletion show that the loss of Ba is the same for the same types of impregnates, therefore the value of the constant A_1 may be obtained from data in Ref. [81], for the case of a $100\mu m$ depleted depth; $A_1 = 15.5$. The activation energy required for the vaporisation of barium, E_{evap}, has shown a variation of 0.4 from $2.8eV$ to $3.2eV$ in recent studies on 411 impregnates; the median value of $3.0eV$ was chosen for these calculations. Using Equ. 7.25 to determine the reference lifetime t_{ref} and substituting the

[1] The Arrhenius Equation relates reaction rates, K to temperature, $K = A\exp^{\frac{E}{RT}}$

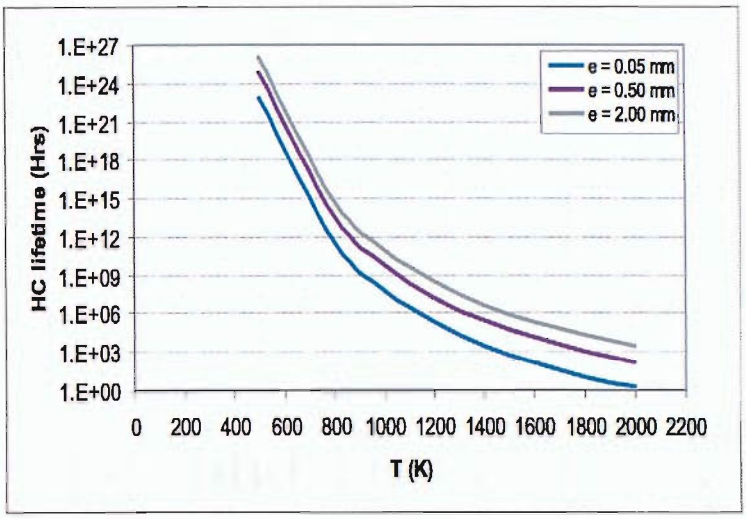

Figure 7.8: Dependence of HC lifetime on operating temperature for various depleted depths

value into Equ. 7.26 stated in Ref. [126] allows the HC lifetime t to be determined.

$$e = A\sqrt{t} \longrightarrow t = t_{ref}\left(\frac{e}{e_{ref}}\right)^2 \tag{7.26}$$

Where A is a constant. The reference depleted depth is taken to be $e_{ref} = 100\mu m$ and the reference time t_{ref} is the time taken for Ba reserves to deplete to a depth of $100\mu m$ within the pore. Equ. 7.26 was used to estimate the HC lifetime for various depleted depths; the results are shown in Fig. 7.8. The results show that increasing the possible depleted depth by an order of magnitude produces an increase in lifetime of two orders of magnitude while decreasing the temperature by 50^o doubles the lifetime. The insert temperatures determined in this study (see section 6.6) range from $1000-1800K$ depending on operating conditions. Within this temperature range the calculated HC lifetime varies from 1×10^{11} to $2 \times 10^4 hrs$, for a depleted depth of $500\mu m$. The trends demonstrated by the lifetimes presented in Fig. 7.8 imply that the maximum attainable pore depth should be used to make available the largest possible reserve of Ba hence maximising HC life. For a HC insert temperature of $1400K$, typical for a HC operating with a anode current of $5.0A$, a lifetime of $300,000hrs$ is attainable with pore depths of $500\mu m$. This is well above the suggested $t \approx 50,000hrs$ required for the Prometheus project for missions to the outer planets [127].

Chapter 8

Conclusions and Future Work

8.1 Summary of Research Findings

A novel HC has been successfully tested under a variety of conditions. It has been established that it is possible to gain direct access to the HC internal plasma without detrimental effects on the performance of the component. It has also been shown that it is possible to develop diagnostic equipment with the necessary temperature rating on a scale appropriate for studying commercial models of HCs. This unique experimental set up has provided the opportunity to collect localised data at various points along the length of the HC. This has resulted in the first spatially resolved measurements of the electron temperature and insert temperature determined using non invasive techniques on a commercial space rated HC. The original aspects of this investigation are outlined below and the main conclusions drawn from the research findings are summarised.

Optical Emission Spectra

Optical emission spectra were recorded at three different axial positions 1.4mm from the HC tip, 2.7mm and 11.1mm for two different external electrode separations. All previous spectroscopic studies of the HC plasma have recorded space averaged spectra along the axis from an external vantage point. The qualitative analysis of the spectra provides an insight into the characteristics of the HC internal plasma. The earlier space averaged spectra show intense activity in UV and visual regions of the spectrum with a high abundance

of ionised spectral lines. The spectra recorded in this investigation may be classified into two sets 1) The active plasma located nearest to the tip, up to $\sim 3mm$ away and 2) The hot gas observed in the region of probe 3, 11.1mm from the tip. The spectra recorded in the furthest upstream position display few discrete spectral lines and are dominated by thermal emissions from the insert. The spectra obtained from the regions nearest to the tip display discrete spectral lines, however the spectra are dominated by neutral line transitions that appear in the near infrared region of the spectrum. On comparing the spectra with those obtained from an external vantage point it is clear that the majority of ionisation occurs within the HC tip. This provides the first experimental confirmation of the active region theory for HCs with inserts impregnated with earth metal oxides.

Electron Temperature

The electron temperature has been determined using three independent methods, line intensity ratio methods for the LTE and CR regimes and the ratio of continuum bremsstrahlung radiation. All show good agreement with each other. The electron temperature profile determined for an argon discharge shows a typical decrease of $0.2eV$ over a distance 1.4mm; this is significant considering that the maximum error for the electron temperature at probe position 1 in geometry 1 was $\approx 0.1eV$ and at probe 2 the maximum error was $\approx 0.08eV$. The theoretically determined profile requires modification in order to provide a closer agreement with the experimental result. Decreasing the keeper/anode separation from $60mm$ to $30mm$ resulted in a decrease in the electron temperature of approximately $0.3eV$ for a maximum error of ≈ 0.06 at probe 1 in geometry 2. The difference between the electron temperatures decreases with increasing anode current. This is the first occasion that the influence of electrode separation on electron temperature has been investigated. The influence of propellant mass on electron temperature in the region closest to the tip shows that increasing the atomic mass from 38.95 a.u. for argon to 131.13 a.u. for xenon causes the electron temperature to increase by almost a factor of two under most conditions, for example $T_{eAr} = 0.42 \pm 0.2eV$ compared with $T_{eXe} = 0.789 \pm 0.02eV$ for $I_A = 5.0A$ and $\dot{m} = 3.0mgs^{-1}$.

Ion Fraction

The ion fraction determined in the region 1.4mm from the HC tip has shown that increasing the atomic mass of the propellant gas increases the ion fraction whilst decreasing the sensitivity of the ion fraction to mass flow rate. For a krypton discharge a maximum ion fraction of 15% is achieved for $I_A = 2.0A$ and 10% for $I_A = 10.0A$ with $\dot{m} = 1.0mgs^{-1}$, while the ion fraction ranges from 5% to 0.3% for $\dot{m} = 3.0mgs^{-1}$ with $\lambda_n = 850.887$ and $\lambda_{z+1} = 468.041nm$. The xenon discharge ion fraction is 22% and 16% for $I_A = 2.0A$ and $I_A = 10.0A$ respectively with $\dot{m} = 1.0mgs^{-1}$ and 20% and 10% for $\dot{m} = 3.0mgs^{-1}$. There is typically a 5% decrease in ion fraction on increasing the anode current from 2.0 to $10.0A$ with $\lambda_n = 828.012nm$ and $\lambda_{z+1} = 716.483nm$. It has been stated that the HC discharge is fully ionised. These results indicate that at least 80% of ionisation must occur within the orifice and chamfer region if the HC is to produce a fully ionised plasma.

Electron Number Density

The number density is highly sensitive to the electron temperature, this has resulted in differences over orders of magnitude for the densities calculated for the various inert gas propellants. The electron density results indicate that the argon plasma conforms to the corona regime, krypton to the CR regime and xenon to either the CR or LTE regime depending on the electron temperature of the discharge. For future investigations it will be advantageous to calculate the electron number density independently without reliance on any other experimental data.

Insert Temperature

The insert surface temperature was determined using the ratio of continuum radiation in the near infrared region of the spectrum. Planck's formula was used to calculate the temperature and Wien's displacement law was used as a means of verifying the temperature value obtained using Planck's formula and also enabled the spectral distribution of thermal emissions to be determined. The insert temperature peaks in the region of probe 2 ($2.7mm$ from the tip) achieving temperatures approximately 400^o higher at $I_A = 2.0A$ and 100^o at $I_A = 10.0A$ than that achieved at probe 1 for an argon discharge. The dependence of the insert temperature on mass flow rate decreases as the atomic mass of the propellant

gas increases; decreasing the electrode separation also reduces the influence of mass flow rate on temperature. The critical factor in dictating the insert temperature is the anode current. An increase in temperature of $\sim 400^o$ is observed for an increase in current of $I_A = 2.0A$ to $I_A = 10.0A$ for krypton and xenon discharges at probe position 1; an increase of $\sim 650^o$ is observed for argon propellant.

Influence of Changing Inert Gas Propellant

A comparison of the localised electron temperature of a HC operating on a variety of inert gas propellants has not been performed previously. In the current investigation the electron temperature has increased with increasing atomic mass of the propellant gas. The following maximum electron temperatures were achieved for $\dot{m} = 1mgs^{-1}$: $T_{eAr} = 0.63 \pm 0.01eV$, $T_{eKr} = 0.71 \pm 0.02eV$ and $T_{eXe} = 1.26 \pm 0.3eV$. The insert temperature does not display a consistent dependence on the propellant used i.e. a constant relationship between temperature and atomic mass is not observed when keeping the remaining operating parameters constant. The dominant factors in determining HC operating temperature are current and to a lesser extent mass flow rate as discussed above.

Effect of Electrode Separation

The performance of the HC, in particular mode change characteristics, have been seen in earlier studies to be strongly influenced by anode geometry. In this investigation the impact of anode separation on the electron temperature and insert temperature were studied for the first time. A reduction in the keeper/anode separation causes a decrease in the discharge power for a given anode current and mass flow rate. The electron temperature was observed to decrease by a maximum of $0.55eV$ for the case of an argon discharge. The insert temperature typically decreases with decreasing electrode separation for a given set of operating parameters, however there does not appear to be a consistent pattern regarding the level of decrease one can expect to observe.

Theoretical Calculations

Theoretical calculations have been performed using experimental results as input parameters. This allows the experimental data to be evaluated in terms of whether the results obtained are consistent with existing theory. The theoretical results often provide the only

data available for comparison as no experimental data exist for direct comparison with the experimentally determined plasma parameters and insert temperatures of the current investigation.

Plasma Parameters

The plasma potential, discharge current and current densities were calculated using experimental values of the electron temperature, number density and insert temperature for the HC operating on krypton propellant. On comparing the theoretical results with space averaged plasma parameter results it can be seen that good a agreement between the electron current densities is achieved, indicating that the thermal characteristics are similar in both cases. The ion current densities differ by two orders of magnitude. This is expected due to the small degree of ionisation observed in the insert region. The main discrepancy occurs for the plasma potential which is considerably less than that found in previous studies; this may be due to the reduced values of localised electron number density and ion current density compared to space averaged values.

Electron Temperature Profile

The theoretical electron temperature profile provides a crude estimate of the dependence of the electron temperature on axial position as gradients in all other parameters have been neglected. In order to develop an accurate model all plasma parameters such as electron current density, ion fraction, conductivity etc. must be determined at each axial coordinate. This approach will require the development of a computer code to perform all of the necessary calculations.

Insert Temperature

The insert temperature has been calculated by equating the insert energy balance equation to the steady state conduction and radiation equation. The theoretical calculation of the insert temperature has shown that macroscopic space averaged thermal power losses from conduction through the HC and radiation from the tip cannot be equated to the microscopic insert energy balance processes in order to obtain a temperature relating to a specific axial position. In order to calculate the temperature at a known position and obtain a value that agrees with experimental values the power loss at that position due to conduction and radiation must be determined. In this way differences between theory and experiment

of $\sim 1000^{o}$ as has been observed in this investigation may be avoided. The calculations performed are again reliant upon the use of experimental data for inputs. This method does not demonstrate the reliance of the temperature on operating parameters such as mass flow rate and current. It would be ideal if the insert temperature could be determined from first principles using operating parameters and HC geometry as input parameters. Unfortunately only empirical formulae exist that relate insert temperature to mass flow rate and current, therefore calculations from first principles could not be performed.

HC Lifetime

The HC life was determined for various insert temperatures and barium depletion depths. It is necessary to maximise pore depth to obtain the largest possible reserve of barium, if the lifetimes required for missions to the outer planets which are in excess of $50,000hrs$ are to be achieved. A lifetime of $300,000hrs$ (34 yrs) is attainable for temperatures of $1400K$ which have been observed for discharge currents of less than $5.5A$. It is therefore the conclusion that the HC is capable of performing extended missions provided that alternative end of life mechanisms do not result in premature component failure.

8.2 Recommendations for Future Work

The current investigation on the internal plasma of HCs has provided an insight into steady state operation. There are remaining areas relating to HC performance and the underlying physics that require further investigation. They are as follows;

- Testing the modified T6 HC and standard space rated HCs in full thruster configuration.
- Develop models that predict plasma parameter profiles and thermal characteristics both in steady state and transient operation.
- Further investigation of the steady state and transient properties of the modified T6 HC in diode configuration (see Sections 8.2.1 and 8.2.2).

It has been well documented that the HC configuration influences the performance of the device. From the perspective of electric propulsion applications it is advisable to test HCs in full thruster configuration. In this way the steady state and transient performance of the component can be studied in a real thruster environment using a variety of diagnostic instruments. The influence of using alternative inert gas propellants can be investigated and life tests can be performed in order to assess life limiting mechanisms. Testing the HC in diode configuration provides a simple and cost effective method of carrying out investigations. Further experiments that may be performed in either configuration are outlined in Sections 8.2.1 and 8.2.2. An objective of this investigation was to provide data sets that may be used for code validation. Current models for HC operation do not provide temperature profiles that agree well with experimental data and there is little or no data on plasma property profiles and transient behaviour particularly for argon and krypton discharges.

8.2.1 Steady State Plasma Parameters

The data analysis performed in this investigation in an attempt to extract plasma parameter values from the collected spectra was limited by the availability of atomic constants for the observed spectral lines. The determination of transition probabilities and Gaunt factors is not trivial. However, atomic databases have made improvements in the coverage of the data for a range of wavelengths and elements. If these improvements continue, in the near future calculations may be performed using the corona model as outlined in Appendix B. This would allow a comparison of all possible techniques for electron temperature calculation and establish the most appropriate method for use with the HC internal plasma.

Further experiments may be performed which collect data from all of the available probe access holes in order to develop complete profiles. Investigations into the influence of propellant mass on HC performance and plasma characteristics may be carried out using neon and helium. Also, the effect of orifice diameter on plasma parameters and thermal characteristics should be investigated. The current T6 programme has used a maximum

orifice diameter of $1.6mm$ but in the current investigation an orifice diameter of $0.5mm$ was used.

The results obtained in this investigation for the electron temperature and number density may be independently verified by the use of electrostatic probes also known as Langmuir probes. The use of alternative diagnostic equipment will provide a means of assessing the extent to which electric probes perturb the plasma under investigation. Also, data may be collected that cannot be obtained with the use of spectroscopic techniques; this includes the electron energy distribution function that is obtained from the second derivative of the current voltage characteristic, the plasma potential from the x axis intercept of the current voltage characteristic and the sheath potential. The design of electrostatic probes with the necessary dimensions and temperature rating was investigated in the preliminary stages of this experimental campaign. The procurement of appropriate insulating materials was not trivial and resulted in the method being abandoned at the design stage. A feasible probe design and data acquisition circuit is shown in Appendix F.

8.2.2 Plasma Formation and Transient Phenomena

An investigation into plasma formation processes may be performed in order to investigate plasma breakdown in the insert region. Breakdown theory for static gases with uniform pressure distributions between parallel electrodes is explained by Paschens Law (Equ. 8.1).

$$V_{bd} = \frac{BPd}{\ln\left(\frac{APd}{\ln(1\backslash\gamma_T)}\right)} \tag{8.1}$$

Where V_{bd} is the breakdown voltage, d is the electrode separation, P is the gas pressure, γ_T is the Townsend coefficient which is the number of electrons liberated per ion impact, the coefficient $A = (P\lambda_{ei})^{-1}$ and $B = A\chi(g,z)$ where λ_{ei} is the mean free path for electron impact ionisation [128]. This theory does not extend to cylindrical electrodes with variable cross sections as is the case with HCs. The effect of a high velocity gas flow with temperature and pressure gradients should be investigated and the influence of the impregnated insert and the presence of barium and calcium should be addressed.

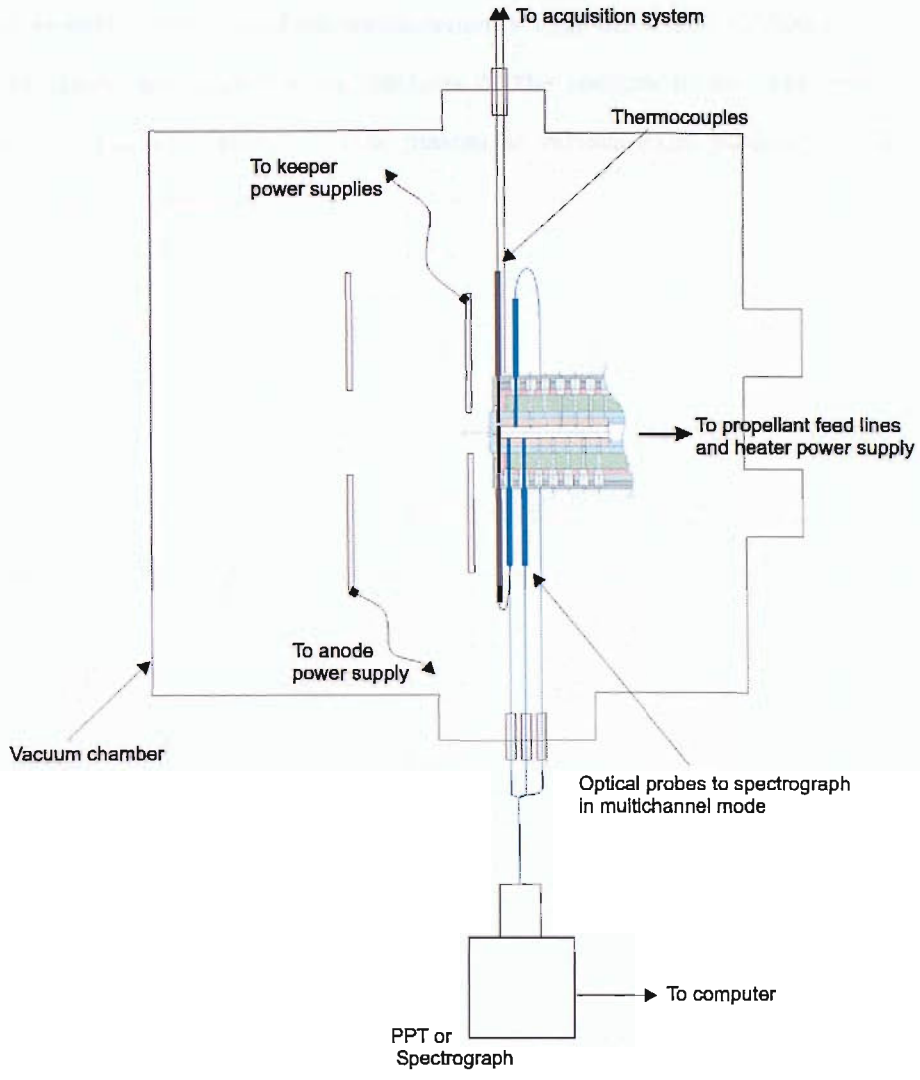

Figure 8.1: Proposed experimental set up for investigation into plasma formation in the HC insert.

Fig. 8.1 shows a possible experimental set up for future investigations. Future experiments will require the procurement of custom designed thermocouples with a temperature rating of $2000K$ and diameter of $500\mu m$. The thermocouples will record the tip temperature at breakdown and ensure the appropriate thermal conditions are met i.e. breakdown occurs under the same thermal conditions so that the influence of operating parameters such as electrode separation and mass flow rate may be investigated. A photo multiplier tube may be used to record broadband (white light) optical emission, but the use of an imaging spectrograph with a data acquisition rate of the order of nano seconds will provide spectral

resolution as well as time resolved measurements that allow the evolution of the plasma to be investigated and quantitative analysis of the spectra to be performed. This will provide information on the state of the plasma at various axial positions prior to, during and directly after breakdown.

References

[1] D. G. Fearn. Spacecraft ion propulsion development in the united kingdom. *Proc. Instn. Mech. Engrs.*, Vol. 211 Part G:pp 103–112, 1996.

[2] I. M. Ahmed Rudwan. *Physics of Hollow Cathode Breakdown and Steady–State Operation with Several Inert Gas Propellants.* PhD thesis, Department of Aeronautics and Astronautics, University of Southampton, PhD thesis 2003.

[3] A. K. Malik, M. P. Monterde, and M. G. Haines. Spectroscopic measurements on xenon plasma in a hollow cathode. *J. Phys. D: Appl. Phys.*, 33:2037–2048, 2000.

[4] P. J. Wilbur. Advanced ion thruster research. Technical report, NASA–CR–168340, Lewis research center, January 1984.

[5] E. Stuhlinger. Electrical propulsion systems for space ships with nuclear power sources. *J. Astronautics*, Vol 2:pp 146, 1955.

[6] G. R. Brewer. *Ion Propulsion.* Gordon and Breach Science Publishers, 1970.

[7] P. G. Hill and C. R. Peterson. *Mechanics and Thermodynamics of Propulsion.* Addison–Wesley Publishing Company inc., 1965.

[8] R. G Jahn. *Physics of Electric Propulsion.* McGraw–Hill, 1968.

[9] M. Martinez-Sanchez and J. E. Pollard. Spacecraft electric propulsion–an overview. *Journal of Power and Propulsion*, Vol. 14 No. 5:pp 1167–1179, 1998.

[10] P. J. Wilbur, R. J. Jahn, and F. C. Curran. Space electric propulsion plasmas. *IEEE Trans. on Plasma Sci*, Vol. 19 No. 6:pp 688–699, 1991.

[11] R. Killinger, R. Kukies, M. Surauer, H. Gray, G. Saccoccia, L. Van Holtz, and A. Tomasetto. Artemis orbit raising inflight experience with ion propulsion. *The 28th International Electric Propulsion Conference*, 96:1–10, 2003.

[12] D. G. Fearn and A. R. Martin. The promise of electric propulsion for low cost interplanetary missions. *Acta Astronautica*, Vol. 35:pp615–624, 1995.

[13] G. Colasurdo and L Casalino. Missions to asteroids using solar electric propulsion. *Acta Astronautica*, Vol. 50 No. 11:pp705–711, 2002.

[14] D. R. Giuseppe. Capability of solar electric propulsion for planetary missions. *Planetary and space science*, 49:pp 1437–1444, 2001.

[15] M. D. Rayman, P. Varghese, D. H. Lehman, and L. L. Livesay. Results from the deep space 1 technology validation mission. *Acta Astronautica*, 47 No. 2–9:pp 475–487, 2001.

[16] M. D. Rayman and P. Varghese. The deep space 1 extended mission. *Acta Astronautica*, 48 No. 5–12:pp 693–705, 2001.

[17] J. Kugelberg, P. Bodin, S. Persson, and Rathsman P. Accommodating electric propulsion on SMART-1. *Acta Astronautica*, 55:pp 121–130, 2004.

[18] D. R. Giuseppe. SMART-1: The first small mission for advanced research in technology. *Acta Astronautica*, 45:pp 337–345, 1999.

[19] B. H. Foing and G. D. Racca. The esa smart 1 mission to the moon with solar electric propulsion. *Adv. Space Res*, 23 No. 11:1865–1870, 1999.

[20] G. Saccoccia. Introduction to the European activities in electric propulsion. *The 28th International Electric Propulsion Conference, paper 341*, 2003.

[21] ESA webpage, [online]. *http://www.sci.esa.int/science-e/www/area/index.cmf?fareaid=27*, 2005.

[22] NASA webpage, Jet Propulsion Laboratory, CalTech, [online]. *http://lisa.jpl.nasa.gov/LISAbrochure.pdf*, Sept 2005.

[23] M. Landgraf, R. Jehn, W. Flury, M. Fridlund, A. Karlsson, and Léger. IRSI/DARWIN: Peering through the interplanetary dust cloud. *ESA bulletin*, Feb 2001.

[24] H. R. Kaufman. An ion rocket with an electron bombardment ion source. *National Aeronautics and Space Administration Technical Note*, TN D–585:pp1–38, 1961.

[25] H. R. Kaufman, R. S. Robinson, and D. C. Trock. Inert gas thruster technology. *J. Spacecraft and Rockets*, Vol 20 No. 1:pp77–83, 1983.

[26] V. K. Rawlin and W. R. Kerslake. Sert ii: Durability of the hollow cathode and future applications of hollow cathodes. *J. Spacecraft and Rockets*, Vol. 7 No. 1:pp14–20, 1970.

[27] J. S. Sovey, V. K. Rawlin, and M. J. Patterson. Ion propulsion development projects in U.S.: Space electric rocket test 1 to deep space 1. *J. Power and Propulsion*, 17 No. 3:517–526, 2001.

[28] D. G. Fearn, A. R. Martin, and P. Smith. Ion propulsion development in the uk. *AIAA Paper*, 93-2603:pp 1–21, 1993.

[29] C. H. Edwards, M. Potts, and D. Rogers. Life verification of the T6 ion extraction grids for the GOCE application. *AIAA paper 04-3134*, 2004.

[30] D. G. Fearn. The development of ion propulsion in the UK: A historical perspective. *28th International Electric Propulsion Conference*, 192:1–10, 2003.

[31] M. J. Patterson and P. J. Wilbur. Plasma contactors for electrodynamic tethers. *NASA TM - 88850*, 1986.

[32] M. J. Patterson and P. J. Wilbur. Plasma contactor design for electrodynamic tether applications. *Adv. Space Res.*, Vol. 8 No. 1:pp 211–224, 1988.

[33] D. E. Parks, I. Katz, B. Buchholtz, and P. Wilbur. Expansion and electron emission characteristics of a hollow cathode plasma contactor. *J. Appl. Phys.*, 74 no. 12:7094–7100, 1993.

[34] I. Katz, B. M. Gardner, M. J. Mandell, and G. A. Jongeward. Model of plasma contactor performance. *J. Spacecraft and Rockets*, 34 no. 6:824–828, 1997.

[35] H. B. Simpson, N. C. Wallace, D. G. Fearn, and M. K. Kelly. A summary of the QinetiQ hollow cathode development programme in support of the European high power Hall effect and gridded thrusters. *The 28th International Electric Propulsion Conference, paper 214*, 2003.

[36] S. W. Patterson and D. G. Fearn. The generation of high energy ions in hollow cathode discharges. *International Electric Propulsion Conference*, IEPC–99–125:pp695–702, 1999.

[37] S. D. Kovaleski. Life model of hollow cathodes using a barium calcium aluminate impregnated tungsten emitter. *NASA/CR–2001–211290*, 2001.

[38] Louis R. Falce. Dispenser cathode technology review. Semicon Associates.

[39] D. E. Siegfried and P. J. Wilbur. A model for mercury orificed hollow cathodes: Theory and experiment. *AIAA Journal*, 22 No. 10:1405–1412, 1984.

[40] J. L. Delcroix and A. R. Trindade. Hollow cathode arcs. *Adv Electron Electron Phys.*, 35:87–190, 1974.

[41] C. M. Ferreira and J. L. Delcroix. Theory of the hollow cathode arc. *J. Appl. Phys.*, Vol 49 No. 4:pp2380–2395, 1978.

[42] M. Mitchner and C. H. Kruger. *Partially ionized gases.* Wiley, 1973.

[43] K. U. Riemann. The bohm criterion and sheath formation. *J. Phys. D: Appl. Phys.*, pp 493–518, 1991.

[44] R. N. Franklin. The plasma–sheath boundary region. *J. Phys. D: Appl. Phys.*, 36:R309–R320, 2003.

[45] P. Solana, P. Kapadia, and J. Dowden. Gas motion and heat transfer in a hollow cylinder with applications to arc welding. *J. Phys. D: Appl. Phys.*, 32:pp 2529–2536, 1999.

[46] P. Rossetti, F. Paganucci, and M. Andrenucci. A hollow cathode model for application to the electric propulsion. *AIAA, paper 2002-4239*, 2002.

[47] G. A. Csiky. Investigation of a hollow cathode discharge plasma. *7th International Electric Propulsion Conference,paper 69-258*, pages pp1–10, 1969.

[48] D. E. Siegfried and P. J. Wilbur. An investigation of mercury hollow cathode phenomena. *13th IEPC AIAA paper 78-705*, pages 1–11, 1978.

[49] C. M. Philip. A study of hollow cathode discharge characteristics. *AIAA Journal*, Vol 9 No. 11:pp2191–2196, 1971.

[50] M. J. Mandell and I. Katz. Theory of hollow cathode operation in spot and plume modes. *Joint Prop. Conf.*, 1994.

[51] M. G. Chalton, G. L. Davis, and D Newson. Investigations on hollow cathodes for ion thrusters. *Electric Propulsion for Space Vehicles Conference*, pages pp141–145, 1973.

[52] G. A. Csiky. Langmuir probe measurements in a discharge from a hollow cathode. *J. Spacecraft and Rockets*, Vol. 7 No. 4:pp474–475, 1970.

[53] D. G. Fearn and C. M. Philip. An investigation of physical processes in a hollow cathode discharges. *AIAA Journal*, 11 No. 2:131–132, 1973.

[54] D. E. Siegfried and P. J. Wilbur. Phenomenological model describing orificed, hollow cathode operation. *AIAA*, 21, no. 1:5–6, 1983.

[55] D. E. Siegfried and P. J. Wilbur. Studies on an experimental quartz tube hollow cathode. *AIAA paper 79-2956*, 1979.

[56] D. G. Fearn, A. K. Singfield, and N. C. Wallace. The operation of ion thruster cathodes using rare gas propellants. *21st International Electric Propulsion Conference*, pages 1–12, 1990.

[57] R. P. Stillwell. Experimental investigation of an argon hollow cathode. *J. Spacecraft and Rockets*, 22, no.1:85–90, 1985.

[58] M. Krishnan, R. G. Jahn, W. F. von Jaskowsky, and K. E. Clark. Physical processes in hollow cathodes. *AIAA Journal*, 15 No. 9:1217–1223, 1977.

[59] A. K. Singfield. A study of hollow cahtode discharge characteristics using xenon. *Working Paper SP(90)WP13, RAE*, pages 1–18, 1990.

[60] M. J. Patterson and J. E. Foster. Hollow cathode micro–thruster performance. *The 27th International Electric Propulsion Conference, paper 226*, pages 1–16, 2001.

[61] M. T. Domonkos, G. J. Gallimore, A. D. Williams, and M. J. Patterson. Low–current hollow cathode evaluation. *AIAA 99–2575*, pages 1–24, 1999.

[62] D. G. Fearn and S. W. Patterson. Characterisation of the high current hollow cathode for the T6 ion thruster. *34th JPC, paper 3346*, pages 1–12, 1998.

[63] J. E. Foster and M. J. Patterson. Plasma emission characteristics from a high current hollow cathode in an ion thruster. *38th JPC, paper 4102*, pages 1–14, 2002.

[64] C. B. Carpenter and M. J. Patterson. High–current hollow cathode development. *The 27th International Electric Propulsion Conference, paper 274*, pages 1–8, 2001.

[65] P. Gessini and S. B. Gabriel. The hollow cathode as a micro–ion thruster. *The 27th International Electric Propulsion Conference, paper 233*, pages 1–18, 2001.

[66] R. V. Kennedy. Theory of the arc hollow cathode. *J. Phys. D: Appl. Phys.*, Vol. 34:pp787–793, 2001.

[67] P. J. Turchi and A. Salhi. Low power plasma thruster based on hollow cathode discharge. *30th AIAA JPC, paper 3126*, pages 1–7, 1994.

[68] S. W. Patterson and M. Domonkos. Sensitivity of hollow cathode performance to design and operating parameters. *35th Joint Propulsion Conference and Exhibit*, AIAA–99–2576:pp1–6, 1999.

[69] I. Katz. A model of hollow cathode plasma chemistry. *Joint propulsion conference*, AIAA 2002-4241:1–15, 2002.

[70] I. Katz, J. R. Anderson, J. E. Polk, and D. M. Goebel. Model of hollow cathode operation and life limiting mechanisms. *The 28th International Electric Propulsion Conference*, 243:1–9, 2003.

[71] D. M. Murray, O. R. Tutty, and S. B. Gabriel. Numerical modelling of the gas flow in an ion thruster hollow cathode. *2nd European Spacecraft Propulsion Conference*, ESA SP–398, 1997.

[72] M. Jugroot and J. K. Harvey. DSMC neutral and charged particle simulation of a kaufman-type ion thruster. *Proceedings of the 10th International Congress on Plasma Physics*, 2000.

[73] M. W. Crofton. The T6 hollow cathode: Measurements and modeling. *34th Plasmadynamics and Lasers, paper 4171*, pages 1–11, 2003.

[74] F. T. Crawford and S. B. Gabriel. Modelling small hollow cathode discharges for ion microthrusters. *33rd AIAA Plasmadynamics and Lasers, paper 2101*, pages 1–11, 2002.

[75] K. G. Hutchinson and S. Gabriel. Conceptual design of a micro ion thruster. *The 27th International Electric Propulsion Conference*, 2001.

[76] P. Gessini, S. B. Gabriel, and D. G. Fearn. Hollow cathode thrust, specific impulse and ion flux measurements using a target. *The 28th International Electric Propulsion Conference, paper 253*, pages 1–10, 2003.

[77] F. T. Crawford and S. B. Gabriel. Microfluidic model of a micro hollow cathode for small ion thrusters (invited). *33rd AIAA Fluid Dynamics Conference, paper 3580*, pages 1–7, 2003.

[78] F. T. Crawford and S. B. Gabriel. Numerical simulation of the hollow cathode plasma using a PIC–DSMC code. *The 28th International Electric Propulsion Conference paper 027*, pages 1–10, 2003.

[79] E. S. Rittner, W. C. Rutledge, and R. H. Ahlert. On the mechanism of operation of the barium aluminate impregnated cathode. *J. App. Phys.*, 28:pp 1468–1473, 1957.

[80] E. S. Rittner. On the mechanism of operation of the type b impregnated cathode. *J. App. Phys.*, 48:pp 4344–4346, 1977.

[81] P. Palluel and A. M. Shroff. Experimental study of impregnated–cathode behaviour, emission and life. *J. Appl. Phys*, 51:2894–2902, 1980.

[82] J. M. Roquais, F. Poret, R. le Doze, J. L. Ricaud, A. Monterrin, and A. Steinbrunn. Barium depletion study on impregnated cathodes and lifetime prediction. *App. Surf. Sci.*, 215:pp 5–17, 2003.

[83] G. Gärtner, P. Geittner, D. Raasch, and D. U. Wiechert. Supply and loss mechanisms of ba dispenser cathodes. *Applied Surface Science*, 146:22–30, 1999.

[84] G. Gaertner, D. Raasch, D. Barratt, and S. Jenkins. Accelerated life tests of crt oxide cathodes. *Appl. Sur. Sci*, 215, 2003.

[85] W. L. Weise. Spectroscopic diagnostics on low temperature plasmas: Techniques and required data. *Spectrochimica*, 46B, no.6/7:831–841, 1991.

[86] D. D. Burgess. Spectroscopy of laboratory plasmas. *Space Science Reviews*, 13:493–527, 1972.

[87] L. A. Dushin, V. I. Privezentsev, and V. S. Taran. Laser interferometry of plasmas. *J. Appl. Spectroscopy*, 25, no.3:1069–1089, 1976.

[88] S. Mazouffre, D. Pagnon, P. Lasgorceix, and M. Touzeau. Temperature of xenon atoms in a stationary plasma thruster. *The 28th International Electric Propulsion Conference, paper 283*, pages 1–10, 2003.

[89] J. Bonnet. LIF-Doppler velocity measurement of xenon atoms in a spt50. *The 28th International Electric Propulsion Conference, paper 300*, pages 1–6, 2003.

[90] J. E. Bailey, H. K. Chung, and A. L. Carlson. Spectroscopic measurements of argon plasma formation by a high–intensity lithium ion beam. *Physical Review Letters*, 82, no.4:739–742, 1999.

[91] M. Touzeau, M. Prioul, S. Roche, N. Gascon, C. Pérot, F. Darnon, S. Béchu, C. Philippe-Kadlec, L. Magne, P. Lasgorceix, D. Pagnon, A. Bouchoule, and M. Dudeck. Plasma diagnostic systems for hall–effect plasma thrusters. *Plasma Phys. Control. Fusion*, 42:B323–B339, 2000.

[92] S. Pellerin, K. Musiol, B. Pokrzywka, and J. Chapelle. Investigation of the cathode region of an electric arc. *J. Phys. D: Appl. Phys.*, 27:pp 522–528, 1994.

[93] B. Pokrzywka, K. Musiol, S. Pellerin, E. Pawelec, and J. Chapelle. Spectroscopic investigation of the equilibrium state in the electric arc cathode region. *J. Phys. D: Appl. Phys.*, 29:pp 2644–2649, 1996.

[94] K. Dzierżęga, B. Pokrzywka, and S. Pellerin. Investigations of the cathode region of an argon acr plasma by degenerate four-wave mixing laser spectroscopy and optical emission spectroscopy. *J. Phys. D: Appl. Phys.*, 37:pp 1742–1749, 2004.

[95] A. K. Malik and D. G. Fearn. The study of the physics of hollow cathode discharges. *23rd International Electric Propulsion Conference*, IEPC–93–026:1–11, 1993.

[96] M. P. Monterde, A. E. Dangor, M. G. Haines, and A. K. Malik. Spectroscopic measurements of the plasma within a hollow cathode. *31st Joint Propulsion Conference AIAA paper 95–2383*, pages 1–9, 1995.

[97] C. Henderson Edwards. *Discharge characteristics and instablities in the UK–25 ion thruster operating on inert gas propellants.* PhD thesis, Department of Aeronautics and Astronautics, University of Southampton, August 1997.

[98] T. M. Jack, S. W. Patterson, and D. G. Fearn. The effect of the keeper electrode on hollow cathode characteristics. *36th Joint Propulsion Conference and Exhibit*, AIAA 2000–3533:1–12, 2000.

[99] S. W. Patterson, M. Jugroot, and D. G. Fearn. Discharge initiation in the T6 thruster hollow cathode. *36th Joint Propulsion Conference and Exhibit*, AIAA 2000–3532:1–10, 2000.

[100] J. D. Swift and M. J. R. Schwar. *Electrical Probes for Plasma Diagnostics.* ILIFFE Books Ltd, 1970.

[101] L. Schott. *Plasma Diagnostics.* North Holland Publishing Company, 1968.

[102] M. P. Monterde, M. G. Haines, A. K. Malik, and D. G. Fearn. Kaufman–type xenon ion thruster coupling plasma: Langmuir probe measurements. *J. Phys. D: Appl. Phys.*, Vol. 30:pp842–855, 1997.

[103] P. C. T. de Boer. Electric probe measurements in the plume of an ion thruster. *J. Power and Propulsion*, Vol. 12 No. 1:pp95–104, 1996.

[104] M. B. Hopkins, W. G. Graham, and T. J. Griffin. Automatic langmuir probe diagnostic. *Rev. Sci. Instrum.*, 58 (3):pp475–476, 1987.

[105] J. F. Waymouth. Perturbation of a plasma by a probe. *Phys. Fluids*, 7:pp 1843–1854, 1964.

[106] lot oriel webpage, [online].
http : //www.lot−oriel.com/site/pages_uk_en/mono_spectro/mono_spectro.php, 2003.

[107] R. W. P. McWhirter. *Plasma Diagnostic Techniques, Chapter 5.* North Holland Pubilshing Company, 1965.

[108] A. P. Thorne. *Spectrophysics, Chapter 11.* Chapman and Hall, 1974.

[109] M. Mitchner and C. H. Kruger. *Partially ionized gases, Chapter 8.* Wiley, 1973.

[110] P. G. Hill and C. R. Peterson. *Mechanics and Thermodynamics of Propulsion, Chapter 3.* Addison–Wesley Publishing Company, inc., 1965.

[111] A. P. Thorne. *Spectrophysics, Chapter 9.* Chapman and Hall, 1974.

[112] R. W. P. McWhirter. *Plasma Diagnostic Techniques, Chapter 6.* North Holland Pubilshing Company, 1965.

[113] C. Aragón, J. Bengoechea, and J. A. Aguilera. Influence of the optical depth on spectral line emission from laser–induced plasmas. *Spectrochimica Acta Part B*, 56:pp 619–628, 2001.

[114] Y. Ralchenko, F.C. Jou, D.E. Kelleher, A.E. Kramida, A. Musgrove, J. Reader, W.L. Wiese, and K. Olsen. NIST atomic spectra database (version 3.0.2), [online]. *http://physics.nist.gov/asd3*, 2004.

[115] Atomic and molecular database in the institute of applied physics and computational mathematics (iapcm), [online]. *http://www.camdb.ac.cn/e/*, 2004.

[116] E. B. Saloman. Energy levels and observed spectral lines of xenon, XeI through XeLIV. *J. Phys. Chem. Ref. Data*, 33, No. 3:pp 765–921, 2004.

[117] J. Sabbagh and N. Sadeghi. Experimental transition probabilities of some Xe(I) lines. *J. Quant. Spec. Rad. Trans.*, 17:pp 297–301, 1977.

[118] J. Cooper. Plasma spectroscopy. *Reports on progress in physics*, 22:35–130, 1966.

[119] W. L. Wiese. Spectroscopic diagnostics of low temperature plasmas: techniques and required data. *Spectrochimica Acta*, 46B, No.6/7:831–841, 1991.

[120] J Richter. *Plasma Diagnostics.* North Holland Pubilshing Company, 1968.

[121] R. J. Golston and P. H. Rutherford. *Introduction to plasma physics, Chapter 11.* Institute of physics, 1995.

[122] P. M. Fishbane, S. Gasiorowicz, and S. T. Thornton. *Physics for scientists and engineers.* Prentice–Hall, 1996.

[123] D. R. Lide. *Handbook of Chemistry and Physics.* CRC Press, Inc, 1995.

[124] A. Salhi and P. J. Turchi. A first principles model for orificed hollow cathode operation. *Joint Prop. Conf.*, AIAA 92-3742, 1992.

[125] A. Salhi and P. J. Turchi. Theoretical modeling of orificed hollow cathode discharges. *IEPC*, 93-024, 1993.

[126] D. M. Goebel, I. Katz, J. Polk, I. G. Mikellides, K. K. Jameson, T Liu, and R. Dongherty. Extending hollow cathode life for electric propulsion in long–term missions. *AIAA*, 2004-5911, 2004.

[127] M. Sauchanka Davis. NASA webpage, Jet Propulsion Laboratory, CalTech, [online]. *http://prometheus.jpl.nasa.gov*, 2005.

[128] J. D. Cobine. *Gaseous conductors.* Dover publications, Inc. New York, 1958.

[129] G. Franz and A. Kelp. Analysis of chlorine-containing plasmas applied III/V semiconductor processing. *J. Vac. Sci. Technol.*, 18:pp 2053–2061, 2000.

[130] D. L. Adams and W. Whaling. Argon branching ratios for spectral intensity calibration. *J. Opt. Soc. Am*, 71:pp 1036–1038, 1981.

[131] W. Whaling, M. T. Carle, and M. L. Pitt. Argon branching ratios for spectrometer response calibration. *J. Quant. Spec. Rad. Trans.*, 20:pp 7–18, 1993.

[132] J. Sugar and A. Musgrove. Energy levels of krypton, Kr I through Kr XXXVI. *J. Phys. Chem. Ref. Data*, 20:pp 859–915, 1991.

[133] M. Aymar and M. Coulombe. Theoretical transition probabilities and lifetimes in Kr I and Xe I spectra. *Atomic Data Nucl Data Tables*, 21:pp 537–566, 1978.

Appendix A

Nomenclature

Variables are shown with their associated units in brackets, these are the typical units used unless stated otherwise in the text.

$A(p,q)$ = Atomic transition probability (s^{-1}).

A_M = Atomic mass.

A_0 = Richardson constant.

a_0 = Bohr radius (m).

$B_\lambda(T)$ = Intensity of continuum radiation.

$\bar{b}_0$ = Impact parameter.

c = Speed of light in vacuo (ms^{-1}).

C_e = Electron thermal velocity (ms^{-1}).

d = Electron separation (m).

E = Electric field strength (Vm^{-1}).

e = Electron charge (C).

F = Thrust (N).

$f(p,q)$ = Atomic (absorption) oscillator strength (dimensionless).

$f^M(V)$ = Maxwellian velocity distribution.

$g(p)$ = Statistical weight of species in state p.

h = Planck's constant.

$I(\nu)$ = Radiation intensity.

j_e = Electron current density (Am^{-3}).

$J(\nu)$ = Emission coefficient.

k = Boltzmann constant.

K_n = Knudsen number.

l = Depth of plasma (m).

$\dot{m}$ = Mass flow rate (mgs^{-1}).

m = Heavy particle mass (Kg).

m_e = Electron mass (Kg).

m_i = Ion mass (Kg).

n_e = Electron density (m^{-3}).

$n(z+1,g)$ = Density of ions in ground state.

$n(z,g)$ = Density of neutrals in ground state.

R = Characteristic length of plasma (m).

R_G = Gas constant.

R_p = Plasma resistance (Ohms).

R_U = Universal gas constant.

$S(T_e,z,p)$ = Ionisation coefficient.

T = Insert surface temperature (K).

T_e = Electron temperature (eV).

t = Time (s).

V = Heavy particle velocity (ms^{-1}).

V_{bd} = Breakdown voltage (V).

V_E = Exhaust velocity (ms^{-1}).

V_p = Plasma potential (V).

ΔV = Change in velocity following a thrusting event (ms^{-1}).

$X(T_e,p,q)$ = Coefficient of electron impact excitation.

Z = Partition function.

z = Atomic charge.

Greek Symbols

$\alpha(T_e, z+1, p)$ = Coefficient of radiative recombination.

α_{ion} = Ionisation fraction.

$\beta(T_e, z+1, p)$ = Coefficient of three body recombination.

γ = Ratio of specific heats.

γ_T = Townsend coefficient.

ϵ_0 = Permittivity of free space.

ζ_z = Number of electrons in valance shell.

λ = Wavelength (nm).

λ_D = Debye length (m).

λ_{mfp} = Mean free path between collisions (m).

$\Delta\nu_D$ = Doppler half width (m).

ν_0 = Central frequency of spectral line (s^{-1}).

$\bar{\nu}_{ee}$ = Mean electron - electron collision frequency (s^{-1}).

$\bar{\nu}_{eh}$ = Mean electron - heavy particle collision frequency (s^{-1}).

ξ_{z+1} = Number of vacancies in the valance shell.

ρ = Mass density (Kgm^{-3}).

ρ_p = Plasma resistivity (Ohm m).

$\rho(\nu)$ = Plasma optical depth (m).

σ_p = Plasma conductivity $(Ohm^{-1}m^{-1})$.

σ_{sd} = Standard deviation.

τ = Characteristic time for plasma to change on macroscopic scale (s).

ϕ_{eff} = Effective work function (V).

ϕ_s = Surface work function (V).

$\phi(\nu_0)$ = Line shaping factor at central frequency.

$\chi(\nu)$ = Absorption coefficient.

$\chi(z, g)$ = First ionisation potential.

Appendix B

Corona Regime Electron Temperature

The line intensity ratio method outlined in section 4.6 forms the basis for the electron temperature calculation. The corona plasma electron temperature may be determined using the same method as that used in the LTE and CR cases i.e. the spectral line intensity may be related to the electron temperature, atomic data and cross section information in such a way as to form the equation of a straight line, as shown by Equ. B.1.

$$\underbrace{\ln\left(\frac{I(p,q)_1\chi(p,q)_1 B_2\bar{g}_2 f(p,q)_2}{I(p,q)_2\chi(\bar{q})_2 B_1\bar{g}_1 f(p,q)_1}\right)}_{y} = \underbrace{-\frac{e}{kT_e}}_{m}\underbrace{\{\chi(q)_1-\chi(q)_2\}}_{x}+\underbrace{\ln C}_{c} \qquad \text{(B.1)}$$

The technique is dependent on the availability of accurate gaunt factors that takes into account quantum mechanical processes, oscillator strengths and branching ratios. The corona model requires the population density of a state to be determined by collisional excitation into the state balanced by depopulation via radiative decay (see Fig. B.1). The branching ratio represents this process. Branching ratios have been determined experimentally and theoretically, but the values are not in agreement and the data sets presented in literature are incomplete [129, 130, 131]. Therefore the branching ratios presented here have been independently determined by taking the ratio of the transition probability of a given spectral line to the sum of the remaining appropriate transition probabilities.

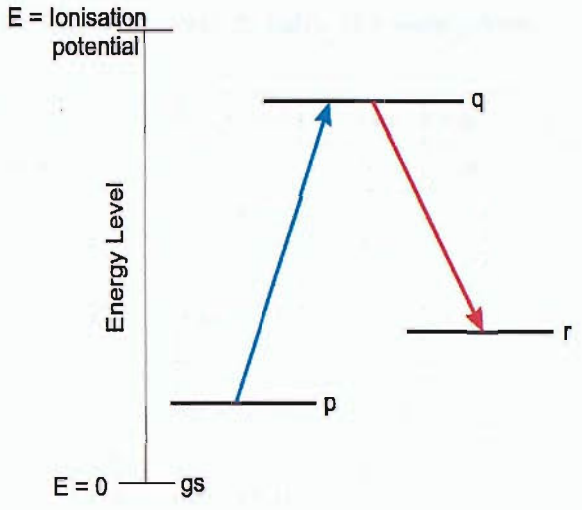

Figure B.1: Generic energy level diagram

The branching ratios were calculated for the atomic species in the states shown in Tables B.1 – B.3.

λ (nm)	State q config.	State r config.	Trans. Prob. (s^{-1})	Branching ratio
763.511	$3p5(2P^0_{3/2})4p$	-	2.45×10^7	0.712
800.6157	-	$3p5(2P^0_{3/2})4s$	4.90×10^6	
922.4499	-	$3p5(2P^0_{1/2})4s$	5.03×10^6	
794.818	$3p5(2P^0_{1/2})4p$	-	1.86×10^7	0.562
714.7042	-	$3s23p5(2P^0_{3/2})4s$	6.25×10^5	
852.1442	-	$3p5(2P^0_{1/2})4s$	1.39×10^7	
826.4522	$3p5(2P^0_{1/2})4p$	-	1.53×10^7	0.531
727.2936	-	$3p5(2P^0_{3/2})4s$	1.83×10^6	
772.4207	-	$3p5(2P^0_{1/2})4s$	1.17×10^7	
840.8210	$3p5(2P^0_{1/2})4p$	-	2.23×10^7	0.725
738.3980	-	$3p5(2P^0_{3/2})4s$	8.47×10^6	
842.465	$3p5(2P^0_{3/2})4p$	-	2.15×10^7	0.667
801.4786	-	$3p5(2P^0_{3/2})4s$	9.28×10^6	
978.4503	-	$3p5(2P^0_{1/2})4s$	1.47×10^6	

Table B.1: Argon Branching Ratios using NIST data

The data used for the calculation of branching ratios for neutral argon spectral lines were obtained from the NIST database. Out of a possible 213 spectral lines in the wavelength range of $\lambda = 0 - 3000nm$ the transition probabilities of 180 lines were stated. All of the

values for the required transitions used in Table B.1 were present in the database.

λ (nm)	State q config.	State r config.	Trans. Prob. (s^{-1})	Branching ratio
760.1544	$4p5(2P^0_{3/2})5p$	-	3.1×10^7	0.738
819.0054	-	$4p5(2P^0_{3/2})5s$	1.1×10^7	
785.4821	$4p5(2P^0_{1/2})5p$	-	2.3×10^7	0.522
557.0288	-	$4p5(2P^0_{3/2})5s$	2.1×10^6	
828.1050	-	$4p5(2P^0_{1/2})5s$	1.9×10^7	
805.9530	-	$4p5(2P^0_{1/2})5s$	1.9×10^7	0.442
850.8870	$4p5(2P^0_{1/2})5p$	-	2.4×10^7	0.531
892.8692	$4p5(2P^0_{3/2})5p$	$4p5(2P^0_{3/2})5s$	3.7×10^7	1

Table B.2: Krypton Branching Ratios using NIST data

The transition probabilities shown in Table B.2 were obtained from the NIST database, of 135 spectral lines in the wavelength range $\lambda = 0 - 3000nm$, 33 lines listed transition probabilities for $\lambda = 116 - 893nm$ fortunately only data in this range was required. The energy level data and configurations were stated in Ref. [132] and cross referenced with the data provided on the Atomic and Molecular Database[1].

λ (nm)	State q config.	State r config.	Trans. Prob. (s^{-1})	Branching ratio
823.1635	$5p5(2P^0_{3/2})6p$	-	2.49×10^7	0.376
828.0116	-	$5p5(2P^0_{3/2})6s$	3.4×10^7	0.502
979.9697	-	$5p5(2P^0_{3/2})6s$	3.10×10^7	
1083.834	-	$5p5(2P^0_{3/2})6s$	2.61×10^6	
3408.41	-	$5p5(2P^0_{1/2})6s$	0.0949×10^6	
881.9410	$5p5(2P^0_{3/2})6p$	-	3.00×10^7	0.498
904.5447	-	$5p5(2P^0_{3/2})6s$	1.07×10^7	
992.3198	-	$5p5(2P^0_{3/2})6s$	1.96×10^7	
895.2250	$5p5(2P^0_{3/2})6p$	-	0.965×10^7	0.146
823.1635	-	$5p5(2P^0_{3/2})6s$	2.39×10^7	
840.9189	-	$5p5(2P^0_{3/2})6s$	1.00×10^6	
916.2652	-	$5p5(2P^0_{3/2})6s$	3.16×10^7	
3624.1600	-	$5p5(2P^0_{1/2})6s$	0.0084×10^6	
4932.2900	-	$5p5(2P^0_{1/2})6s$	2.39×10^7	

Table B.3: Xenon Branching Ratios using theoretical data

[1] website url: http://www.camdb.ac.cn

The determination of branching ratios for neutral xenon lines was the most problematic; of the 174 listed lines in the range $\lambda = 100 - 4000nm$ only 23 are accompanied with transition probabilities. The theoretical transition probabilities determined in Ref. [133] were used to calculate the branching ratios for the excitation of neutral xenon atoms (see Table B.3).

Ar I		Kr I		Xe I	
λ (nm)	$f(p,q)$	λ (nm)	$f(p,q)$	λ (nm)	$f(p,q)$
763.511	0.214	760.154	0.269	823.164	0.243
794.818	0.529	785.482	0.0987	828.012	1.048
826.452	0.157	805.950	0.0617	881.941	0.250
840.821	0.394	850.887	0.261	895.225	0.0696
852.144	0.151	892.869	0.737	-	-

Table B.4: Oscillator strengths required for observed lines for corona regime calculations

The oscillator strength is related to the transition probability by the Ladenburg formula. The oscillator strengths for the argon and krypton transitions are stated in the NIST data tables. The oscillator strengths for xenon lines were calculated using Equ. 4.27 in conjunction with experimentally determined transition probabilities.

The mean gaunt factor is a correction factor for quantum mechanical effects. The lack of accepted values of $\bar{g}$ and the complexity of calculating the value from first principals has prevented the calculation of the corona regime electron temperature.

Appendix C

Program for Insert Temperature Calculation

C.1 Main Program

```
!*****************************************************

! PROGRAM: WallTemp

! PURPOSE: Entry point for the console application.

!*****************************************************

program WallTemp

USE vars

implicit none

!-------------------------------------------------------

! Variables


REAL:: T

REAL,DIMENSION(:,:):: RawData(392,2)

INTEGER:: er, i, j, k, m, n, nodata, jmax,kmax, mmax
```

```
CHARACTER(len=100)::file1, file2, file3

!Input Data, polynomial curve fit

file1='C:\Results\Input Files\Ar1.dat'

!Writes data: wavelength, intensity and temperature

file2='C:\Results\Temp.dat'

!Writes temperature values to file

file3='C:\Results\Temperature.dat'

nodata=392

jmax=392

kmax=0

mmax=76636

ALLOCATE(Temp(mmax,1))

!-----------------------------------------------------------

! Body of WallTemp

! Read in data over wavelength range 650 to 900nm

! Opening of the data file

OPEN(30,FILE=file1,IOSTAT=er,STATUS='old',ACTION='read')

! Opening of the new data file

OPEN(31,FILE=file2,IOSTAT=er,STATUS='unknown',ACTION='readwrite')

! Opening of the new data file
```

```
OPEN(32,FILE=file3,IOSTAT=er,STATUS='unknown',ACTION='readwrite')

! Initialise variables

i=1

!Reading wavelength and intensity values

DO i=1,nodata,1

READ(30,*) RawData(i,1), RawData(i,2)
END DO

CLOSE(30,IOSTAT=er)

!Temperature calculation

k=1
j=1
n=0
kmax=jmax

WRITE(*,*)"J= ",jmax
WRITE(*,*)"k= ",kmax

DO k=1,kmax,1

DO j=1,jmax,1

IF(j.GE.(k+1))THEN

!WRITE(*,*) RawData(k,1),RawData(j,1)

T=0.014413043*((RawData(k,1)-RawData(j,1))/
```

```
(RawData(k,1)*RawData(j,1)))/Log((RawData(k,2)/
RawData(j,2))*((RawData(k,1)**5)/
(RawData(j,1)**5)))

IF(T.LT.-1)THEN
T=T*(-1)
END IF

IF(T.LT. 10000 .AND. T.GT.0)THEN
WRITE(32,*) RawData(k,1),RawData(k,2),RawData(j,1),
RawData(j,2), T
WRITE(31,*) T
n=n+1
END IF

END IF

END DO

END DO

!Mean temperature and standard deviation calculated
!Read temperature values from beginning of file

Rewind(31) m=1

DO m=1,mmax,1
READ(31,*) Temp(m,1)
END DO
```

```
CALL statistics(mmax)

WRITE(*,*) "mean=", mean
WRITE(*,*) "variance=", variance
WRITE(*,*) "sd=", sd
WRITE(*,*) "N= ",n

CLOSE(32,IOSTAT=er)

CLOSE(31,IOSTAT=er)end program WallTemp
```

C.2 Module

```
!Module to define variables
!-----------------------------------------------

MODULE vars

REAL(KIND=8) :: mean,variance,sd
REAL(KIND=8) , DIMENSION(:,:) , ALLOCATABLE :: Temp

END MODULE vars
```

C.3 Subroutine

```
!Subroutine for computing mean,variance and standard deviation
!-----------------------------------------------

! Input requirement: N, length of vector containing temperature

! Example call: CALL standev(50,temperature)

SUBROUTINE statistics(N)

USE vars
```

```
IMPLICIT NONE

INTEGER(KIND=4) :: j,N

! Compute mean

mean = 0
DO j = 1,N,+1
mean = mean+Temp(j,1)
END DO

mean = mean/real(N)

! Compute variance

variance = 0

DO j = 1,N,+1
variance = variance+(Temp(j,1)-mean)*(Temp(j,1)-mean)
END DO

variance = variance/real(N-1)

! Compute standard deviation

sd = DSQRT(variance)

END SUBROUTINE statistics
```

Appendix D

Example Input File

λ (m)	B_λ (counts)
0.000000901108	2731.23
0.000000900471	2718.4
0.000000899834	2705.62
0.000000899198	2692.87
0.000000898561	2680.17
0.000000897924	2667.5
0.000000897287	2654.88
0.00000089665	2642.3
0.000000896013	2629.76
0.000000895376	2617.26
0.000000894739	2604.8
0.000000894102	2592.38
0.000000893465	2580
0.000000892828	2567.66

Table D.1: Section of input file for argon propellant $\dot{m} = 1.1mgs^{-1}$, $I_A = 2.0A$ in the probe 2 position in geometry 1. Resulting in $T = 1415.004 \pm 14.374K$

Appendix E

Example Output File

λ_1 (m)	$B_{\lambda 1}$(counts)	λ_2 (m)	$B_{\lambda 1}$(counts)	Temperature (K)
0.000000901108	2731.23	0.000000900471	2718.4	1372.48
0.000000901108	2731.23	0.000000850753	1839.76	1386.85
0.000000901108	2731.23	0.000000800306	1172.57	1400.29
0.000000901108	2731.23	0.000000750405	699.861	1410.92
0.000000901108	2731.23	0.000000700414	377.986	1415.66
0.000000901108	2731.23	0.000000650974	174.719	1404.75
0.000000899834	2705.62	0.000000899198	2692.87	1371.72
0.000000899834	2705.62	0.000000850115	1829.98	1387.37
0.000000899834	2705.62	0.000000800306	1172.57	1400.61
0.000000899834	2705.62	0.000000750405	699.861	1411.2
0.000000899834	2705.62	0.000000700414	377.986	1415.88
0.000000899834	2705.62	0.000000650974	174.719	1404.87

Table E.1: Selected lines from the output file the case of argon propellant $\dot{m} = 1.1mgs^{-1}$, $I_A = 2.0A$ in the probe 2 position. Resulting in temperature $T = 1415.004 \pm 14.374K$

Appendix F

Electrostatic Probe Design

Fig. F.1 shows a possible design for a single cylindrical electric probe. The main design considerations are the procurement of components with the required temperature rating that may be machined to the dimensions needed.

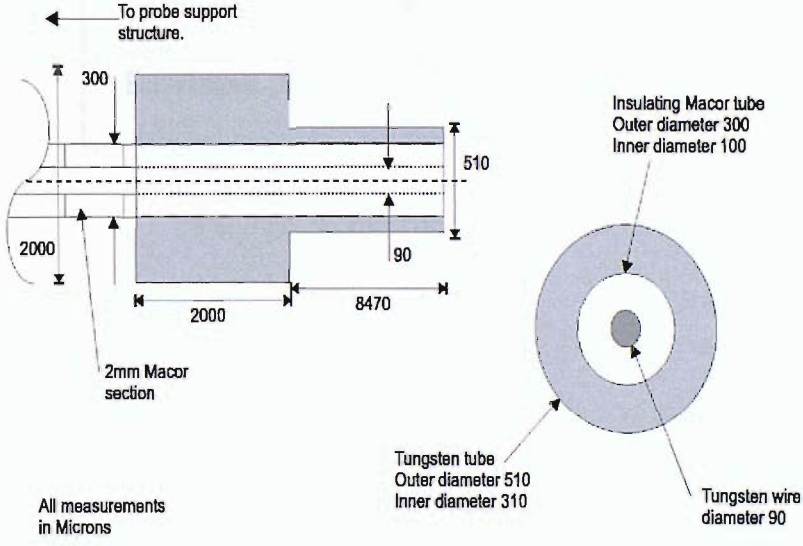

Figure F.1: Schematic of possible electric probe design

F.1 Electric Circuit and Data Acquisition

The probes must be able to collect currents of the order of mA with an accuracy of at least 20%. The circuit diagram shown in Fig. F.2 represents a system capable of collecting data from a maximum of six probes that may then be displayed and recorded using a multichannel digitalising oscilloscope. Alternatively a data acquisition card may be used to store and manipulate the data.

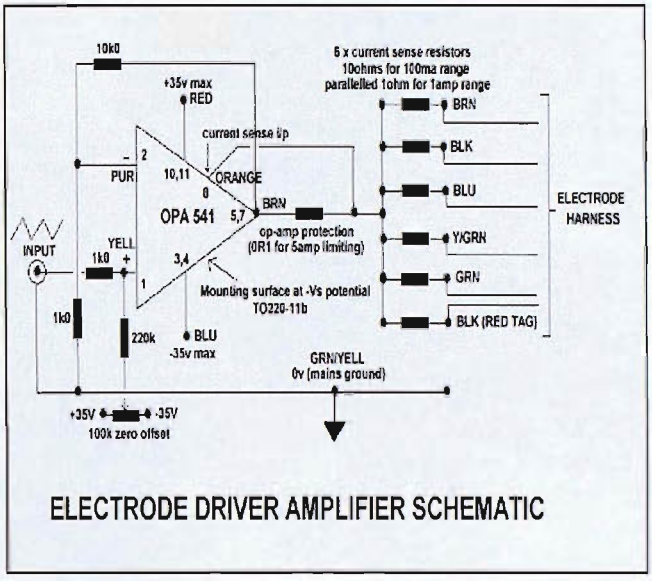

Figure F.2: Electric probe circuit